Uncertainty quantification of the fast flux calculation for a PWR vessel

Laura Clouvel

université
PARIS-SACLAY

cea

UNIVERSITÉ PARIS SUD
Comprendre le monde,
construire l'avenir

Uncertainty quantification of the fast flux calculation for a PWR vessel

Thèse de doctorat de l'Université Paris-Saclay
préparée à l'Université Paris-Sud

Ecole doctorale n°576 Particules, Hadrons, Énergie, Noyau, Instrumentation, Imagerie, Cosmos et Simulation (PHENIICS)
Spécialité de doctorat : Énergie nucléaire

Thèse présentée et soutenue à Saclay, le 13 Novembre 2019, par

Laura Clouvel

Composition du Jury :

Pierre Désesquelles
Professeur des universités, Université Paris-Sud   Président

Ivo-Alexander Kodeli
Enseignant-chercheur, Institut Jožef Stefan, Slovenia   Rapporteur

Bertrand Iooss
Chercheur Senior, EDF R&D /Département PRISME   Rapporteur

Claire Vaglio-Gaudard
Chercheur Expert, CEA-Cadarache/DEN   Examinateur

Pietro Mosca
Ingénieur-chercheur, CEA-Saclay/DEN   Superviseur

Jean-Marc Martinez
Chercheur Expert, CEA-Saclay/DEN   Directeur de thèse

Stéphane Bourganel
Ingénieur-Chercheur, CEA-Saclay/DEN   Invité

Thèse de doctorat

Acknowledgements - Remerciements

Je tiens tout d'abord à remercier très chaleureusement mon directeur de thèse Jean-Marc Martinez et mon encadrant Pietro Mosca, sans qui cette thèse n'aurait pas été aussi formatrice. Je vous remercie pour votre gentillesse, votre patience et votre disponibilité. J'ai appris beaucoup à vos côtés. Je suis très reconnaissante de tout ce que vous m'avez enseigné et du temps que vous m'avez accordé.

Un grand merci également aux membres du jury d'avoir évalué mon travail de thèse: le Professeur Pierre Desesquelles pour en avoir accepté la présidence, le Docteur Claire Vaglio-Gaudard pour avoir accepté d'examiner ce travail, et enfin le Docteur Ivo Kodeli et le Docteur Bertrand Iooss pour avoir pris le temps de lire ma thèse et d'avoir apporté les remarques et les corrections nécessaires.

L'aboutissement de cette thèse, je le dois aussi à tous.tes ceux.elles qui m'ont apporté leurs aides : Florent Chevallier, Fadhel Malouch, Claude Mounier, Frédéric Moreau, Fabrice Gaudier, Sébastien Lahaye, Stéphane Bourgagnel, Baptiste Broto, Anne-Marie-Baudron, Jean-Jacques Lautard. Merci de m'avoir donné les moyens de réaliser ce travail de recherche. J'ai apprécié de travailler à vos côtés tant sur le plan scientifique que sur le plan humain.

Michel et Pierre, un grand merci à vous deux. Vous m'avez fait confiance en me proposant respectivement un stage en Master 1 et 2. C'est quelque part grâce à vous que j'ai découvert mon goût pour la recherche, et que j'ai eu envie de faire cette thèse.

Un petit mot aussi à tous.tes les membres du Service d'Étude des Réacteurs et des Mathématiques appliquées (SERMA) du CEA, que j'ai pu côtoyer tout au long de cette thèse. Merci pour votre bonne humeur et toutes les discussions passionnantes partagées ensemble. Agathe, Andréa, Ansar, Brigitte, Carole, Elsa, Emiliano, Eve, Fatima, Igor, Jocelyne, Laurence, Meilin, Mireille, Nicolas, Pierre, Simone, Tan-Dat, Zarko, je vous souhaite le meilleur pour la suite.

Un grand merci aux nombreux.ses doctorant.e.s, postdoctorant.e.s et stagiaires du SERMA: Laurent, Henri, Margaux, Thomas, Wesley, Esteban, Gregory, Michel, Léandre, Sofiane, Valentin, Paul, Antonio, Dominique, Paolo, Vito, Andréa, Walid. Merci pour tous nos échanges, nos repas et nos pauses café partagés chaque jour, ou presque, pendant plus de trois ans. Vous avez fait de cette thèse un très beau souvenir !

Ami.es d'une vie, de lycée, de classes préparatoires et d'école d'ingénieur ... Benoit, Bérénice, Blandine, Bruce, Chacha, Cindy, Clément, Clotilde, Cycy, Laura, Lauralee, Lauriane, Laetitia, Lise, Ikram, Julie, Maeva, Manuela, Marc, Marie, Nicolas, Petit Soleil, Marion, Mathilde, Ph, Pierre, Pierrot, Renaud, Tarek, Titou. Merci de votre indulgence face à mes absences répétées durant toute cette thèse. Merci également pour tous ces beaux moments partagés un peu partout en France.

Ces trois années de thèse ont aussi été marquées par la rencontre de formidables personnes. Un immense merci à toute l'équipe de l'association Mahassine. Vous êtes la preuve que l'amitié

À mes parents,

Contents

INTRODUCTION

The production of electricity in Pressurized Water Reactors (PWR), consists in harnessing the heat released from the fission of atoms produced in the fuel of the reactor core, by using water as a coolant. The fission reaction results from the absorption of slow neutrons by nuclei of high atomic number. The nucleus splits into two lighter nuclei, called fission fragments and produces an average of 2.5 neutrons. In order to slow down the high-energy neutrons liberated by the fission reaction, the water also plays the role of moderator. A reflector is then installed around the reactor core to reduce neutron leakage by scattering back those which have escaped from the core. Despite the presence of the reflector, some neutrons still reach the reactor pressure vessel. The issue is that intense irradiation can alter the vessel microstructure and have an unfavourable effect on mechanical properties. This phenomenon is one of the major limiting factors to *nuclear reactor lifetime*. The vessel, which cannot be replaced, is actually the second *barrier against the radioactive leakage*. Surveillance programmes are therefore necessary for safety assessment and for verifying the *vessel structural integrity* (Steele, 1983).
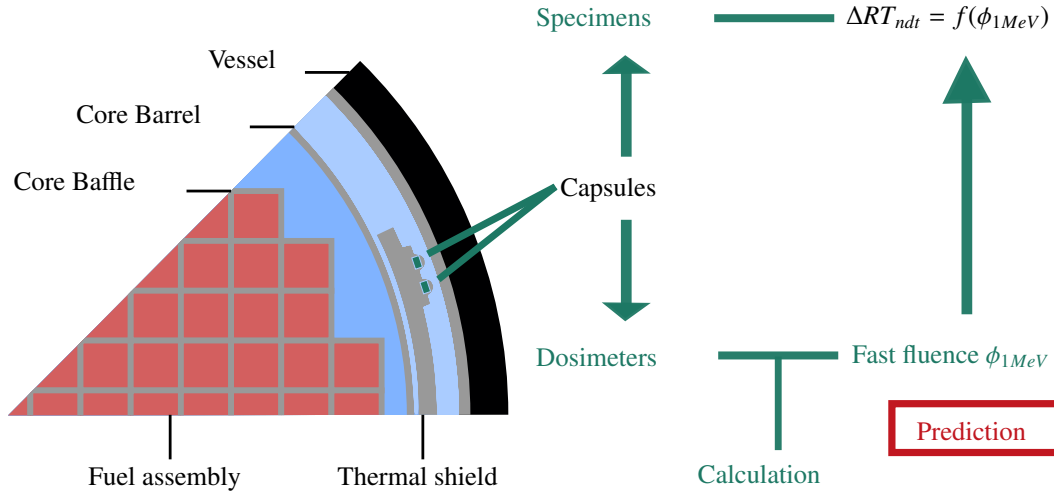
Figure 1: General Methodology in Irradiation Surveillance Programmes

Two tracks are commonly adopted to monitor the effects of neutron irradiation on the reactor vessel under actual operating conditions. They are based on the presence of surveillance capsules containing *steel specimens* and *dosimeters* and placed between the core and the vessel. During normal refuelling periods, steel specimens are removed from the reactor for performing tensile and fracture mechanics tests. Embrittlement rates by irradiation are measured as a shift of *ductile-to-brittle transition toughness temperature* ΔRT_{ndt} that increases with irradiation and describes the ability of material to resist fractures. On the other hand, the fracture toughness is a function of the neutron fluence. Usually, only neutrons with energies above 1 MeV are considered as the particles which produce the radiation damage on the vessel (Margolin et al., 2005). To monitor the radiation damage, it is thus also possible to use dosimeters to assess fast fluence at capsule location using activity measurements and activation codes. This assessment is notably based on tree inputs: the *fast neutron spectrum* ϕ_{1MeV}, the irradiation history and the cross sections drawn from activation dosimetry library (Dupré et al., 2015; Hassler et al., 1985). As capsules are placed upstream of the vessel, it is possible to predict the fast neutron flux received by the vessel and anticipate its embrittlement (OECD/NEA, 1997) following a lead factor f_{anti}. The quality of radiation damage prediction thus depends in part on the calculation of the neutron density ϕ_{1MeV}. In that sense, a lack of knowledge on the fast neutron flux will require larger safety margins on the plant lifetime affecting operating conditions and the cost of nuclear

installations. To make correct decisions when designing plant lifetime and on safety margins for PWR reactors, it is therefore essential to determine the *uncertainty in vessel flux calculations.*

Several publications which deal with the computational methods used in dosimetry programmes have been referenced in the OECD/NEA (1997) report. The latter document provides various methodologies used before 1996 for the fast flux computation and its associated uncertainty. It reports an average difference of 20% between measurements and the in-vessel transport calculations. The reason for this discrepancy is usually interpreted as the combination of different uncertainty and error sources in the simulation tools (Kodeli et al., 1996; Kam et al., 1990; Haghighat et al., 1996; Remec, 1996). The neutron density calculation indeed results from the implementation of successive physical models which depend on uncertain inputs, and on many assumptions involved for the calculation itself. The inaccuracy in the estimate of ϕ_{1MeV} thus arises from the combination of *numerical errors* (convergence criteria, computing methods, etc.), *modelling errors* (material, dimension and placement uncertainties, source distribution, etc.), and the propagation of *nuclear data uncertainties* (cross-sections, neutron spectrum, etc.). The resulting uncertainty on the calculated fast flux is finally estimated to 10 to 30 per cent (1σ) depending on the reactor type and the methodologies involved, while the uncertainty of the measurements are typically lower 5% for the dosimeters of PWR. The large number of results reported in the document shows the difficulty to analyse the calculation and measurement uncertainties according to the studied reactors and the various methodologies involving different codes, nuclear data sets and procedures. More recently, Kodeli (2001) has developed the sensitivity and uncertainty SUSD3D code package for the evaluation of sensitivity profiles and uncertainties on the cross-section data. The code allows carrying out uncertainty and sensitivity analysis and evaluating the contributions of various parameters involved in neutron flux and reaction rate calculations. It is based on a discrete ordinate sensitivity formulation of first-order perturbation theory. The code package was especially used to assess the fast flux uncertainty of the 900 MWe PWR vessel. Hence, Kodeli has shown that the uncertainty of the fast flux received in the most exposed vessel location, is in a 10% range.

However, most of past studies on the uncertainty assessment of the fast flux calculation are based on the *methods of moments* which assumes a linear *output variation*. The method of moments indeed consists in approximating the statistical moments of the system response by means of a truncated Taylor series expansion *y*. The function of interest is expanded about the mean of input variables, and one then calculates the moments of the truncated series (mean and variance). This method was most commonly used because the calculation capabilities of computers prevented from conducting more accurate methods. In a non-linear case, the first order hypothesis appears insufficient for an accurate prediction of the output variance. Higher order expansions could be used to account for skewed distributions, but are detrimental to the rapidity in setting up this method. On the other hand, as mentioned by Smith (1994), the expansion results only return an estimate of the statistical moments and not a distribution. The method ignores the probability distribution of parameters, making it difficult to determine quantiles on the output model. In safety analysis, confidence intervals can be actually useful to quantify the level of confidence that a safety parameter lies in an interval.

An alternative method is the *Total Monte Carlo approach* (TMC) which consists in randomly sampling the input data and propagating the perturbations on the calculation chain. The resulting output of a computer model is therefore considered as a random variable since the inputs are uncertain. The advantage of this method is that it does not make any assumptions on the linear interactions or small input changes among data. It also allows considering the covariance data to ensure consistent perturbations. In that sense, the TMC approach provides more accurate results because it allows propagating a more precise description of input uncertainties in the output calculation while ensuring data consistency and without presupposing the linearity of interactions.

It is within this context that our work was conducted. It consists in conducting a new uncertainty assessment of the fast flux calculation for the PWR vessel considering the data of recent international nuclear libraries and their associated covariances. The thesis is divided in two parts. The first part gives an overview of the background needed to carry out the uncertainty analysis. It is made in two chapters. The first chapter recalls the principle of neutron interactions and neutron transport. The second chapter is focused on methodologies of uncertainty and sensitivity analysis. The second part presents the methods and the results of the thesis. The methodology comprises three steps which are described in the different chapters of this work and illustrated in Fig.2.
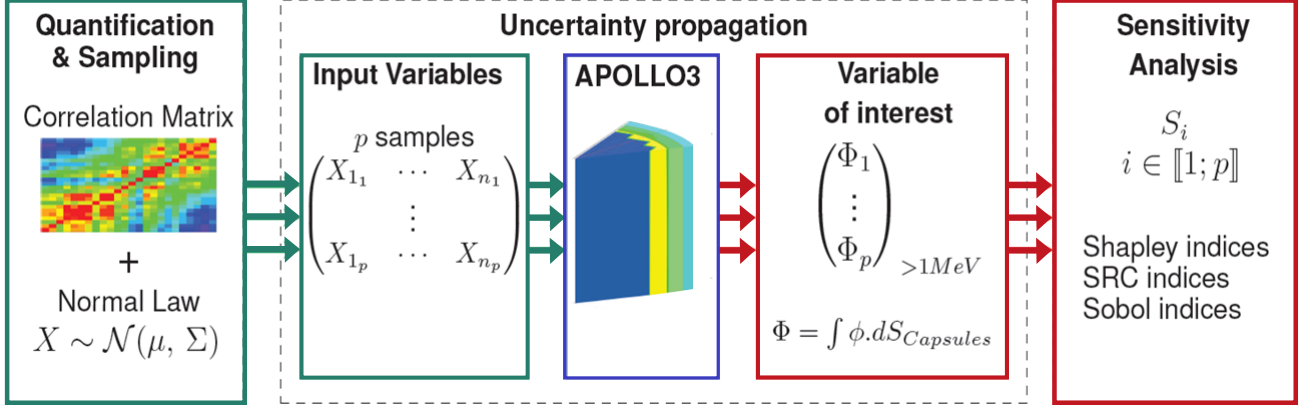
Figure 2: Uncertainty Propagation Scheme

The first chapter consists in defining a fast flux calculation sufficiently quick and accurate in comparison with the reference calculation. In France, fluence calculations are usually based on a stochastic neutron transport codes like TRIPOLI-4® (Brun et al., 2014). The issue is that the TMC sampling requires many perturbations to determine the uncertainty of output accurately. The deterministic methods are computationally faster than the stochastic one and thus they are more suitable to apply the propagation of uncertainties by TMC approach. For this reason, in this chapter, a deterministic scheme for the fast flux calculation is set up. The idea is to use some approximations to reach a compromise between speed and precision which allows carrying up a sufficient number of calculations. Another advantage of deterministic methods is that they provide flux distribution in all points of a modelled system in a single calculation, allowing conducting sensitivity analysis in different locations of the reactor and for different energy groups.

The second chapter presents the modelling of uncertainties, the random sampling of data and the methods used to keep the consistency among input data. As Kodeli (2001), we focus on the sources of uncertainty which may be treated statistically, i.e. the nuclear data (fission spectrum, energy and angular distribution of cross sections) and the technological uncertainties (power distribution, geometry, water temperature). Specifically, covariances and probability distributions are defined. Correlation matrices associated with nuclear data are reconstructed in coherence with the deterministic calculation scheme. We notably see that the reconstruction of the cross-section covariances can lead to the generation of ill-conditioned matrices. We show that using the singular value decomposition, it is possible to regularise simultaneously these matrices and sample the random variables.

The third chapter introduces the results of the uncertainty propagation in the fast flux calculation. It presents the sensitivity analysis conducted to assess the contribution of each input on the fast flux variance. In this context, the objective of sensitivity analysis is to help to prioritise efforts for uncertainty reduction and data improvement. Moreover, to consider the dependence

among input data in the sensitivity analysis, we use the concept of the Shapley value, recently suggested by Owen et al. (2017) and Iooss et al. (2019). Especially, when a linear model describes the behaviour of the output, Shapley indices can be computed analytically (Broto et al., 2018). However, the main drawback of this method is its exponential time complexity. To avoid this issue and rank the contribution of each input, we propose to use in the case of high-dimensional input spaces an alternative method based on Johnson's indices (Johnson, 2000). The two methods are compared and give similar results. Johnson indices allow us to pursue a comprehensive sensitivity analysis and to show the importance to consider the correlation data to preserve the physical consistency of data during uncertainty propagation and sensitivity analysis.

STATE-OF-THE-ART

This part presents an overview of the background needed to carry out the uncertainty analysis conducted in this thesis. It is made in two chapters. The first chapter recalls the principle of neutron interactions and neutron transport. The second chapter is focused on methodologies of uncertainty and sensitivity analysis.

Chapter I

Nuclear Background

One of the key problems in nuclear analysis is the evolution of the neutron population which governs the functioning of reactors and the main interactions with matter. The following sections present the various quantities and the theoretical background involved in such analysis. Before tackling the equations governing the time variation of the total neutron population, various quantities are introduced and a description of main interactions within a reactor is given.

1 Neutron interactions in reactor physics

During their paths within the reactor, neutrons, which are considered as point particles, can collide with atomic nuclei, producing a variety of nuclear reactions. Usually, the *microscopic cross section* is used to characterise the probability that a neutron will interact with a nucleus. It is denoted σ and expressed in *barn* where 1 *barn* = $10^{-24} cm^2$. This quantity is characterised by the energy levels of the target nuclei, and strongly depends on the speed of the neutrons. Depending on the nuclei and the energy range, the cross sections evolve differently and can be modelled by different theories. Generally, 3 energy ranges are identified to describe the likelihood of a neutron interaction: the *thermal* (< 1 eV), the *epithermal* (1 eV − 10 keV) and the *fast regions* (> 10 keV).
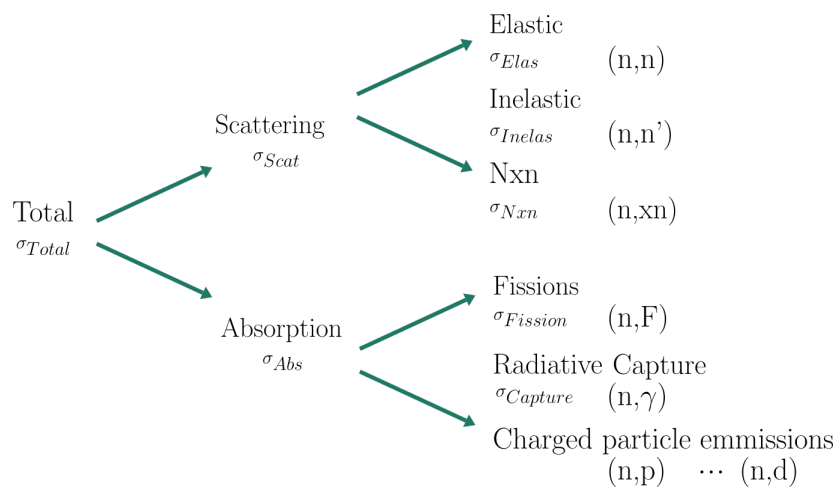
Figure I.1: Decomposition of the total cross section

Different types of neutron interactions are involved in nuclear reactors. By additivity of probability, the *total cross section* $\sigma_{Total}(E)$ can be decomposed into a sum of partial cross sections $\sum_p N_p \sigma_p(E)$, which describe the different sorts of interactions for each nucleus (Fig.I.1). A distinction is made between scattering and absorption processes. The most important *scattering reactions* are elastic and inelastic processes where the nucleus keeps the same number of protons and neutrons. In *absorption processes*, the neutron is absorbed by the target nucleus and three types of reactions can occur. If the nucleus is fissile, it can split into two lighter nuclei, called fission fragments and can produce one or more neutrons. Various secondary radiation emissions (Radiative capture) or charged particle emissions can also arise.
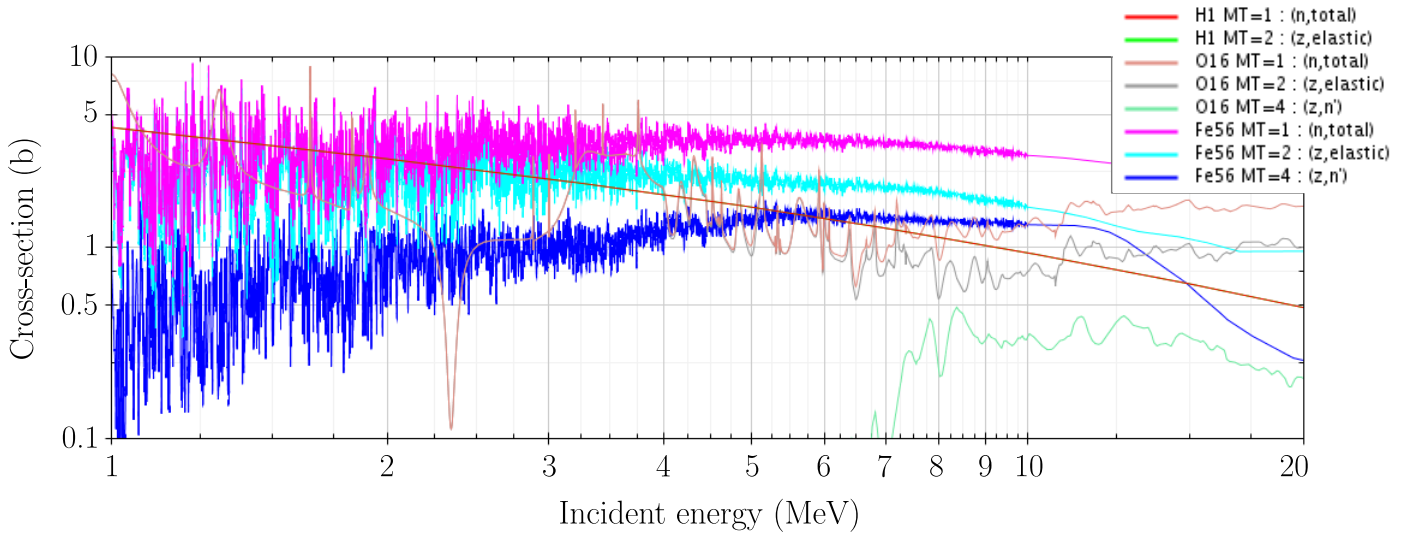
Figure I.2: Cross sections of ^{56}Fe, ^{16}O and ^{1}H for various reactions *MT* depending on the incident neutron data
JEFF-3.3 evaluation from JANIS Books

In thermal reactors, fissions mostly result from the absorption of slow neutrons by nuclei of high atomic number. The nucleus splits into two lighter nuclei, called fission fragments and often produces an average of 2.5 neutrons with an energy of about 1 MeV or more, which will in turn interact with matter. Most of the fast neutrons which escape from the core are scattered back by the reflector and slowed down by water, which acts as a moderator, until they reach thermal equilibrium. During elastic scattering, the speed and direction of a neutron are changed due to elastic collisions with a nucleus. In water reactors, hydrogen (see Fig. I.2) is a good neutron moderator because of its mass, which is almost identical to that of a neutron. During a collision with hydrogen, the neutron thus loses a part of its kinetic energy and hence slows down.

If the energy of the incident neutron is close to the energy of an excited state of the nucleus, resonance peaks can also be observed, revealing the quantum nature of nuclear interactions. Resonances are often observed in the epithermal range, where cross sections can vary very quickly. For the major structural materials, as ^{56}Fe (Fig. I.2), the resonance region is extended up to 1 MeV. Another property of the ^{56}Fe in fission reactors is its ability to slow down fast neutrons by inelastic scattering.

2 Boltzmann neutron transport equation in isotropic bounded domain

The neutron transport equation describes the distribution of neutrons in space, energy and time. There are two main forms of neutron transport equation which involves different techniques of resolutions:

- the *integro-differential form* which expresses the balance between neutron loss and gain in a volume element and which is explicitly solved by the deterministic codes,

- the *integral form* where the transport process is viewed from the perspective of an individual neutron instead of dealing with the entire neutron population described by the flux.

2.1 The integro-differential equation

The integro-differential equation gives a balance statement of neutrons in a time range dt around the point $(\vec{r}, E, \vec{\Omega})$ of the phase space and on elementary volume $d\vec{r}.dE.d\vec{\Omega}$ (Reuss, 2012), where $\vec{r}, E, \vec{\Omega}$ respectively describe the space, the energy and the direction of motion ($\vec{\Omega} = \frac{\vec{v}}{v}$). The angular neutron flux $\psi(\vec{r}, E, \vec{\Omega}, t)$ models the neutron density per unit volume at the time t and assuming that:

$$\begin{cases} \psi(\vec{r}, E, \vec{\Omega}, t = 0) = \psi_0(\vec{r}, E, \vec{\Omega}) \\ \text{On the contour area } \partial V, \psi(\vec{r}, E, \vec{\Omega}, t) = 0 \end{cases} \qquad \text{(I.1)}$$

The scalar flux $\Phi(\vec{r}, E, t)$ is obtained by integration of the angular flux over all directions:

$$\Psi(\vec{r}, E, t) = \int_{4\pi} \psi(\vec{r}, E, \vec{\Omega}, t) d^2\vec{\Omega}. \qquad \text{(I.2)}$$

Using the scalar flux $\Psi(\vec{r}, E, t)$, it is consequently possible to determine the quantity of interest in neutron transport analysis, i.e. the rates of neutron-induced reactions throughout the reactor core which is an observable quantity defined by:

$$\tau(\vec{r}, E, t) = N(\vec{r}, t)\sigma(E)\Psi(\vec{r}, E, t) = \Sigma(\vec{r}, E, t)\Psi(\vec{r}, E, t), \qquad \text{(I.3)}$$

where $N(\vec{r}, t)$ is the density of nuclei, and $\sigma(E)$ and $\Sigma(\vec{r}, E, t)$ are the microscopic and the macroscopic cross sections which measure the probability that a neutron has an interaction respectively per target nucleus and per centimetre path length.

For easier modelling of the interactions between neutrons and nucleus, some assumptions are considered and allow writing the transport equation.

Hypothesis
  i. The interactions among neutrons are ignored because the neutron density is small compared to the density of medium,
 ii. Between collisions, the neutrons move in a straight line and with a constant speed,
iii. The relativistic effects are neglected,
 iv. The probability that a neutron becomes a proton by β^- decay is also neglected.

The variation of the angular flux in time $\frac{1}{v}\frac{\partial \psi(\vec{r},E,\vec{\Omega},t)}{\partial t}$ thus results from the balance between gain and loss of neutrons:

- The term of streaming of neutrons within space and energy, and the term of the total neutron collision rate determined by the total cross section, $\Sigma_t(\vec{r},E,t)$

$$\mathbf{L}\psi(\vec{r},E,\vec{\Omega},t) = \vec{\Omega}.\vec{\nabla}\psi(\vec{r},E,\vec{\Omega},t) + \Sigma_t(\vec{r},E,t)\psi(\vec{r},E,\vec{\Omega},t). \tag{I.4}$$

- The term of neutron scattering from the initial energy E' and direction Ω' into energy E and direction Ω,

$$\mathbf{H}\psi(\vec{r},E,\vec{\Omega},t) = \int_0^\infty dE' \int_{4\pi} d^2\vec{\Omega}' \Sigma_S(\vec{r},E' \rightarrow E, \vec{\Omega}' \rightarrow \vec{\Omega},t)\psi(\vec{r},E',\vec{\Omega}',t). \tag{I.5}$$

In nuclear reactors, mediums can be considered as isotropic, making the scattering cross sections dependent only on the energy transfer $E' \rightarrow E$, and on the relative deviation $\vec{\Omega}.\vec{\Omega}'$:

$$\mathbf{H}\psi(\vec{r},E,\vec{\Omega},t) \approx \int_0^\infty dE' \int_{4\pi} d^2\vec{\Omega}' \Sigma_S(\vec{r},E' \rightarrow E, \vec{\Omega}.\vec{\Omega}',t)\psi(\vec{r},E',\vec{\Omega}',t) \tag{I.6}$$

- The term of neutron source emitted isotropically by fission and obtained from the spectrum $\chi_i(E,E')$ for each fissile isotope i present in the core and for $v(E')$ the average number of neutrons emitted[1]:

$$Q_{fiss}(\vec{r},E,t) = \frac{1}{4\pi} \sum_i \int_0^\infty dE' \chi_i(E,E')(v\Sigma)_{f,i}(\vec{r},E',t)\phi(\vec{r},E',t), \tag{I.7}$$

- The term of external source,

$$Q_{ext}(\vec{r},E,\vec{\Omega},t). \tag{I.8}$$

Often, the external source is neglected $Q_{ext} = 0$ in PWR studies.

Boltzmann integro-differential transport equation

Finally, the Boltzmann's operators $\mathbf{H}$, $\mathbf{L}$ give the following transport equation:

$$\frac{1}{v}\frac{\partial \psi(\vec{r},E,\vec{\Omega},t)}{\partial t} + \mathbf{L}\psi(\vec{r},E,\vec{\Omega},t) = \mathbf{H}\psi(\vec{r},E,\vec{\Omega},t) + Q_{fiss}(\vec{r},E,t) \tag{I.9}$$

2.2 The steady state integro-differential equation

Several basic types of neutron transport problems exist, depending on the type of problem being solved. Usually, a stationary solution of the transport equation is sought and the temporal variations are generally approached by a succession of steady states. Let consider for the following sections, the stationary flux $\phi(\vec{r},E)$.

---

[1]In the sequel, ψ and ϕ will be used to describe the angular flux and the scalar flux, respectively.

2.2.1 The critical equation

A fission reactor is by definition a multiplying system. It means that the time evolution of a neutron population depends on the neutron balance, i.e. the ratio between productions and losses described in the Eq. I.9. If productions and losses exactly balance, the neutron flux is constant. Most of the time, reactors operate at a constant power, i.e. with a constant number of neutrons. In such conditions, the flux is distributed on the critical mode which satisfies the steady-state neutron transport equation.

For simulating all the possible reactor states (critical, subcritical, supercritical) without having to solve a time-dependent equation, it is still possible to guarantee the balance between gain and loss of neutrons in the equation, and thus the stationarity. It consists in artificially adjusting the source term by dividing it by an effective multiplication factor k_{eff}.

Steady-state transport equation for critical calculations

Mathematically, the k_{eff} corresponds to the eigenvalue of the neutron transport problem:

$$\mathbf{L}\psi(\vec{r}, E, \vec{\Omega}) = \mathbf{H}\psi(\vec{r}, E, \vec{\Omega}) + \frac{1}{k_{eff}}Q_{fiss}(\vec{r}, E) \tag{I.10}$$

In that way, three interpretations of the effective multiplication factor appear:

- $k_{eff} = 1$ - The reactor is *critical*. There is a perfect balance between production and loss of neutrons,

- $k_{eff} < 1$ - The reactor is *sub-critical*. The removal of neutrons excesses the fission process and the chain reaction is not maintained,

- $k_{eff} > 1$ - The reactor is *super-critical*. There is a growth of the neutron population.

2.2.2 The steady-state equation at fixed sources

For the estimation of the reactor vessel flux, the common approach is to perform stationary fixed-source transport calculations. It consists in imposing a known neutron source Q which results from a previous critical calculation and in determining the resulting neutron distribution throughout the problem by solving the stationary Boltzmann equation.

Steady-state transport equation with fixed sources

$$\mathbf{L}\psi(\vec{r}, E, \vec{\Omega}) = \mathbf{H}\psi(\vec{r}, E, \vec{\Omega}) + Q(\vec{r}, E, \vec{\Omega}) \tag{I.11}$$

2.3 The steady-state integral equation

For some applications, an integral form of the neutron transport equation can be useful. It is in fact possible to deduce an integral form of the neutron transport equation by using the method of characteristics (Bell, G. I. and Glasstone S., 1970). The aim is to find the curves $\vec{r}(s)$ and $t(s)$, i.e. the characteristics, along which a partial differential equation becomes an ordinary differential equation that can be formally integrated (Courant, R. and Hilbert D., 2008). In this work, we consider only the steady-state integral form which will be used in the following chapters.

So, let us reconsider the integro-differential form of the steady-state neutron transport Eq.I.11. By expressing the position of a neutron as a function of its curvilinear abscissa s along its trajectory, and considering variations of ϕ around the point $\vec{r} = \vec{r}_0 - s\vec{\Omega}$, we can write the following equation:

$$-\frac{d}{ds}\psi(\vec{r}_0 - s\vec{\Omega}, E, \vec{\Omega}) + \Sigma_t(\vec{r}_0 - s\vec{\Omega}, E)\psi(\vec{r}_0 - s\vec{\Omega}, E, \vec{\Omega})$$
$$=$$
$$\int\int \Sigma_S(\vec{r}_0 - s\vec{\Omega}, E' \to E, \vec{\Omega}.\vec{\Omega}')\psi(\vec{r}_0 - s\vec{\Omega}, E', \vec{\Omega}') + Q(\vec{r}_0 - s\vec{\Omega}, E, \vec{\Omega})$$

(I.12)

The curve passing through the point $\vec{r}_0$ is the straight path followed by a neutron arriving in $\vec{r}_0$ at the energy E since its last collision. Before the integration of the variations of the flux along the straight line leading to the point $\vec{r}$, we introduce an *integrating factor* defined as the probability that a neutron has to reach $(\vec{r}, E, \vec{\Omega})$ without collision: $e^{-\tau(s)}$ where $\tau(s) = \int_0^s \Sigma_t(\vec{r}_0 - s'\vec{\Omega}, E, \vec{\Omega})ds'$ is the *optical distance* illustrated in Fig. I.3.
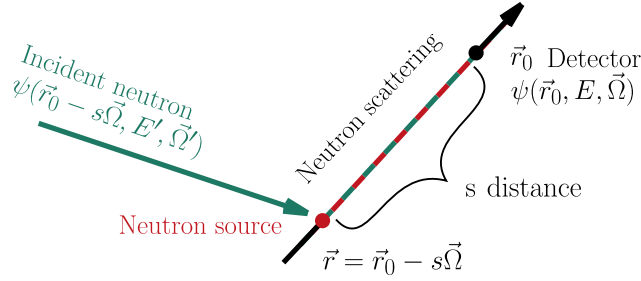
Figure I.3: Characteristic curve

Considering that:

$$\frac{d}{ds}\left[e^{-\tau(s)}\psi(\vec{r}_0 - s\vec{\Omega}, E, \vec{\Omega})\right]$$
$$=$$
$$e^{-\tau(s)}\left[-\Sigma_t(\vec{r}_0 - s\vec{\Omega}, E)\vec{\Omega}\psi(\vec{r}_0 - s\vec{\Omega}, E, \vec{\Omega}) + \frac{d}{ds}\psi(\vec{r}_0 - s\vec{\Omega}, E, \vec{\Omega})\right],$$

(I.13)

we can then write, thanks to the Eq. I.12, the following relation:

$$-\frac{d}{ds}\left[e^{-\tau(s)}\psi(\vec{r}_0 - s\vec{\Omega}, E, \vec{\Omega})\right]$$
$$=$$
$$e^{-\tau(s)}\left[\int\int \Sigma_S(\vec{r}_0 - s\vec{\Omega}, E' \to E, \vec{\Omega}.\vec{\Omega}')\psi(\vec{r}_0 - s\vec{\Omega}, E', \vec{\Omega}') + Q(\vec{r}_0 - s\vec{\Omega}, E, \vec{\Omega})\right]$$

(I.14)

To integrate this equation over the characteristics s from 0 to s_0 and consider the presence of boundaries, we assume that there is a value s_0 such that outside this boundary the flux is null.

Integral steady-state transport equation with fixed sources

Finally, the steady-state integral equation is given by:

$$\psi(\vec{r}, E, \vec{\Omega}) = \int_0^{s_0} ds \exp\left[-\int_0^s \Sigma_t(\vec{r}_0 - s'\vec{\Omega}, E)ds'\right] S(\vec{r}_0 - s\vec{\Omega}, E, \vec{\Omega})$$

$$+ \int_0^{s_0} ds \exp\left[-\int_0^s \Sigma_t(\vec{r}_0 - s'\vec{\Omega}, E)ds'\right] \Sigma_S(\vec{r}_0 - s\vec{\Omega}, E' \to E, \vec{\Omega}.\vec{\Omega}')\psi(\vec{r}_0 - s\vec{\Omega}', E', \vec{\Omega}')$$

(I.15)

The angular flux $\psi(\vec{r}, E, \vec{\Omega})$ thus results from the two terms at the right-hand side of Eq. I.15 :

- The first is the source $S(\vec{r}_0 - s\vec{\Omega}, E, \vec{\Omega})$ of neutrons emitted at $\vec{r} = \vec{r}_0 - s\vec{\Omega}$ and at the energy E in the direction $\vec{\Omega}$.

- The second is the term of neutron scattering $\Sigma_S(\vec{r}_0 - s\vec{\Omega}, E' \to E, \vec{\Omega}.\vec{\Omega}')$ from the initial energy E' and direction Ω' into energy E and direction Ω.

3   Solving the neutron transport equation

As explained previously, there are two general approaches for solving the transport equation and modelling neutron evolution within a reactor:

- the deterministic method based on the *integro-differential* equation I.9 which can be simplified with suitable approximations, for example, with the discretisation of the phase space and on the numerical methods involving the spatial and energetic processing of the neutron propagation,

- the stochastic method which simulates the motions of many neutrons to model how they interact with matter, and statistically solves the *exact complete integral* form of the transport equation.

The choice of the method depends on the criteria of speed and accuracy required for calculations. The random sample necessary to accurately describe the different possible directions of neutrons makes the use of stochastic methods expensive. However, with improved computing performance, they are being increasingly used as reference calculations because they provide a more accurate description of the reactor physics. On the other hand, deterministic methods are often preferred for quick first-hand calculations. The following sections therefore introduce both solving approaches.

3.1   Deterministic method

Many methods have been proposed to construct finite numerical approximations of the integro-differential transport equation and discretise the energy, angular and spatial dependence of flux. In this section, we focus on simplifications and approximations that will be used in the thesis.

3.1.1 Energy discretisation by multigroup formalism

Most deterministic methods use a multigroup approach based on the energy discretisation. The energy is in fact discretised in different intervals called groups that form a multigroup mesh. The number of energy groups depends on the desired precision for simulations and on the energy domain studied. In that sense, it is possible to convert each term of the Eq. I.11 in a multigroup form:

Multigroup and differential form of the steady-state transport equation

$$\vec{\Omega}.\vec{\nabla}\psi^g(\vec{r},\vec{\Omega}) + \Sigma_t^g(\vec{r})\psi^g(\vec{r},\vec{\Omega}) = Q^g(\vec{r},\vec{\Omega}). \qquad (I.16)$$

In practice, the multigroup discretisation may be performed in many instances of a computational scheme. The first energy condensation occurs when the NJOY Nuclear Data Processing System (MacFarlane, 2017) convert pointwise data into multigroup form, as discussed later in Section 4.3. The next energy condensation can then arise in lattice code to energetically condense and spatially homogenise the cross section data into the structure needed for the reactor core calculation.

Specifically, multigroup cross sections are defined following conservation of the multigroup reaction rate $\sigma^g(\vec{r})\phi^g(\vec{r})$, that is, equalising the integral value of the pointwise reaction rate $\sigma(E)\phi(\vec{r},E)$ on the group g. For each group of the energy mesh, the multigroup cross section is thus defined by:

$$\sigma^g(\vec{r}) = \frac{\int_g \sigma(\vec{r},E)\phi(\vec{r},E)dE}{\phi^g(\vec{r})}, \qquad (I.17)$$

where $\phi^g(\vec{r}) = \int_g \phi(\vec{r},E)dE$ is the multigroup flux solution of the Boltzmann multigroup equation.

This formalism, however, raises several practical difficulties (Coste-Delcaux, 2006):

- the pointwise flux $\phi(\vec{r},E)$ is unknown,
- the multigroup flux $\phi^g(\vec{r})$ is solution of the Boltzmann multigroup equation for which the multigroup cross sections are the input parameter of deterministic codes,
- the multigroup cross sections are intrinsic to the geometry of the problem to solve.

To create cross sections which are independent of the geometry, an alternative method consists in replacing the flux in the equation I.17 by a weight function $w(E)$ which is representative of the spectrum and independent of position. The multigroup cross sections are thus said to be at *infinite dilution*:

$$\sigma^g \approx \frac{\int_g \sigma(E)w(E)dE}{\int_g w(E)dE}. \qquad (I.18)$$

The approximation is acceptable for non-resonant nuclei for which the cross section is relatively smooth but it is not sufficiently accurate for the resonant nuclei when the energy mesh is too broad. In fact, the existence of resonances leads to a depreciating flux. This phenomenon is called energy self-shielding, and it is the more influential the greater the concentration of resonant nuclei is. To capture efficiently the self-shielding effect, the first possibility is to refine energy mesh taking an exact account of the variations of cross sections and flux. The problem is that the calculation time strongly depends on the energy group number. Another possibility is to employ a self-shielding method as the Livolant-Jeanpierre and the subgroup methods (Livolant and Jeanpierre, 1974; Coste-Delcaux, 1996).

3.1.2 Approximation of angular dependence by the S_N method of discrete ordinates

To derive the angular dependence, one of the best-established methods is the *collocation* method of discrete ordinates (S_N). The method consists in choosing $M = N(N + 2)$ isolated directions (*ordinates*) $\omega = \{\vec{\Omega}_m; m = 1..M\}$ as:

$$\psi(\vec{r}, \vec{\Omega}) \approx \begin{cases} \psi(\vec{r}, \vec{\Omega}_m) \text{ if } \vec{\Omega} = \vec{\Omega}_m \text{ and } \vec{\Omega}_m \in \omega \\ 0 \text{ and } \vec{\Omega} \notin \omega \end{cases} \tag{I.19}$$

S_N angular discretisation of the steady-state transport equation with fixed sources

The steady-state transport equation I.11 with fixed sources can thus be written for one group g and one direction m as:

$$\mathbf{L}_m^g \psi^g(\vec{r}, \vec{\Omega}_m) = \mathbf{H}_m^g \psi^g(\vec{r}, \vec{\Omega}_m) + Q^g(\vec{r}, \vec{\Omega}_m), \tag{I.20}$$

with

$$\mathbf{L}_m^g \psi^g(\vec{r}, \vec{\Omega}_m) = \vec{\Omega}_m.\vec{\nabla}\psi^g(\vec{r}, \vec{\Omega}_m) + \Sigma_t^g(\vec{r})\psi^g(\vec{r}, \vec{\Omega}_m), \tag{I.21}$$

$$\mathbf{H}_m^g \psi^g(\vec{r}, \vec{\Omega}_m) = \int_{4\Pi} d\vec{\Omega}' \Sigma_s(\vec{r}, g' \rightarrow g, \vec{\Omega}_m.\vec{\Omega}')\psi^g(\vec{r}, \vec{\Omega}_m), \tag{I.22}$$

and evaluating the angular integral by the Wick quadrature formula (Lee, 1961) with M weights ω_m:

$$\frac{1}{4\Pi}\int_{4\Pi} d\vec{\Omega}f(\vec{\Omega}) = \sum_{m=1}^{M} \vec{\Omega}_m f(\vec{\Omega}_m), \tag{I.23}$$

Usually the M directions and weights are fixed by a Gauss quadrature formula. The resulting system of M equations is thus solved and the $\psi^g(\vec{r}, \vec{\Omega}_m)$s are the unknowns of the system.

3.1.3 Spatial discretionary by discontinuous finite element

The last approximation used for solving partial differential equations is the spatial discretisation. In particular, the method of discontinuous finite element can be associated with an S_N approach for a mesh-by-mesh resolution that does not require the resolution of the overall system of unknowns. It consists in expressing the flux on each mesh C as a basis function (polynomial) w in the projection space and without imposing the continuity of flux at interfaces among neighbour mesh.

Spatial discretionary by discontinuous finite element

The discrete formulation on the mesh of contour ∂C^- is then given by:

$$\int_C \vec{\Omega}_m.\vec{\nabla}\phi^m w d\vec{r} + \int_{\partial C^-} \vec{\Omega}_m.\vec{n}_e(\psi_e^+ - \psi_e^-)w d\vec{r} + \int_C \Sigma_S \phi w d\vec{r} = \int_C q_m w d\vec{r}. \tag{I.24}$$

3.2   Monte Carlo method

The Monte Carlo method was introduced by John Von Neumann and Stanley Ulam. This method allows finding a statistical solution to the *integral equation* I.15 where the transport process is viewed from the perspective of an individual neutron instead of dealing with the entire neutron population when solving the integro-differential form.

3.2.1   Stochastic neutron propagation by Markovian process

Let us now reconsider the integral equation introduced in the previous section 2.3. By using the following identity:

$$\int_0^\infty f(\vec{r}_0 - s\vec{\Omega})ds = \int f(\vec{r})\left(\delta(\vec{\Omega} - \frac{\vec{r}_0 - \vec{r}}{|\vec{r}_0 - \vec{r}|})\right)\frac{d\vec{r}}{|\vec{r}_0 - \vec{r}|^2}, \tag{I.25}$$

the line integral equation can be transformed into a volume integral equation (Vassiliev, 2017).

To simplify the notations, one commonly defines the two following kernels (Nowak, 2018):

- the *transition kernel*, i.e. the probability density for a particle at $\vec{r}$ to reach the distance $s = |\vec{r}_0 - \vec{r}|$ without collision and to be subject at a collision at $\vec{r}_0$,

$$T(\vec{r} \to \vec{r}_0, E, \vec{\Omega}) = \Sigma_t(\vec{r}_0 - s\vec{\Omega}, E)e^{-\tau(s)}\left[\delta(\vec{\Omega} - \frac{\vec{r}_0 - \vec{r}}{|\vec{r}_0 - \vec{r}|})\frac{1}{|\vec{r}_0 - \vec{r}|^2}\right], \tag{I.26}$$

- the *collision kernel*, i.e. the probability for a particle entering a collision at $(\vec{r}_0, E', \vec{\Omega}')$ to be scattered in energy E and direction $\vec{\Omega}$,

$$C(\vec{r}_0, E' \to E, \vec{\Omega}' \to \vec{\Omega}) = \frac{\Sigma_S(\vec{r}_0 - s\vec{\Omega}, E' \to E, \vec{\Omega}.\vec{\Omega}')}{\Sigma_t(\vec{r}_0 - s\vec{\Omega}, E)}. \tag{I.27}$$

The two kernels allow introducing the *collision density* defined as $\tau(P) = \Sigma_t(P)\phi(P)$, the rate at which particles undergo a collision at P:

$$\tau(P) = S_1(P) + \int \tau(P'')dP'P'', \tag{I.28}$$

where S_1 is the source of the first collision.

The collision density can also be written as a *Neumann series expansion*:

$$\tau(P) = \sum_n^\infty \tau_n(P). \tag{I.29}$$

Each term of this series can be obtained by recurrence of the previous one following the formulation:

$$\tau_n(P) = \int ... \int S(P_0)T(P_0 \to P_1)K(P_1 \to P_2)...K(P_{n-1} \to P)dP_0 P_1...dP_{n-1}, \tag{I.30}$$

such as $K(P' \to P) = T(P' \to P)C(P'' \to P)$.

Eq. I.30 shows that the state of the neutron at the step n is determined by the state of the neutron at the previous step $n - 1$. The random process of the neutron propagation thus follows a *Markovian process*. The resolution of the integral neutron transport equation can thus be achieved by simulating a chain of events which constitutes the history of each neutron source.

3.2.2 Analogue simulation

We can now understand how the Monte Carlo approach simulates the stochastic nature of neutron transport through matter, i.e. by tracing the *random walk* of an individual neutron in matter and considering the various interactions that may determine its history.

Let us imagine the behaviour of a single neutron from its source to a tally (a detector). In a nuclear reactor, the fission is the main source of neutrons. The fission source can be described by its distribution in space (directly linked to the power of assemblies in the reactor), its distribution in energy (defined by a spectrum) and its distribution in direction (often considered as isotropic). These distributions can be characterised by a cumulative probability distribution function which allows randomly defining a location and an energy for any considered neutron. The random walk and the state of the neutron then depend on the geometry of the crossed domain and on the physical properties of the matter. The distance to the next collision and the type of the next interaction are thus sampled following the total cross sections. If the reaction type is absorption, the neutron history is terminated, the energy and location of the absorbed neutron are recorded, and another history is started. If a scattering event is sampled, the direction and the energy of the considered neutron are changed and a new sampling occurs to determine the distance to the next collision. If the sampled interaction is fission, a number of neutrons are produced, and so on. Finally, to determine the flux at the specific position of the detector, the Monte Carlo approach simulates many neutron random walks and counts the neutrons reaching the detector.

The procedure just described is usually called the *analogue scheme* meaning that the particles are transported in a way corresponding to the physical interactions with matter. The analogue simulations use in fact the fundamental conservation laws (energy momentum, angular momentum, etc.) which describe the physical phenomena encountered by the neutron during its way.

3.2.3 Non-analogue simulation

One of the issues with the Monte Carlo approach is the slow convergence of its calculations due to the limited number of simulated trajectories. To limit the statistical error on results, Monte Carlo codes must simulate a large number of particles, making simulations too time-consuming. Moreover, the analogue simulation remains inefficient to simulate the neutron population in nuclear reactors. in consequence it becomes favourable to use biasing techniques or variance reduction techniques for emphasising neutrons that are most likely to contribute to the tally. This type of simulation is usually known as the *non-analogue scheme*. It consists in associating weight with neutrons and adjusting the neutron weight at each event in its history (Marguet, 2011). For example, the weight decreases for neutron-absorbing media. A threshold s is then used conditionally to ignore any neutron with a contribution that is too low, and for which continuing the path would be useless. Other approaches can ignore the neutrons that are in an uninteresting part of the phase space, such as the Russian roulette method. Depending on the physical systems simulated, many other different methods are used for non-analogue schemes to accelerate Monte Carlo simulations (Nowak, 2018).

4 Nuclear data evaluation

The reliability of input data is an essential factor in obtaining adequate results with simulation codes. These inputs are derived from evaluated nuclear data libraries which are based on the experimental measurements and the theoretical nuclear models. However, they could not be used directly in reactor simulation codes. Fig. I.4 illustrates an example of steps used to produce multigroup data for deterministic codes. All the steps are described more precisely in the

following sections. They are based on the tools and codes, the purpose of which is aiming to provide a better modelling of the physical data, to estimate the associated uncertainties and to reduce the calculation bias.
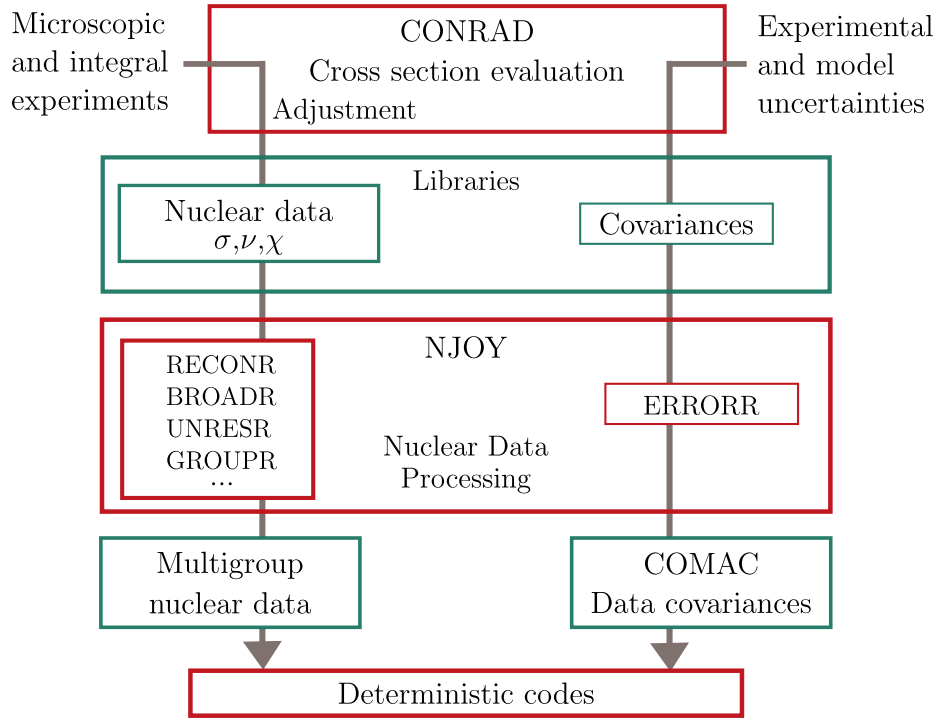
Figure I.4: Multigroup data generation for deterministic codes.

4.1 From experiments to libraries

The nuclear data are given using the standardised format ENDF in international libraries as for example ENDF/B-VII (the American Library) (McLane, 2005), JEFF-3 (the European library) (JEFF-3.1, 2013), JENDL-4 (the Japan Library) (JENDL-4.0, 2011).

Libraries contain the fundamental physical parameters needed for modelling nuclear interactions for several incident particles and for a large set of materials and isotopes. Because of the complexity of nuclear interactions and the incapacity of theory to describe them accurately, parameters are often defined by the iterative evaluation process combining validated physical models and data assimilation experiments. It consists in involving Bayesian inferences (Kessedjian, 2015) to adjust the theoretical parameters of models by maximum likelihood and by reducing uncertainties. Two types of experiments are used for this evaluation. Differential experiments allow measuring microscopic quantities as functions of the energy of the incoming particle, such as cross sections, fission yields and angular distributions. Integral experiments measure macroscopic quantities as cross sections integrated on neutron flux and can then be used for validating and adjusting nuclear data libraries. The resulting evaluated nuclear data corresponds to the best estimates of the quantities of interest, i.e. the mean values as defined in the next section 1 of Chapter II.

4.2 Sources of uncertainties in nuclear data evaluations

In practice, nuclear data cannot be accurately estimated because in the evaluation process, there exist a succession of sources of uncertainties which can be divided in two types:

- *Aleatory uncertainty* due to the random nature of the system or to the statistical effects of detection in microscopic experiments. These can be handled by repeating independent measurements under the same conditions. Following the central limit theorem, one can then determine the best estimates and associated variances,

- *Epistemic uncertainty* which produces systematic errors, for example, due to the methods of measurements and reconstructions (normalisation, background subtraction, calibration, etc.) or due to the measurement resolution which can be identified by diversifying the methods and instruments.

The final uncertainty of a quantity of interest results thus from the propagation of these uncertainties on the iterative evaluation process. As explained in the previous Section 4.1, the uncertainty quantification is carried out during the data evaluation process, and generally, following a *Bayesian approach* that provides a better assessment of the uncertainty than the frequentist approach (King et al., 2019; Kessedjian, 2015).

In data libraries, the characterisation of uncertainties is given by covariance matrices. The latter encloses two types of information: the accuracy of each evaluated data, encoded in the variances, and the correlations among data, which reveal their consistency and the analysis choices during their evaluation process. In fact, the evaluated data tend to be correlated for several reasons. Some parameters can for example be involved in evaluation of different data. Some adjustment processes can also create correlations among data (as normalisation, marginalisation, consistent adjustment, ...) (Privas, 2015). The covariance data defined in a library is thus evaluated following the methodology adopted to obtain the central values of the nuclear data defined in the same library. This is why they are attached to the data of their own library.

In the ENDF format (McLane, 2005), the nuclear data which describe the neutron interactions are given in the Files from 1 to 5 and the corresponding covariance data are provided in sections MF-31-32-33-34-35 as presented in Tab. 2. Specifically, the MF32-file and the MF33-file give the covariances, respectively, on the resonances parameters (MF2) and on the pointwise cross sections (MF3).

Data	Files	Corresponding Covariances
The average number of neutrons per fission	MF1-MT452	MF31
Resonance parameters	MF2	MF32
Neutrons cross sections	MF3	MF33
Angular distribution of secondary particles	MF4	MF34
Energy distribution of secondary particles	MF5	MF35

Table I.1: Transport data for the description of neutron interactions

4.3 NJOY treatments for simulation codes

As explained previously, the interaction between a neutron and a nucleus depends on the energy of the incident particle and on the temperature of the target. The energy dependence can be described by a pointwise or a multigroup formalism.

In the evaluated nuclear data files, data are provided by a pointwise representation. A series of treatments is necessary to convert them into continuous-energy cross section format which is usable by reactor physics codes. A very widely used data processing system is named NJOY (MacFarlane, 2017) and is being developed at the Los Alamos National Laboratory (USA).

NJOY contains various modules. As an illustration, some modules for generating pointwise and multigroup cross sections are succinctly presented in the following sections.

4.3.1 Generation of point-cross sections in PENDF Files

- RECONR - The first step of treatment is to rebuild the pointwise values as a function of the neutron incident energy in the laboratory frame of reference for a target nuclei in the ground state ($T = 0K$) from ENDF resonance parameters and interpolation schemes. Interpolation schemes consist in describing nuclear data by a set of points associated with an interpolation law (linear or cubic) which allows rebuilding the data for any parameter value (incident energy or temperature).

- BROADR - The pointwise values are then broadened considering the Doppler effect by convolution of the "$0K$" values with the velocity distribution of the target nuclei. At this step, the cross sections can be used by the Monte Carlo codes and are defined following a PENDF-format.

- UNRESR, HEATR, THERMR - Some modules can also compute cross sections for specific energy ranges or applications. The module UNRESR computes, for example, effective self-shielded pointwise cross sections in the unresolved energy range. HEATR generates pointwise heat production cross sections and radiation damage production cross sections. THERMR produces cross sections and energy-to-energy matrices for free or bound scatterers in the thermal energy range.

4.3.2 Generation of multigroup cross sections in GENDF Files

- GROUPR - For the deterministic codes, the cross sections rather should be converted to multigroup formalism as defined by Eq. I.18. It generates various types of multigroup data: self-shielded multigroup cross sections, group-to-group scattering matrices, photon production matrices, and charged-particle multigroup cross sections from pointwise input. At the end of the GROUPR process, the multigroup data are provided in a GENDF-format.

a   Multigroup cross sections   The cross sections are given by weighting the pointwise cross sections $\sigma(E)$ on the multigroup spectrum $w(E)$ and following the concept of generalised group (with a feed function $F(E) = 1$):

$$\sigma^g = \frac{\int_g \sigma(E)w(E)dE}{\int_g w(E)dE}. \tag{I.31}$$

b   Two-body multigroup scattering   The two-body multigroup scattering cross sections are calculated according to the Bondarenko flux weighting model (MacFarlane, 2017) and the concept of a generalised group:

$$\sigma_l^{g' \to g} = \frac{\int_{g'} F_l^g(E')\sigma(E')w(E')dE'}{\int_{g'} w(E')dE'}, \tag{I.32}$$

- $\sigma(E')$: the pointwise microscopic cross section at E',
- $w(E')$: the weight function at E',
- F_l^g: the l-th Legendre component of the normalised probability of scattering into arrival energy group g from initial energy E'.

In the case of elastic and inelastic neutron scattering, the output energy E is completely determined by the E' incident energy and the center-of-mass cosine of the scatter angle ω:

$$\omega = \frac{E(1 + A)^2 - E^2(1 + R^2)}{2RE'}, \tag{I.33}$$

The relation between the center-of-mass and the laboratory cosines of the scatter angle are related by:

$$\mu = \frac{1 + R\omega}{\sqrt{1 + R^2 + 2R\omega}}, \tag{I.34}$$

where A is the ratio between the target mass to neutron mass of the neutron and R is a function of the energy level of the excited nucleus ($Q = 0$ and $R = A$ for elastic scattering).

The feed for two-body scattering is computed using a Gaussian integration scheme with the $f(E' \to E, \omega) = f(E', \omega)$ probability of scattering from E' to E through a center-of-mass cosine ω:

$$F_l^g(E') = \int_{\omega_1(E')}^{\omega_2(E')} f(E', \omega)P_l[\mu(\omega)]d\omega. \tag{I.35}$$

$\omega_1(E')$ and $\omega_2(E')$ are evaluated for E equal to respectively the upper and lower bounds of g'. P_l is defined from the Legendre polynomials.

The scattering probability is given by a Legendre polynomial series:

$$f(E', \omega) = \sum_{k=1}^{L} \frac{2k - 1}{2} a_k(E')P_k(\omega), \tag{I.36}$$

where the Legendre coefficients $a_k(E')$ are retrieved from the ENDF File 4. Equations I.32 and I.36 introduce finally the angular distribution and the correlation between the energy of the incident neutron and the emission angle after the scattering process.

4.3.3 Reconstruction of multigroup covariances with the module ERRORR

- ERRORR -

The module ERRORR of MacFarlane (2017) converts energy dependent covariance information in ENDF format into multigroup form by combining the covariance information from the File 33 with the data of the File 3 (defined Section 4.2, see Table4.2) . This calculation is based on the creation of an input script which describes the input instructions and specifications needed to generate the desired covariance matrix. In an ERRORR input, the instructions are presented in a card format (see Manual NJOY, MacFarlane (2017)). Each card is parametrised by a list of options which define the different steps of the ERRORR process, and by a succession of "tape" which refers to intermediate input or output files used during the process. Finally, ERRORR allows determining covariances for various energy meshes.

Chapter II

Statistics Background

Uncertainty analysis are increasingly being used in nuclear calculation (neutron dosimetry, reactor design, criticality assessments, etc.) to deduce the accuracy of safety parameters (fast fluence, reactivity coefficients, criticality, etc.) and to establish safety margins. Generally, the calculation of quantities of interest results from the implementation of successive physical models, which depend on uncertain inputs and on assumptions relative to methods involved for the calculation itself. The inaccurate evaluation of quantities thus results from the combination between modelling errors, numerical errors and the propagation of input uncertainties through the simulation tools. Under these circumstances, sensitivity analysis evaluate the impact of input uncertainties in terms of their relative contributions to uncertainty in the output. They help to prioritise efforts for uncertainty reduction, improving the quality of the data.

The intent of this chapter is thus to present the background needed to carry out uncertainty analysis and sensitivity analysis in the context of nuclear models.

1 Basic concepts in modelling uncertainty

1.1 First and Second Central moment

Let us consider a real parameter y which results mathematically from the *interactions* of real input parameters, described by $y = f(\mathbf{x})$ and as illustrated by Fig. II.1. In that context, the aim of uncertainty analysis is to determine the output uncertainty of y considering the uncertainties of input parameters $x_1, ..., x_n$.

$$ x_1 \quad \Rightarrow \quad \boxed{f(x_1, ..., x_n)} \quad \Rightarrow \quad y $$
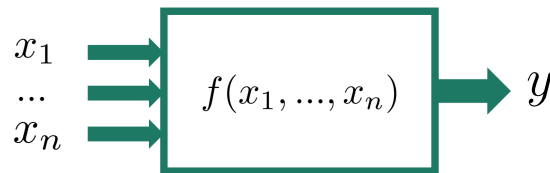
Figure II.1: Physical model

The uncertain data can be represented as continuous random variables $\mathbf{X} = (X_1, ..., X_n)$[1] defined on the probability space $(\Omega, \mathcal{F}, \mathbb{P})$, where Ω is the sample space, $\mathcal{F}$ the σ-algebra and

---

[1]In the sequel, the capital letter X will be used to represent the random variable itself and the corresponding lower-case letter to denote the observed value of x. The random vector will be represented by an upper-case bold letter $\mathbf{X}$, and the vector which contains the observed value by $\mathbf{x}$.

$\mathbb{P}$, the probability measure. The multivariate probability distribution of the random vector $\mathbf{X}$ is characterised by the *Cumulative Distribution Function* (CDF), such as:

$$F_{\mathbf{X}}(x_1, x_2, ..., x_n) = \mathbb{P}(X_1 \leq x_1 \text{ and } X_2 \leq x_2, ..., \text{ and } X_n \leq x_n), \tag{II.1}$$

and which obeys the following conditions:

$$\begin{array}{c} F_{\mathbf{X}} \text{ is monotone increasing,} \\ F_{\mathbf{X}}(x_1 = -\infty, x_2 = -\infty, ..., x_n = -\infty) = 0 \\ F_{\mathbf{X}}(x_1 = +\infty, x_2 = +\infty, ..., x_n = +\infty) = 1 \end{array} \tag{II.2}$$

The joint *Probability Density Function* (PDF), can then be computed as a partial derivative of Eq. II.1:

$$p_{\mathbf{X}}(\mathbf{x}) = \left. \frac{\partial^n F_{\mathbf{X}}(\mathbf{x})}{\partial x_1 \partial x_2 ... \partial x_n} \right|_{\mathbf{x}}, \tag{II.3}$$

where $\mathbf{x} = x_1, x_2, ..., x_n$.

As expressed by Eq. II.2, $F_{\mathbf{X}}$ provides a complete representation of the set of n random variables, and consequently, $p_{\mathbf{X}}$ is normalised:

$$\int_{x_1} ... \int_{x_n} p_{\mathbf{X}}(\mathbf{x}) dx_1 dx_2 ... dx_n = 1. \tag{II.4}$$

For $i = 1, .., n$, we can also define the *marginal density function* associated with the variable X_i alone, by integrating $p_{\mathbf{X}}$ over all values of the other $n - 1$ variables:

$$p_{X_i}(x_i) = \int p_{\mathbf{X}}(x_1, x_2, ..., x_n) dx_1 ... dx_{i-1} dx_{i+1} ... dx_n = \int p_{\mathbf{x}}(\mathbf{x}_{-i}, x_i) d\mathbf{x}_{-i}. \tag{II.5}$$

In this way, the distribution of the random variable X_i admits a probability density function, and the expectation of X_i can therefore be calculated as the *first central moment*:

Expectation

$$\mathbb{E}[X_i] = \int_{x_i} x_i p_{\mathbf{x}_i}(x_i) dx_i. \tag{II.6}$$

In the same way, we can assess the joint probability density function of two random variables X_1, X_2:

$$p_{X_1, X_2}(x_1, x_2) = \frac{\partial^2 F_{\mathbf{X}}(x_1, x_2)}{\partial x_1 \partial x_2}, \tag{II.7}$$

with $F_{\mathbf{X}}(x_1, x_2) = P(X_1 \leq x_1 \text{ and } X_2 \leq x_2)$, is straightforwardly derived by integrating $p_{\mathbf{X}}$ over all variables other than X_1 and X_2.

In this respect, one important quantity is the *covariance* between X_1 and X_2 which measures the *joint variability* of the two variables, expressed as the second central moment:

Covariance

$$cov(X_1, X_2) = \int_{x_1} \int_{x_2} (x_1 - \mathbb{E}[X_1])(x_2 - \mathbb{E}[X_2]) p_{X_1, X_2}(x_1, x_2) dx_1 dx_2. \tag{II.8}$$

Finally, we consider the random variable Y which describes the probability distribution of $y = f(\mathbf{x})$, expressed by $Y = f(\mathbf{X})$. It is straightforward to derive its expectation value:

$$\mathbb{E}[Y] = \mathbb{E}[f(\mathbf{X})] = \int_{S(\mathbf{x})} f(\mathbf{x}) p_{\mathbf{x}}(\mathbf{x}) d\mathbf{x}. \tag{II.9}$$

Uncertainty

The *uncertainty* of Y is defined as the *standard deviation* σ_Y which is the square root of the *variance var* $(f(\mathbf{X}))$, another quantity expressed by a second central moment:

$$Var[Y] = \sigma_Y^2 = \mathbb{E}[(f(\mathbf{X}) - \mathbb{E}[f(\mathbf{X})])^2]. \tag{II.10}$$

1.2 Maximum entropy probability distribution

In practice, the full joint probability density function $p_{\mathbf{X}}(\mathbf{x})$ is not all the time known. To circumvent this lack of information, one key concept is the *information entropy* introduced by Shannon (Shannon, 1948). The corresponding formula for a continuous random variable X with a probability density function $p_X(x)$ is given by:

$$h[p] = \int_x p_X(x) ln(p_X(x)) dx. \tag{II.11}$$

When some information is provided (for example, the first and second central moments) but not enough to describe the full probability distribution of a variable, the principle of maximum entropy, first expounded by Jaynes (Jaynes, 1957), states that the probability distribution which best represents the current state of knowledge is the one with largest entropy $h[p]$. In particular, when the mean μ and the variance σ^2 is selected as descriptors of the data, the Gaussian distribution ($\mathcal{N}(\mu, \sigma^2)$) is the best distribution to represent the information entropy. For some other practical cases, when the minimum and maximum values a and b are known, the uniform distribution ($U(a, b)$) is the distribution which maximises the entropy.

2 Linear models

When it comes to studying the variation of a model output, linear models can be very profitable because they can readily simplify the setting up of regression, uncertainty quantification and sensitivity analysis. The main question is whether a linear regression is sufficient to model the behaviour of a random variable Y in the range of uncertainties of inputs.

To illustrate this, one can consider an experimental design with p observations of n input variables and of the corresponding output response y of a model. The estimation of a linear regression consists in assessing, from the observed measurements, a vector of unknown parameters $\boldsymbol{\beta} \in \mathbb{R}^n$ which allows describing the following linear relationship between the random variable of interest Y and the n deterministic variables:

$$Y = \beta_0 + \mathbf{x}\boldsymbol{\beta} + \epsilon, \tag{II.12}$$

where ϵ is the error term.

It is assumed that each observation y_k of Y satisfies:

$$y_k = \beta_0 + \mathbf{x}_k \boldsymbol{\beta} + \epsilon_k, \tag{II.13}$$

where $\mathbf{x}_k \in \mathbb{R}^n$ is the k-th observations of the n variables $(x_1, ..., x_n)$, and denoted as:

$$\mathbf{x}_k = \begin{pmatrix} x_{(k,1)} & \cdots & x_{(k,n)} \end{pmatrix}, \tag{II.14}$$

ϵ_k is a zero-mean Gaussian noise, as for all k the random variables ϵ_k are independent and identically distributed ($\epsilon_k \simeq \mathcal{N}(0, \sigma^2)$). We can thus assume the fact that:

$$\mathbb{E}(Y|x_1, ..., x_n) = \beta_0 + \mathbf{x}_k \boldsymbol{\beta} \text{ and } Var(Y) = \sigma^2. \tag{II.15}$$

The matrix format of Eq. II.13 gives:

$$\mathbf{Y} = \mathbf{X}\boldsymbol{\beta} + \boldsymbol{\epsilon}, \tag{II.16}$$

where,

$$\mathbf{X} = \begin{pmatrix} 1 & x_{(1,1)} & \cdots & x_{(1,n)} \\ \vdots & \vdots & \vdots & \vdots \\ 1 & x_{(p,1)} & \cdots & x_{(p,n)} \end{pmatrix}, \mathbf{X} \in \mathbb{R}^{p \times n} \text{ is the } \textit{design matrix}, \tag{II.17}$$

$$\mathbf{Y} = \begin{pmatrix} y_1 & \cdots & y_p \end{pmatrix}^t, \mathbf{Y} \in \mathbb{R}^p \text{ is the } \textit{response vector}, \tag{II.18}$$

$$\boldsymbol{\beta} = \begin{pmatrix} \beta_1 & \cdots & \beta_n \end{pmatrix}^t, \boldsymbol{\beta} \in \mathbb{R}^n \text{ is the } \textit{coefficient vector}, \tag{II.19}$$

$$\boldsymbol{\epsilon} = \begin{pmatrix} \epsilon_1 & \cdots & \epsilon_p \end{pmatrix}^t, \boldsymbol{\epsilon} \in \mathbb{R}^p \text{ is the } \textit{error vector}. \tag{II.20}$$

Ordinary Least Squares

In the case where the number of samples p is greater than the number of input variables n, and the $X^t X$ is a positive-definite matrix, the optimal *coefficient vector* $\boldsymbol{\beta}$ of a linear regression problem is given by the *Ordinary Least Squares* which states that assuming the Gaussian distribution of the error ϵ, the maximum likelihood estimator is:

$$\hat{\boldsymbol{\beta}} = \underset{\boldsymbol{\beta} \in \mathbb{R}^n}{\arg \min} \|\mathbf{Y} - \mathbf{X}\boldsymbol{\beta}\|_2^2. \tag{II.21}$$

The minimisation II.21 gives then:

$$\hat{\boldsymbol{\beta}} = (\mathbf{X}^t\mathbf{X})^{-1}\mathbf{X}^t\mathbf{Y}, \tag{II.22}$$

in the case where matrix X is of full rank.

Since all outcomes y_k are equiprobable, Eq. II.6 gives the mean of the observed data $\bar{y}$ as:

$$\bar{y} = \frac{1}{p} \sum_{k=1}^{p} y_k. \tag{II.23}$$

Empirically, the variability of the data set can then be measured using three following classic formulas SST, SS_{Res}, SS_{Reg} (related by SST $= SS_{Reg} + SS_{Res}$):

- The *total sum of squares* (total variance),

$$\text{SST} = \sum_{k=1}^{p} (y_k - \bar{y})^2, \tag{II.24}$$

- The *explained sum of squares*,

$$\text{SS}_{Reg} = \sum_{k=1}^{p} (\hat{y}_k - \bar{y})^2, \tag{II.25}$$

- The *residual sum of squares*,

$$\text{SS}_{Res} = \sum_{k=1}^{p} (y_k - \hat{y}_k)^2 = \sum_{k} \epsilon_k^2, \tag{II.26}$$

where $\hat{y}_k = \hat{y}(\mathbf{x}_k)$ is the prediction resulting from the linear model.

Thereafter, to measure the quality of the linear regression, the following coefficients can be calculated:

$R^2 = 1 - \dfrac{\sum_{k=1}^{p}(y_k - \hat{y}_k)^2}{\sum_{k=1}^{p}(y_k - \bar{y})^2}$	$R_{adj}^2 = 1 - \|1 - R^2\|\left\|\dfrac{p-1}{p-(1+n)}\right\|$	$Q^2 = 1 - \dfrac{\sum_{k=1}^{p}(y_k - \hat{y}_{k,-k})^2}{\sum_{k=1}^{p}(y_k - \bar{y})^2}$
The coefficient of determination	The adjusted coefficient	The LOO-cross-validated R^2

Table II.1: **Linearity verification**

R^2 is thus expressed as the ratio of the explained variance to the total variance. When R^2 is close to 1, we can assume that the linear regression is validated. Similarly, the R_{adj}^2 is defined but it penalizes in addition the statistic if the sample size is not very great compared to the number of variables.

Moreover, Q^2 is defined as the value of R^2, using the sampling data set, but where each predicted value $\hat{y}_{k,-k}$ is given from Leave-One-Out cross validation, i.e. with a linear model $\hat{y}_{(\mathbf{x},-k)}$ estimated from the set of $p - 1$ points $\{1, \ldots, k-1, k+1, \ldots, p\}$. The numerator of Q^2 is therefore defined as the *Predictive Residual Error Sum of Squares* defined by Allen (1974).

3 Uncertainty quantification

There are two main methods to conduct an uncertainty analysis: the method of moments based on truncated Taylor series expansion and the Monte Carlo method. This section presents the background which will be necessary in this thesis to determine which of the methods are adequate to evaluate the uncertainty and to strengthen its evaluation.

3.1 Uncertainty propagation by deterministic approach

The method of moments consists in approximating the statistical moments of the system response by means of a truncated Taylor series expansion of the output y. The Taylor series expansion is a representation of a infinitely differentiable function as an infinite sum of terms that are calculated from the values of the functions' derivatives at a real or complex point. In a linear case and for small perturbations, the function can be expanded considering the nominal

values of the input variables $\mathbf{x}^{(0)} = (x_1^{(0)}, ..., x_n^{(0)})$ and the Taylor expansion is truncated at the first order:

$$f(\mathbf{x}) \simeq f(x_1^{(0)}, ..., x_n^{(0)}) + \sum_{i=1}^{n} \left.\frac{\partial f}{\partial x_i}\right|_{\mathbf{x}^{(0)}} \delta x_i, \qquad \text{(II.27)}$$

where $\delta x_i = x_i - x_i^{(0)}$ is the change in the parameter x_i.

Since for all $i = 1..n$, $\left.\frac{\partial f}{\partial x_i}\right|_{\mathbf{x}^{(0)}}$ is independent of the statistical nature of the input parameters, straightforward calculations which follow from the substitution of Eq. II.27 into II.8, II.9 and II.10 yield:

$$Var(y) = \sum_{i=1}^{n} \sum_{j=1}^{n} \left.\frac{\partial f}{\partial x_i}\right|_{\mathbf{x}^{(0)}} \left.\frac{\partial f}{\partial x_j}\right|_{\mathbf{x}^{(0)}} cov(x_i, x_j). \qquad \text{(II.28)}$$

Linear approximation of the model variability by deterministic approach

The deterministic approach thus dissociates the inherent sensitivities of the system defined by the vector $S = \left(\left.\frac{\partial f}{\partial x_i}\right|_{\mathbf{x}^{(0)}}\right)_{i=1..n}$ from the variability of the model inputs defined by the matrix $\Sigma_x = \left(cov(x_i, x_j)\right)_{(i=1..n, j=1..n)}$ as:

$$Var(y) = S \Sigma_x S^t. \qquad \text{(II.29)}$$

3.2   Uncertainty propagation by Monte Carlo approach

The main principle of Monte Carlo approach is to consider the input data of the model as random variables, and propagates many randomly selected samples of input data. The results of these evaluations allow determining the uncertainty on the output model and to apply in return sensitivity analysis considering the input and output data. The Monte Carlo approach can be divided into four main steps which are illustrated by Fig. II.2.
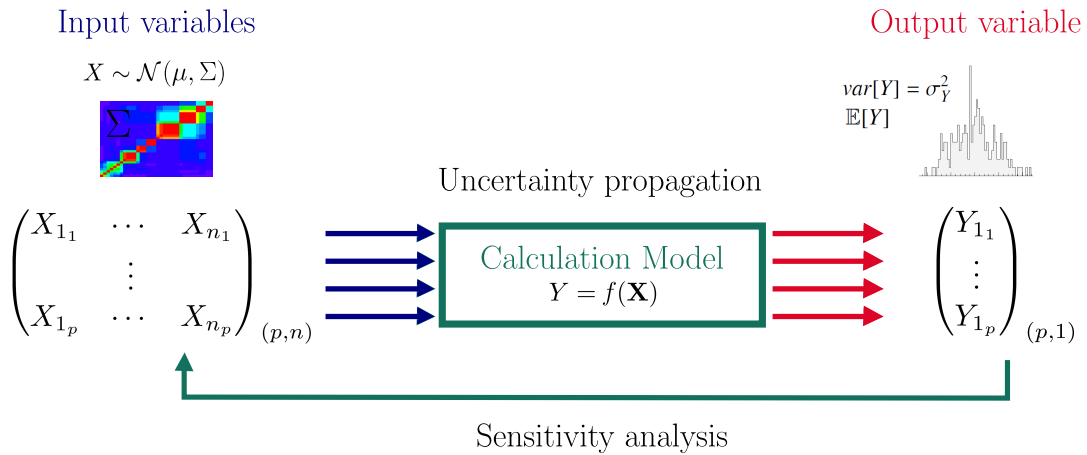
Figure II.2: The Total Monte Carlo approach

The first is the *uncertainty quantification* of the input data which consists in defining the variability and the distribution of the input variables. As explained in the previous section 1.2,

the variable distributions are not all the time known but they can be approached by maximum entropy principle.

The second step is the *random generation of samples*. There are many ways to sample inputs from the probability distributions. One of the most basic is the *simple random sampling* which generates the p samples from the joint distribution of the input variables and produces unbiased estimates of the mean and the variance of X (Saltelli et al., 2008). *Stratified sampling* can also be applied to achieve a better coverage of the sample space. There, the idea is to partition the sample space into disjoint strata of same probability.

The objective of the third step is to propagate the samples on the calculation model to evaluate the results of the model output. Finally, the results allow determining the *final uncertainty* of the output and to set up a *sensitivity analysis* to interpret the output variability.

4   Sensitivity analysis

There are various ways to define the concept of sensitivity of an output model depending on the study purposes. The use of sensitivity analysis can indeed be motivated for various reasons. For example, if the goal is to select the main parameters affecting a physical model, the sensitivity is defined as the *direct importance* of a parameter on the output of a model (i.e. how the output changes from a given perturbation of the input parameter). In the context of uncertainty analysis, the objective is in general to identify how the uncertainties of parameters can affect the *output variability*.

In this respect, sensitivity analysis are generally classified in two types (Smith, 2014).

- *Local sensitivity analysis* study the behaviour of the model response around a chosen point and focuses on the variability of the response, often defined by the partial derivative $\frac{\partial y}{\partial x_i}$.

- *Global sensitivity analysis* study the impact of the variability of model input factors on the output variable, considering the range and the shape of the probability density of inputs, and the simultaneous variation of all inputs.

In a context of uncertainty analysis, it appears natural to focus on global sensitivity analysis. Among the latter, *variance-based methods* appear to be interesting because they allow decomposing the variance of the output of the model $Y = f(X_1, ..., X_n)$ into components which can be attributed to the contribution of each $(X_1, ..., X_n)$. Variance-based methods for sensitivity analysis were first proposed by Cukier et al. (1973). They will be extensively used in our work. In this section, we will first introduce the case of *independent inputs*, and eventually explain the difficulty encountered in their application to the case of *correlated input data*.

4.1   Variance-based methods with independent inputs

4.1.1   Standardised regression coefficient for linear models

Most of the sensitivity models are based on the decomposition of the output variability. In the linear case (see Section 2), it can be expressed as:

$$Var(Y) = \sum_i^n \beta_i^2 Var(x_i) + 2 \sum_{j>i} \beta_i \beta_j cov(x_i, x_j) + \sigma_\epsilon^2. \tag{II.30}$$

The variance of y can thus be decomposed into the dispersion due to the regression itself and the dispersion due to the estimation errors, which are empirically and respectively defined by $\frac{1}{p} SS_{Reg}$ and $\frac{1}{p} SS_{Res}$.

If the linear regression is validated following Tab. 2 ($R^2 \simeq 1$), it is assumed that $SS_{Res} \simeq 0$.

SRC^2 indices

With independent inputs (for each $i \neq j$, $cov(x_i, x_j) = 0$), the variance can be decomposed as $Var(Y) = \sum_i^n \beta_i^2 Var(x_i)$. In that sense, we can define the standardised regression coefficient SRC_i associated with the deterministic variable x_i, as:

$$SRC_i = \beta_i \sqrt{\frac{Var(x_i)}{Var(Y)}}. \tag{II.31}$$

4.1.2 Sobol indices for non-linear and non-monotonic models

The method of Sobol (1993) is a global sensitivity analysis method based on variance decomposition which can handle non-linear and non-monotonic models. It consists in the decomposition of a square-integrable function f which defines the output of the model $y = f(\mathbf{x})$ as a function of n independent random variables $x_1, ..., x_n$ of the n dimensional unit cube $[0, 1]^n$.

As shown by Hoeffding (1992), f can in fact be represented as a sum of elementary functions of increasing dimensions:

$$f(\mathbf{x}) = f_0 + \sum_{u \subseteq [1:n]} f_u(\mathbf{x}_u). \tag{II.32}$$

As explained in (Sobol, 1993), the decomposition II.32 is, moreover, unique if the following assumptions are verified:

- The constant f_0 has the value,

$$f_0 = \int_{[0,1]^n} f(\mathbf{x})d\mathbf{x}, \tag{II.33}$$

- the integrals of the summands $f(\mathbf{x_u})$ with respect to any of their own variables are zero,

$$\int_{[0,1]} f_u(\mathbf{x_u})dx_k = 0 \text{ with } k \in \mathbf{u}, \tag{II.34}$$

- all the summands are mutually orthogonal,

$$\int_{[0,1]^n} f_u(\mathbf{x_u})f_v(\mathbf{x_v})d\mathbf{x} = 0 \text{ with } \mathbf{u} \neq \mathbf{v}. \tag{II.35}$$

A direct application of the above definitions leads to the decomposition II.32 the output variance $Var(Y)$. In fact, in a stochastic context, where $X_1, ..., X_n$ are independent random variables described by known probability distributions, it can be shown that:

$$Var(Y) = \sum_{i=1}^n V_i + \sum_{i<j}^n V_{ij} + ... + V_{1...n}, \tag{II.36}$$

where, V_i, V_{ij}, ..., $V_{1,2,...,n}$ are the variances $Var(f_i)$, $Var(f_{ij})$, ..., $Var(f_{1,2,...,n})$ defined as:

$$
\begin{aligned}
V_i &= Var[\mathbb{E}(Y|X_i)] \\
V_{ij} &= Var[\mathbb{E}(Y|X_i, X_j)] - V_i - V_j \\
V_{ijk} &= Var[\mathbb{E}(Y|X_i, X_j, X_k)] - V_{ij} - V_{ik} - V_{jk} - V_i - V_j - V_k \\
&\vdots \\
V_{1..p} &= Var(Y) - \sum_{i=1}^{n} V_i - ... - \sum_{1 \le i_1 < ... < i_{n-1} \le n} V_{i_1,...,i_{n-1}}.
\end{aligned}
\tag{II.37}
$$

Similarly, for all $u \subseteq [1 : n]$, we can deduce from this decomposition the Sobol sensitivity indices which determine the input contributions to the total output variance. These contributions are characterised by the ratio of the partial variance to the total variance as summarised by Eq. II.38 and II.39.

Sobol indices

For all $u \subseteq [1 : n]$, the complete Sobol index S_u^c, which measures the full contribution of the group of variables $\mathbf{X_u}$ to the total output variance, is given by:

$$
S_u^c = \frac{Var(\mathbb{E}(Y|X_u))}{Var(Y)}.
\tag{II.38}
$$

Likewise, we define the Sobol index S_u, which assesses the impact of the interaction of the inputs $(X_i)_{i \in u}$ on the model output variability, such as:

$$
S_u = \frac{1}{Var(Y)} \sum_{v \subseteq u} (-1)^{|u|-|v|} Var(\mathbb{E}(Y|X_v)),
\tag{II.39}
$$

where $|u|$ and $|v|$ are the cardinal of u and v.

First and Total Sobol indices

Specifically, the first-order index measures the impact of the variation of X_i on the variation of Y by:

$$
S_i = \frac{Var[\mathbb{E}(Y|\mathbf{X_i})]}{Var(Y)},
\tag{II.40}
$$

and the total indices, which measures the total impact of X_i, including all interactions with other parameters:

$$
S_{T_i} = 1 - \frac{Var[\mathbb{E}(Y|\mathbf{X_{-i}})]}{Var(Y)}.
\tag{II.41}
$$

Remark. *For a linear model with uncorrelated inputs, we can note that $S_i = SRC_i^2$. For an additive model, $f = f_0 + \sum_{i=1}^{n} f_{[i]}$ implies that $S_{T_i} = S_i$ and $\sum_{i=1}^{n} S_i = 1$. This makes it easier to interpret the results of the sensitivity analysis.*

4.2   Variance-based methods for dependent inputs by Shapley indices

As previously explained, the Sobol and SRC^2 indices are based on the independence of model inputs. They thus fail to provide the correct weight of the variables on the output uncertainty if these variables are correlated as expressed by Eq. II.36 and V.5. Many techniques have been developed to estimate variance-based sensitivity indices for correlations among data.

A first method is to generate an orthogonal set of variables by a Gram–Schmidt process (Bedford, 1998) and evaluate the sensitivity indices on that same set of inputs. One drawback of this approach is the effects of orthogonalisation which makes interpretation difficult. Xu et al. (2008) provides an alternative method based on the decomposition of the model output variance into a *structural* and a *correlative contribution*. Xu et al. (2008) has specifically calculated these quantities for a linear model of *y* as a function of the *n* input parameters.

Structural and Correlative contributions

- The *total contribution*

$$S_j = \frac{Cov(f_j, y)}{Var(Y)} = S_j^a + S_j^b, \tag{II.42}$$

- The *structural contribution*

$$S_j^a = \frac{Var(f_j)}{Var(Y)}, \tag{II.43}$$

- The *correlative contribution*

$$S_j^b = \frac{Cov(f_j, \sum_{k \neq j}^n f_k)}{Var(Y)}, \tag{II.44}$$

as a reminder, $f_j \overset{\text{def}}{=} \mathbb{E}(Y|X_j) - \mathbb{E}(Y)$.

The main issue of this method is that the functional decomposition is not unique and depends on the choice of the surrogate model. To address this problem, Kucherenko (Kucherenko et al., 2012) proposes a generalisation of Sobol indices for which the dependencies are seen as constraints in the inputs space. With a copula-based approach, the arbitrary case of correlated variables is reduced to the case of correlated multivariate normal distribution. For this latter case, the numerical assessment of the first order effect and the total indices are straightforward. However, the first order indices can be greater than the total indices depending on the level of correlation between inputs, resulting in potential difficulties of interpretation.

In this context, the Shapley values defined in Eq. II.45, have recently been suggested by Owen (Owen et al., 2017) who reminds that the Shapley method is the only one which satisfies necessary properties intuitively: additivity, non-negativity, full contribution, and ordering independence.

In contrary to the dependent data ANOVA, the Shapley values are always positive and do not depend on any assumption about the input distribution. Similarly, Iooss (Iooss et al., 2019) has compared the Shapley values with the Sobol indices in the case of a linear model and an Ishigami function (also used in (Kucherenko et al., 2012)) to illustrate the Kucherenko's approach. As explained by Iooss, the dependencies between inputs leads to a rebalancing of the corresponding Shapley effects, while there is a cumulative effect of correlations on the Sobol' indexes. For these reasons, in the following the Shapley values will be preferentially used in our work for measuring importance of dependent inputs.

Shapley values

The Shapley index associated with the variable X_i is given by:

$$S h_i = \frac{1}{n} \sum_{u \subseteq -\{i\}} \binom{n-1}{|u|}^{-1} (c(u \cup \{i\}) - c(u)), \tag{II.45}$$

where $\{x_1, ..., x_n\}$ is the set of uncertainty variables, $|u|$ is the cardinality of the subset $u \subseteq \{1, ..., n\}$, $-\{i\}$ defines the set of indices $\{1, ..., n\}$ without i and $c(.)$ is the following cost function:

$$c(u) = \frac{Var[\mathbb{E}(Y|X_u)]}{Var(Y)}. \tag{II.46}$$

The difference $(c(u \cup \{i\}) - c(u))$ measures the elementary impact of x_i in each subgroup of variables. In this way, the correlations are taken into account in these indices. The sum of these indices is normalised, $\sum_{i=1}^{n} S h_i = 1$.

Methods and Results

This part presents the methods and the results of the fast flux uncertainty assessment. The methodology comprises three steps which are described in the different chapters.

Chapter III

Deterministic calculation of the neutron fast flux

The Total Monte Carlo statistic approach, used in our work for the uncertainty propagation, requires a considerable number of samples for a correct uncertainty assessment. The first step of our work thus consists in developing a calculation sufficiently rapid and accurate for the estimate of the fast neutron flux.
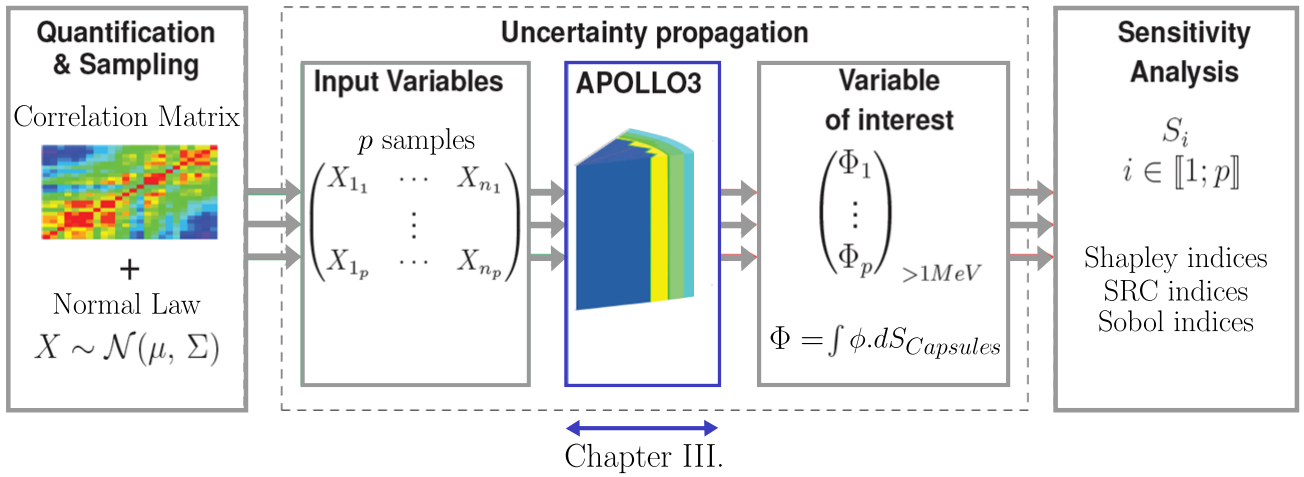
Figure III.1: Uncertainty propagation scheme: in blue the specification of the deterministic calculation

In neutron transport, reference tools are usually based on stochastic codes, like TRIPOLI-4® (Brun et al., 2014) which are computationally too expensive to apply an uncertainty propagation by TMC approach. Alternatively, a deterministic scheme can be set up to quickly calculate the neutron fast flux. The idea is to reach by some approximations a compromise between speed and precision which allows to carry out a large number of calculations. Another advantage of deterministic methods is that they provide flux distribution in all points of the modelled system in one calculation, allowing conducting sensitivity analysis in different locations of the reactor and for different energy groups. For these reasons, in this chapter, we develop a deterministic scheme for the calculation of the neutron fast flux Φ_{1MeV}.

Fast neutron flux over 1 MeV

The fast neutron flux over 1 MeV is eventually given by:

$$\Phi_{1MeV} = \sum_{g \geq 1MeV} \Phi^g(\vec{r}) \tag{III.1}$$

where Φ^g denotes the spectral distribution of flux at the energy group g.

Fig. III.2 introduces the methodology used to perform the deterministic calculation. The left-hand side describes the different steps involved in the development of the final scheme and presented in the following sections. The right side illustrates the two steps of verification of the scheme by comparison with the TRIPOLI-4® reference calculation. All the neutron calculations have been carried out with TRIPOLI4®(Brun et al., 2014) and APOLLO3®(Schneider et al., 2016).

TRIPOLI4® is the fourth generation of the continuous-energy radiation transport Monte Carlo code developed by the Service d'études des Réacteurs et de Mathématiques Appliquées (SERMA) at CEA/Saclay. It is devoted to shielding, reactor physics with depletion, criticality safety and nuclear instrumentation for both fission and fusion systems. APOLLO3® is a multipurpose code, successor of the French codes APOLLO2/CRONOS2 and ECCO/ERANOS2, offering a common set of tools for lattice and core simulations. The development is carried out as well at SERMA Saclay. It allows to perform 2 steps (2D-lattice in transport/3D-core in diffusion and transport) neutron schemes but also 1 step transport calculation without homogenisation on small 3D geometries (multi-clusters, mock-up).

Section 1 of the chapter is devoted to the TRIPOLI-4® reference calculation of our study. Section 2 presents the methodology developed which generates multigroup data adapted to the deterministic calculation for the whole reactor. The deterministic scheme is achieved following a two-step approach. A first calculation using APOLLO2 (Sanchez et al., 2010) prepares homogenised and collapsed cross sections in order to reduce the processing time and memory needed for the final calculation. The choice of the fine-group library and an optimised energy mesh are precisely detailed in subsections 2.1 and 2.2. Lastly, Section 3 describes and verifies the final 3D deterministic scheme by comparison with the TRIPOLI-4® reference scheme. Two types of calculation are set up: a *direct flux calculation* for the uncertainty propagation of all the uncertain data, and an *adjoint flux calculation* for the sensitivity analysis of the source perturbations.

The final goal of this study is to assess the uncertainty on the fast flux calculation. The work is thus based on the assumption that if the bias b between the reference calculation and the deterministic calculation is *relatively constant regardless of the perturbations*, the *variability of the deterministic calculation* is representative of the *variability of the reference calculation*. This hypothesis will be developed and verified in the chapter V.
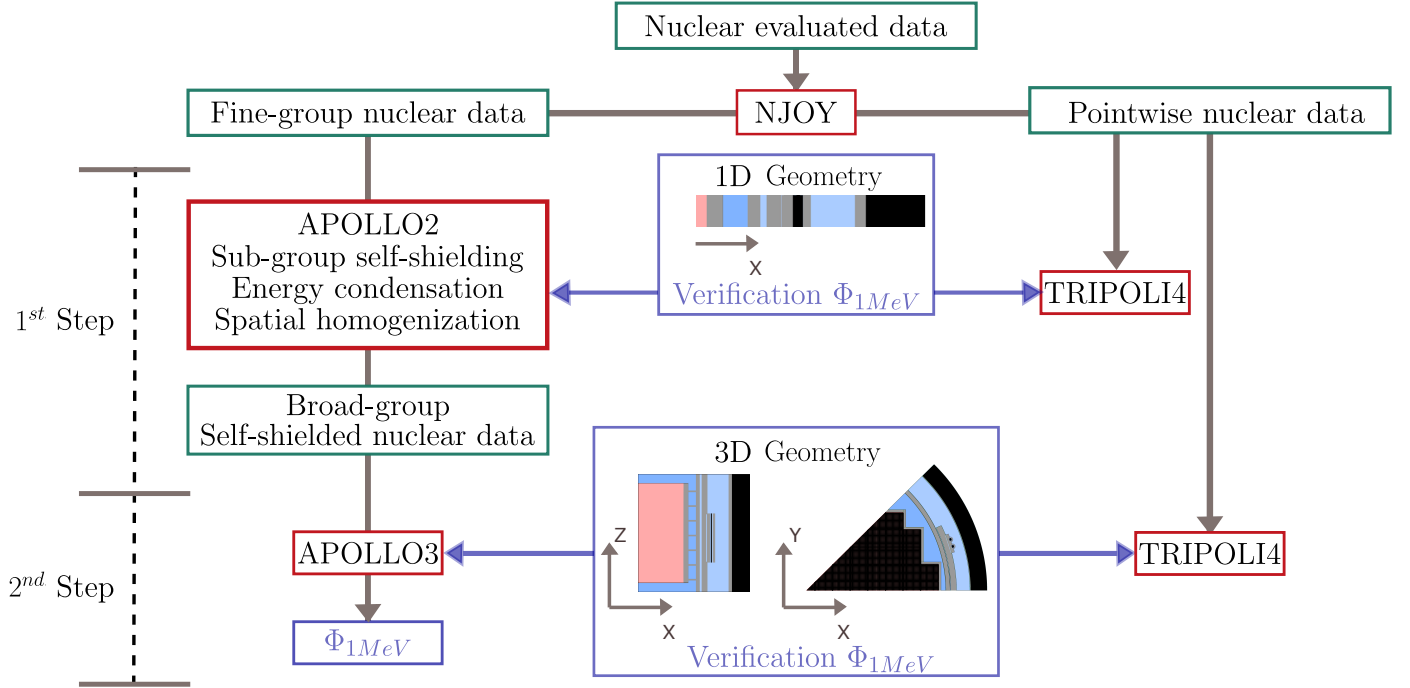
Figure III.2: Setting up the deterministic fast flux calculation.

1 Fast flux reference calculation with the TRIPOLI-4® stochastic code

In neutron simulations, pointwise Monte Carlo calculations are used as reference for the deterministic scheme. In this work, the reference calculation is carried out with the TRIPOLI-4® code (version 4.9 (Brun et al., 2014)) without modelling bias and as precisely as possible.

1.1 Description of the reference calculation

In our work, we use the fixed-source simulation mode of TRIPOLI-4® to solve the steady-step neutron transport equation. The source is imposed, and particles are then tracked from the source until their disappearance. For convenience, the TRIPOLI-4® code organizes particles in batches, which are consecutively simulated. Each batch begins with the same imposed source, hence the name of the simulation mode. The average tally and the associated variances are finally estimated from the series of batches, assuming statistical independence of the variables.

The *geometry*, implemented in the simulation, is an eighth of core which is made representative of a complete PWR core following rotational symmetry. There are 12 regions associated with 5 media (UO_2, hot water, cold water, stainless steel and steel) that model the baffles, the surveillance capsules, the stiffeners, , and the water of the primary circuit. The water temperature profile varies axially from $\sim 290°$ in the core inlet to $\sim 325°$ in the core outlet. The core is made up of 26 assemblies containing 17x17 cells of UO_2. The water, fuel, zircaloy claddings, guide and instrumentation guides are modelled separately without homogenisation.

The *pointwise nuclear data* are supplied by the JEFF-3.1.1 evaluation (JEFF-3.1, 2013). The results are computed for 3 main *neutron tallies* as illustrated in Fig. III.3: two surveillance capsules placed at the azimuths of 20° and 17°, and the point placed in front of the vessel which received the largest neutron flux. The latter is commonly known as *hot spot*.

51
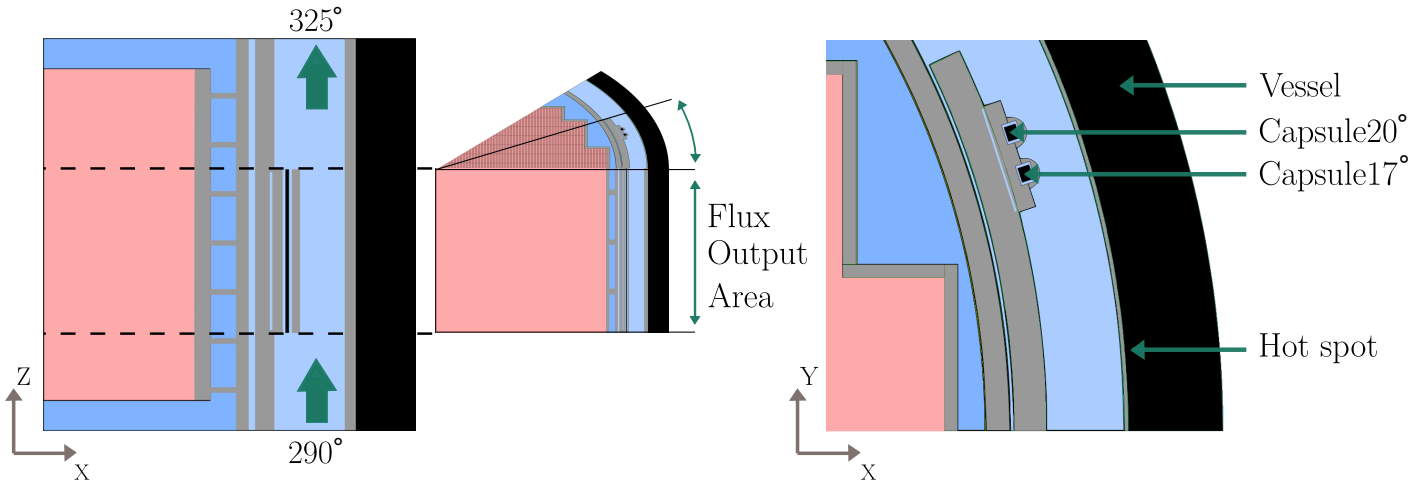
Figure III.3: Flux output area.

1.2 Identification of the assemblies which contribute most to the fast neutron flux to simplify the neutron source modelling

The *neutron source* is described axially and radially from representative data of PWR with a thermal power of 3000 MW. Two fission spectra are defined for both the fissile isotopes ^{235}U and ^{239}Pu.
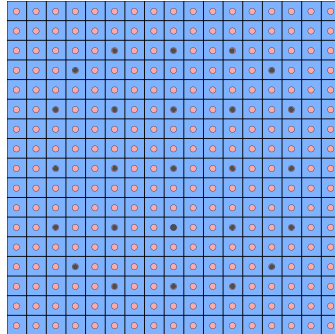
17x17 Cells of UO2

Figure III.4: Neutron source configuration.

The peripheral assemblies are those which contribute most to the neutron flux received by the capsules and the vessel, because of their proximity. In order to reduce the time needed for calculation of the future deterministic scheme, it is beneficial to simplify the configuration of the source. This is done by including in the model, only the assemblies which generate the quasi-totality of the neutron flux which reaches the vessel.

Fig. III.5 depicts the relative neutron source contributions to the surveillance capsules. As expected, the peripheral assemblies are those which have the greatest contribution. Tab. III.1, on the other hand, shows that the configuration C is sufficient to model the neutron source accountable for the fast neutron flux received by the surveillance capsules, and as a consequence, by the vessel situated behind the reflector.
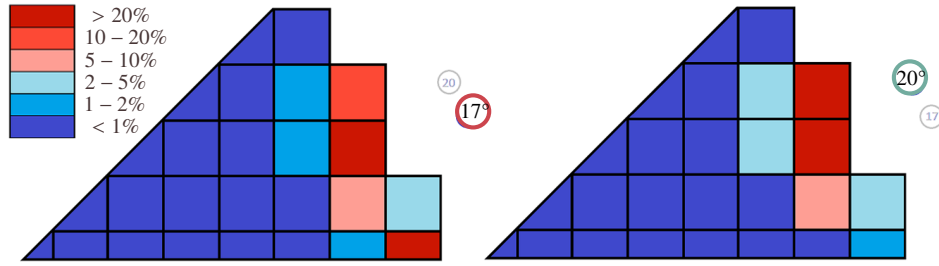
Figure III.5: Neutron source contribution of each assembly.
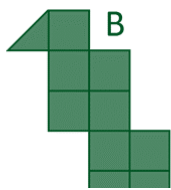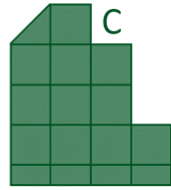
	Configuration A	Configuration B	Configuration C
Capsule 20°	93,93%	97,89%	99,92%
Capsule 17°	94,14%	97,98%	99,92%
	Neutron contribution		

Table III.1: Neutron contribution depending on the source configuration calculated with the
Monte Carlo TRIPOLI-4® code.

2 Generation and verification of multigroup homogenised and collapsed cross sections

One of the key issues in the optimisation of the multigroup calculation is based on the definition of multigroup parameters defined specifically for the reactor design studied. In the past, multigroup libraries have been created to give a fine description of the group-averaged cross sections for different types of reactor.

The aim of the subsection 2.1 is thus to choose a fine-group library adapted to the fast flux calculation. In order to reduce the time need for calculation of the final deterministic scheme, an optimisation of the energy mesh will be proposed in the subsection 2.2 in the view of calculating collapsed cross sections. The transport calculations are carried out with the APOLLO2 (Sanchez et al., 2010) discrete ordinate solver with an S32 angular discretisation and a P5 approximation for the scattering cross sections. The method of subgroups is preferred for self-shielding in order not to lose information in the resonant energy domain, especially for light nuclei which present resonances over 1 MeV (as the ^{56}Fe - Figure I.2).

For an account of the flux attenuation through the reflector, the twelve media involved in the reactor geometry have been described associating a set of different cross sections with each medium. A simplified slab model, which corresponds to a section cut of the reactor going from the core peripheral to the inner part of the vessel, is thus presented in Fig. III.6. Vacuum boundary conditions are applied on the right end side and an external source distributed in energy according to the fissile spectra of the core is set on the left end side.

Finally, homogenised and collapsed cross sections will be produced to reduce the resources needed for the final reactor calculation with APOLLO3®.

1: Source   5-10: Down-comer
2: Core Baffle   6: Thermal shield
3: By-pass   7-9: Capsule holder   11: Vessel liner
4: Core Barrel   8: Capsules   12: Vessel
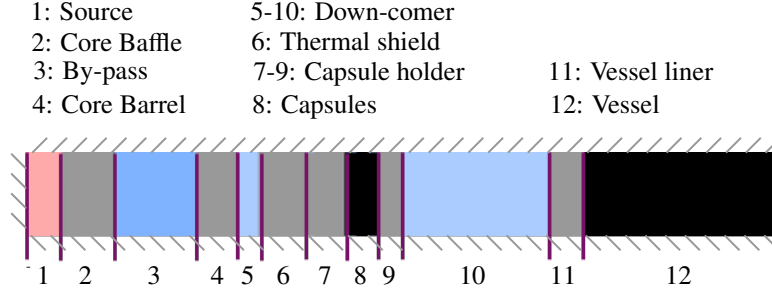
Figure III.6: Slab of 12 self-shielding regions.

2.1 Determination of a fine multigroup library adapted to the energy range of interest

As mentioned in the previous chapter, the reliability of the input cross sections is an essential prerequisite for obtaining accurate results. In vessel monitoring, as it is expected for a fast reactor, the flux of interest is mainly concentrated around fast energy groups (above 1 MeV). This is why the choice of a multigroup library adapted to the fast energy region is required for the cross-section calculations. In this energy range, multigroup libraries based on the JEFF3.1.1 evaluation, have already been created for a fine description of fast sodium reactors (Mosca et al., 2013). The resulting libraries have been declined over optimised 300, 600 and 1200 group energy meshes. Even if those libraries were not created for PWR, they present fine energy groups over 1 MeV.

$1 - \Phi_{1MeV}^{A2}/\Phi_{1MeV}^{T4}$	**300 groups**	**600 groups**	**1200 groups**	3σ - T4
Capsule	-1.48%	-0.81%	-0.69%	0.38%
Vessel	-1.25%	-0.69%	-0.44%	1.20%

Table III.2: Comparison between the Φ_{1MeV} calculated with APOLLO2 ($A2$) in a slab and for different multigroup libraries and the TRIPOLI-4® reference calculation ($T4$)

Tab. III.2 shows the accuracy of the different deterministic solutions with respect to the reference TRIPOLI-4® calculation, using the total flux over 1 MeV Φ_{1MeV} as a discriminant parameter. One can notice that doubling the number of groups from 300 to 600 increases the accuracy by a factor close to 2, whereas a further refinement of the energy mesh is less beneficial. Fig. III.7 shows that the corresponding multigroup fluxes in the vessel are within TRIPOLI-4® error bars in the energy range [1 MeV, 20 MeV]. Those results reveal that the 600-group mesh optimised for subgroups self-shielding offers a good compromise between simulation time and precision, for the description of the cross-section over 1 MeV in the slab geometry.

2.2 Assessment of an optimised energy mesh for cross-section collapse

The fine 600-group energy mesh contains 96 groups over 1 MeV. The number of groups is too large to be used for a tridimensional core calculation. In order to reduce the calculation time and memory, a coarse mesh needs to be adapted for the specific context of fast flux. The objective is to establish whether or not a coarse mesh offers a better compromise between simulation time and precision. To achieve this, the Adaptive Energy Mesh Constructor integrated in the nuclear data processing project GALILEE (Mosca et al., 2011) has been used.

The principle of AEMC is to build a multigroup mesh from predefined requisites of precision and calculation time. For a given self-shielding model and number of groups, AEMC looks for
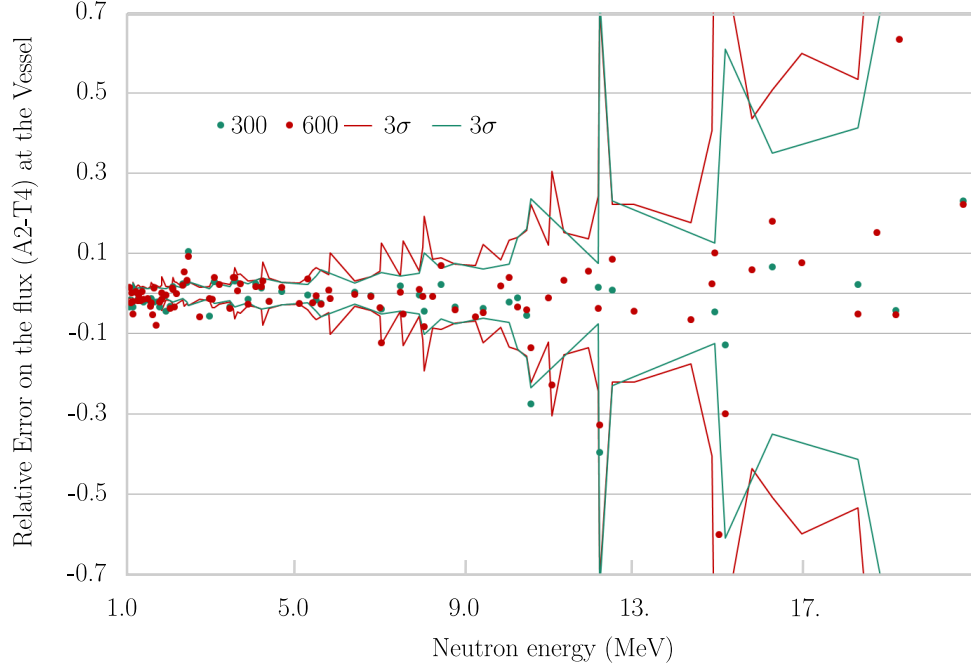
Figure III.7: Relative error on the multigroup flux between the reference TRIPOLI-4® and the
APOLLO2® calculations.

the optimal bounds of a multigroup mesh that minimises the numerical errors of the multigroup
transport solutions for a predefined set of problems. The methodology is presented in Fig. III.8.
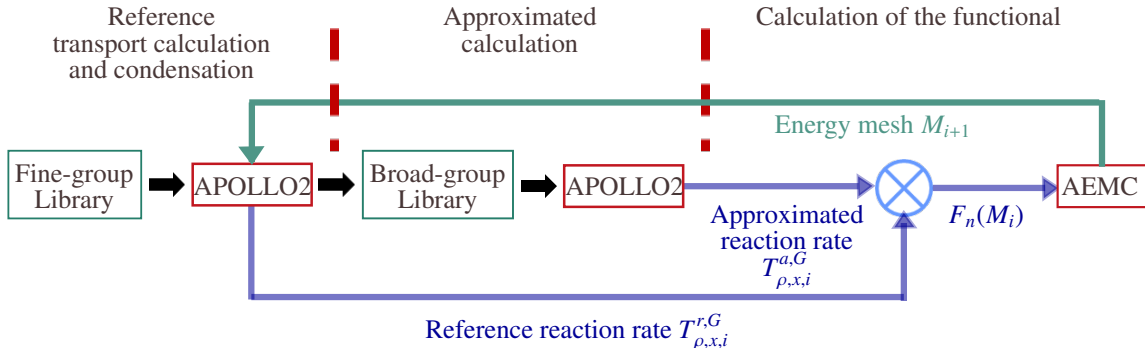
Figure III.8: The AEMC optimisation.

The AEMC is used to define a coarse mesh M_c starting from the 600-group mesh M_f.
The optimisation can be parametrised in terms of medium temperature, isotope concentrations
and neutron slowing-down sources. Since the optimisation of the energy mesh depends on the
neutron spectrum characterisation by the application, the optimisation is achieved on the slab
geometry of the previous section, considering a pure uranium and plutonium fission source.
The reference SN calculation is thus carried out over the fine 600-group energy mesh while
the approximate one is obtained from collapsed cross sections by flux homogenisation over a
coarser energy mesh optimised by AEMC.

The AEMC optimisation of the energy mesh M_c of NG groups is carried out using an iter-
ative particle swarm algorithm. All the reference reaction rates, probability tables, and multi-
group cross sections are first computed on the fine mesh M_f and stored at the beginning of the
coarse optimisation. A set of N_p meshes is then fixed. Between each iteration, the position of

each mesh changes among the various possible meshes of the 96 groups defined over 1 MeV for the reference mesh. For each mesh M_i in the set:

- Cross sections, probability tables, and reference reaction rates are collapsed from the reference mesh M_f,

- The multigroup transport equations are solved for each problem,

- A functional is computed and a convergence check is done.

If M_i satisfies the convergence criteria, then M_i is the final optimised mesh; otherwise, if the criteria are not satisfied for any mesh in the set, a new set of meshes is produced by the particle swarm algorithm.

The calculation of the functional $F(M_c)$ (derived in Mosca et al. (2011)) is done as the following:

$$F(M_c) = \sum_{i=1}^{N} \alpha_i [F_i(M_c)]^2 + \sum_{k=1}^{NG} [G_k(M_c)]^2, \qquad \text{(III.2)}$$

where,

- $N = NI.NM.NR.NG.NC$ is the total number of components,

- NI, the number of isotopes,

- NM, the number of media,

- NR, the number of reactions,

- NC, the number of problems to be considered in the optimisation ($NC = 2$ for two types of source).

The $F_i(M_c)$ components represent the discrepancy between the reference isotopic reaction rate $T_{\rho,x,i}^{r,G}$ and its approximate value $T_{\rho,x,i}^{a,G}$, renormalised by the corresponding total isotopic reaction rates $T_{\rho,x,i}^{r}$ and $T_{\rho,x,i}^{a}$:

$$F_n(M_c) = \left[\frac{T_{\rho,x,i}^{r,G}(M_c)}{T_{\rho,x,i}^{r}(M_c)} - \frac{T_{\rho,x,i}^{a,G}(M_c)}{T_{\rho,x,i}^{a}(M_c)} \right], \qquad \text{(III.3)}$$

$$\alpha_n = \frac{T_{\rho,x,i}^{r}(M_c)}{T_{\rho,i}(M_c)}, \qquad \text{(III.4)}$$

$$T_{\rho,i}^{r,a}(M_c) = \sum_{x} T_{\rho,x,i}^{r,a}(M_c), \qquad \text{(III.5)}$$

with $1 \le \rho \le NR, 1 \le G \le NG, 1 \le i \le NI, 1 \le x \le NM.NC$.

The $G_k(M_c)$ components measure the discrepancy between the reference and the approximate leakage terms:

$$G_k(M_c) = \left[\frac{J^{r,G}(M_c)}{J^{r}(M_c)} - \frac{J^{a,G}(M_c)}{J^{a}(M_c)} \right]. \qquad \text{(III.6)}$$

In the aim of determining an optimum number of groups, we carried out several optimisations with various NG groups. The main results of these calculations are presented in Fig. III.9, III.10, and III.11, while the final meshes are presented in Fig. III.12.
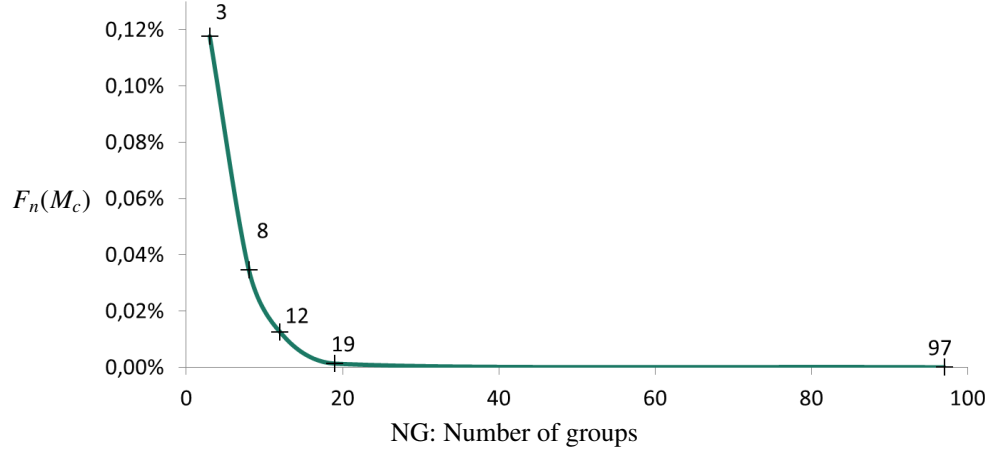
Figure III.9: Functional value of the energy mesh optimisation versus the number of groups.

Fig. III.9 provides the result on the functional value determined by the AEMC for the various optimised mesh. In the same way, Fig. III.10 presents the relative discrepancies between the calculations carried out with the optimised mesh and with the reference mesh for various energies and for the 12 media of the slab (Fig. III.6). Both figures show that the optimum number of groups in terms of accuracy seems to be around 19, including one group below 1 MeV. The differential error between the flux calculated by APOLLO2 with the 19G mesh and with the 97G mesh is indeed less than 0.4%.
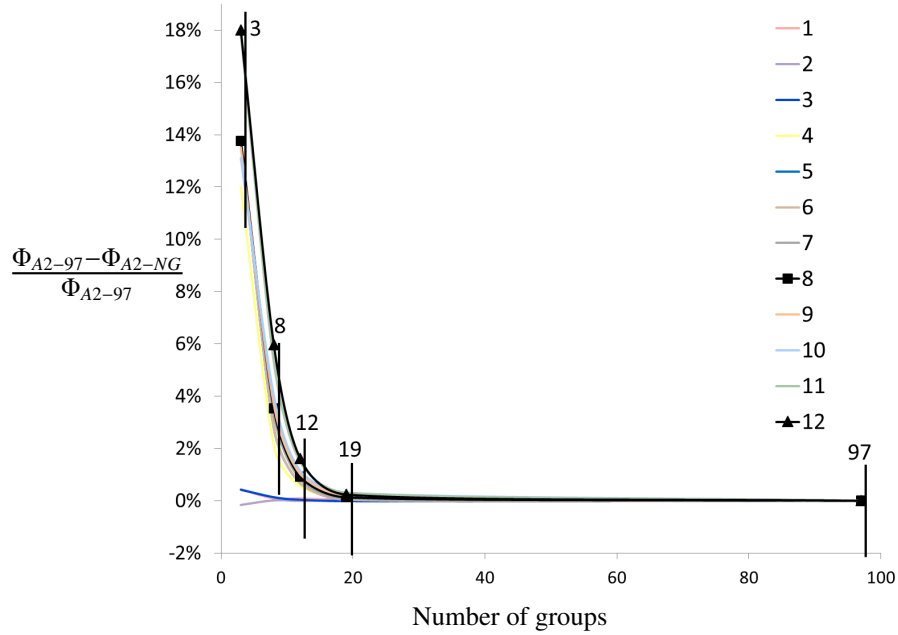
Figure III.10: Difference relative on the Φ_{1MeV} APOLLO2 calculation between the reference mesh with 97 groups and the optimised mesh at *NG* groups.

We finally determined an optimised mesh of 19 groups including one group below 1 MeV. To evaluate the accuracy of the homogenised and collapsed cross sections generated by APOLLO2 on this slab containing 12 media (Fig. III.6) for assessment of the

57

neutron flux with TRIPOLI-4®.
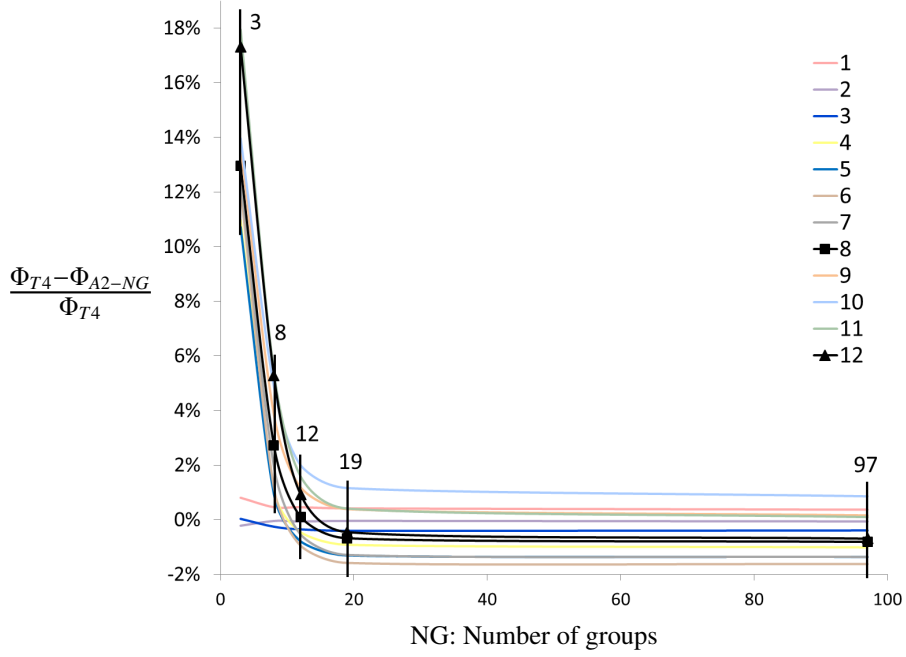
Figure III.11: Relative differences between Φ_{1MeV} calculated with the TRIPOLI-4® reference, and Φ_{1MeV} calculated with APOLLO2 and the optimised mesh at *NG* groups.

Fig. III.11 confirms that the optimum number of groups selected from the 97 groups over 1 MeV of the $600G$ multigroup library, is $19G$. Indeed, the differential error between the flux calculated by APOLLO2 with the $19G$ and TRIPOLI-4® is comparable in the media of the slab. The 19G mesh will thus be used in the next sections.
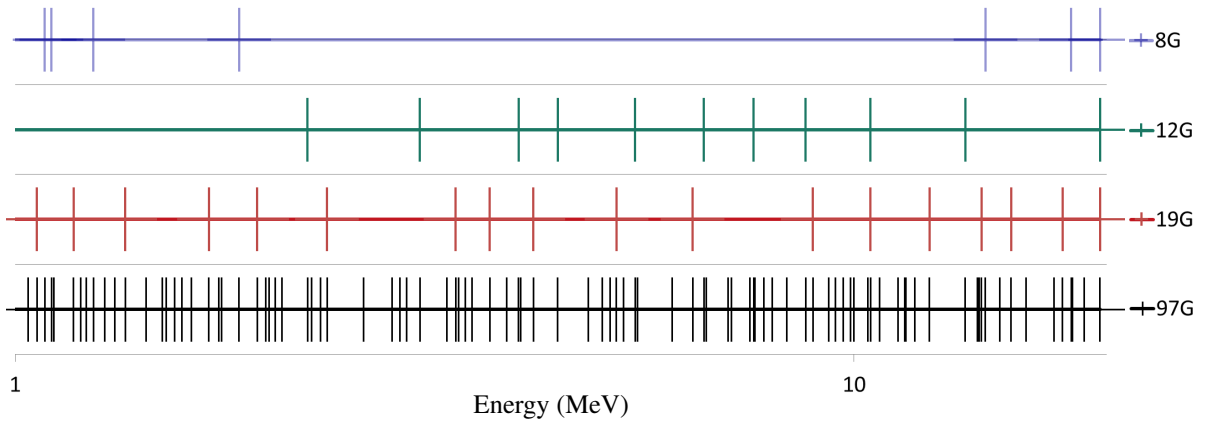
Figure III.12: Energy meshes resulting from the AEMC optimisation.

3 Deterministic calculation of the neutron fast flux and verification with the reference stochastic calculation

As previously mentioned, the *geometry* used in the deterministic scheme is an eighth of a PWR core. The reflector geometry is obtained by axial extrusion of five basic radial geometries. The axial temperature profiles of the water in the core and in the reflector correspond to standard operating conditions as defined for the reference calculation. The *homogenised and collapsed cross sections* generated by APOLLO2 on the 19G mesh are used to define the 11 shielding regions of the reflector.

Unlike the reference scheme, each assembly of the source is a standard 17x17 UO$_2$ *homogeneous pin cell*. The homogenisation is justified by the fact that neutron mean free path in UO$_2$ fuel and in bored hot water is higher than the size of the cells at energies beyond 1 MeV. The *power distribution* is identical to the reference case but it is homogenised on the fuel cells and discretised into 56 axial planes.
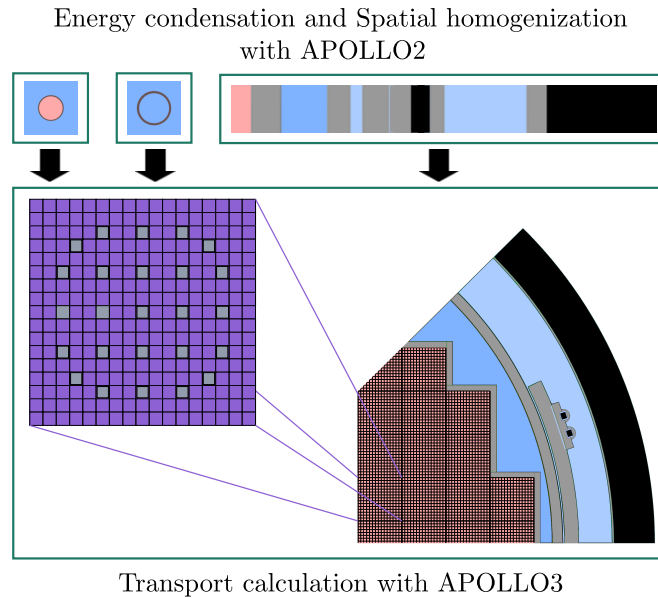
Figure III.13: Input data of the transport calculation.

This *numerical scheme* is based on the MINARET 3D-SN solver of the APOLLO3® code which uses the Galerkin discontinuous finite element approximation and an unstructured spatial mesh. The transport calculations are parallelised with respect to the angular directions. Self-shielded cross-section libraries are processed by a slab calculation corresponding to a section cut of the reactor going from the core to the inner part of the vessel.

The multigroup cross sections are collapsed over the 19-group energy mesh optimised by the Adaptive Energy Mesh Constructor (AEMC: see Mosca et al. (2011)). The calculation is performed using a P3 Legendre approximation for the scattering cross sections, an S8 angular discretisation, with a radial mesh size of 2 cm and an axial mesh size of 10 cm. The radial and the axial polynomial orders are set equal to 1 and 0 respectively and the relative error per group on the flux is constrained to be lower than 10^{-4}. These parameters follow from a preliminary convergence analysis and are consistent with the modelling strategy used for fluence calculation (Steele, 1983).

The fast neutron flux over 1 MeV is finally given by:

$$\Phi_{1MeV} = \sum_{g \geq 1MeV}^{18} \Phi^g(\vec{r}) \qquad \text{(III.7)}$$

where Φ^g denotes the spectral distribution of flux at the energy group g.

3.1 Direct flux calculation

Only the peripheral assemblies of the core included in configuration C of Tab. III.1, are taken into account in the direct transport calculation. This simplification reduces the CPU time by one third, preserving the accuracy of the solution because 99% of the flux received by the vessel and the surveillance capsules is due to neutrons from the peripheral assemblies. The spectra used for the final calculation are presented in Figure III.14.
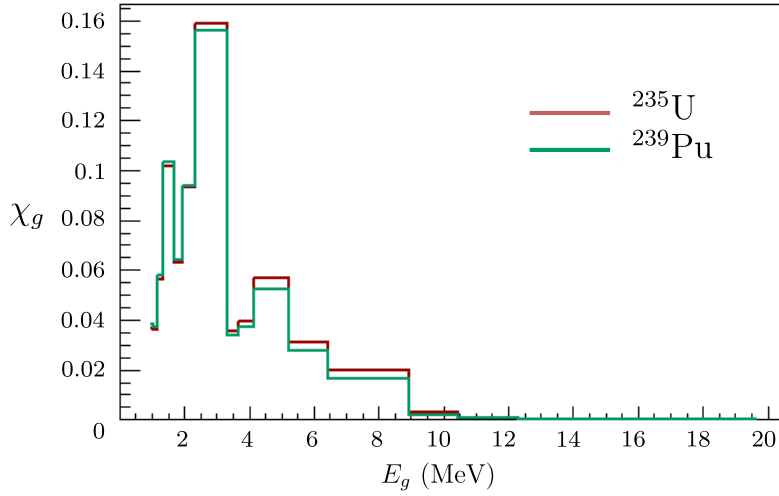
Figure III.14: ^{235}U and ^{239}Pu multigroup spectra.

Tab. III.3 assesses the relative error on the total flux as compared with the TRIPOLI-4® reference calculation, and shows that it is lower than 1%. Fig. III.15 shows that the multigroup flux discrepancy in the vessel is lower than 5% between 1 and 20 MeV. These results prove that the higher complexity of the 3D core has a negligible impact on the accuracy, contrary to the case of the multigroup approximation, because the results on the slab test (Fig. III.7) are comparable to those of the 3D configuration (Fig. III.15).

Medium	$\dfrac{\Phi_{1MeV}(T4) - \Phi_{1MeV}(A3)}{\Phi_{1MeV}(T4)}$	$3\sigma - T4$
Hot spot	0.61%	0.24%
Capsule 20°	0.86%	0.09%
Capsule 17°	0.30%	0.09%

Table III.3: Relative error on the total flux over 1 MeV between the reference TRIPOLI-4® (T4) and the APOLLO3® (A3) calculations

The integral of the flux over 1 MeV (Φ_{1MeV}) was calculated with APOLLO3® in at several specific locations of the reactor in less than 20 minutes. The calculation required a total memory
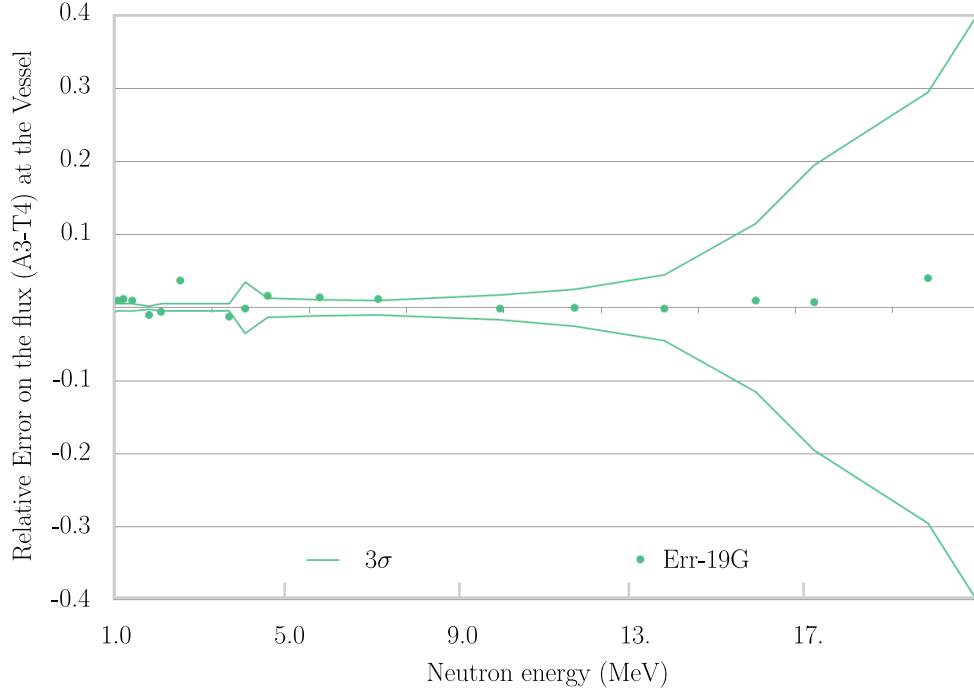
Figure III.15: Relative error on the multigroup flux between the reference TRIPOLI-4® and the APOLLO3® calculations.

of 113 Gb with a MPI [1] parallel computing on a LINUX CenOS6.4 cluster of 80 processors. The corresponding TRIPOLI-4® reference calculations required 6 hours with the same demand for processor resources. This demonstrates the appropriateness of MINARET calculations to perform uncertainty studies of neutron flux using a Total Monte Carlo approach for the statistical definition of perturbations.

3.2 Adjoint flux calculation

It is also possible to develop a flux model based on the calculation of the adjoint flux. The adjoint flux quantifies the average number issued from the history of an initial neutron with a fixed energy and at a given point of the phase space $(\vec{r}, \vec{\Omega})$. It measures the *importance* of the initial neutron in response of interest.

Assuming a detector k characterised by the macroscopic cross section Σ_k, the response I^g associated with the neutron scalar flux Φ^g is given by:

$$I^g = < \Sigma_k^g, \Phi^g > .\tag{III.8}$$

The flux Φ^g results from a source of neutrons S and can be obtained by solving the steady Boltzmann Eq. I.11.

$$\mathbf{L}^g \Phi^g(\vec{r}, \vec{\Omega}) = \mathbf{H}^g \Phi^g(\vec{r}, \vec{\Omega}) + S^g(\vec{r}),\tag{III.9}$$

where $\mathbf{L}^g$ defines the multigroup term of streaming of neutrons and of the total neutron collision rate determined by the total cross section, as:

$$\mathbf{L}^g = \vec{\Omega}.\vec{\nabla} + \Sigma_t^g,\tag{III.10}$$

---

[1]Message Passing Interface

and $\mathbf{H}^g$ defines the multigroup term of neutron scattering from the initial energy groups g' and directions Ω' into energy groups g and direction Ω, as:

$$\mathbf{H}^g = \sum_{g'} \int_{4\pi} d^2\vec{\Omega}' \Sigma_S^{gg'}(\vec{\Omega}.\vec{\Omega}'). \tag{III.11}$$

To evaluate the impact of a neutron source perturbation on the calculated responses, the first way is thus to solve the steady-state Boltzmann equation for each sample of perturbed sources. It consists in solving the adjoint equation by using the sensitivity of the detector defined by the macroscopic cross section as the source of the equation. The adjoint flux Φ^{g*} is in fact the solution of the equation at fixed sources:

$$\mathbf{L}^{g*}\Phi^{g*}(\vec{r},\vec{\Omega}) = \mathbf{H}^{g*}\Phi^{g*}(\vec{r},\vec{\Omega}) + \Sigma_k^g, \tag{III.12}$$

where,

$$\mathbf{L}^{g*} = -\vec{\Omega}.\vec{\nabla} + \Sigma_t^g, \tag{III.13}$$

$$\mathbf{H}^{g*} = -\sum_{g} \int_{4\pi} d^2\vec{\Omega}\Sigma_S^{gg'}(\vec{\Omega}.\vec{\Omega}'). \tag{III.14}$$

Mathematically, for any operator A, its adjoint operator A^* satisfies the following property for any functions f and g:

$$< f, Ag >=< A^*f, g > . \tag{III.15}$$

By writing $\mathbf{A}^g = \mathbf{L}^g - \mathbf{H}^g$, the interest response I^g of the detector k with Eq. III.12, III.8 and III.9, is thus given by:

$$I^g =< \Sigma_k^g, \Phi^g >=< \mathbf{A}^{g*}\Phi^{g*}, \Phi^g >=< \Phi^{g*}, S^g > . \tag{III.16}$$

The equation III.16 shows that the response of a detector can be assessed by convolution of the adjoint flux on the neutron source $S^g(\vec{r})$ and so, the results of all parametric study on the source. In our work, the responses considered are the multigroup flux over 1 MeV at the capsules. The first step of the adjoint flux is thus to compute and store, with the MINARET solver, the adjoint flux associated with the response multigroup flux at the different locations of interest by imposing the source $S^{g*}(\vec{r})$:

$$S^{g*}(\vec{r}) = \begin{cases} 1 & \text{if } r \in V, \text{ volume of interest} \\ 0 & \text{if not} \end{cases} \tag{III.17}$$

Tab. III.4 shows that the relative distance between the flux associated with the direct calculation and the adjoint calculation is negligible, while the calculation time is 3 minutes for the adjoint approach and 20 minutes for the direct approach.

	Capsule 17°	Capsule 20°	Calculation Time
Adjoint	1.82e+11	1.56e+11	3 min
Direct	1.82e+11	1.56e+11	20 min
Relative distance	-0.01%	-0.01%	-

Table III.4: Comparison between the direct and adjoint approaches for the calculation of Φ_{1MeV} at the nominal conditions.
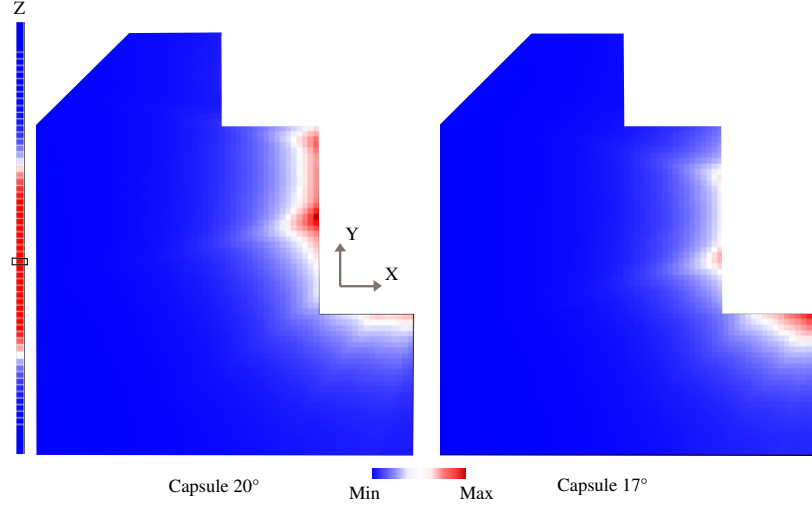
Figure III.16: Spatial distribution of the adjoint flux associated with the responses of the
capsules, and in the median plane of the core.

Fig. III.16 shows the spatial distribution of the adjoint flux at the median plane of the core
and associated with the surveillance capsules.

Eventually, the multigroup scalar flux Φ^g is assessed in all the regions of interest (capsules
and vessel) by convolution of the adjoint flux with the neutron source of the core:

$$\Phi^g = < S^g, \Phi^{g*} > \tag{III.18}$$
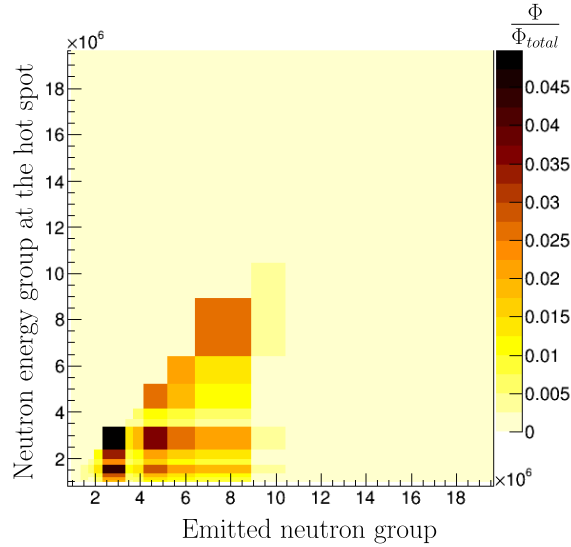
Figure III.17: Contributions of the emitted neutrons by the source to the neutrons received by a
fixed point at the hot spot.

The integral flux over 1 MeV Φ_{1MeV} is then given by: $\Phi_{1MeV} = \sum_g \Phi^g$, as $E^g > 1$ MeV. Fig.
III.17 finally illustrates the multigroup scalar flux affecting the vessel depending on the energy
of neutrons emitted in the core. The matrix is a triangular matrix because the neutron emitted
at a given energy cannot reach the vessel with a higher energy. There is no up-scattering for
the neutron energy over 1 MeV. Most neutrons are emitted between the groups 6 and 12 and
received at the fixed point of the vessel in groups 12 and under. Moreover, one can notice that

the group 7, 10, 11 and 12 are associated with larger flux values because they are defined by larger energy intervals.

4 Conclusion

In this chapter, we have developed a deterministic calculation of the fast flux Φ_{1MeV} which is sufficiently rapid and accurate to be used in a Total Monte Carlo approach of uncertainty propagation. This scheme is based on the 3D-SN solver MINARET of the APOLLO3® code which uses the Galerkin discontinuous finite element approximation. Self-shielded cross-section libraries are processed by a slab calculation corresponding to a section cut of the reactor going from the core to the inner part of the vessel. The multigroup cross sections are collapsed over the energy mesh optimised by the Adaptive Energy Mesh Constructor (AEMC). It consists of a single group between 10^{-11}MeV and 1MeV and 18 energy groups greater than 1MeV. The calculation is performed using a P3 approximation for the scattering cross sections.

With this scheme the total flux over 1 MeV (Φ_{1MeV}) is calculated in different locations of the reactor in less than 20 minutes with an error lower than 1% with respect to the TRIPOLI-4® reference on a tridimensional PWR geometry (Mosca et al., 2018). The next step will now consist in quantifying and modelling the uncertainties, and propagating them in the deterministic scheme developed.

Chapter IV

Modelling uncertainties and propagation in fast flux calculations

In the chapter III, we have developed and described the deterministic calculation of the fast flux Φ_{1MeV}. The next step of the Total Monte Carlo approach is to generate perturbations on the input parameters of the calculation model. This chapter is thus devoted to modelling the input uncertainties of the fast flux model, and their propagation in the calculation chain. It consists in three sub-steps:

- determining the uncertain parameters of our study,

- quantifying the uncertainty of each parameter which is regarded as random variable,

- and generating random samples to propagate in the fast flux calculation.
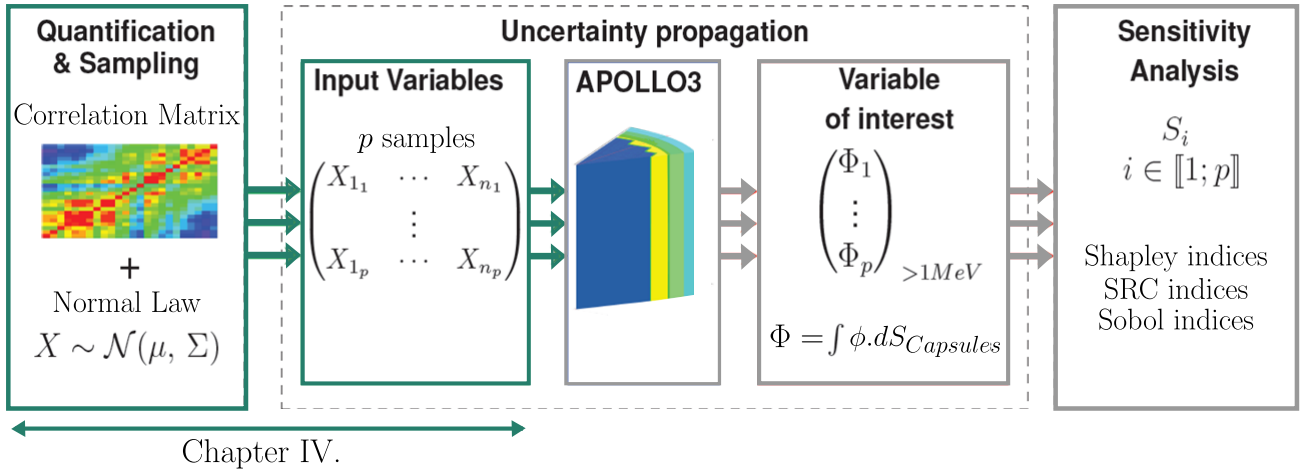
Figure IV.1: Uncertainty propagation scheme: in green the specification of the uncertainty modelling

Section 1 provides the uncertainty sources of the deterministic scheme of the fast flux and compares them with those of the reference calculation. Section 2 and Section 3 then depict the general approach involved in this thesis to model and propagate uncertainties respectively. Finally, Section 4 describes in details the various dedicated methodologies designed to quantify and propagate uncertainties for distinct specific subgroup of parameters.

We emphasise that one of the main contributions in this thesis is to fully account for the dependency information among variables to achieve a complete global sensitivity analysis. The aim is to understand how correlation data can influence the variability of an output model in order to demonstrate the need to maintain efforts to provide accurate correlation data. A special attention will therefore be devoted to ensure the overall consistency of data during the parameter perturbation.

The uncertainty propagation is piloted by URANIE(Blanchard et al., 2019), the CEA uncertainty and sensitivity analysis platform developed in the *Laboratoire de Génie Logiciel pour la Simulation* (LGLS) of the *Service de Thermohydraulique et de Mécanique des Fluides* (STFM) at CEA/Saclay.

1 Uncertainty sources in fast flux calculations

The fast flux calculation is based on solving the neutron transport equation. As introduced in Chapter I, the multigroup and differential form of the steady-step equation is given by:

$$\vec{\Omega}.\vec{\nabla}\phi^g(\vec{r}, \vec{\Omega}) + \Sigma_t^g(\vec{r})\phi^g(\vec{r}, \vec{\Omega}) = Q^g(\vec{r}, \vec{\Omega}). \tag{IV.1}$$

The inaccurate evaluation of the fast flux can consequently result from all the assumptions and parameters linked to the resolution of the neutron transport equation, i.e. the *numerical errors* (convergence criteria, computing methods, etc.), the *modelling errors* (material, dimension and placement uncertainties, source distribution, etc.), and the propagation of *nuclear data uncertainties* (cross-sections, neutron spectrum, etc.) through the simulation tools. The numerical errors cannot be treated statistically because they are intrinsic to the calculation method. They can be reduced and estimated with the comparison between theory and experiment. For that reason, this thesis focusses on the quantification of the data uncertainties. The source of uncertainties are thus the input data of the neutron transport equation solved by the APOLLO3® code and summarised in Tab. IV.1.

Tab. IV.1 shows the large number of uncertain parameters which will be perturbed for the uncertainty quantification of the fast flux. Additionally, most of the data are correlated. It means that a special attention should be devoted to ensure the overall consistency of data during the parameter perturbation. We will notably discuss on the importance to take into account the correlation data in the modelling step of uncertainties.

In the previous chapter III, we have shown that the calculation bias with respect to the TRIPOLI-4® reference calculation is lower than 1% in the nominal conditions of the PWR reactor. The difference between both calculations mainly comes from the numerical errors introduced by the deterministic calculation. Actually, one must draw a distinction between the *numerical errors* (multigroup formalism, self-shielding, angular and spatial discretisation, etc.) of the deterministic scheme, and the *statistical errors* of the stochastic scheme which can be reduced by increasing the number of random draws simulated with the Monte Carlo code 1.1. At this stage of the study, we assume that the differences between the two types of calculations are independent of the perturbations which will be introduced by the propagation of uncertainties. This hypothesis will be developed and verified in Chapter V.

Data	Random variables	Number of variables		Correlation
Nuclear	Fission spectrum $\chi_f^g : {}^{239}\text{Pu} - {}^{235}\text{U}$	$2N_{groupes}$	36	in energies
	Cross sections σ_ρ^g	$N_{reactions}N_{groupes}N_{iso}$	1440	among reactions and energies
	Angular distribution of cross-sections $\sigma_{sl}^{gg'}$	$N_L N_{groupes} N_{iso}$	108	among Legendre order and energies
Technology	Power distribution	$N_{assembly}$	25	by assembly positions
	Geometry (Manufacturing tolerance)	$N_{parameters}$	8	-
	Water temperature (Reflector and fuel)	$N_{Temperatures}$	2	-

Table IV.1: Uncertainty sources of the fast flux calculation with APOLLO3® code

2 Uncertainty modelling strategy

In this section, the choice made to define the uncertainties of the input parameters of the fast flux calculation is discussed.

2.1 Probability distributions by entropy maximisation

As explained in Chapter II, sensitivity analysis and uncertainty propagation are conditioned by the selection of probability distributions for the perturbations of input parameters. It is therefore necessary to choose probability distributions which are consistent with the data knowledge and which introduce no additional and groundless information.

It is known that the most common distribution function for measured quantities is the normal distribution. It stems from the central limit theorem which states that the distribution of the mean, or sum, of *n* independent observations taken from any distribution, or even different distributions, with finite mean and variance approaches a normal distribution as *n* approaches infinity. So, if the measurement is the result of a large number of independent parameters, the expected distribution is normal. In reality the measurement is never described by an infinite number of observations, but a few observations are often sufficient to approach the distribution of the measurement by a normal law. Moreover, uncertain variables of physical models are not always directly measurable or observable, but their uncertainties can, for example, result from the propagation of uncertainty or a least squares parameter fitting and thus derived analytically in explicit form. In that case, when the mean and the variance are selected as descriptors of the data, the Gaussian distribution is used to best describe the current state of knowledge. It is a direct application of the principle of maximum entropy introduced in Chapter II Section 1.2.

Nevertheless, it has to be emphasised that when the considered physical quantities are by definition positive, the normal distributions can be inadequate for large variances because they can induce negative values during the random sampling (Lahaye, 2018). This case will be discussed further for the cross sections in Section 4.3.4.

On the other hand, in this study, there are some variables for which the mean is not known. In that case, if the uncertainty is described by a variation range with bounding limits, the uniform distribution appears most adequate and it is assumed that the probability of finding values between the limits is unity.

2.2 Use and interpretations of Bravais-Pearson correlation for modelling dependencies

There are different ways to measure an association between two variables. One of the most used is the Pearson-product-moment correlation which measures the possible linear relationship between two continuous variables:

$$r_{yx} = \frac{Cov(Y, X)}{\sqrt{var(X)var(Y)}}.$$ (IV.2)

The Pearson correlation is usually used for jointly normally distributed data. The joint normal distribution is not a necessary condition to use a Pearson coefficient but ensures that, in that case, there is an equivalence between uncorrelatedness and independence. One should keep in mind that a relationship between jointly normally distributed data is always linear. Reciprocally, if the two variables are non-linearly related, the use of bivariate normal distribution can be questioned. An alternative type of correlation is the Spearman rank correlation which measures a possible monotonic association among variables. In nuclear evaluated libraries, correlations are given by definition at the Pearson's sense. This is why this definition is used in our work, bearing in mind the framework of its interpretation.

Moreover, it should be noted that if the accuracy of the sensitivity analysis will be conditioned by the quality of the covariance matrices used, the purpose of this work is not to assess quality of covariance data provided by evaluated nuclear data files. Correlation data provided by evaluators are in fact supposed corrects. In reality, for the interpretation of their influence, it is important to know that in nuclear evaluated library, covariance files are incomplete and the absence of covariance data does not imply that the evaluated uncertainty or the correlation is zero (McLane, 2005). This implies that we are limited by the information contained in the data libraries to sample the uncertain variables of the fast flux calculation. According to the ENDF manual (McLane, 2005), evaluators should not unintentionally enter explicit zero covariance components into a file if uncertainties or correlations are not evaluated as zero or negligible. In that sense, we assume in our work that the presence of zeroes in covariance matrices inform on the linear independence of data.

On the other hand, one must keep in mind that the evaluation process is often based on a limited number of experiments and observations that makes the result statistically insignificant. The degree of accuracy on covariance data in current evaluated files is therefore limited. In the next chapter V, the need to maintain efforts aimed at providing accurate correlation data will be more analysed and discussed.

Lastly, we would like to remind the fact that the occurrence of correlation is not equivalent to the existence of causality. It is important to understand the meaning and the possible origin of correlations. The correlation between two variables is often confused with causation but in reality, it is possible to have different types of interpretation of this correlation:

- Firstly, two variables Y and X can be correlated accidentally. Normally, the step of modelling and quantification of input uncertainties excludes this possibility because only correlations among variables which are physically connected, are considered.

- Another possibility is that a correlation between Y and X can mean Y causes X and not the reverse.

- Finally, it is also possible that there is an indirect linkage between Y and X explained by a hidden variable Z. We can easily imagine this case in nuclear processes. As an illustration, just let us imagine two experiments, the purpose of which is to determine respectively two distinct nuclear variables X_1 and X_2. The latter are indirectly rebuilt from two physical models which depend on the direct measurement of observables a, b, and c as $X_1 = f(a, b)$

and $X_2 = g(b, c)$. Intuitively, we can anticipate a non-zero correlation between X_1 and X_2 due to the common contribution of the variance of b.

These three examples show us that a good understanding of the origin of correlations is necessary to fully interpret the origin of uncertainties. In the case of nuclear data, we can, moreover, anticipate the difficulty to interpret the results of sensitivity analysis, whatever the method used, considering that there is sometimes a lack of information provided by experimentalists on the origin of potential correlations described in the international libraries. To inform our discussion, one cannot lose sight that nuclear evaluated data tend to be correlated mainly because of adjustment processes such as energy normalisation, marginalisation, consistent adjustment, etc. (Chapter I).

3 Perturbation methodology of uncertain variables by Cholesky decomposition

The objective of this step is to select p samples of n input correlated data that respect a multivariate normal law of expected value $M = (\mu_1, ..., \mu_n)$ and a covariance matrix Σ. This means that if $X_{(p,n)}$ is the matrix which contains the samples, the covariance matrix Σ must be the measure of the joint variability of the random samples with $\Sigma = \mathbb{E}\left[(X - \mathbb{E}[X])^t (X - \mathbb{E}[X])\right]$ and with $M = \mathbb{E}[X]$.

To achieve this, an upper triangular matrix U is determined by the method of Cholesky decomposition $\Sigma = U^t U$ where Σ is a *positive-definite* matrix. It means:

Positive definite matrix

For all non zero vectors $x \in \mathbb{R}^n$, $x^t \Sigma x > 0$. $\qquad$ (IV.3)

In addition, it may be noted that Σ is positive definite if, and only if, it has a unique Cholesky factorization as $\Sigma = U^t U$. The p samples of each random variable are then obtained according to:

Random sampling by Cholesky decomposition

$$X_{(p,n)} = \begin{pmatrix} \mu_1 & \cdots & \mu_n \\ & \vdots & \\ \mu_1 & \cdots & \mu_n \end{pmatrix}_{(p,n)} + AU. \qquad (IV.4)$$

The matrix $A_{(p,n)}$ is generated from n random Gaussian variables $\mathcal{N}(\mu = 0, \sigma^2 = 1)$ by a Latin Hypercube Sampling, a method explained thereafter. $U_{(n,n)}$ is determined by the Cholesky decomposition of the positive definite matrix Σ.

Finally, by measuring the joint variability of the random samples determined in Eq. IV.4, one can easily demonstrate, thanks to the linearity of expectation, that the experiment plan is well defined by the expected matrix $M_{(p,n)}$ and covariance matrix Σ:

$$\mathbb{E}[X] = \mathbb{E}[M] + \mathbb{E}[AU] = \mathbb{E}[M] + \mathbb{E}[A]U = M, \qquad (IV.5)$$

and,

$$\mathbb{E}\left[(X - \mathbb{E}[X])^t (X - \mathbb{E}[X])\right] = \mathbb{E}\left[U^t A^t A U\right] = U^t \mathbb{E}\left[A^t A\right] U = U^t U = \Sigma. \qquad (IV.6)$$

3.1 Optimal Latin Hypercube Sampling

The **Latin Hypercube Sampling** divides the sample space into p equally probable subspaces, and selects simultaneously for each segment, one value representing this subspace. The partition into equally probable intervals enables taking into account non-uniform density of probability like for instance a normal distribution. Moreover, it is carried out according to a Maximin constraint which means that we search the configuration with the maximal d_{min}, where $d_{min} = min_{i,j} \|x_i - x_j\|_2$ is the minimal Euclidean distance between two points of the design of experiments. In that sense, the **Latin Hypercube Sampling** used here is a **space filling design**. This methodology is widely used because it allows to ensure a good representativeness of the domain of variation with a reduced number of samples.

3.2 Spectral decomposition as alternative to Cholesky decomposition for ill-conditioned matrices

In practice, the algorithm for computing the Cholesky decomposition IV.4 of Σ depends on the *condition number* $\kappa(\Sigma)$, which defines the ratio between the largest and the smallest eigenvalue of Σ:

$$\kappa(\Sigma) = \frac{\lambda_{max}}{\lambda_{min}}. \tag{IV.7}$$

The larger the condition number, the more ill-conditioned the system. The issue is that the use of an ill-conditioned matrix in the field of numerical mathematics (matrix inversion, matrix decomposition, linear system resolution, ...) can lead to round-off errors.

There are various reasons that may lead to an ill-conditioned matrix. The high-dimensional space or the successive processes to estimate Σ (as the generation of multigroup covariances with ERRORR, see next Section 4.3), can for example led to an ill-conditioned matrix.

However, the ill-conditioned matrix can make the Cholesky factorization difficult. In fact, the classic method of resolution is based on assessing the terms of the matrix U used in the Eq. IV.4 by the following iterations:

$$\text{for } j = 1, .., n, \, U_{j,j} = \sqrt{\Sigma_{j,j} - \sum_{k=1}^{j-1} U_{j,k}^2}, \tag{IV.8}$$

and,

$$U_{i,j} = \frac{1}{U_{j,j}} \left(\Sigma_{i,j} - \sum_{k=1}^{j-1} U_{i,k} U_{j,k} \right) \quad \text{pour } i > j. \tag{IV.9}$$

When the matrix Σ is ill-conditioned, it is impossible to compute it due to an accumulation of the rounding errors which makes negative the term $\Sigma_{j,j} - \sum_{k=1}^{j-1} U_{j,k}^2$. To work around this, there are various options. A first possibility consists in regularising the Σ matrix by fixing a ϵ value chosen to decrease the condition number $\kappa(\Sigma)$ (Riley, 1955) and approach the covariance matrix by:

$$\hat{\Sigma} = \Sigma + \epsilon I, \tag{IV.10}$$

where I is the identity matrix.

An alternative method is to use the *spectral filtering* of Σ. Actually, by construction and definition, Σ is a *normal real* matrix. Therefore, according to the spectral theorem, Σ admits a unitary *eigendecomposition*:

Spectral decomposition

$$\Sigma = Q\Lambda Q^t = \sum_{i=1}^{n} \lambda_i \vec{q}_i \vec{q}_i^t \qquad \text{(IV.11)}$$

where $\vec{q}_i$ are the *eigenvectors* of Σ and Λ is a diagonal matrix.

Remark. *Σ is a square normal matrix if, and only if, $\Sigma^t\Sigma = \Sigma\Sigma^t$. Σ is an hermitian matrix if, and only if, $\Sigma = \bar{\Sigma}^t$, where $\bar{\Sigma}^t$ contains the complex conjugate of Σ^t. A real symmetric matrix is thus Hermitian and normal.*

Because the eigenvalues $\lambda_1, ..., \lambda_n$ are real, we can then order them in decreasing order of their absolute values, i.e. $|\lambda_1| \geq ...|\lambda_n|$. At this step, it is possible to relate the *spectral decomposition* IV.11 to the *singular value decomposition* IV.12 by using the fact that $P = Q\text{diag}\{\text{sign}(\lambda_i)\}$ and $S = \text{diag}\{|\lambda_i|\}$. Moreover, the definite positiveness of Σ, ensure that the eigenvalues are positive and that $P = Q$.

Singular Value decomposition of square matrices

The singular value decomposition of a matrix $X_{(p,n)}$ is a generalisation of the spectral decomposition for the rectangular matrix:

$$X_{(p,n)} = P_{(p,n)} S_{(n,n)} Q_{(n,n)}^t, \qquad \text{(IV.12)}$$

where $P_{(p,n)}$ and $Q_{(n,n)}$ are the matrices which contain respectively the eigenvectors of $X_{(p,n)}^t X_{(p,n)}$ and $X_{(p,n)} X_{(p,n)}^t$, S and is a diagonal matrix which contains the singular values of $X_{(p,n)}$.

At this stage, the first solution is the *truncated singular value decomposition*. It consists in discarding all the singular values that are smaller than a threshold ϵ. It is also possible to directly use the singular value decomposition to achieve the random sampling following Eq. IV.4. Indeed, we can use the fact that:

$$QSQ^t = QS^{1/2}S^{1/2}Q^t = (S^{1/2}Q^t)^t(S^{1/2}Q^t), \qquad \text{(IV.13)}$$

and note $U = S^{1/2}P^t$.

In our work, we will thus use the Cholesky decomposition via the **TDecompChol** class of the framework ROOT (Brun, R. and Rademakers, F., 1997), when the matrix is well conditioned and, the **TDecompSVD** class when the matrix is ill-conditioned. Numerically, some of the smaller singular values of Σ can be negatively close to zero. If this occurs, we replace the value by zero in the diagonal matrix S.

4 Uncertainty definition and perturbation of input parameters of the fast flux calculation

The sampling is performed with the platform URANIE (Blanchard et al., 2019) which pilots the design of experiments.

4.1 Technological parameters: geometry, water temperature in primary circuit, and impurities in steel

This section describes the modelling uncertainty of technological parameters: manufacturing tolerance of in-vessel components, water temperature of the primary circuit and the composition of impurities in steel. They are often described in a variation range defined by a minimum and maximum values. By maximum entropy principle (see Chapter II Section 1.2), we thus consider that the variation of the uncertain variables follows a uniform law. Specifically, for temperature sampling, the perturbation is the same at each axial step of the core, since the total power of the reactor is not an uncertain variable of the study.

Parameters		$\pm a$ (%)
Azimuth	α	± 1.79
Internal Vessel Radius	R_{intves}	± 0.29
Internal Envelope Radius	R_{intenv}	± 0.24
External Envelope Radius	R_{extenv}	± 0.06
Internal Shield Radius	R_{intsh}	± 0.27
Capsule thickness	$E_{capthick}$	± 1.20
Water gap	E_{watgap}	± 16.67
Capsule position	E_{cappos}	± 0.01
Water temperature	T_{water}	± 0.33

Table IV.2: Support of the uniform law $\mathcal{U}(-a, +a)$ which defines the uncertainties of the technological parameters - The values are centered normalized to the nominal values of the parameters.

4.2 Neutron source

In PWRs, the number of neutrons emitted by each assembly k in the energy group g depends on the *spatial terms* $S_{k,i}$ and the *fission spectra* $\chi_{i,g}$ (normalised by $\int \chi(E)dE = 1.0$), which defines the probability for a neutron to be emitted in the energy group g by the isotope i (uranium or plutonium) Kodeli (1993):

$$Q_{k,i}^g = S_{k,i}\chi_{i,g}. \tag{IV.14}$$

In the assembly k, the number of neutrons coming from the fissions of the uranium and plutonium isotopes can be derived as:

$$S_{k,i} = \sum_{p \in k} \frac{P_p f_i \nu_i}{f_{conv} V_p(\sum_j f_j E_{fj} + E_0)}, \tag{IV.15}$$

where:

- P_p, is the global power released in the fuel pin p of the assembly k (Watt),

- V_p, the volume of the fuel pin p (cm^3),

- f_{conv}, conversion factor ($J.eV^{-1}$),

- f_i, the fission fraction of the isotope i,

- ν_i, the average number of neutrons emitted by the isotope i,

- E_{fj}, the mean recoverable energy per fission j

- E_0, the energy produced by the capture of neutrons.

In the definition of neutron source, the main sources of uncertainties are the *power distribution* and the *fission spectra*. Comparatively, the uncertainties due to the other terms are lower than 0.2% and are thus neglected in the study. When modelling uncertainties of the PWR parameters, the spatial neutron source of one eighth of the PWR core is thus perturbed by proportionality to the power distribution and the fission spectra, as presented in next section 4.2.1.

4.2.1 COMAC covariances of the prompt fission neutron spectrum

In the core, the neutrons are emitted in an isotropic way according to the energy spectrum defined for the two fissile isotopes ^{235}U and ^{239}Pu, as illustrated in Fig. III.14 of previous chapter III. The number of fissions that takes place in the core is thus linked to the proportion of fissile atoms (^{235}U-^{239}Pu) which is taken, in this work, at a *fixed burn-up* representative of the average condition of the core. In addition, only the uncertainty modelling of the prompt fission neutron spectrum (PFNS) is accounted for. The prompt neutrons, which are immediately emitted by a nuclear fission event, are actually more likely to cause fast fission and to leak from the core, in comparison with *delayed neutrons*.

In evaluated nuclear data libraries, PFNS is often described from the Madland-Nix model $\chi^{L,H}(E, T_m, E_f^{L,H})$, grounded on the evaporation theory of fission fragments, and defined from the residual temperature of the fissioning nucleus T_m, the energy of prompt neutrons E, and the energy of the heavy and light fission fragments $E_f^{L,H}$. There aren't many international libraries yet, which give covariance data on PFNS. Berge (2015) has proposed covariance data for the PFNS definition of JEFF-3.1.1, which has recently been included in the COMAC V2.0 files. To ensure consistency with the library JEFF-3.1.1 used for the deterministic and reference flux calculation of our work, the COMAC V2.0 files were thus chosen for the definition of uncertainties on the spectrum. COMAC (COvariance MAtrices from Cadarache, version 0.1) is in fact a project developed by the SPRC Neutron Physics Service at CEA-Cadarache to provide, with the code CONRAD (Archier et al., 2014), relative multigroup covariance matrices for the most important nuclear data (cross sections, multiplicities - prompt and delayed neutrons, prompt fission neutron spectrum, fission yields).

In order to generate a realistic set of covariances which is consistent with the JEFF-3.1.1 evaluation and with the experiments, Berge et al. (2015) has first used a Madland-Nix model of $\chi(E)$ to describe the thermal neutron induced by the fission of isotopes. She has determined, following the Madland-Nix model, the Pearson correlations on the spectrum as a function of energy (defined in Eq. IV.16). A Bayesian adjustment process of the model parameters has then been achieved to take into account systematic experimental uncertainties using a marginalisation technique (Habert et al., 2010) available in the CONRAD code.

$$corr\left(\chi_i, \chi_j\right) = \frac{\sum_k \sum_l cov(x_k, x_l) \frac{\partial \chi_i}{\partial x_k} \frac{\partial \chi_j}{\partial x_l}}{\sqrt{\sum_k \sum_l cov(x_k, x_l) \frac{\partial \chi_i}{\partial x_k} \frac{\partial \chi_i}{\partial x_l}} \sqrt{\sum_m \sum_n cov(x_m, x_n) \frac{\partial \chi_j}{\partial x_m} \frac{\partial \chi_j}{\partial x_n}}} \qquad \text{(IV.16)}$$

E_g	8.21E+05	1.35E+06	2.23E+06	3.69E+06	6.07E+06	1.00E+07
E_{g+1}	1.35E+06	2.23E+06	3.68E+06	6.07E+06	1.00E+07	1.96E+07
σ_{U235} (%)	1.42	0.89	0.57	3.90	10.76	22.93
σ_{P239} (%)	2.45	1.07	2.35	4.85	8.77	17.24

Table IV.3: Standard deviation of χ_g for both the isotopes ^{235}U and ^{239}Pu

The covariances associated with ^{235}U and ^{239}Pu are described in COMAC-V2.0 files on the 33-group ECCO mesh (Fig. IV.2). The correlation data and the uncertainties on the multigroup neutron spectra are finally presented in Fig. IV.3 and in the Tab. IV.3 for the six groups over 1 MeV of the 33-group ECCO mesh.
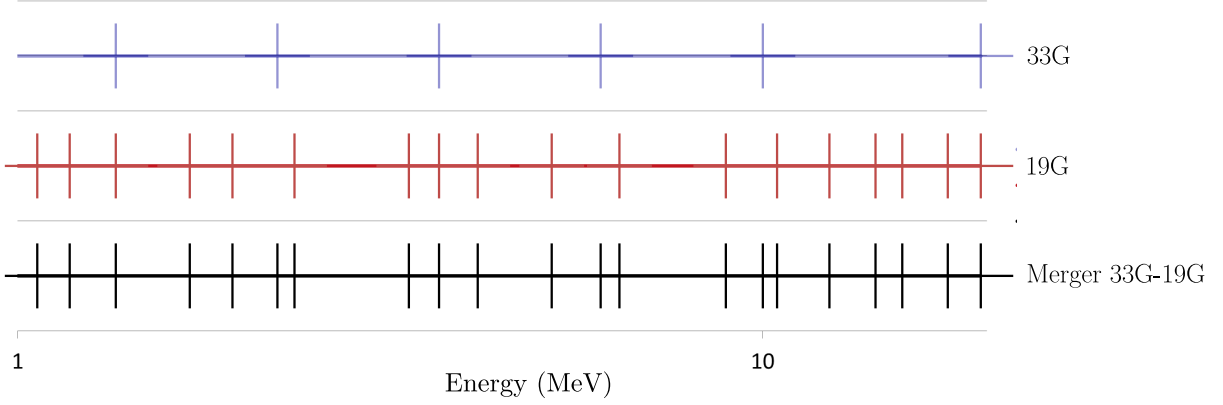
Figure IV.2: Comparison between the 19G mesh of the APOLLO3® calculation and the 33G mesh of the COMAC covariances.

(a) U235.

(b) ^{239}Pu.
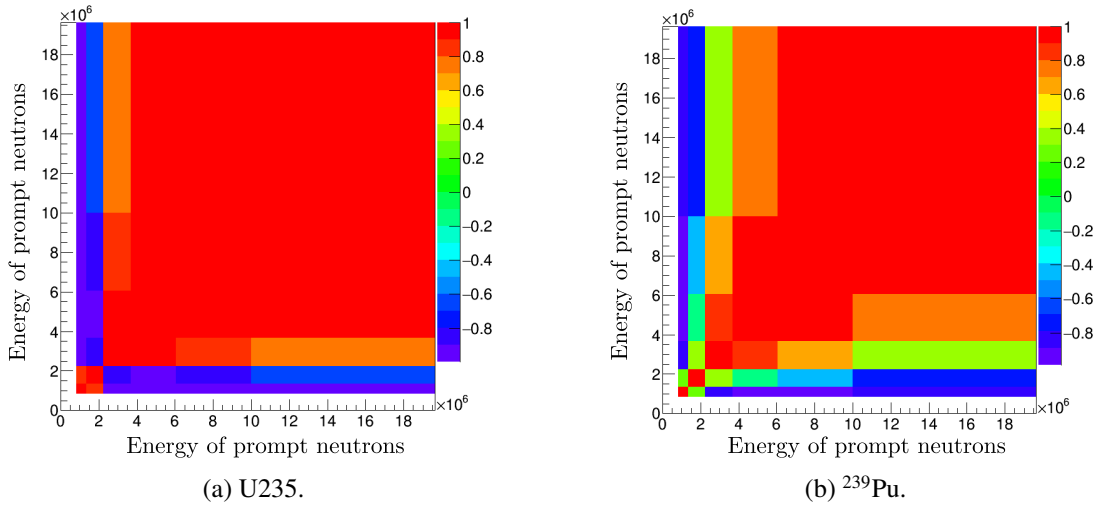
Figure IV.3: Energy correlations of the PFNS (nth,f) on the 6 mesh over 1 MeV of the 33G mesh

The covariance matrix from the Berge calculation can be divided into two sub-domains (see Fig. IV.3). For two E_i and E_j belonging to the same subdomain, $\chi(E_i)$ and $\chi(E_j)$ tend to be correlated, whereas for two distinct subdomains, $\chi(E_i)$ and $\chi(E_j)$ tend to be anti-correlated.

This phenomenon is due to the normalisation constraint of the spectrum: $\int \chi(E)dE = 1$.

4.2.2 Consistent perturbations of the neutron multigroup spectra on the 19G mesh

As the energy boundaries of the COMAC mesh do not correspond to the mesh involved in the flux calculation of APOLLO3® (Fig. IV.2), a modification is required to perturb correctly the fission spectrum as explained thereafter. The idea is to use the *principle of addition of probabilities* to transpose the perturbations sampled from the COMAC matrix to the 19G energy mesh.

Principle of addition of probabilities on the neutron spectrum

By definition, the fission spectrum can be calculated in a larger group G such as:

$$\chi^G = \sum_{g \in G} \chi^g. \tag{IV.17}$$

By analogy to the ERRORR procedure (MacFarlane, 2017), we similarly introduce three different energy grids to achieve the energy transposition:

- UsG: The "User grid" with N_{Us} groups, is the multigroup structure in which the output multigroup covariances are to be produced, i.e. the 19G mesh of APOLLO3®,
- CG: The "COMAC grid" with N_{CG} groups, is the 33G mesh, on which the covariances are defined,
- UnG: The "Union grid" with N_{Un} groups, is the joint mesh of UsG and CG.

Let us consider the following example in Tab. IV.4.

UsG: User Grid		χ_1		χ_2	
CG: COMAC Grid	f_1		f_2		f_3
UnG: Union Grid	χ_I	χ_{II}		χ_{III}	χ_{IV}

Table IV.4: Example for the transposition of meshes

The generation process will be carried out following six successive steps:

- **Sampling of the neutron spectra** from the covariance matrix on the CG (COMAC grid)
  Using the sampling methodology based on the Cholesky decomposition of the covariance matrix and presented in Section 3, one can obtain the 3 relative perturbation factors f_1, f_2, f_3 associated with the 3 groups of the CG mesh. In our case, it corresponds to 6 groups of the COMAC mesh.

- **Determination of the Union Grid** UnG

- **Determination of the nominal multigroup spectra** defined by $\chi_{\mathbf{UnG,0}}$ on each group of UnG with the module GROUPR of NJOY,

- **Determination of the perturbed multigroup spectra** $\chi_{\mathbf{p}}$ on the union grid UnG as,

$$\begin{aligned}
\chi_{I,p} &= f_1 \times \chi_{I,0} \\
\chi_{II,p} &= f_2 \times \chi_{II,0} \\
\chi_{III,p} &= f_2 \times \chi_{III,0} \\
\chi_{IV,p} &= f_3 \times \chi_{IV,0}
\end{aligned} \tag{IV.18}$$

- **Condensation of the perturbations** on the final mesh UsG and **normalization on the spectrum**: By *principle of addition of probabilities*, it is finally easy to write:

$$\chi_{1,p} = \chi_{\text{I},p} + \chi_{\text{II},p} = f_1 \times \chi_{\text{I},0} + f_2 \times \chi_{\text{II},0}$$
$$\chi_{2,p} = \chi_{\text{III},p} + \chi_{\text{IV},p} = f_2 \times \chi_{\text{III},0} + f_3 \times \chi_{\text{IV},0}$$

(IV.19)

This procedure can be cast in a matrix form as follows:

$$\mathbf{X_{UsG}} = \mathbf{F_{UsG,UnG}X_{UnG}},$$

(IV.20)

where X_{UnG} contains the N_{Un} values of the multigroup neutron spectra on the union mesh UnG,

$$\mathbf{X_{UnG}} = \begin{pmatrix} \chi_1 \\ \vdots \\ \chi_{N_{Un}} \end{pmatrix},$$

(IV.21)

and $F(\mathbf{K}, I)$ describes the projection of the relative perturbations between the two meshes UsG and UnG, through N_{Us} lines and N_{Un} columns:

$$F(\mathbf{K}, I) = \begin{cases} f_{\mathbf{K}I} \text{ if } I \in \mathbf{K} \\ 0 \text{ if not.} \end{cases}$$

(IV.22)

By noting N_k the number of subgroups I of UnG containing in the group K of UsG, F is detailed as:

$$\mathbf{F_{UsG,UnG}} = \begin{pmatrix} f_{11} & \cdots & f_{1N_1} & & & & & \\ & & & \ddots & & & \mathbf{0} & \\ & & & & f_{\mathbf{K}1} & \cdots & f_{\mathbf{K}N_K} & \\ & \mathbf{0} & & & & & \ddots & \\ & & & & & & & f_{\mathbf{N_{Us}}1} & \cdots & f_{\mathbf{N_{Us}N_{N_{Us}}}} \end{pmatrix}.$$

(IV.23)

(a) ^{235}U.

(b) ^{239}Pu.
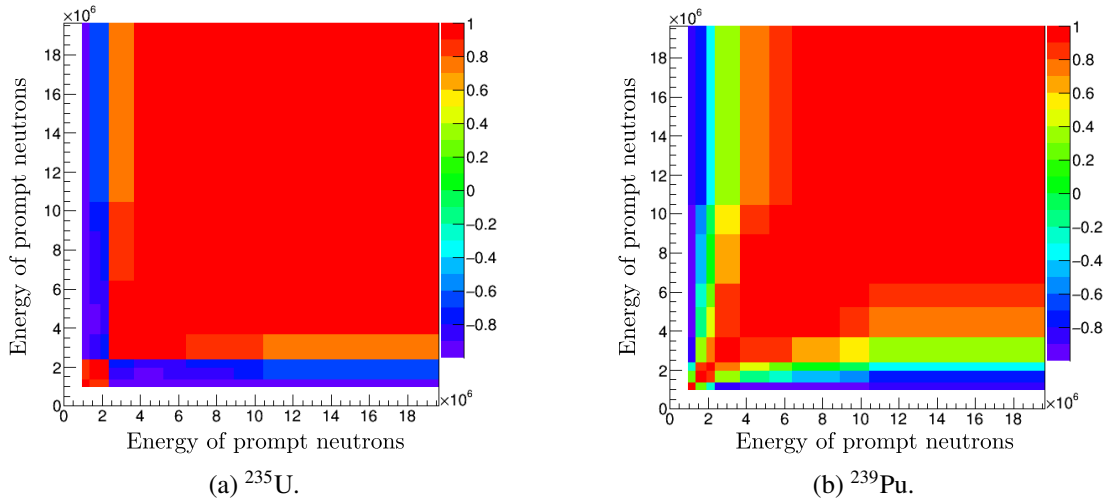
Figure IV.4: Prompt fission spectrum covariances projected on the 19G energy mesh

Finally, Fig. IV.4 illustrates the correlation matrices, obtained from the projection of perturbations on the 19G-mesh, and which share the same shape as the correlation matrices in Fig. IV.3.

4.2.3 Power map distribution

Three actions are commonly undertaken in order to assess the assembly power of nuclear reactors.

The first action is achieved by *calculation*. Usually, calculation of the radial and axial power is carried out solving the *diffusion equation* which is a simplification of the Boltzman transport equation (Marguet, 2011). The latter is resolved on 2 energy groups and considering several input data: the location and characteristics of the assemblies in the core, the moderator/fuel temperature and density, the boron concentration, the nominal operating point, the cycle length, etc(Castro González, 2018). As pointed out in the previous chapters of this manuscript, the uncertainty of this kind of calculation comes from the modelling errors, the uncertainties of input data and the numerical errors.

The second action is the *measurement*. The assembly power is not directly measured but it is reconstructed from a physical model and a local activity measurement (Bouriquet, 2015). The uncertainty associated to the assembly power measurement thus stems from the measurement itself and from the reconstruction process (Ezure, 1988; Bouriquet et al., 2015).

The third action consists in a comparison between calculation and measurements, which yields adjustments of the calculated power. Indeed, there generally exists a bias between calculated and measured assembly relative powers which are within 2-5% depending on the considered burn-up (Cabellos et al., 2014). As shown by Castro González et al. (2016), the assembly power can be considered as an ensemble of integral observables whose predictions can be improved by a *Bayesian inference* considering integral measurements. Turning back to the uncertainty of the power calculation and the estimated power, the Bayesian updating provides the best estimates of assembly powers and their associated uncertainties.

When defining the input uncertainty of the assembly power, it is thus essential to know which input data are used to define the core power in fluence calculations:

- the calculated power P_C,
- the measured power P_M,
- the adjusted P_{adj}.
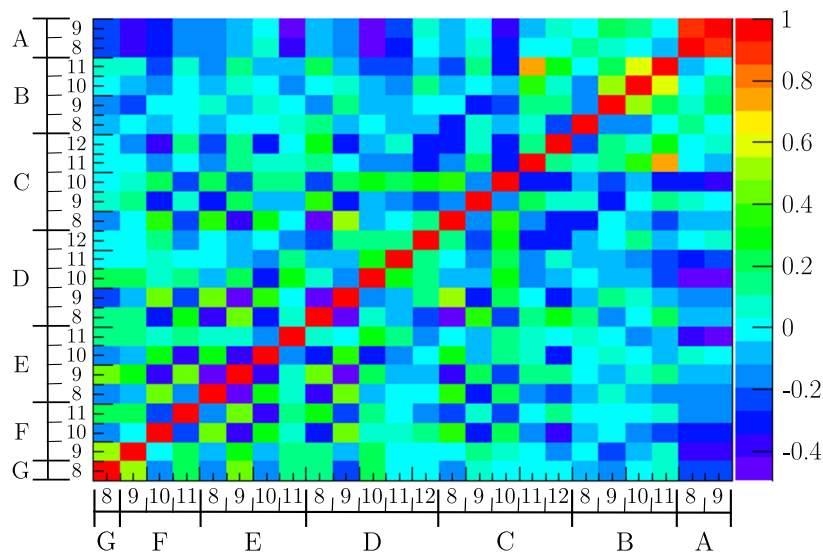
Figure IV.5: Input correlation data.

In this thesis, we focus on the propagation of the measurement uncertainties in order to give a first approximation of effects on the fast flux. In reactors, some assemblies are uninstrumented. We thus use the symmetry of the core to extrapolate the covariance data among the uninstrumented assemblies. The uncertainties on the power map are modelled by a standard deviation of 1% to 4% depending on the position of the assembly in the core and by a correlation matrix presented in Fig. IV.5 which is representative of the spatial correlation among assemblies. Each assembly is described as a standard 17x17 UO_2 homogeneous pin cells but the perturbation is carried out according to an assembly-wise approximation (Fig. IV.6).
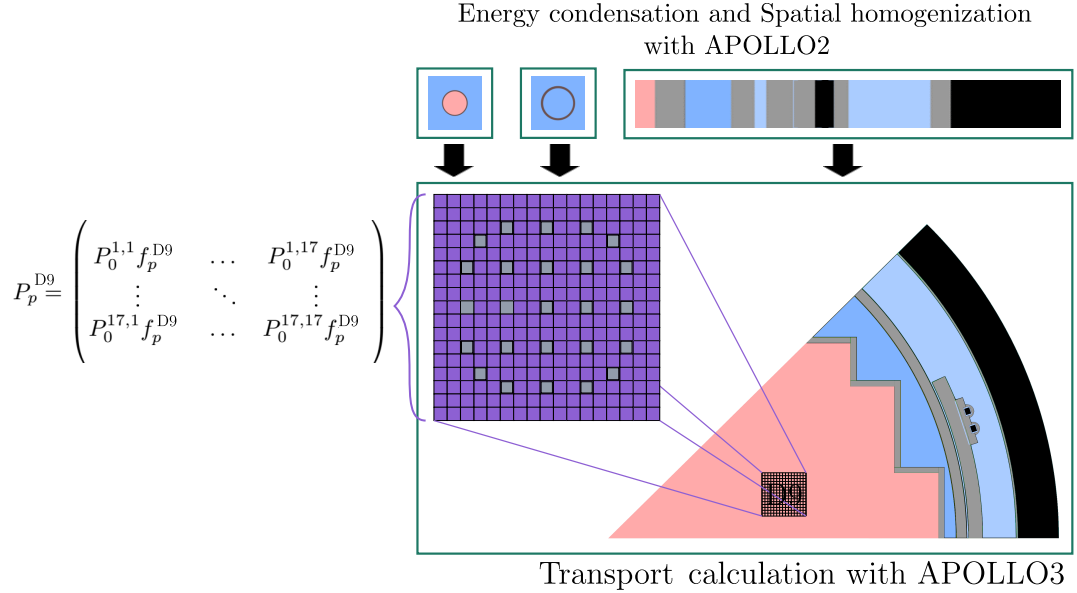
Figure IV.6: Assembly-wise perturbations.

4.3 Multigroup cross sections

The cross sections are often identified as the main source of uncertainties in transport calculation (Kodeli, 2001). Indeed, they are not perfectly known because there exists a succession of sources of uncertainties in their evaluation process. The uncertainties are characterised in data libraries in the form of covariance matrices which inform on the accuracy of the data.

Specifically, cross sections tend to be correlated for several reasons. Some reactions and some isotopes can first be involved in evaluation of various cross sections. For instance, the elastic and inelastic cross-sections of ^{56}Fe are anti-correlated due to the fact that the total cross section, which can be obtained from transmission measurements, is often better known than its partial cross sections (elastic and inelastic). Consequently, anti-correlations have to be introduced in the modelling of partial cross sections to guarantee the best estimate of the variance of the total cross-section. Furthermore, other adjustment processes can also create correlations among cross sections (as normalisation, marginalisation, consistent adjustment, etc. : Privas (2015)), especially in terms of energy. Under these circumstances, covariance matrices describe the analysis choices made during the evaluation process of cross sections (see Chapter I Section 4.2). A major effort must be made to preserve the coherence among data.

This section thus presents the methodology implemented to perturb the cross sections of the isotopes and reactions involved in the attenuation of neutrons until the vessel (see Fig. IV.7). The final objective is to produce perturbations on the multigroup neutron cross sections following the uncertainty data. In order to obtain these perturbations, the first step is to retrieve the uncertainty data, i.e. the covariance data. The following subsections describe the methodology involved in the definition of the uncertainty for the cross section of each isotope and reaction. For this aim, I developed various C++ functions in the processing system GALILEE-1 (Coste-Delclaux et al., 2016) in order to retrieve the information needed to rebuild the covariance matrices of interest. This methodology can be divided into 6 main steps based on the chain of codes GALILEE-NJOY-URANIE described below and schemed by Fig. IV.7

- Step 1 Reading information on the consistency of the cross sections of each isotope and nuclear reaction (Section 4.3.2),

- Step 2 Generating multigroup covariances matrices on the mesh of 18 energy groups over 1 MeV with the ERRORR module of NJOY (Section 4.3.3),

- Step 3 Retrieving the multigroup covariances from the GCOV files (Section 4.3.3),

- Step 4 Retrieving the nominal values of each pointwise cross sections and each isotope (Section 4.3.5),

- Step 5 Randomly sampling N_p new perturbed values with the platform URANIE(Section 4.3.4),

- Step 6 Consistent perturbations of the N_p PENDF files (Section 4.3.5),

- Step 7 Calculation of the N_p perturbed GENDF files with the module GROUPR of the NJOY code (Section 4.3.6),

- Step 8 Determining the perturbation factors of the multigroup cross sections for the reactions used by the deterministic code APOLLO3® for the resolution of the neutron transport equation (Section 4.3.6).
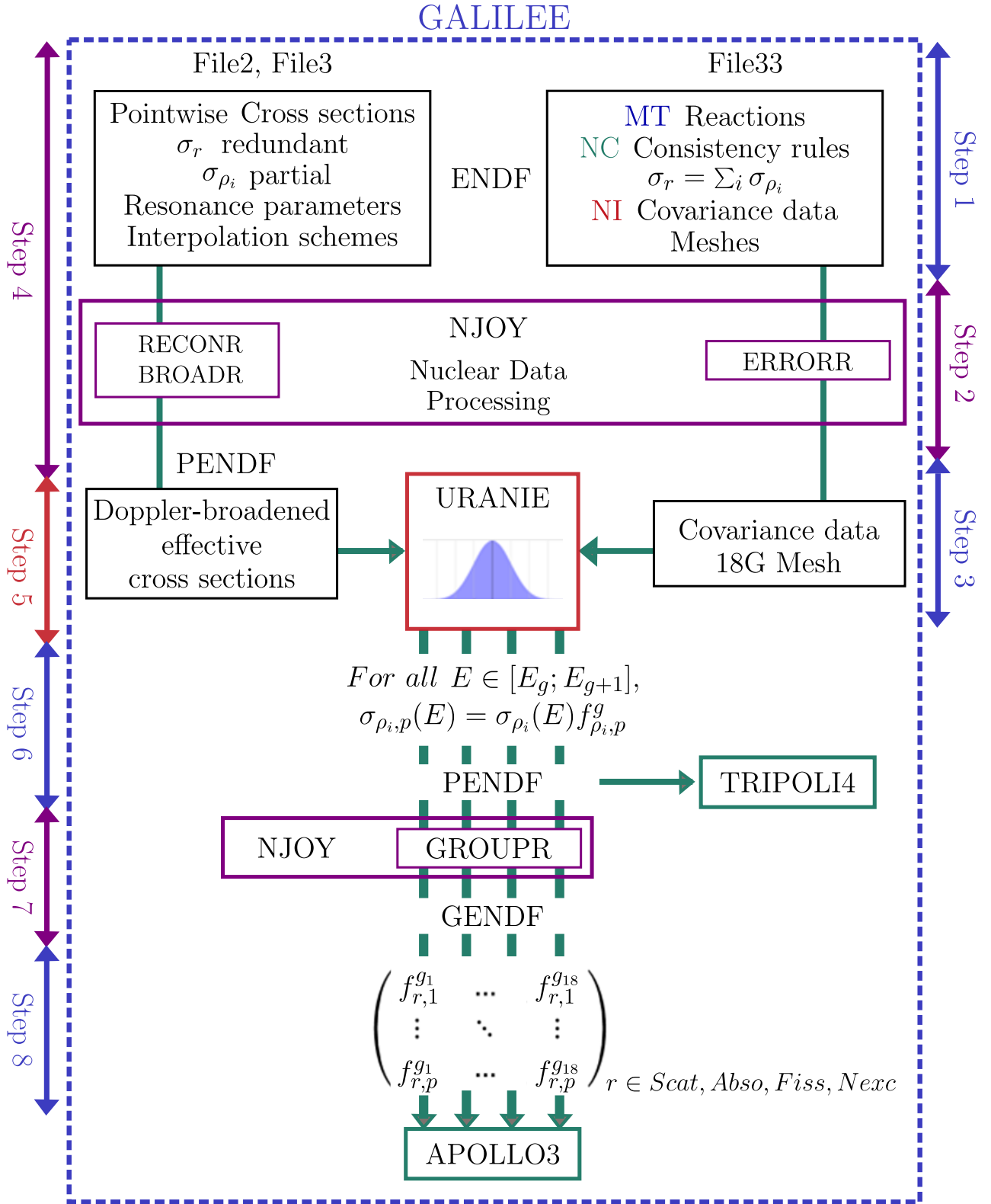
Figure IV.7: Computing chain for the perturbations of cross sections.

4.3.1 Choice of libraries for the definition of covariances

In the view of covering all the isotopes in the modelled reactor, the choice of a nuclear data library is a preliminary step. As pointed out in the state-of-the-art part (Chapter I Section 4.2), covariances provide not only the uncertainties on nuclear data, but also assess the coherence among data and implement all the theoretical choices made for the data modelling. The covariance data defined in a library is in fact evaluated in accordance with the methodology adopted to obtain the central values of the nuclear data defined in the same library. This is why they are attached to the data of their own library.

In this work, the library used to define the input nuclear data of fast flux calculation is the JEFF-3.1.1 library. The issue is that the covariance matrices are not all the time provided by international libraries for the full nuclear data even if a particular effort has been made since 2005 to improve and extend the covariance data (Salvatores et al., 2018). To work around this issue, we choose to use the same list as the COMAC files for the uncertainty analysis of the fast flux.

Libraries			
JEFF-3.2	**ENDFB7R1**	**JENDL40**	**TENDL12**
^{50}Cr	^{54}Fe	^{10}B	^{58}Fe
^{52}Cr	^{57}Fe	^{16}O	
^{53}Cr	^{55}Mn		
^{54}Cr	^{235}U		
^{56}Fe	^{238}U		
^{58}Ni	^{90}Zr		
^{60}Ni	^{91}Zr		
^{61}Ni	^{92}Zr		
^{62}Ni	^{94}Zr		
^{64}Ni	^{96}Zr		
^{238}U	^{1}H		

Table IV.5: List of nuclei and libraries used for the propagation of the cross-section uncertainty

4.3.2 Reading information on the consistency of the cross sections

As explained in Chapter I Section 4.2, the international library is written in the ENDF format (McLane, 2005) which contains various types of files. In our work, we focus on the uncertainty in the fast energy range ($E > 1$MeV). In this range, all the information can be retrieved from File 33. Indeed, File 33 gives the covariance data associated with File 3 which provides the pointwise cross sections out of their resonance domains and evaluated at infinite dilution. In the resolved domain of resonances, covariances are given by combination of File 33 with File 32, which defines the uncertainties on the resonance parameters. The effect of self-shielding can in fact be not negligible for resonant nuclei. In the fast energy range ($E > 1MeV$), we assume, at this stage of the study, that the impact of the self-shielding on the cross section perturbations is negligible. This assumption will be verified in the next chapter, particularly for the ^{56}Fe isotope, which contains weak resonances in the fast energy range (see Chapter I Section 1).

Finally, it is possible to define, in File 33, two types of data within the ENDF-format: the

$NI - Type$ which describes the covariances provided by File 3 on various meshes, and the
$NC - Type$ which gives the relations among redundant cross sections.

a NI sections

The $NI-type$ section gives the covariances between two reactions for various energy groups,
and in different subsections. They allow rebuilding the final data by summing all the terms of
each subsection associated with the particular reactions, such as:

$$Cov\left(\sigma_{MT_1}(E_1), \sigma_{MT_2}(E_2)\right) = \sum_{n=1}^{NI} Cov\left(\sigma_{MT_1}(E_1), \sigma_{MT_2}(E_2)\right)_n . \tag{IV.24}$$

Each subsection is notably parametrised by a constant LB which indicates how the final
covariances have to be calculated from the data of File 33. The covariance data can, moreover,
be defined on an absolute or a relative basis. Tab. IV.6 gives an example of the five main
formalisms of File 33 provided by the ENDF-format.

LB	$cov(x, y)$	Data in File 33	
0	F_{ij}	Table (E_i, F_{Ii})	$F_{ij} = 0$ if $i \ne j$
1	$F_{ij}x_0y_0$		
2	$F_{ii}F_{jj}x_0y_0$		
3	$F_{ii}F'_{jj}x_0y_0$	Tables (E_i, F_{ii}) and (E_j, F'_{jj})	$F_{ij} = 0$ and $F'_{ij} = 0$ if $i \ne j$
4	$F_{ii}F'_{ii}F'_{jj}x_0y_0$		
5	$F_{ij}x_0y_0$	Table (E_i) and Matrix which contains the F_{ij}	
		With $E_i \le E_x < E_{i+1}$ and $E_j \le E_y < E_{j+1}$	

Table IV.6: Example of covariance formalism available in the File 33 within the ENDF-format

Fig. IV.8 gives an illustration of the **NI** section for the ^{16}O isotope. In that case, we can find
information on the uncertainty of the cross section defined by the $MT = 16$ which corresponds
to the production of two neutrons and a residual ((n,2n): reaction). In order to build the final
covariance, File 33 only gives one subsection in the formalism $LB = 5$.

Figure IV.8: Example of file 33 providing the information to retrieve the uncertainties of the
MT-16 (n,2n) cross sections of the ^{16}O isotope.

b NC sections

The $NC - type$ sections are used to indicate for one reaction how to obtain the associated covariance matrix from the covariances of other reactions described in **NI** sections. The major purposes are to eliminate a large fraction of the mostly redundant information from the ENDF-B tape, and to ensure the physical consistency imposed by the relations between redundant and partial cross sections.

Actually, many reactions are often combined in neutron transport codes to simplify notations (MT = 1 the total cross section, MT = 4 the inelastic scattering, MT = 18 the fission reaction, etc.). The complete list of the definitions of the MT numbers can be found in Appendix B of the ENDF manual (McLane, 2005).

Physical consistency of cross sections
according to the ENDF nomenclature

The physical consistency of the redundant reactions is given by:

$$\sigma_{1-TOTAL} = \sigma_{2-ELAS} + \sigma_{4-INELAS} + \sigma_5 + \sigma_{NEXCESS} + \sigma_{18-FISSION} + \sigma_{101-DISAPP}, \quad \text{(IV.25)}$$

where,
$$\sigma_{4-INELAS} = \sigma_{50-91}$$
$$\sigma_{18-FISSION} = \sigma_{19} + \sigma_{21-91}$$
$$\sigma_{NEXCESS} = \sigma_{11} + \sigma_{16} + \sigma_{17} + \sigma_{22-30} + \sigma_{32-37} + \sigma_{41-42} + \sigma_{44-45}$$
$$\sigma_{101-DISAPP} = \sigma_{102-117}$$
$$\sigma_{103-z,p} = \sigma_{600-649}$$
$$\sigma_{104-z,d} = \sigma_{650-699}$$
$$\sigma_{105-z,t} = \sigma_{700-749}$$
$$\sigma_{106-z,He} = \sigma_{750-799}$$
$$\sigma_{107-z,\alpha} = \sigma_{800-849}$$

σ_5, sum of all reactions not given explicitly in another MT number.

For example, in a $NC - type$ section described for the MT reaction and for the energy range $[E_1; E_2]$, NCI number of pairs of values $\{C_I, MT_I\}$ are given to describe the relation:

$$\sigma_{MT}(E) = \sum_{I=1}^{NCI} C_I * \sigma_{MT_I}(E), \quad \text{(IV.26)}$$

where the *evaluated cross sections* $MT_1, ..., MT_I, ...MT_{NCI}$ are given in the same energy range in File 3 in the record $(MAT, 3, MT_I)$. The cross sections $\sigma_{MT}(E)$ will hereinafter be called *derived*.

Fig. IV.9 illustrates the simple case of an **NC** section for the ^{16}O isotope. According to the **NC** section, the covariance matrix of the elastic cross section (MT = 2) can be rebuilt from the covariance matrices of 78 other reactions (MT = 1,16,22, etc.) on the energy range [1.E-5 eV, 2.E+7 eV].

c Retrieving construction rules

The first step of our work is thus to develop a utility program to retrieve the construction rules provided by File 33 and using the tools of the GALILEE-1 processing system (Coste-Delclaux et al., 2016).

```
          8.016000+3 1.585750+1          0   MT   0   NC   0   NI   1 82533  2    1
          0.000000+0 0.000000+0          0        2        1        1 82533  2    2
          0.000000+0 0.000000+0          0        0        0        0 82533  2    3
   E      1.000000-5 2.000000+7          0        0       76       38 82533  2    4
   C_I    1.000000+0 1.000000+0-1.000000+0 1.600000+1-1.000000+0 2.200000+1 82533  2    5
         -1.000000+0 2.800000+1-1.000000+0 5.100000+1-1.000000+0 5.200000+1 82533  2    6
  MT_I   -1.000000+0 5.300000+1-1.000000+0 5.400000+1-1.000000+0 5.500000+1 82533  2    7
         -1.000000+0 5.600000+1-1.000000+0 5.700000+1-1.000000+0 5.800000+1 82533  2    8
         -1.000000+0 5.900000+1-1.000000+0 6.000000+1-1.000000+0 6.100000+1 82533  2    9
         -1.000000+0 6.200000+1-1.000000+0 6.300000+1-1.000000+0 6.400000+1 82533  2   10
         -1.000000+0 6.500000+1-1.000000+0 6.600000+1-1.000000+0 6.700000+1 82533  2   11
         -1.000000+0 6.800000+1-1.000000+0 6.900000+1-1.000000+0 7.000000+1 82533  2   12
         -1.000000+0 7.100000+1-1.000000+0 7.200000+1-1.000000+0 7.300000+1 82533  2   13
         -1.000000+0 7.400000+1-1.000000+0 7.500000+1-1.000000+0 7.600000+1 82533  2   14
         -1.000000+0 7.700000+1-1.000000+0 7.800000+1-1.000000+0 7.900000+1 82533  2   15
         -1.000000+0 9.100000+1-1.000000+0 1.020000+2-1.000000+0 1.030000+2 82533  2   16
         -1.000000+0 1.040000+2-1.000000+0 1.070000+2                       82533  2   17
          0.000000+0 0.000000+0          0        0        4        2 82533  2   18
          1.000000-5 0.000000+0 2.000000+7 0.000000+0                       82533  2   19
```

Figure IV.9: Example of file 33 providing the information to retrieve the uncertainties of the MT-2 elastic cross sections of the ^{16}O isotope.

**C++ Program: reading the reconstruction rules
of the uncertainties provided by File 33 of ENDF libraries**

The C++ program can be divided into four steps. For each isotope, it:

- reads File of the chosen library for the considered isotope,

- retrieves the list of sections of File 33, associated with various MT reactions,

- determines for each section the number of **NC** and **NI** subsections,

- determines 3 main information (the list of $MT - MT1$ reactions for which cross sections are correlated, the energy meshes on which the covariances are defined, the consistency rules among cross sections),

- stores the information on different maps which could be later reused, notably for the perturbations of the cross sections.

Finally, the code supplies, according to the ENDF format, four potential outputs:

- The MT defined in File 33,

- The list of $MT - MT1$ reactions which cross sections are correlated,

- The energy meshes on which the covariances are defined,

- The consistency rules among cross sections.

We retrieve the consistency rules for all the main isotopes present in our application, and for the corresponding international library defined according to Tab. IV.5. Fig. IV.10,IV.11,IV.12 present the results for the isotopes ^{56}Fe, ^{16}O and ^{1}H. Similar information for the other isotopes are detailed in Appendix G.

MeV

9.5e+5   2.0e+7

NI: Covariances	MT: 2; 4; 16; 22; 28; 102-107
NC: "Derived" cross sections	MT: 1 MT_i: 2; 4; 16; 22; 28; 102-107 C_i: 1; ...; 1
NCa: "Derived" cross sections (added to ensure consistency)	$\forall MT \in \{51\text{-}82\}$ $f_{MT} = f_{(MT_i=4)}$

Figure IV.10: Construction rules of the uncertainties associated with the cross sections of ^{56}Fe for various reactions MT. The notation **NC-a** is explained in Section 4.3.5.

MeV

9.5e+5   2.0e+7

NI: Covariances	MT: 1; 16; 22; 28; 51-79; 91; 102-104; 107
NC: "Derived" cross sections	MT: 2 MT_i: 1; 16; 22; 28; 51-79; 91; 102-104; 107 C_i: 1; -1; ...; -1 - MT: 4 MT_i: 51-79; 91 C_i: 1; ...; 1

Figure IV.11: Construction rules of the uncertainties associated with the cross sections of the ^{16}O for various reactions MT.

MeV

9.5e+5   2.0e+7

NI: Covariances	MT: 2; 102
NC: "Derived" cross sections	MT: 1 MT_i: 2; 102 C_i: 1; 1

Figure IV.12: Construction rules of the uncertainties associated with the cross sections of the ^{1}H for various reactions MT.

85

4.3.3 Generating multigroup covariance matrices on the mesh of 18 energy groups over 1 MeV with the ERRORR module of NJOY

The previous section has allowed us to determine the construction rules defined by the ENDF format to construct covariances for cross sections. As it will be explained in next Section 4.3.5, the perturbations will be carried out on the pointwise cross sections. To perturb these cross sections, we can use the covariance matrices defined in the international libraries. One of the main difficulties in this use is to treat the large number of uncertain variables. For the cross sections which allow defining various interactions involved in the reactor, there are more than 1400 uncertain parameters, if we consider all the given reactions and the energy groups over 1 MeV defined in the international libraries for each isotope. Specifically, the covariances are defined for various energy meshes.

This is why, the covariance retrieving is automated as much as possible. In order to simplify the processing, we therefore rebuild the covariance matrices of the cross sections for each reaction and isotopes, on the same mesh, i.e. the 19G-mesh used for the fast flux calculation. This strategy delivers several advantages. Indeed, it allows to:

- Randomly sample the cross sections in a manner consistent with the reference 19G-mesh,

- Avoid approximations in the data perturbations,

- Conduct a sensitivity analysis of the neutron fast flux in function of the input parameters defined on energy groups which are sufficiently representative of the energy distribution of the calculation mesh,

- Synthesise the information of File 33 in only one relative covariance matrix for each isotope and reaction.

In order to achieve this, we use the ERRORR module of NJOY (MacFarlane, 2017) which converts energy dependent covariance information in ENDF format into multigroup form by combining the covariances of File 33 with the data of File 3. This calculation relies on the creation of an input script which describes the input instructions and specifications needed to generate the desired covariance matrix. In an ERRORR input, the instructions are presented in a card format. Each card is parametrised by a list of options which define the different steps of the ERRORR process, and by a succession of "tapes" which refer to intermediate input or output files used during the process. In our case, the management of input and output data of the ERRORR module is carried out by the GALILEE system (Mounier, 2011). Our work therefore consists in providing to the GALILEE code the input information needed to fix the ERRORR calculation. This information is computed in accordance with the ENDF rules determined in Section 4.3.2.

C++ Program: production of input files for the ERRORR module

The C++ program can be divided into two steps. For each isotope, it:

- translates the consistency information in the GALILEE format,

- writes in a file the latter information which is later used.

After the ERRORR treatment, the new multigroup covariances are given for each isotope in different files following a GCOV format (MacFarlane, 2017). Fig. IV.13 gives an illustration of

the GCOV file produced by the ERRORR module for the cross sections of the ^{16}O isotope and the (z,2n) reaction defined by $MT = 16$ in the ENDF format.

```
           8.016000+3 1.585750+1          0  MT1   0   NC   0   NI   1 82533 16 MT  1
           0.000000+0 0.000000+0          0        16       0         1 82533 16     2
           0.000000+0 0.000000+0          1  LB    5       15         5 82533 16     3
    E      1.000000-5 1.665000+7 1.800000+7 1.900000+7 2.000000+7 0.000000+0 82533 16     4
   Fxy     0.000000+0 0.000000+0 0.000000+0 8.100000-1 2.813130-1 1.553580-1 82533 16     5
           8.100000-1 1.073250-1 8.100000-1                                  82533 16     6
                                                                             82533  099999
```

Figure IV.13: Example of GCOV file providing the multigroup covariances on the 19G-mesh and produced by the ERRORR module for the MT-16 (z,2n) cross sections of the ^{16}O isotope.

**C++ Program: reading
the GCOV files produced by the ERRORR module**

The C++ program can be divided into two steps. For each isotope, it:

- retrieves from the consistency rules the list of MT which will be perturbed,

- reads the corresponding multigroup covariances on the 19G-mesh.

4.3.4 Randomly sampling of the pointwise cross sections and ill-conditioned matrix

As briefly explained in Section 2.1, when the considered physical quantities are positive definite, the normal distributions can be inadequate for large variances because they can induce negative values during the random sampling (Lahaye, 2018). In his article, Lahaye (2018) suggests using the following distributions, when the mean and the variances are known:

- the *Gaussian law*, for small variances ($\sigma < \frac{1}{4}\mu$),

- the *fitted truncated Gaussian law*, for intermediate variances ($\frac{1}{4}\mu \leq \sigma < \frac{1}{2}\mu$),

- the *log-normal law*, for large variances ($\sigma > \frac{1}{2}\mu$).

In reality, for the case of cross sections, few of them have a standard deviation σ which is greater than $\frac{1}{2}\mu$. Moreover, the condition of Gaussian law is a necessary condition to use the Pearson's correlations defined in libraries, as mentioned in Section 2.2. The cross sections are thus perturbed using a Gaussian law and the negative values produced by the sampling are truncated.

4.3.5 Consistent perturbations of the pointwise cross sections defined by the PENDF files

The inputs of the APOLLO3® code have to be in a multigroup format. However, in order to compare the results between the reference TRIPOLI4® calculations which require pointwise data, and the APOLLO3® calculations, we decided to perturb, as a first time, the pointwise cross sections from the corresponding multigroup cross sections.

Furthermore, the perturbations will be carried out on the pointwise cross sections after the RECONR and BROADR calculations and directly in the provided PENDF, in order to take into account the effect of the Doppler broadening of the resonances. As previously assumed, the

impact of the self-shielding on the cross-section perturbations is considered as negligible. Since Doppler effect is negligible on light nuclei and also on heavy nuclei above the resonance energy range (energy higher than 300 keV), we perturbed the pointwise cross sections directly in the PENDF file, in order to avoid the need to generate a large number of PENDF with NJOY.

To perturb the pointwise cross sections, we use the construction rules retrieved as explained in Section 4.3.2. Sometimes, the consistency rules provided by the ENDF files are incomplete and do not allow ensuring physical coherence of data. To work around this issue, in our C++ program we define a new type of data **NC-a** which adds consistent rules to the original ENDF-file in order to ensure the data consistency.

C++ Program: Perturbations of the PENDF files

To ensure consistency, the following strategy is chosen for each isotope. The C++ program:

- retrieves from the consistency rules the list of MT_i (reactions to perturb) and MT (redundant reactions) contained in the **NI** and **NC** sections,

- verifies if the **NC** sections give a consistent and full definition of cross sections of the ENDF File 3; otherwise, new pairs of values C_I, MT_I are added in a fictive **NC-a** section to ensure the data consistency,

- retrieves the nominal values $\sigma_{MT_i}^{Nominal}$ and $\sigma_{MT}^{Nominal}$ of the cross sections associated with all the MT and MT_i involved in the **NI**, **NC** and **NC-a** sections,

- randomly samples the cross sections σ_{MT_i}, for all MT_i defined in **NI** sections and in the energy range $[E_1; E_2]$ included partially or totally in [950 keV; 20 MeV],

- calculates the perturbations of the redundant cross sections Σ_{MT} associated with the **NC** and **NC-a** sections such as:

$$\Sigma_{MT}^p = \sum_i C_i \times (\Sigma_{MT_i}^p - \Sigma_{MT_i}^{Nominal}) + \Sigma_{MT}^{Nominal}. \tag{IV.27}$$

Figures IV.10,IV.11,IV.12 give an illustration of the final consistency rules used for the isotopes ^{56}Fe, ^{16}O and ^{1}H. The other isotopes are detailed in Appendix G.

4.3.6 Propagation of perturbations on the multigroup cross sections

For each perturbed PENDF files, we then determined the corresponding GENDF files by using the GROUPR module of NJOY. The last C++ function of the chain allows retrieving the perturbation factors used to perturb the input cross sections of the APOLLO3® code. It is important to note that the *self-shielding calculation* with the APOLLO2 code is not renewed for each perturbation of the cross section. In fact, at this stage of the study, we assume that the effect of the cross-section perturbations on the energy self-shielding is negligible because in the energy range of interest, the resonances of the studied isotopes are generally low or non-existent. This assumption will be verified in the next chapter.

C++ Program: retrieving
the multigroup cross sections with GALILEE-1

The C++ program can be divided into two steps. For each isotope, it:

- retrieves all the multigroup cross sections,

- determines the redundant cross sections and combines the cross sections in common aggregate reactions used by APOLLO3® (scattering, absorption, fission and excess),

$$\sigma_{1-TOTAL} = \sigma_{2-ELAS} + \sigma_{4-INELAS} + \sigma_5 + \sigma_{NEXCESS} + \sigma_{18-FISSION} + \sigma_{101-DISAPP}$$
$$\sigma_{4-INELAS} = \sigma_{50-91}$$
$$\sigma_{SCAT} = \sigma_{2-ELAS} + \sigma_{4-INELAS}$$
$$\sigma_{18-FISSION} = \sigma_{19} + \sigma_{21-91}$$
$$\sigma_{NEXCESS} = \sigma_{11} + \sigma_{16} + \sigma_{17} + \sigma_{22-30} + \sigma_{32-37} + \sigma_{41-42} + \sigma_{44-45}$$
$$\sigma_{101-DISAPP} = \sigma_{102-117}$$

(IV.28)

- fill an input file which contains the perturbation factors for multigroup cross sections σ_r^g and matrices at different l Legendre orders $\sigma_l^{g' \to g}$.

Fig. IV.15, IV.15 and IV.17 provide the correlation between the scattering and absorption cross sections of the ^{56}Fe, ^{16}O and ^{1}H isotopes, resulting from the generated perturbations of the GENDF files. The standard deviation associated with the ^{56}Fe, ^{16}O and ^{1}H isotopes, and resulting from this process are presented in Appendix B.

We can see that the correlation matrices of the aggregate reactions, thus combine, thank to the ERRORR module, the correlative structure of their partial cross sections. For instance, for the ^{1}H in the library ENDF-B7R1, (McLane, 2005) used to define the uncertainties of the cross sections, the scattering cross sections is entirely described by the elastic cross section. The library provides the uncertainty of the elastic cross section which comprises only one energy group in the considered energy range from 1 to 20 MeV. This is why the scattering cross section of ^{1}H is highly correlated in this energy range.

(a) $Cov((\sigma_{ABSO}(E_1), \sigma_{ABSO}(E_2)))$.

(b) $Cov(\sigma_{SCAT}(E_1), \sigma_{SCAT}(E_2))$.

Figure IV.14: Correlation Matrix associated with the absorption (left panel) and scattering
(right panel) reactions of the cross sections of the isotope ^{1}H, and among the 18 energy groups
of the 19G-mesh which are above 1 MeV.

(a) $Cov((\sigma_{ABSO}(E_1), \sigma_{ABSO}(E_2)))$.

(b) $Cov(\sigma_{SCAT}(E_1), \sigma_{SCAT}(E_2))$.

Figure IV.15: Correlation Matrix associated with the absorption (left panel) and scattering
(right panel) reactions of the cross sections of the isotope ^{16}O, among the 18 energy groups of
the 19G-mesh which are above 1 MeV.

Figure IV.16: Correlation Matrix between the scattering and absorption cross sections of the
^{16}O, among the 18 energy groups of the 19G-mesh which are above 1 MeV.

(a) $Cov((\sigma_{ABSO}(E_1), \sigma_{ABSO}(E_2))$.

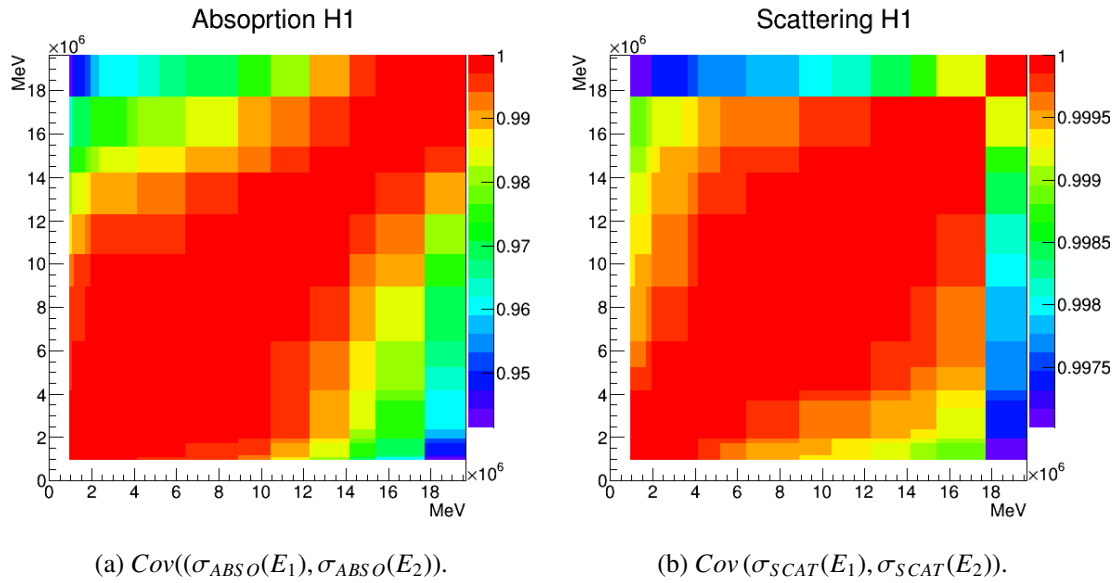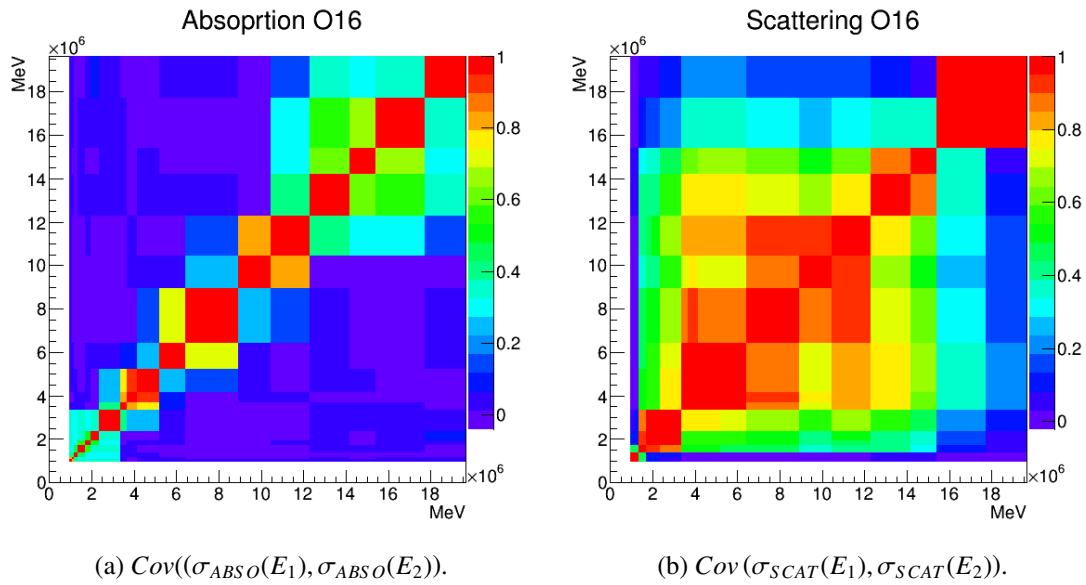(b) $Cov(\sigma_{SCAT}(E_1), \sigma_{SCAT}(E_2))$.

Figure IV.17: Correlation Matrix associated with the absorption (left panel) and scattering
(right panel) reactions of the cross sections of the isotope ^{56}Fe, among the 18 energy groups of
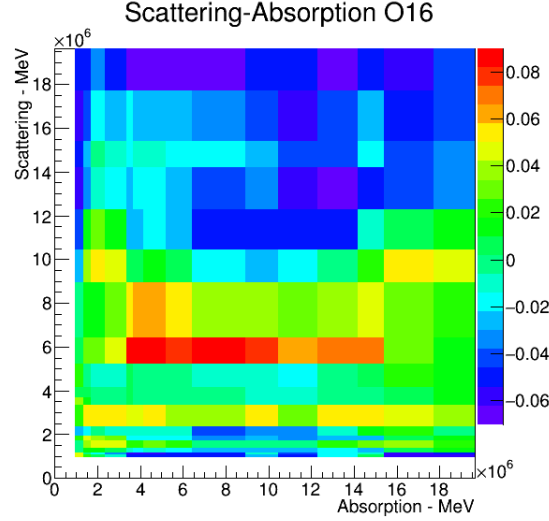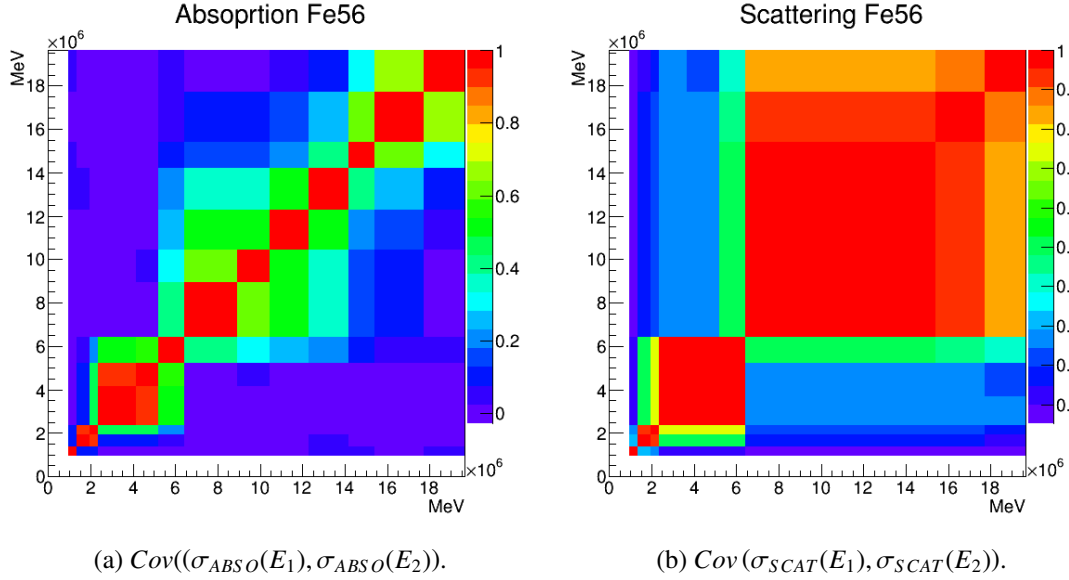the 19G-mesh which are above 1 MeV.

4.4 Double-differential scattering cross section

In the fast energy range, the flux attenuation is dominated by elastic and inelastic scattering.
As explained in Chapter I Section 4.3.2, the reconstruction of the multigroup scattering $\sigma_l^{g' \to g}$
depends on the pointwise microscopic cross-section but also on a term of angular distribution.
These two parameters are uncertain and they should therefore ideally be accounted for in order
to assess the uncertainty on the scattering cross section. The uncertainty related to the pointwise
cross sections has already been evaluated by a large number of authors. However the impact of
the angular distribution uncertainty on the fast neutron flux has never been studied, even if some
authors have already raised this question (Vasiliev et al., 2018).

As illustrated in Appendix F, some libraries provide variance-covariance data on scattering
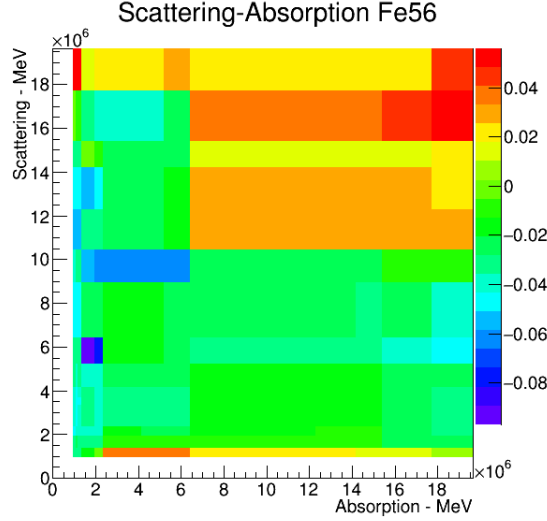
Figure IV.18: Correlation Matrix between the scattering and absorption cross sections of the ^{56}Fe, among the 18 energy groups of the 19G-mesh which are above 1 MeV.

angular distributions for some isotopes. In this work, we propose a methodology to account for the uncertainty of the neutron scattering angular distribution, and notably a preliminary quantitative assessment of its importance on the fast flux, in particular, for ^{56}Fe which is the main isotope of the structural materials. The sensitivity analysis of the fast neutron flux will be presented in the next chapter.

In the ENDF-6 formalism, angular distributions are given in File 4 (see Chapter I Section 4.3.2) and are generally expressed as normalised probability distributions $f(E', \omega)$ at incident energy E' from Legendre polynomial coefficients $a_k(E')$ through a centre of mass cosine ω:

$$f(E', \omega) = \sum_{k=1}^{L} \frac{2k-1}{2} a_k(E') P_k(\omega). \tag{IV.29}$$

File 34 provides the relative covariances $F(a_{l_1}(E_1'), a_{l_2}(E_2'))$ between Legendre coefficients at incident energies E_1' and E_2' and for various orders l_1 and l_2. File 3 contains the microscopic neutron cross sections for different reactions. File 33 is used to give the relative covariances $F(\sigma(E_1'), \sigma(E_2'))$ between the cross-sections of different reactions at incident energies E_1' and E_2'.

Figures IV.19 and IV.20 plots the relative covariances retrieved from the JEFF-3.2 evaluation. In the perturbations of the cross sections, elastic and inelastic scattering are considered. Fig. IV.19 shows the relative covariances $F(\sigma(E_1'), \sigma(E_2'))$ between elastic and inelastic cross sections.

For the ^{56}Fe isotope, File 34 only provides the relative covariances $F(a_{l_1}(E_1'), a_2(E_2'))$ for the elastic reaction. Figure IV.20 presents a zoom of $F(a_{l_1}(E_1'), a_2(E_2'))$ at energies higher than 1 MeV up to a Legendre order P_3. The highest standard deviation for $a_3(E')$ is around 1 MeV (28%) and for the elastic cross-section at energies higher than 2 MeV (8.3%).
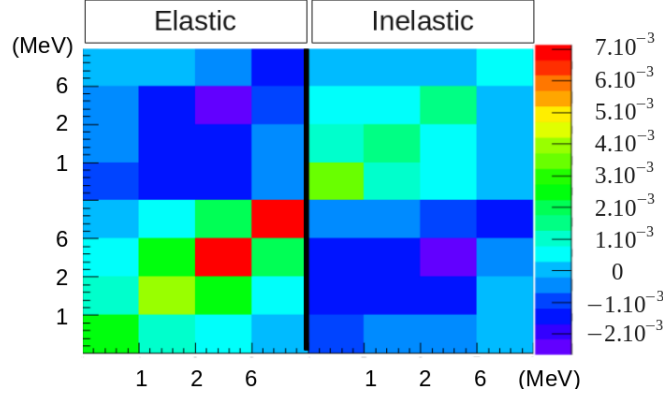
Figure IV.19: $F(\sigma(E'_1), \sigma(E'_2))$, the relative covariance matrix of elastic and inelastic cross-sections on the energy range [1ı20]MeV.
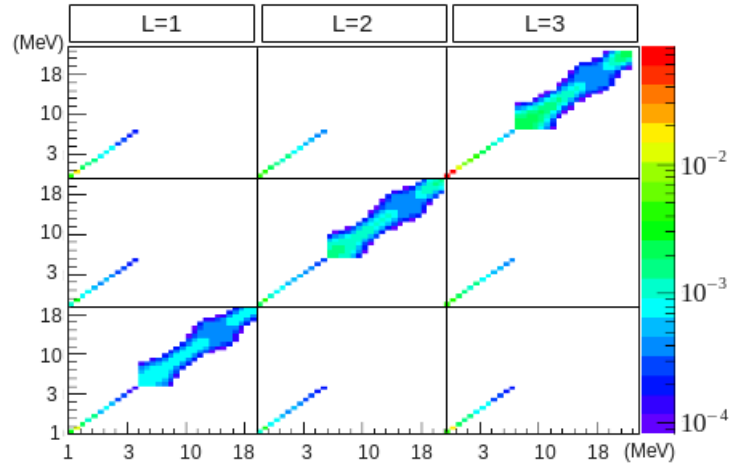

Figure IV.20: $F(a_{l_1}(E'_1), a_2(E'_2))$, the relative covariance matrix of Legendre coefficients on the energy range [1ı20]MeV.

Pointwise cross-section and Legendre coefficients can be separately sampled and perturbed because there is, at the moment, no information on the correlation between the two data. The methodology to perturb the pointwise cross sections has been presented in the previous Section 4.3 and the Legendre components are directly perturbed and written in ENDF files. As previously, the perturbation of the neutron cross-section is carried out after the RECONR and BROADR calculations.

The resulting values are stored in pointwise files and for each couple of random PENDF and ENDF files, the GROUPR module of NJOY processes the multigroup scattering cross-sections. It is also supposed that self-shielding is not affected by the perturbation of the scattering cross-section because the ^{56}Fe presents few narrow resonances in the energy range $[1 - 20]$MeV. From the resulting GENDF files, the perturbation coefficients of multigroup transfer matrix and scattering cross-sections are deduced in relation to nominal values as:

$$(f_l^{g' \to g})_p = \frac{\sigma_{l,p}^{g' \to g}}{\sigma_{l,0}^{g' \to g}} \text{ and } f_p^{g'} = \frac{\sigma_{s,p}^{g'}}{\sigma_{s,0}^{g'}}. \tag{IV.30}$$

5 Conclusion

In this chapter, we have introduced the methodology to quantify, model and propagate the input uncertainties of the deterministic flux calculation. Considering the input parameters as random variables, we have presented the strategy to generate consistent perturbations and propagate them in the fast flux calculation following the Total Monte Carlo approach.

In particular, covariances and probability distributions are defined. We notably see that the reconstruction of the covariances of cross sections can lead to the generation of ill-conditioned matrices. We show that using the singular value decomposition, it is possible that the uncertainties of five variable groups has been independently modelled and propagated in the fast flux calculation:

- the technology parameters: the geometry, the water temperature in the primary circuit, and the impurities in steel,

- the neutron prompt spectrum,

- the power map distribution,

- the double-differential scattering cross section,

- the cross sections.

In particular, a calculation chain has been implemented to perturb the multigroup cross sections. It is based on the use of three main codes and platforms:

- the processing system GALILEE-1 (Coste-Delclaux et al., 2016), to retrieve the information needed to model the uncertainties,

- the NJOY code (MacFarlane, 2017) to produce with the ERRORR procedure the covariance matrices on the 19G-Mesh, and to generate the perturbed multigroup cross sections,

- the URANIE platform (Blanchard et al., 2019), to randomly sample the input parameters.

343 covariance matrices (associated with the total and partial reactions of 25 isotopes) has been reconstructed with the ERRORR module in coherence with the 19G-Mesh. They define the variance and the correlation of 6174 variables (343 reactions $\times$ 18 energy groups). We have shown that the covariance process can produce ill-conditioned matrices which make their Cholesky decomposition impossible. To deal with this issue, we have proposed an alternative method, based on the spectral decomposition, in order to simultaneously regularise these matrices and sample the random variables. Eventually, a methodology has been carried out to preserve the consistency between the redundant and partial cross sections, following the information given by the international libraries. The pointwise cross sections of the 25 isotopes have then been perturbed and propagated in the GROUPR procedure of NJOY. The resulting multigroup cross sections have been combined in two common aggregate reactions used by APOLLO3®: the scattering and the absorption reactions. In the next chapter, we will present the results of the uncertainty propagation in the fast flux calculation and the sensitivity analysis of the relative contribution of each input on the output variance. The objective is to identify the parameters which could, with a better knowledge, reduce the uncertainty of the fast neutron flux.

Chapter V

Uncertainty quantification and sensitivity analysis of the fast neutron flux

The aim of this chapter is to provide the final uncertainty on the fast neutron flux resulting from the Total Monte Carlo approach set up in the previous Chapter IV. In this context, we carry out a global sensitivity analysis to evaluate the impact of input uncertainties in terms of their relative contributions to the output uncertainty. The objective is to identify the parameters which could, with a better knowledge, reduce the uncertainty of the fast neutron flux.

In particular, a methodology to consider the correlation among parameters is proposed. The concept of the Shapley value in game theory, recently suggested by Owen (Owen et al., 2017), is applied. Its use is notably discussed in the context of high-dimensional input spaces. To circumvent this issue, an alternative method based on Johnson values (Johnson, 2000) is proposed to rank the contributions within the large number of parameters involved.
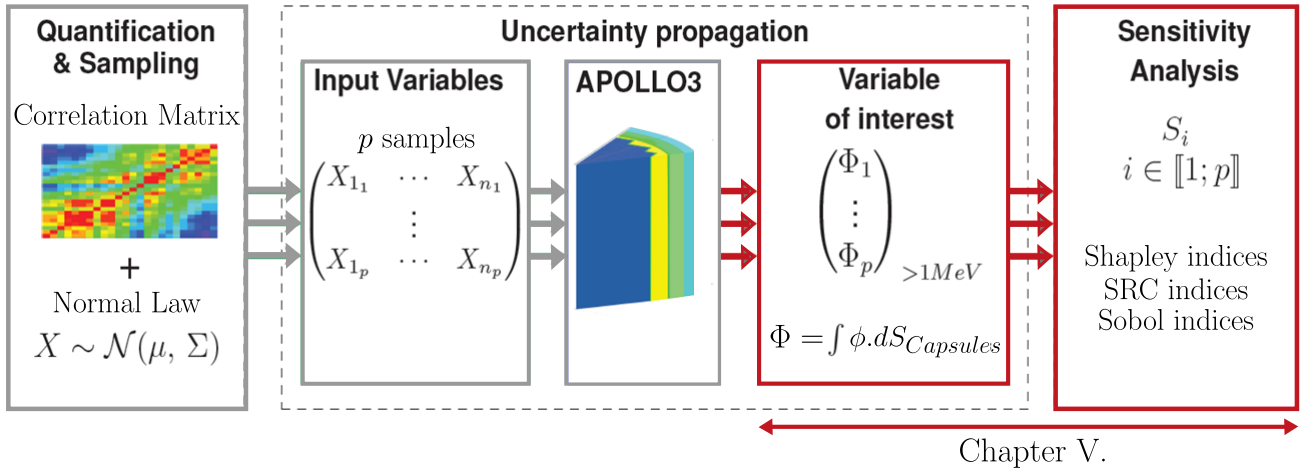

Figure V.1: Uncertainty propagation scheme: in red, the specification of the deterministic calculation.

Sections 1 and 2 describe the general strategy involved in this thesis to implement sensitivity analysis in the case of a large number of correlated input parameters. Linear prediction models are first introduced in Section 1 and are used, in Section 2, to simplify the implementation of sensitivity analysis involved in our work.

Section 3 then presents the uncertainty quantification of the fast flux Φ_{1MeV} and the global sensitivity analysis achieved using the URANIE platform (Blanchard et al., 2019).

Due to the large number of input parameters of the fast flux calculation, we adopt an iterative strategy for the uncertainty quantification and the sensitivity analysis of the fast neutron flux. Five different designs of experiments are independently carried out, considering the following set of variables:

- the technological parameters: the geometry, the water temperature in primary circuit, and the impurities in steel,

- the neutron prompt spectrum,

- the power map distribution,

- the cross sections,

- the double-differential scattering cross section.

The uncertainty modelling of these variables was described in Chapter IV, Section 4. For each sub-set, an uncertainty propagation and a sensitivity analysis of the fast flux are performed. This allows us to assess the most influential parameters for each sub-group of variables.

The last study propagates the uncertainty of all variables in order to quantify the resulting uncertainty on the fast neutron flux. The final uncertainty of Φ_{1MeV} is given according to the most common definition, that is, by a quantification of the standard deviation $\sigma_{\Phi_{1MeV}}$ (see Eq. V.1).

Uncertainty quantification of the fast neutron flux

The uncertainty of the fast neutron flux is quantified in terms of the *standard deviation*, $\sigma_{\Phi_{1MeV}}$. For a set of p observations (samples) resulting from the uncertainty propagation on n variables, the uncertainty quantification of Φ_{1MeV} is given by:

$$\sigma_{\Phi_{1MeV}} = \sqrt{Var(\Phi_{1MeV})} = \sqrt{\frac{1}{p}\sum_{k=1}^{p}(\Phi_k - \bar{\Phi})^2}, \text{ where } \bar{\Phi} = \frac{1}{p}\sum_{k=1}^{p}\Phi_k. \qquad (V.1)$$

---

1 Linear prediction of the fast neutron flux

In the past, the calculation tools did not allow to carry out a large number of computations to explore the space of input parameters. It was often assumed that the perturbation problem can be approximated by a linear formulation (OECD/NEA, 1997; Kodeli, 2001). With increasing computational performances of computers, it is now possible to verify the linear assumption by achieving a sufficient number of calculations to maximize the representativeness of the input space. Therefore, the objective of this section is to propose a methodology to validate the

linear assumption in modelling the fast flux perturbation, regardless of the large number of input parameters (~ 1600: see Chapter IV Tab. IV.1), and of possible *interactions and correlations*[1].

1.1 Determination and verification of the linear model of the fast flux calculated by APOLLO3®

The propagation of perturbations in the APOLLO3® calculation model defined in Chapter III, allows us to determine a statistical design with p observations of the n input variables and of the corresponding output response y. The *Ordinary Least Square* method presented in Chapter II Section 2, thus allows to estimate the linear regression on the fast flux.

To measure the quality of the linear regressions of the following studies, we will first use the *coefficient of determination R^2*, the *adjusted coefficient R^2_{adj}*, the *LOO-cross-validated coefficient of determination Q^2*, as defined in Chapter II Tab. 2. If the coefficients are close to 1, we can consider that the linear models give a satisfactory description of the variations of the fast neutron flux calculated by the deterministic scheme (implemented in Chapter III) in the range of input uncertainties.

In the forecoming sections, we will show that the use of linear models can simplify the implementation of sensitivity analysis to take into account the possible correlations among data. This may be especially useful in nuclear studies for which linear formulations appear frequently in the definition of perturbation models.

1.2 Using the linear model to quantify the uncertainty of the fast flux calculated by the TRIPOLI-4® reference

The aim of this section is to validate the use of the APOLLO3® code for the sensitivity analysis of the fast flux, normally, calculated by the TRIPOLI-4® reference code.

Let us consider a bias b between the calculation with APOLLO3® and TRIPOLI-4®:

$$y_{T4} = y_{A3} + b. \tag{V.2}$$

The main question is whether the uncertainty propagation in the deterministic scheme allows to quantify the uncertainty on the fast flux which is normally calculated by the TRIPOLI-4® reference scheme. The idea is to suppose that if the bias b is relatively constant regardless of the perturbations ($Var(b) \simeq 0$), the variability of the deterministic calculation is representative of the variability of the reference calculation:

$$Var(y_{T4}) = Var(y_{A3} + b) = Var(y_{A3}). \tag{V.3}$$

Similarly, if the linear model $\hat{y}_{A3} = \sum_i^n \hat{\beta}_{A3,i} x_i$ of the deterministic calculation is validated and b is relatively constant, we can assume that $\hat{y}_{A3} + \bar{b}$ is a good approximation of y_{T4}, and use the linear model as a base of the sensitivity analysis presented in the next sections. Fig. V.2 illustrates the effect of constant bias.

In other words, it consists in determining if the linear model can be generalized to an independent data set of p_{T4} TRIPOLI-4® calculations, following the *cross-validation*:

$$Q^2_{T4} = 1 - \sum_{k=1}^{p_{T4}} \frac{\left(y_{T4}(k) - (\sum_i^n \hat{\beta}_{A3,i} x_i(k) + \bar{b})\right)^2}{(y_{T4}(k) - \bar{y}_{T4})^2}. \tag{V.4}$$

---

[1]One must differentiate between the concept of interaction, which describes the joint effects of several variables (without their solely effect) on another variable, and the concept of correlation which describes the dependence or association among the considered variables.
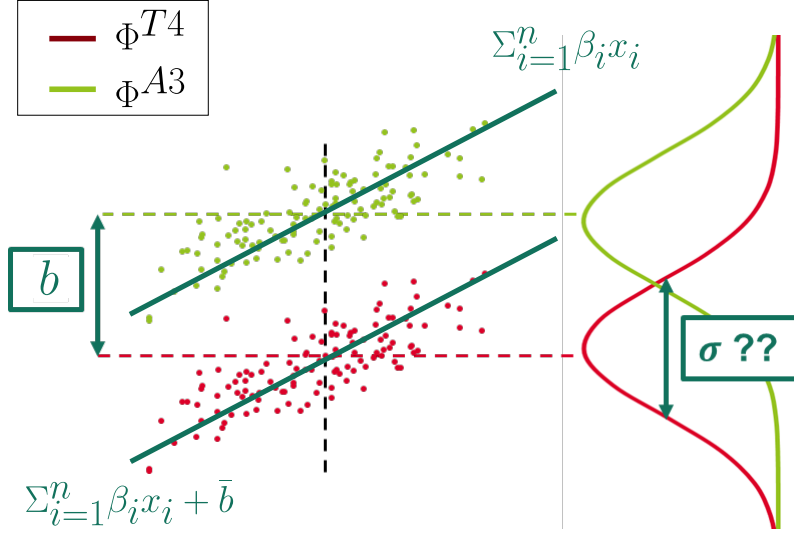
Figure V.2: Illustration of the methodology involved to validate the use of an alternative model
for the fast flux calculation.

In the following sections, the coefficient Q^2_{T4} will be calculated from p_{T4} points $X_{p_{T4},n}$ of the
experiment plan $X_{p_{A3},n}$. This experiment plan contains the perturbations of the input parameters
used to calculate the fast flux from the deterministic code APOLLO3® . Two of the p_{T4} points
will be associated with the maximum and minimum flux obtained by the flux calculation. The
others will be randomly selected from the experiment plan. TRIPOLI-4® calculations will then
be performed for each of these points. Fig. V.3 illustrates an example of such a cross-validation
of the linear model determined to predict the fast flux calculated with APOLLO3® by compar-
ison with TRIPOLI-4®. It depicts the resulting fast flux calculated from the p_{T4} points of the
cross-validation as a function of a parameter X. The same procedure will be used in the various
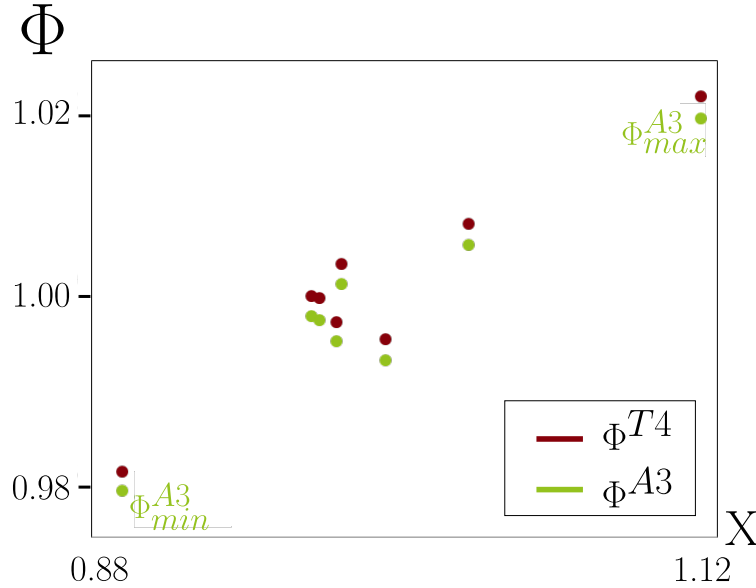studies of the forecoming Section 3.

Figure V.3: Comparison between the normalized fast flux calculated by APOLLO3® and
TRIPOLI-4® on 8 points depending on a standardized parameter X.

2 Variance-Based sensitivity indices in linear models

As explained in Chapter II Section 4, there are various methods to determine the sensitivity of a model output depending on the purposes of the study. In the context of uncertainty analysis, the objective is in general to identify how the uncertainties of parameters can affect the output variability. Some analysis can actually help to prioritize efforts for uncertainty reduction by improving preferentially the quality of the most influential input data.

It is in this context that the present thesis is drawn up. Here, the methods of sensitivity analysis are used to understand how the input uncertainties can interact and influence the flux variability $Var(\Phi_{1MeV})$, directly related to the standard deviation, $\sigma_{\Phi_{1MeV}}$, which is the most common definition of uncertainty (see Eq. V.1). It consists in identifying the origin of the output uncertainty of a model, i.e. the attribution of the proportion of the variance in Y accounted for by that of X_i. The methods presented therein are therefore based on the variance decomposition of the output model.

The aim of this section is to determine an optimal method to carry out a global sensitivity analysis in the case of dependent inputs and linear models. It is inspired by the work of Chao et al. (2008) and Bi (2012), who have provided reviews of the different methods to quantify the relative importance of variables on linear model involved respectively in public health studies and in sensory studies. The methods presented by Chao et al. (2008) and Bi (2012) are, mostly, not known in nuclear studies. Among the methodologies reported, we will focus on the *General Dominance Analysis* and the *LMG measure* initially proposed by Budescu, D. V. and Azen, R. (2003) and Lipovetsky, S. and Conklin, M. (2001) respectively, the *Shapley values*, normally used in game-theory, and the *Johnson indices*.

In the view of interpreting those sensitivity indices, Section 2.1 firstly introduces the basic concepts related to multicollinearity.

Section 2.3 and Section 2.4 eventually present, in the main lines, the differences between the various methods, and therefore the strategy involved in the thesis to achieve the sensitivity analysis.

2.1 Basic concepts dealing with multicollinearity

In the linear case, the variance decomposition can be expressed (Eq. V.5) as:

$$Var(y) = Var(\hat{y} + \epsilon) = \sum_{i}^{n} \beta_i^2 Var(x_i) + 2 \sum_{j>i} \beta_i \beta_j cov(x_i, x_j) + \sigma_\epsilon^2. \qquad \text{(V.5)}$$

However, in the case of dependent indices, some authors have shown the difficulty to interpret them (see Chapter II). The main cause for this is the direct use of full correlations, without transformations such as orthogonalization, which do not allow to distinctly decompose the contribution of each input variable in the output variable. This introduces the concept of *multicollinearity* which can be described as the linear interaction effect of variables so highly correlated, that the ranking of their influence on an output model becomes difficult. To change our point of view, we explore others types of correlation presented in the following sections. For an intuitive view of the meaning of various concepts, we will introduce the widely used example of Venn (1880) diagram in Fig. V.4.
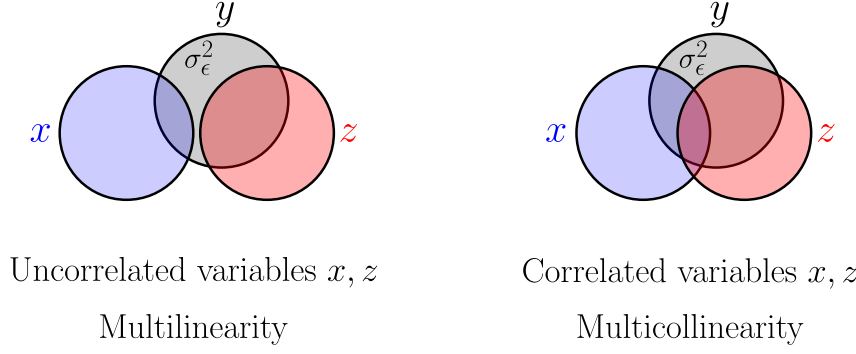
Uncorrelated variables x, z

Multilinearity

Correlated variables x, z

Multicollinearity

Figure V.4: Schematic illustration multicollinearity effects with a variable y and two correlated predictors x and z.
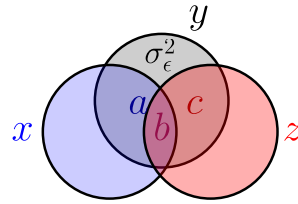
2.1.1 The squared multiple correlation

Empirically, the variance of y (see Eq. V.5) can be given the p measurements y_k, following:

$$Var(y) = \frac{1}{p} \sum_{k=1}^{p} (y_k - \bar{y})^2, \text{ with } \bar{y} = \frac{1}{p} \sum_{k=1}^{p} y_k. \qquad (V.6)$$

It can also be decomposed into the dispersion due to the regression itself, and the dispersion due to the estimation errors σ_ϵ^2, which are respectively defined by $\frac{1}{p} \sum_{k=1}^{p} (\hat{y}_k - \bar{y})^2$ and $\frac{1}{p} \sum_{k=1}^{p} (y_k - \hat{y}_k)^2$.

Dividing $\frac{1}{p} \sum_{k=1}^{p} (\hat{y}_k - \bar{y})^2$ by the empirical variance $\frac{1}{p} \sum_{k=1}^{p} (y_k - \bar{y})^2$ yields, *coefficient of determination* R^2 as defined in Chapter II, Tab. 2. It indeed measures the proportion of variation in y linearly accounted for by the n variables, i.e the *squared multiple correlation* $R^2_{y(x_1,...,x_n)}$.

$$R^2_{y(x,z)} = \frac{a+b+c}{a+b+c+\sigma_\epsilon^2}$$

Multicollinearity

Figure V.5: Illustration of the squared multiple correlation with a variable y and two correlated predictors x and z.

Fig. V.5 illustrates the squared multiple correlation with a variable y and two correlated predictors x and z. Here, the variance of y is equal to $a+b+c+\sigma_\epsilon^2$. It shows that if the dispersion due to the estimation errors tends towards zero, $R^2_{y(x,z)}$ is a good measure of the weight of x and z on the variability of the output model y. In that way, if the linearity assumption is verified, measurement of the weight of x_i on the variability of y defined by a problem with n variables $(x_1, ..., x_n)$ can be perceived as the relative contribution of x_i on $R^2_{y(x_1,...,x_n)}$.

2.1.2 The full correlation

As mentioned in Chapter I Section 2.2, one of the most used is the Pearson product moment correlation which measures the possible linear relationship between two continuous variables. Empirically, we can define the following zero-order correlation between y and a predictive variable x_i as:

$$r_{y,x_i} = \frac{\sum_{k=1}^{p}(x_{i,k} - \bar{x}_i)(y_k - \bar{y})}{\sqrt{\sum_{k=1}^{p}(x_{i,k} - \bar{x}_i)^2 \sum_{k=1}^{p}(y_k - \bar{y})^2}}. \tag{V.7}$$

It measures the direct predictive ability of x_i ignoring the contribution of all other variables in the model. The *squared multiple correlation* can then be decomposed as:

$$R^2_{y(x_1,...,x_n)} = \sum_{i=1}^{n} \beta_i r_{y,x_i}. \tag{V.8}$$

In the case of independent inputs, Eq. V.8 can be rewritten as $R^2_{y(x_1,...,x_n)} = \sum_{i=1}^{n} r^2_{y,x_i} = \sum_{i=1}^{n} SRC_i^2$, shows that the full correlations, and the SRC_i^2 indices, are sufficient to decompose the squared multiple correlation and the variance of y.

$$r^2_{yz} = \frac{c}{a+b+c+\sigma_\epsilon^2} \quad r^2_{yx} = \frac{a}{a+b+c+\sigma_\epsilon^2}$$

$$R^2_{y(x,z)} = \frac{a+c}{a+b+c+\sigma_\epsilon^2}$$

Uncorrelated variables x, z

Multilinearity

$$r^2_{yx} = \frac{a+b}{a+b+c+\sigma_\epsilon^2} \quad r^2_{yz} = \frac{c+b}{a+b+c+\sigma_\epsilon^2}$$

$$R^2_{y(x,z)} = \frac{a+b+c}{a+b+c+\sigma_\epsilon^2}$$

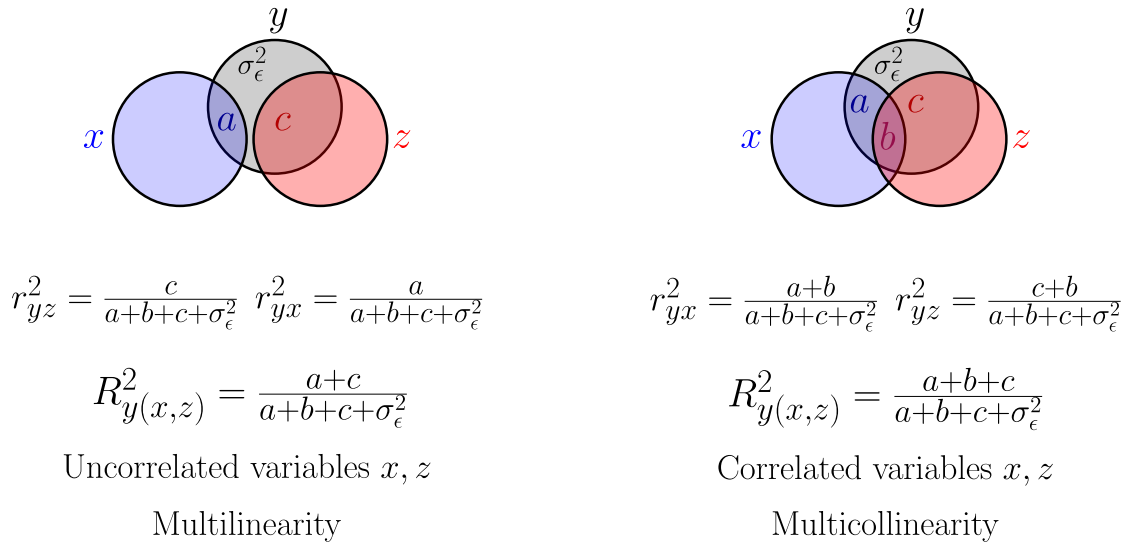Correlated variables x, z

Multicollinearity

Figure V.6: Illustration of the relation between the squared multiple correlation and the full correlation with a variable y and two correlated predictors x and z.

Intuitively, one can understand the limitations in the use of full correlations. As mentioned in previous Chapter 2.2 Section IV, it is possible that there is an indirect linkage between y and x explained by a hidden variable z. An example often cited in the literature (Rakotomalala, 2017) is the full correlation between the hair length and the body size of a person. For instance, if we look at a sample of the European population, this correlation is negative but it is obvious that there is no causal link between the two parameters. In reality, in the European society, women are statistically smaller and have longer hair than men. On the other hand, as depicted by Fig. V.6, a part of the y variance can be explained by the combination of several variables making the interpretation of the decomposition by full correlations, difficult.

Geometrical interpretation of the full correlation

Considering the Euclidean space whose the norm on a p-dimensional vector $\mathbf{x}$ can be written as:

$$\|\mathbf{x}\| \overset{\text{def}}{=} \sqrt{\sum_{k=1}^{p} x_k^2}. \tag{V.9}$$

The scalar product of the p-dimensional vector $\mathbf{x}$ and $\mathbf{y}$ can be defined by:

$$< \mathbf{x}, \mathbf{y} > \overset{\text{def}}{=} \sqrt{\sum_{k=1}^{p} x_k y_k}. \tag{V.10}$$

From Eq. V.9 and V.10, the cosine between the two vectors is:

$$cos(\mathbf{x}, \mathbf{y}) = \frac{< \mathbf{x}, \mathbf{y} >}{\|\mathbf{x}\|\|\mathbf{y}\|}. \tag{V.11}$$

If we now consider the p-dimensional vectors $\mathbf{x}$ and $\mathbf{y}$ as formed by the p observations of the random variables X and Y respectively, we can therefore interpret the full correlation as the *cosine of the angle between the two vectors*.

2.1.3 The partial correlation

In order to take into account the effect of a control variable, one can use the *partial correlation* which quantifies the degree of association between two random variables, while controlling the effect of an extra variable. In other words, it measures the residual information of x on y which is not explained by the control variable. In linear case, the partial correlation is given by the correlation between the residuals ϵ_x and ϵ_y resulting from the linear regression of x with z and of y with z, respectively:

$$r_{(y,x)|z} \overset{\text{def}}{=} r_{\epsilon_y,\epsilon_x}. \tag{V.12}$$

Moreover, the relation between the partial correlation can be computed from the full correlation and the square multiple correlation:

$$r_{(y,x)|z}^2 = \frac{R_{y(x,z)}^2 - r_{y,z}^2}{1 - r_{y,z}^2}. \tag{V.13}$$

It is worth noting that, similarly to the full correlation, the partial correlation does not give information on the causality, but only helps with the interpretation of the relation among data.

Geometrical interpretation of the partial correlation

By analogy with the geometrical interpretation of the full correlation, let us consider the vectors $\mathbf{x}$, $\mathbf{y}$ and $\mathbf{z}$ formed by the p observations of the random variables X, Y, Z.
Similarly, we can define the vectors $\epsilon_\mathbf{x}$ and $\epsilon_\mathbf{y}$ which are by definition orthogonal to $\mathbf{z}$: $\epsilon_\mathbf{x} \cdot \mathbf{z} = 0$ and $\epsilon_\mathbf{y} \cdot \mathbf{z} = 0$.
In that sense, one can geometrically interpret the partial correlation as the cosine of the angle between the projections $\epsilon_\mathbf{x}$ and $\epsilon_\mathbf{y}$ of $\mathbf{x}$ and $\mathbf{y}$, respectively, onto the hyperplane perpendicular to $\mathbf{z}$ (Zeng et al., 2017).

Let us now return to the case of a linear model: $Y = \beta_1 X + \beta_2 Z + \epsilon$, as X and Z are dependent random variables and ϵ is a random variable independent of X and Z with $\mathbb{E}(\epsilon) = 0$. Using the residue definition and the Gaussian model,

$$
\begin{aligned}
\epsilon_y &= Y - \mathbb{E}(Y|Z) \\
&= \beta_1 X + \beta_2 Z + \epsilon - \mathbb{E}(\beta_1 X + \beta_2 Z|Z) \\
&= \beta_1 (X - \mathbb{E}(X|Z)) \\
&= \beta_1 \epsilon_x + \epsilon.
\end{aligned}
\tag{V.14}
$$

The partial correlation between ϵ_x and ϵ_y is therefore equal to ± 1:

$$
\begin{aligned}
r_{(y,x)|z} &= \frac{\mathbb{E}(\epsilon_y, \epsilon_x)}{\|\epsilon_y\|\|\epsilon_x\|} = \mathrm{sign}(\beta_1), \\
r_{(y,z)|x} &= \frac{\mathbb{E}(\epsilon_y, \epsilon_z)}{\|\epsilon_y\|\|\epsilon_z\|} = \mathrm{sign}(\beta_2).
\end{aligned}
\tag{V.15}
$$

For a linear model, the partial correlation does not provide any additional information on the influence level of X and Y on Z. Therefore, the semi-partial correlation, which is a more discriminative coefficient, will be presented.

Remark. *Using the Law of total expectation,*

$$
\begin{aligned}
< \epsilon_x, Z > &= \mathbb{E}(\epsilon_X Z) \\
&= \mathbb{E}(XZ - \mathbb{E}(X|Z)Z) \\
&= \mathbb{E}(\mathbb{E}(XZ - \mathbb{E}(X|Z)Z)|Z) \\
&= \mathbb{E}(Z\mathbb{E}(X|Z) - \mathbb{E}(X|Z)Z) \\
&= 0.
\end{aligned}
\tag{V.16}
$$

as $\mathbb{E}(X|Z)$ is a linear form in Z and corresponds to the orthogonal projection of X on the variable space $(1, Z)$.

2.1.4 The semi-partial correlation

a The zero-order semi-partial correlation $r_{y,(x|z)}$

Contrary to the partial correlation (see Eq. V.12), the *semi-partial correlation* is an asymmetrical measure. The intention here is not to *control* another variable z, but to quantify the additional explanatory power of a variable x on the variance y. The semi-partial correlation is given by the correlation between the variable y and the residuals ϵ_x resulting from the linear regression of x with z:

$$
r_{y,(x|z)} = r_{y,\epsilon_x}.
\tag{V.17}
$$

Moreover, the relation between the semi-partial correlation can be computed from the full correlation and the square multiple correlation:

$$
r^2_{y,(x|z)} = R^2_{y(x,z)} - r^2_{y,z}.
\tag{V.18}
$$

In fact, let us return to the case of the linear model: $Y = \beta_1 X + \beta_2 Z + \epsilon$, as X and Z are dependent random variables and ϵ is a random variable independent of X and Z with $\mathbb{E}(\epsilon) = 0$.

To make the demonstration simpler, let us consider that X and Z are standardized, as $\mathbb{E}(X) = \mathbb{E}(Z) = 0$ and $Var(X) = Var(Z) = 1$. The covariance between both variables is thus defined as:

$$\begin{cases} \mathbb{E}(X|Z) = \rho Z \\ \mathbb{E}(Z|X) = \rho X \\ \mathbb{E}(XZ) = Cov(X, Z) = \rho \end{cases}, \tag{V.19}$$

and we can then write:

$$\begin{aligned} r_{y(x|z)} &= r_{y,\epsilon_x} \\ &= \frac{\mathbb{E}(Y(X - \mathbb{E}(X|Z)))}{\|Y\|\|X - \mathbb{E}(X|Z)\|} \\ &= \frac{\mathbb{E}((\beta_1 X + \beta_2 Z)(X - \rho Z))}{\|Y\|\|X - \rho Z\|} \\ &= \frac{\beta_1(1 - \rho^2)}{\|Y\|\|X - \rho Z\|}, \end{aligned} \tag{V.20}$$

and since $\|X - \rho Z\|^2 = \mathbb{E}(X^2 + \rho^2 Z^2 - 2\rho XZ) = 1 - \rho^2$,

$$r_{y,\epsilon_x}^2 = \frac{\beta_1^2(1 - \rho^2)}{\|Y\|^2}. \tag{V.21}$$

Moreover, the coefficient of determination are given by:

$$R_{y(x,z)}^2 = \frac{Var(\mathbb{E}(Y|X, Z))}{\|Y\|^2} = \frac{\beta_1^2 + \beta_2^2 + 2\rho\beta_1\beta_2}{\|Y\|^2}, \tag{V.22}$$

and,

$$r_{y,z}^2 = \frac{Var(\mathbb{E}(Y|Z))}{\|Y\|^2} = \frac{\beta_1^2\rho^2 + \beta_2^2 + 2\rho\beta_1\beta_2}{\|Y\|^2}. \tag{V.23}$$

Then, Eq. V.22 and V.23 give:

$$R_{y(x,z)}^2 - r_{y,z}^2 = \frac{\beta_1^2(1 - \rho^2)}{\|Y\|^2} = r_{y,(x|z)}^2 \quad \text{Q.E.D.} \tag{V.24}$$

Fig. V.7 shows the difference between the partial correlation and the semi-partial correlation on the classic example of Cohen, J. and Cohen, P. (2014). The semi-partial correlation appears to be relative to the total variance of y contrary to the partial correlation.

b   The multiple semi-partial correlation $r_{y,(x|z_1,...,z_l)}$

The $l-$order semi-partial correlation is a generalization of the zero-order semi-partial correlation, which introduces several control variables:

$$r_{y,(x|z_1,...,z_l)} = r_{y,\epsilon_x}, \tag{V.25}$$

Multicollinearity

Partial correlation
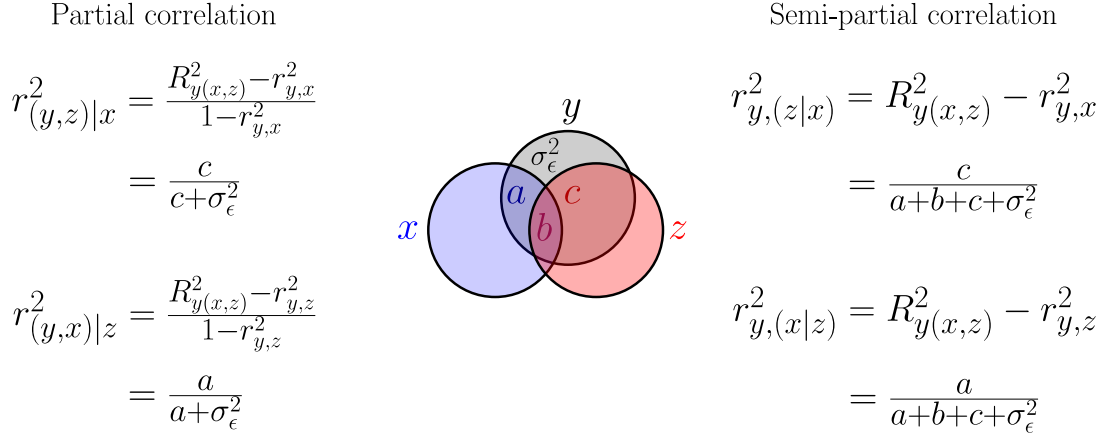
$$r^2_{(y,z)|x} = \frac{R^2_{y(x,z)} - r^2_{y,x}}{1 - r^2_{y,x}}$$

$$= \frac{c}{c + \sigma^2_\epsilon}$$

$$r^2_{(y,x)|z} = \frac{R^2_{y(x,z)} - r^2_{y,z}}{1 - r^2_{y,z}}$$

$$= \frac{a}{a + \sigma^2_\epsilon}$$

Semi-partial correlation

$$r^2_{y,(z|x)} = R^2_{y(x,z)} - r^2_{y,x}$$

$$= \frac{c}{a + b + c + \sigma^2_\epsilon}$$

$$r^2_{y,(x|z)} = R^2_{y(x,z)} - r^2_{y,z}$$

$$= \frac{a}{a + b + c + \sigma^2_\epsilon}$$

Figure V.7: Illustration of the relation between the partial and semi-partial correlation with a variable y and two correlated predictors x and z.

as r_{y,ϵ_x} is defined in a linear framework by:

$$r_{y,\epsilon_x} = \frac{\mathbb{E}(Y(X - \mathbb{E}(X|Z_1, ..., Z_l))}{Var(Y)Var(X - \mathbb{E}(X|Z_1, ..., Z_l))}. \tag{V.26}$$

An alternative method to quantify $r^2_{y,(x|z_1,...,z_l)}$ consists in assessing the additional explanatory power of x by comparing the two regressions considering respectively the groups of variable $x, z_1, ..., z_l$ and $z_1, ..., z_l$. Indeed, the previous demonstration (Eq. V.24) can be generalized to the linear model $Y = \sum \beta_i X_i + \epsilon$:

$$r^2_{y,(x|z_1,...,z_l)} = R^2_{y(x,z_1,...,z_l)} - R^2_{y(z_1,...,z_l)}. \tag{V.27}$$

Likewise, the additional explanatory power of a variable x_i on the variance y considering the group of control variables $\mathbf{u}$ can be written and defined by the following multigroup semi-partial correlation:

$$r^2_{y,(x_i|\mathbf{u})} = R^2_{y(x_i,\mathbf{u})} - R^2_{y(\mathbf{u})}. \tag{V.28}$$

The R^2 calculation are then easily calculated from the p-experiments of $\mathbf{X}$ and Y. In the following sections, we will show the particular interest of Eq. V.28 in the sensitivity analysis of linear models.

2.2 Structural contributions by Standardized regression coefficient

One can easily notice that the *standardized regression coefficient* introduced in Chapter II Section 4.1.1, fails to provide the correct weight of the variables on the output uncertainty if these variables are correlated:

$$Var(Y) = \sum_i SRC_i^2 Var(Y) + 2 \sum_{j>i} \beta_i \beta_j cov(X_i, X_j). \tag{V.29}$$

However, it is important to note that the SRC^2 indices are equal to the *structural contributions* defined by Xu et al. (2008) and introduced in Chapter II Section 4.2. In this way, SRC^2 indices can be used to inform on the direct importance of a parameter on the output of model.

2.3 Analytical definition of the Shapley indices

For all the reasons mentioned in Chapter II Section 4.2, the Shapley indices is used in this section to take into account the correlations among data in the sensitivity analysis.

On the other hand, as shown by Broto et al. (2019, 2018), if the linear regression $\hat{y} = b_0 + \mathbf{x}^T \mathbf{b}$ is valid, and the variables are represented by a $\mathbf{x} \sim \mathcal{N}(\mu, \Sigma)$ Gaussian vector of mean μ and covariance Σ, then the Shapley indices for the variable x_i are given by the following analytical formula:

$$Sh_i = \frac{1}{n\mathbf{b}^T\Sigma\mathbf{b}} \sum_{u \subseteq -i} \binom{n-1}{|u|}^{-1} [\mathbf{b}_{-u}^T (\Sigma_{-u,-u} - \Sigma_{-u,u}\Sigma_{u,u}^{-1}\Sigma_{u,-u})\mathbf{b}_{-u}$$
$$- \mathbf{b}_v^T (\Sigma_{v,v} - \Sigma_{v,u+i}\Sigma_{u+i,u+i}^{-1}\Sigma_{u+i,v})\mathbf{b}_v], \tag{V.30}$$

where v and $-u$ are the complementary of respectively $u + i$ and u in $\{1, 2, \ldots, n\}$. This formula has been recently implemented in the URANIE package and allows to simplify the determination of the Shapley indices (Martinez, 2018).

2.3.1 Interpretation of the link between Shapley values, General Dominance Indices and LMG measures to deal with multicollinearity

In their articles, Chao et al. (2008) and Bi (2012) report two others methods: the *General Dominance Analysis* and the *LMG measure* initially proposed by Budescu, D. V. and Azen, R. (2003) and Lipovetsky, S. and Conklin, M. (2001) respectively. The two methods are actually specific cases of the Shapley method normally used in game-theory. Their advantage is that they do not rely on the Gaussian condition of the input parameters.

The Dominance analysis proposed by Budescu, D. V. and Azen, R. (2003) is based on the measure of the *elementary contribution* of any given variable x_i to a given subset model $y(\mathbf{u})$ by the increase in R^2 that results from adding that predictive variable to the regression model. Considering $x_1, ..., x_n$, the set of uncertain variables, $|\mathbf{u}|$ the cardinality of the subset $\mathbf{u} \subseteq 1, ..., n$, $-\{i\}$ the set of indices without i, and R^2 the squared multiple correlation estimated for each subset of variables, the Budescu indices B_i are noted as:

$$B_i = \frac{1}{n} \sum_{u \subseteq -\{i\}} \binom{n-1}{|u|}^{-1} (R_{y(u \cup \{i\})}^2 - R_{y(u)}^2). \tag{V.31}$$

Using Eq. V.28, we can establish a link between B_i and the square multiple semi-partial correlation:

$$B_i = \frac{1}{n} \sum_{u \subseteq -\{i\}} \binom{n-1}{|u|}^{-1} r^2_{y,(x_i|\mathbf{u})}.$$ (V.32)

In the same way, the square multiple semi-partial correlation is directly linked to the term of $seqR^2(x_i \cup S_{\mathbf{u}})$ that Lipovetsky, S. and Conklin, M. (2001) describes as the portion of R^2 allocated to predictor x_i.

Finally, in the linear Gaussian case, the three methods refer to the same Shapley indices. In the following sections, we will call them *Shapley indices*.

2.3.2 Reduction of the computational cost by forming independent groups of variables

The complexity of the calculation of Shapley indices is related to 2^n, the number of possible subsets in a set of size n. A method for reducing the number of operations consists in permuting the rows-columns of the covariance matrix to obtain a Σ block diagonal matrix (Broto et al., 2019, 2018). The blocks of the matrix form independent groups of random variables. For each variable i associated with one subset $C(j)$ of correlated variables, the Shapley indices $\hat{S}h_i$ are calculated considering the linear regression model of the output: $\hat{y}_{C(j)} = \sum_{k \in C(j)} b_k x_k$. The final Shapley indices Sh_i associated with each variable x_i in a $C(j)$ subset are then determined using the corresponding sub-matrix $\Sigma_{C(j)}$ by:

$$Sh_i = \hat{S}h_i \frac{Var(\hat{y}_{C(j)})}{Var(y)},$$ (V.33)

where $Var(\hat{y}_{C(j)}) = \mathbf{b}^T_{C(j)} \Sigma_{C(j)} \mathbf{b}_{C(j)}$ and $\mathbf{b}_{C(j)}$ are the coefficients associated with the $C(j)$ subgroup in the linear regression model. With this approach, the number of values to be determined is reduced to $\sum_j 2^{|C(j)|}$, where $|C(j)| < n$.

Remark. *This method offers new prospects for the use of Shapley indices. Indeed, the observation of the covariance matrices provided by the nuclear libraries, shows that some of them could be approached by a block diagonal structure. In literature, there exist some block-diagonalisation methods which could be used (Devijver, E. and Galopin, M., 2018). The idea is thus to detect the block diagonal matrix the closest to the initial matrix. The application of the Shapley analysis on the new matrix, could allow to assess approximated sensitivity indices of our problem. As a reminder, with the analytical formula presented in(Broto et al., 2019), a reduction of one dimension divides the computing time by two.*

2.4 Johnson's relative weights indices for high-dimensional correlated data

The complexity of the calculation of Shapley indices is related to 2^n, the number of possible subsets in a set of size n. When there are too many variables it can be impossible to compute the Shapley indices. This is why it is proposed here to use the Johnson Indices which can give a good approximation of the multicollinearity effects on the sensitivity analysis. The idea of Johnson (1966) is to transform the matrix of the experiment plan $X_{p,n}$ in an orthogonal matrix $Z_{p,n}$, as similar as possible in the least-square sense. Building on this idea, Johnson (2000)[2] has

---

[2]Note that they are two different authors.

proposed a similar approach. It consists in finding (always in the least-square sense) Z and Π
such as:

$$
\left\{
\begin{array}{ll}
X = & Z\Pi \\
Z^t Z = & I \\
Z = \underset{W_{(p,n)}}{\arg \min}(X - W)^t(X - W)
\end{array}
\right. ,
\tag{V.34}
$$

where Π defines the linear transform of X on Z.

Johnson shows that the solution of V.34 is $Z = PQ^t$ and $\Pi = Q\Delta Q^t$ where P and Q are the matrix
defined by the singular value decomposition $X = P\Delta Q$. In that sense, the new set of *uncorrelated
variables* $Z_1, ..., Z_j, ..., Z_n$ is *maximally correlated with the original set of correlated variables*
$X_1, ..., X_i, ..., X_n$ (the columns of X).

The regression of Y_p on $Z_{p,n}$ allows to determine $\alpha = (Z'Z)^{-1}Z'Y = QP'Y$ which are stan-
dardized regression coefficients and represents the predictable variance in Y accounted for by
Z:

$$
Var(Y) = \sum_{j}^{n} \alpha_j^2 Var(Z_j) = \sum_{j}^{n} \alpha_j^2.
\tag{V.35}
$$

The α_j^2s are considered to be *close approximations to the relative weights of the original set*
of correlated variables $X_1, ..., X_i, ..., X_n$, but they do not give close representations, particularly
if some original variables are highly correlated. To take into account the correlation effects,
Johnson J. W. thus suggested to regress X on Z:

$$
\Pi = (Z'Z)^{-1}Z'X = Q\Delta Q'.
\tag{V.36}
$$

Let us normalise,

$$
\pi_{ij}^{*2} = \frac{\pi_{ij}^2}{\sum_{i,j} \pi_{ij}^2}.
\tag{V.37}
$$

Since X is a linear transformation of the Z uncorrelated variables, the sum of the π_{ij}^{*2}s is
equal to one and any π_{ij}^{*2} represents the proportion of variance in z_j accounted by x_i.

Finally, the proportionate contribution of X_i to Y can be estimated by multiplying the pro-
portion π_{ij}^{*2} of each Z_j accounted for by X_i by the proportion α_j^2 of variance in y accounted for
by Z_j. In other words, since $\sum_{i=1}^{n} \pi_{ij}^{*2} = 1$, the decomposition of Johnson is a decomposition by
relative weights as:

$$
\sum_{i=1}^{n} \sum_{j=1}^{n} \alpha_j^2 \pi_{ij}^{*2} = \sum_{j=1}^{n} \alpha_j^2 (\sum_{i=1}^{n} \pi_{ij}^{*2}) = Var(Y).
\tag{V.38}
$$

Finally, the Johnson index associated with the variable x_i can be expressed as:

$$
J_i = \frac{\sum_{j=1}^{n} \alpha_j^2 \pi_{ij}^{*2}}{Var(Y)}.
\tag{V.39}
$$

3 Determination of the main contributors to the fast flux uncertainty

As previously explained, two studies have been carried out. The first is presented here. It consists in an analysis of each group of dependent variable. The aim is to reduce the number of final variables to preselect the most important ones in the final interpretation and uncertainty propagation.

We use the Shapley, Johnson and SRC^2 indices to understand how correlations can have an influence on the uncertainty of the fast flux.

3.1 Technological parameters: geometry, water temperature in primary circuit, and impurities in steel

The input variables perturbed in this section, correspond to the technological parameters (see Fig. V.8) whose uncertainties were modelled in Section 4.1:

- the azimuth (α) of the capsules,
- the internal vessel radius (R_{intves}),
- the internal envelope radius (R_{intenv}),
- the external envelope radius (R_{extenv}),
- the internal shield radius (R_{intsh}),
- the capsule thickness ($E_{capthick}$),
- the water gap (E_{watgap}),
- the capsule position (E_{cappos}),
- the water temperature (T_{water}).
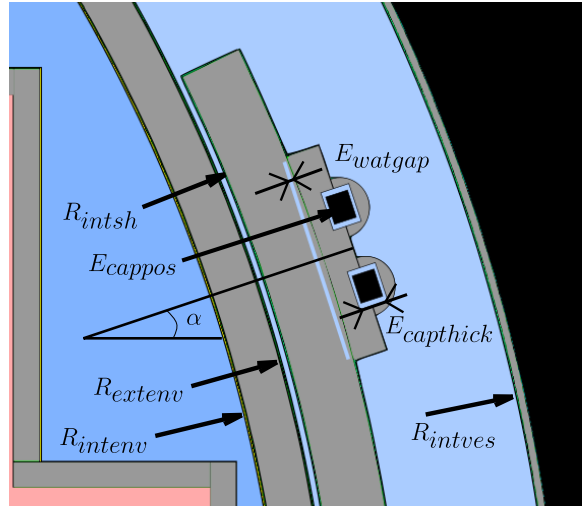
Figure V.8: Location of
the perturbed geometrical parameters.

Tables V.1 and V.2 present the results of the uncertainty propagation of the perturbed parameters for an experiment design composed of 200 samples. The quantity of impurities in the steel materials is an negligible uncertain parameter. The relative error on the Φ_{1MeV} between a calculation with the presence of impurities and a calculation without impurities is in fact negligible. The impact of impurities is thus neglected in the following uncertainty propagation of the technological parameters.

By using the output samples of the uncertainty propagation, we determine a linear model to predict the fast neutron flux at various location of the reactor. Tab. V.1 illustrates the validation of this linear model and thus, the representativeness of the results with regard to the fast flux reference calculation, according to Section 1.2. We can so use the linear model to analyse the behaviour of the fast neutron flux, when variations in the defined technological parameters occur.

	Capsule17°	Capsule20°	Hot spot
R^2	0.998	0.996	0.999
R^2_{adj}	0.998	0.996	0.9995
Q^2	0.997	0.995	0.994
Q^2_{T4}	0.987	0.991	0.984

Table V.1: Validation of the linear model of the fast neutron flux as a function of technological parameters.

In Tab. V.2, the anticipation factors is defined as:

$$f_{anticip} = \frac{\Phi_{Capsules-1MeV}}{\Phi_{Hotspot-1MeV}}, \qquad (V.40)$$

It shows that the anticipation factors are more sensitivity to the perturbations of the technological parameters due to the fact that we notably perturb geometrical parameters which modify the spatial distribution of neutrons in the capsules and the vessel.

	Capsule17°	Capsule20°	Hot spot	$f_{anticip-17°}$	$f_{anticip-20°}$
$\dfrac{\sigma}{\sigma_{HotSpot}}$ (%)	0.56	0.36	1.00	1.16	1.07

Table V.2: Standard deviation σ of the fast neutron flux at the capsules and the hot spot. Due to confidentiality, the standard deviations are normalized to the standard deviation at the hot spot.

The independence of the parameters ensures the variance decomposition of the fast neutron flux (see Section 4.1.1) by the SRC^2 indices. We thus determine the SRC^2 indices resulting from the achieved TMC approach.

Fig. V.9a, V.9b show that the fast flux received by the *capsules* is more sensitive to the uncertainties of the *azimut*, the *internal shield radius* and the *internal envelope radius*. The variation of the fast flux at the vessel is mainly influenced by the *internal vessel radius*. These latter parameters have a direct bearing on the quantity of water and steel traversed by the neutrons. The impact of these parameters on the fast flux thus results from a competition between the effects of steel materials and those of water on the neutron population produced by the core of the reactor and reaching the capsules or the vessel. To support the following analysis, we consider Fig. I.2 of Chapter I, which presents the main cross sections of the isotopes ^{56}Fe, ^{16}O and ^{1}H in the fast energy range.

Fig. V.10, V.11 and V.13 depict the correlations between the technological parameters and the multigroup flux in the capsules 17˚, 20˚and in the hot spot respectively. They notably traduce a preponderant role of the water in the lower energies around 1 and 3 MeV, and of the steel for the higher energies (see Fig. I.2 of Chapter I). As a reminder, a portion of the fast neutrons which escape from the core are scattered back by the reflector and slowed down by water, until

(a) SRC^2 indices on the fast neutron flux at the Capsule 17° as a function of the input parameters.

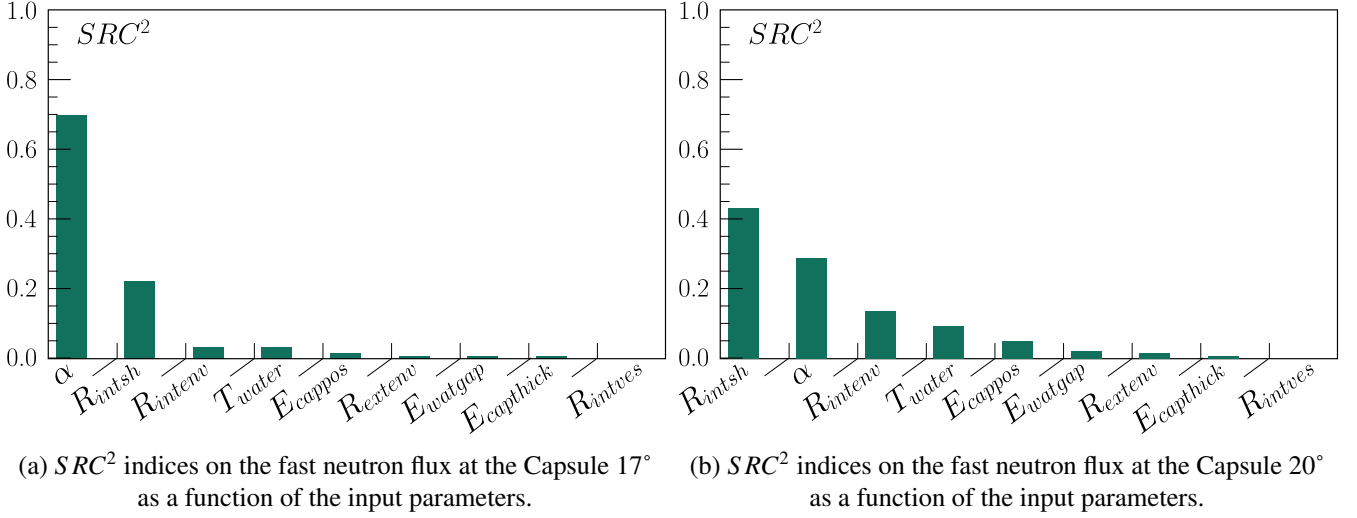(b) SRC^2 indices on the fast neutron flux at the Capsule 20° as a function of the input parameters.

Figure V.9: **Sensitivity analysis -**
Interest output: the fast flux ϕ_{1MeV} at the capsules 20° and 17°
Perturbed variables: the technological parameters.

they reach thermal equilibrium. The neutron loses a part of its kinetic energy and hence slow down, mainly during a collision with hydrogen, and by inelastic scattering with ^{56}Fe.
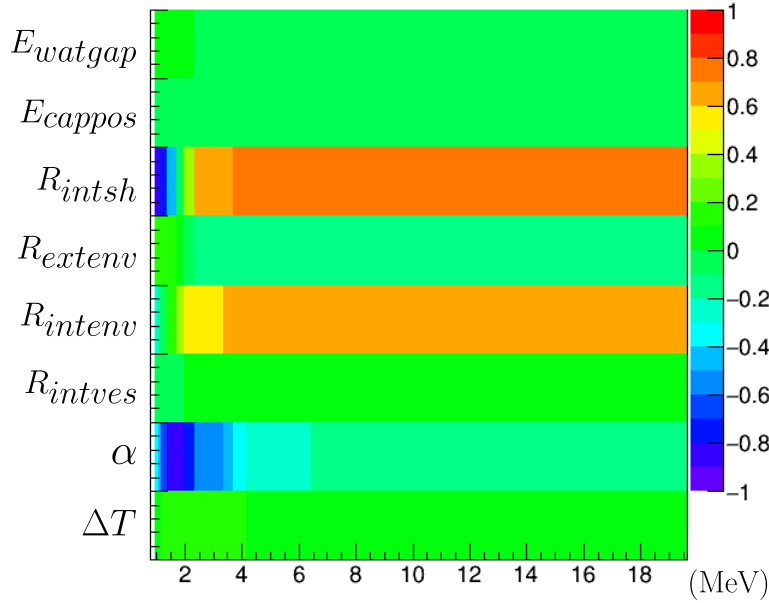
Figure V.10: Correlation data between the technological parameters and the multigroup flux Φ_g at the capsule 17°.

The *shield internal radius* and the *internal vessel radius* are positively correlated with the multigroup flux in the energy range between 3 and 20 MeV because of two effects. Firstly, in this energy range, the elastic scattering of the isotope ^1H is increasingly lower, contrary to the ^{56}Fe cross sections. The neutron transfer is therefore dominated by the iron cross sections. Secondly, an increase of radius leads to a decrease of the steel thickness. The latter effect reduces the impact of the ^{56}Fe elastic and inelastic scattering on the fast neutrons. The neutrons are less scattered back by the reflector, and the flux at the capsules increases.

111

Similarly, in the energy range between 1 and 3 MeV, the radius are negatively correlated with the multigroup flux. The rise of the *shield internal radius* and the *internal vessel radius* enhance the elastic back-scattering of hydrogen.

The *angular position* is anti-correlated with the multigroup flux. In fact, a decrease in the angular position brings the capsules closer to the peripheral assemblies, and increases the neutron flux which is, especially, peaked in the energy range of fission spectrum (between 1 and 3 MeV). The probability that neutrons with this energy reach the capsule is therefore greater.
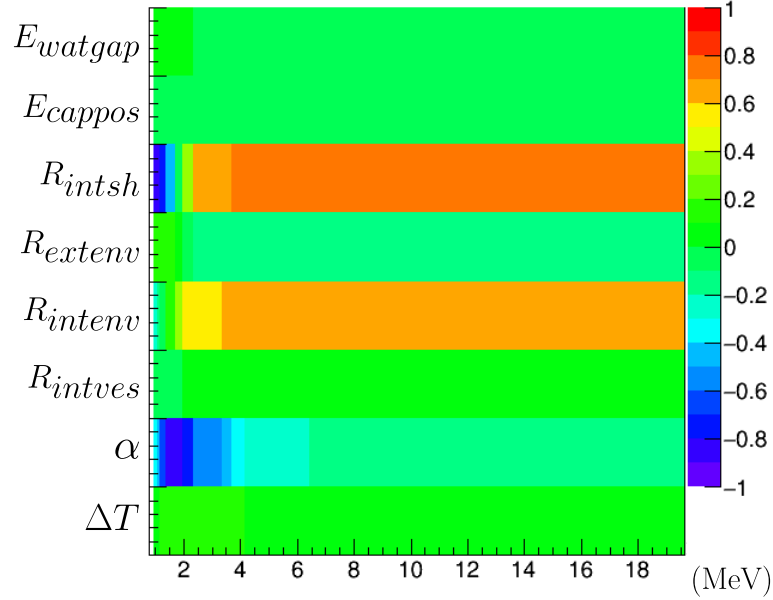
Figure V.11: Correlation data between the technological parameters and the multigroup flux Φ_g at the capsule 20˚.

Fig. V.12 shows that the fast flux received by the *hot spot* is more sensitive to the uncertainties of the *internal vessel radius* because of its extremity.
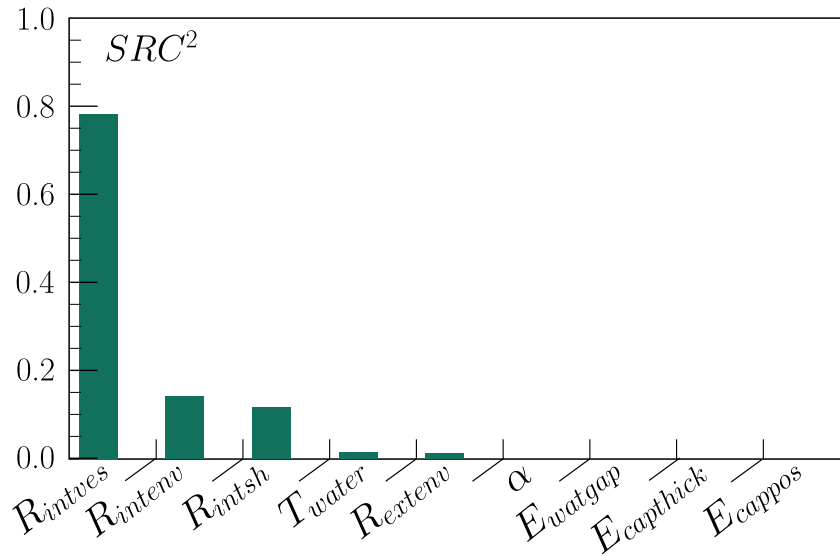
Figure V.12: SRC^2 indices on the fast neutron flux at the hot spot as a function of the input parameters.

112

The *internal shield radius* and the *internal envelope radius* are positively correlated with the multigroup flux for the highest energies. This is similar to the effect described in Fig. V.10 and V.11 because the neutrons reaching the capsules or the hot spot of the vessel pass, in the same way, through the envelope and the thermal shield.

The *internal vessel radius* is anti-correlated with the multigroup flux for the lower energy. In fact, a modification of the *internal vessel radius* change the water quantity which is crossed by the fast neutrons. A greater internal radius leads to a rise of the water quantity and thus decreases, by slowing down, the number of neutrons with an energy around 1 and 3 MeV.
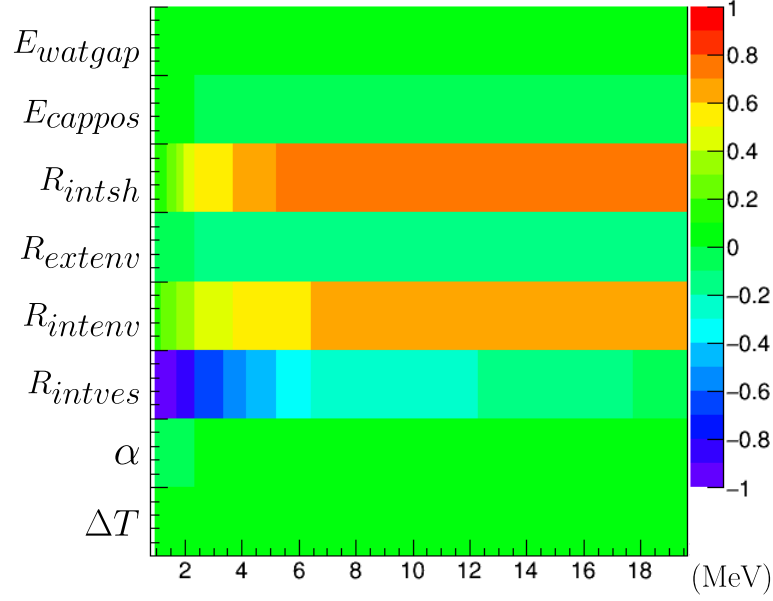
Figure V.13: Correlation data between the technological parameters and the multigroup flux Φ_g at the hot spot.

3.2   Neutron source

As explained in the previous chapter 4.2, the source term in the transport equation can be decomposed in an *energy distribution term* described by the fission spectra and a *spatial distribution term* which notably depends on the power released in the different pins in the core. In this section, we thus present the results of the sensitivity analysis on the source perturbation through various studies carried out and detailed in the next sections.

For all the studies, a linear regression appears sufficient to model the behaviour of the fast flux in the range of input uncertainties as shown by the Tab. V.3. The regression coefficients (R^2, Q^2, R^2_{adj}) are very close to 1. In particular, the linear model is cross-validated (according the method of Section 1) from 8 TRIPOLI4® calculations with a coefficient $\mathbf{Q^2_{T4}}$ of 0.997. The linear models thus can be used to conduct sensitivity analysis.

Tab. V.4 synthesizes the fast flux standard deviation obtained in these studies. The latter consist in propagating the uncertainty on the *neutron spectrum χ* and on the *measured assembly power P_M*. These studies are achieved at a fixed burn-up. The first thing to notice is that the neutron spectrum has more influence on the fast flux uncertainty than the assembly power. However, the anticipation factor is more sensitivity to the perturbations of the assembly power. It can be explained by the fact that the neutron power defines the spatial distribution of the neutron source. A perturbation of the power of various assemblies thus modifies the spatial distribution of the neutron in the reactor and thus the proportion which reaches the capsules or

	Capsule17°	Capsule20°	Hotspot
R^2	0.998	0.997	0.941
R^2_{adj}	0.998	0.997	0.929
Q^2	0.996	0.996	0.922
Q^2_{T4}	0.988	0.987	0.923

Table V.3: Validation of the prediction linear models of the fast flux in the range of
uncertainties of the power distribution and the fission spectrum.

the vessel.

	Random variables		
	χ	P_M	$P_M + \chi$
Capsule20°	0.85	0.31	0.88
Capsule17°	0.80	0.29	0.83
Hot spot on the vessel	1.00	0.37	1.06
$\mathbf{f_{anticip-20°}}$	0.15	0.39	0.42
$\mathbf{f_{anticip-17°}}$	0.19	0.27	0.34

Table V.4: Fast flux Standard deviation resulting from the propagation of the neutron source
uncertainty. Due to confidentiality, the standard deviations are normalized to the standard
deviation of the fast flux received at the hot spot and obtained for the spectrum perturbations:
$$\frac{\sigma}{\sigma_{\chi,\,\text{Hot Spot}}}.$$

3.2.1 Neutron prompt spectrum

We present, in this section, the results of the uncertainty propagation on the neutron prompt
spectrum. As a reminder, for sampling the neutron spectrum, we have used the covariance data
of the Berge (2015)' work which is based on the Madland-Nix model of the PFNS and recently
included in the COMAC V2.0 files (see Chapter IV Section 4.2.1).

Fig. V.14, V.15 and V.16 illustrate the results of the sensitivity analysis of the fast flux
at various locations (Capsules at 17°and 20°, and vessel hot spot) for the PFNS perturbations.
Figures show that the perturbations of the PFNS associated with the isotope [239]Pu is negligible.
It is due to the fact that at the fixed burn-up considered, the quantity of [239]Pu is negligible.

If we focus on the SRC^2 indices which traduce the structural contribution (see Eq. II.43) of
the PFNS on the fast flux, we can note that the fast flux is more sensitive of the spectrum between
4 and 10 MeV. It is consistent with Fig. III.17 representing the part of neutrons in energy which
reach the hot spot of the vessel. Above 10 MeV, the weight of the neutron spectrum is in fact
significantly lower (see Fig. III.14 ; [235]U and [239]Pu multigroup spectrum).

Capsule 17°	Capsule 20°	Hot spot
$\simeq 45\%$	$\simeq 45\%$	$\simeq 45\%$

Table V.5: Sum of the SRC^2 indices $\sum_i SRC^2_i$ (%) considering fission spectrum uncertainties.

However, it is worth noting that, the sum of the SRC^2 indices associated with each various
group of the [235]U and [239]Pu spectrum is equal to approximately 45%. The SRC^2 indices give
an information on the direct influence of inputs on the output but they do not totally explain
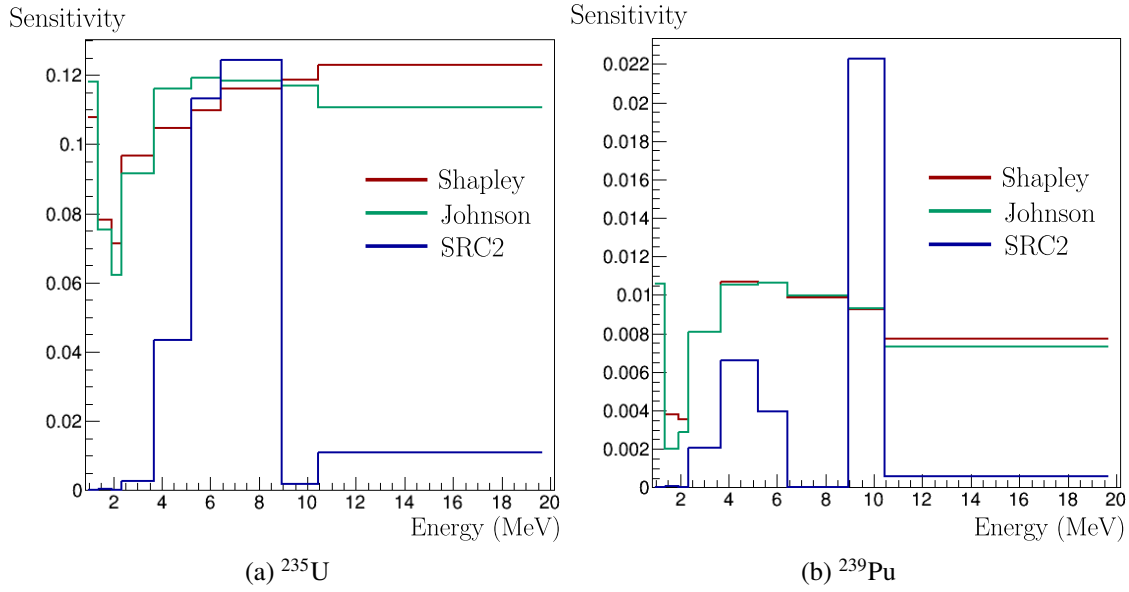
(a) ^{235}U (b) ^{239}Pu

Figure V.14: Sensitivity of the fast neutron flux at the capsule 17˚as a function of the energy
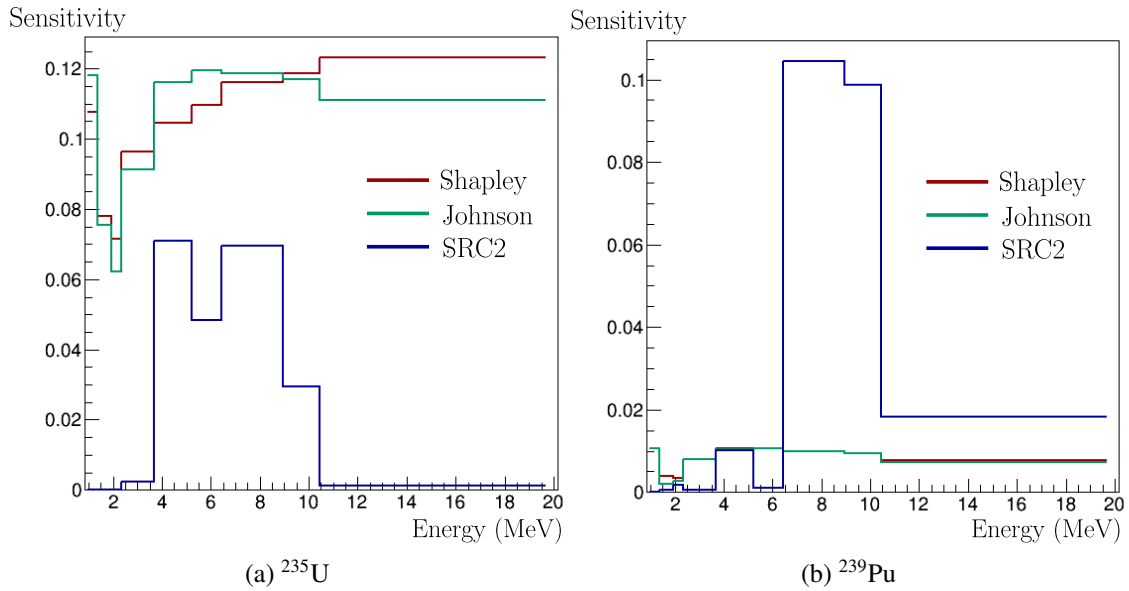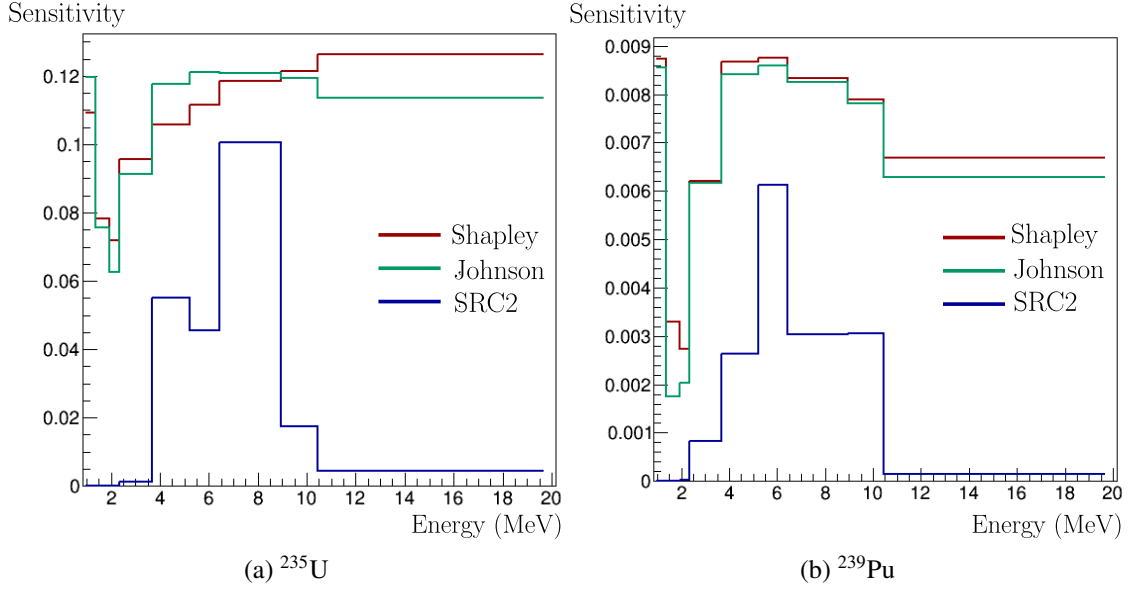distribution of the neutron prompt fission.

(a) ^{235}U (b) ^{239}Pu

Figure V.15: Sensitivity of the fast neutron flux at the capsule 20˚as a function of the energy
distribution of the neutron prompt fission.

the variability of the output contrary to Shapley and Johnson indices. The latter address both
the influence of correlation in the variance decomposition, with a 99% representation of the
output variability. In that sense, they inform on the origin of the uncertainty in terms of missing
knowledge among the input variables.

Fig. V.16, V.15 and V.14 show that the dependence between inputs leads to a rebalancing of
the corresponding Shapley and Johnson values. For example, let us consider the first group of
the neutron spectrum on the various figures. The SRC^2 index associated with this energy group
show that it has no direct influence on the fast flux. Yet, the Shapley and Johnson indices give
higher weight to this variable. It is due to the fact that the first group of the neutron spectrum is
fully anti-correlated with the other groups of the spectrum as shown by the covariance matrix in

(a) ^{235}U　　　　　　　　　　　　　(b) ^{239}Pu

Figure V.16: Sensitivity of the fast neutron flux at the hot spot as a function of the energy
distribution of the neutron prompt fission.

Fig. IV.3. As explained in Section 4.2.1, the form of the covariance matrix of the spectrum is a
result of the *normalisation constraint* (Berge, 2015):

$$\int_0^\infty \chi(E, \vec{x})dE = 1, \text{ for all } \vec{x} \tag{V.41}$$

The *normalisation constraint* depends on the parameters of the Madland-Nix model and
traduce the uncertainty on the spectrum shape. The final uncertainty on the fast flux thus results
from the uncertainties on the parameters themselves and from the uncertainty on the spectrum
shape introduced by the physical model itself.

Remark. *Many important points arise from this study. The first is that if we do not take into
account the correlations among data during the uncertainty quantification of input data, the
final uncertainty of model output may be wrong (Tab. 3.2.1 gives a correlative contribution
to 55%). This demonstrates the need to maintain efforts to provide accurate correlation data.
Secondly, in a context of uncertainty reduction, it appears important to know the origin of cor-
relations, for better dealing with the sources of uncertainties. This idea is reinforced by the fact
that correlations traduce the various analysis choices that were made from the measurements to
the modelling process of data. This study is one example.*

*On the other hand, even if the SRC^2 indices do not take into account the correlative contri-
bution of the input parameters in the decomposition of the variance, they inform on the structural
contribution and thus on the direct influence of parameters. However, in the context of uncer-
tainty reduction, they are not sufficient, due to the various possible correlations and interactions
among data. Conversely, Shapley and Johnson indices give a similar consistent decomposition
of the variance and inform on the impact of the lack of knowledge on the output variable.*

3.2.2　Power map distribution

The spatial neutron source of the core is perturbed in this part by proportionality to the power
distribution. Usually, in nuclear reactors, there are two ways to determine the assembly power
during operating conditions. The first track is based on the local activity measurement (Bouri-
quet, 2015). The uncertainty associated to the assembly power thus stems from the measurement

itself and from a reconstruction process. The second track consists in calculating the assembly power with the information on operating conditions. In this thesis, we focus on the propagation of the measurement uncertainties of the assembly powers. The uncertainty modelling has been presented in Section 4.2.3.

Fig. V.17, V.18, V.19 illustrate the results of sensitivity analysis. The first thing to notice about Fig. V.17, V.18, V.19 is that the contribution of the power associated with the fuel ^{239}Pu is negligible. This is due to the fact that the percentage of ^{239}Pu in the fuel is relatively low compare to the presence of ^{235}U at the burn-up for which the flux is calculated.

We now focus on the contribution of the power associated with the fuel ^{235}U. As previously explained, the SRC^2 *indices* give some information on the *structural contributions* of the perturbed variables on the output variance. In Fig. V.17, we focus on the fast flux received at the hot spot of the vessel. Naturally, the peripheral assemblies ($A9$, $A8$) that are closest to the hot spot, are those with the highest $SRC2$ indices. The neutrons which reach the most the hot spot, are thus mainly produced by the assemblies $A9$ and $A8$.

Capsule 17°	**Capsule 20°**	**Hot spot**
$\simeq 55\%$	$\simeq 55\%$	$\simeq 55\%$

Table V.6: Sum of the SRC^2 indices $\sum_i SRC_i^2$ (%) considering power distribution uncertainties.

The issue is that the sum of $SRC2$ is equal to 55% of the total variance associated with the fast flux ϕ_{1MeV} (Tab. 3.2.2). It means that the $SRC2$ indices do not explain the entire variability of the fast flux contrary to the *Shapley and Johnson indices*.

If we now look the *Shapley and Johnson indices*, we can see that they give similar results on the influence of the input parameters. Compare to the $SRC2$ results, some assemblies ($F9$, $F10$, $E11$, $D10$, $D11$, $C10$) seem to contribute more to the output uncertainty of the fast flux. We can then observe that the $F9$, $F10$, $E11$, $D10$, $D11$ and $C10$ assemblies are those which are the most correlated with the assembly $A9$, $A8$, according to correlation matrix in Fig. V.17b.

In Fig. V.18, the peripheral assemblies ($B11$, $B10$ and $A9$) are those that contribute the most to the fast flux received by the capsule 20°according to the $SRC2$ indices which do not explain the entire variability of the fast flux contrary to the *Shapley and Johnson indices*.

The *Shapley and Johnson indices* rebalance the weight of input parameters on the output variance by notably considering the assemblies $C9$ and $B9$ which are more correlated with $B11$ and $B10$ (Fig. V.18).

A similar analysis can be done for Fig. V.19. the peripheral assemblies ($B11$, $B10$ and $A9$) are also those that contribute the most to the fast flux received by the capsule 17°. The $A9$ assembly has a greater influence to the fast flux at the capsule 17°because it is closer to the latter capsule than the capsule 20°. For the capsule 17°, the *Shapley and Johnson indices* rebalance the weight of input parameters on the output variance by notably considering the assemblies $B9$ and $A8$ which are more correlated with $A9$ and $B8$ (Fig. V.19b and V.19).

Fig. V.20 to V.22 illustrate the Jonhson indices on the multigroup flux at the different emplacements. One can notice that the power of the internal assemblies have no direct influence on the multigroup flux, contrary to the peripheral ones. It shows that considering the correlations between the internal and peripheral assemblies in the sensitivity analysis lead to a rebalancing of the corresponding Johnson effects.
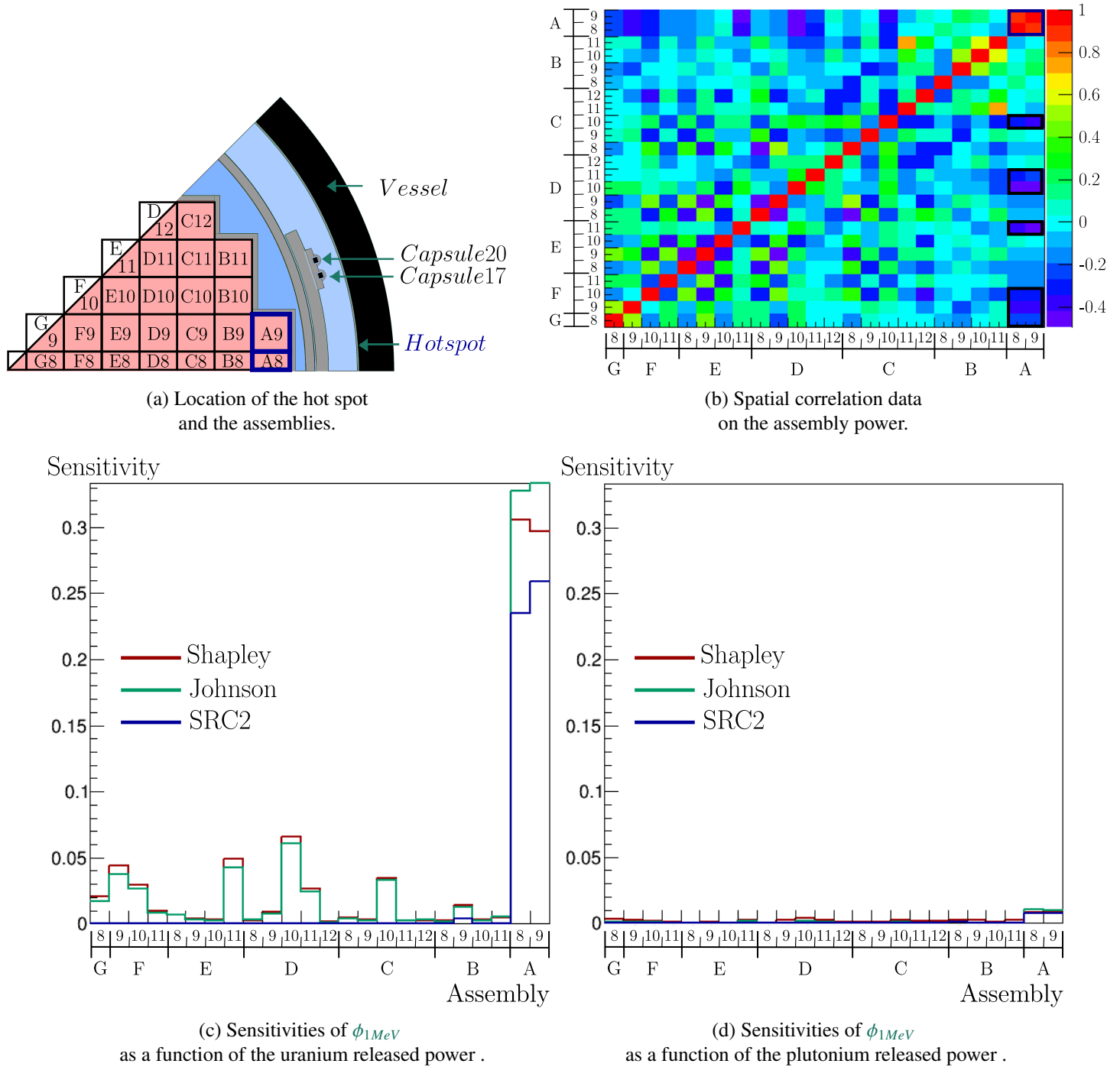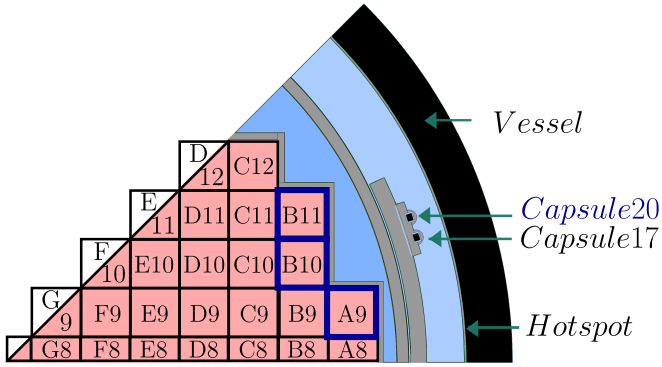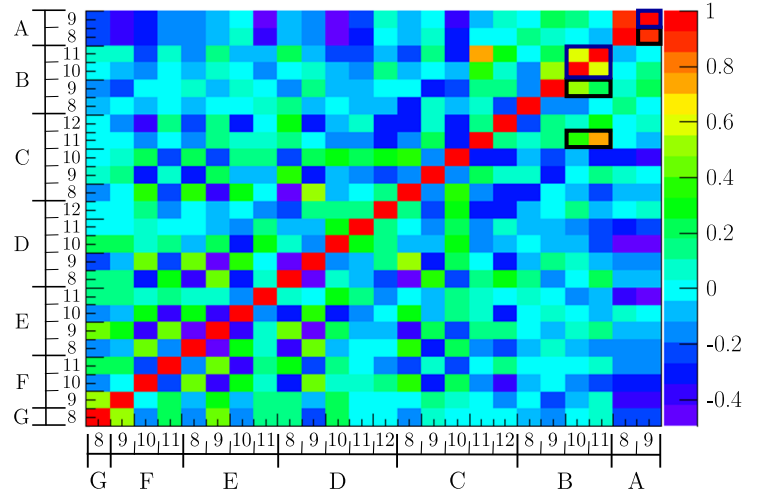
(a) Location of the hot spot
and the assemblies.

(b) Spatial correlation data
on the assembly power.

(c) Sensitivities of ϕ_{1MeV}
as a function of the uranium released power .

(d) Sensitivities of ϕ_{1MeV}
as a function of the plutonium released power .

Figure V.17: **Sensitivity analysis -**
Interest output: the fast flux ϕ_{1MeV} at the hot spot,
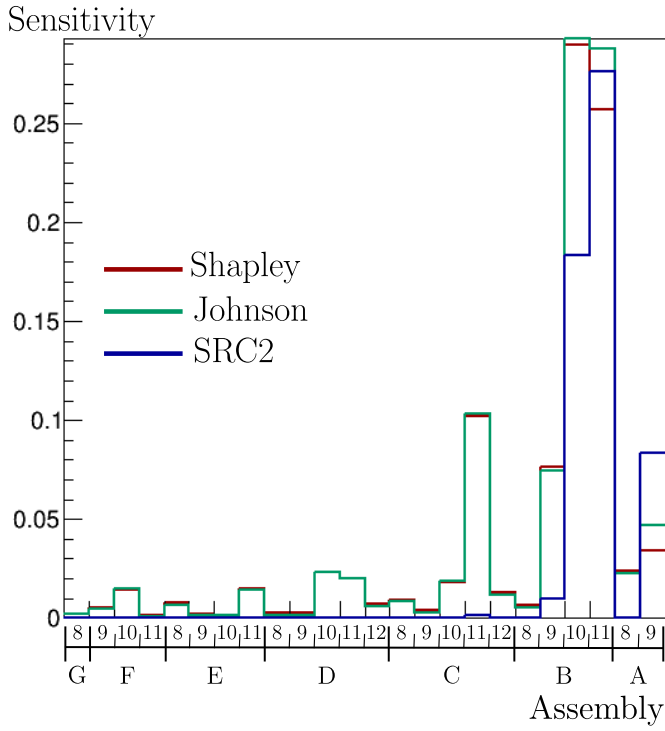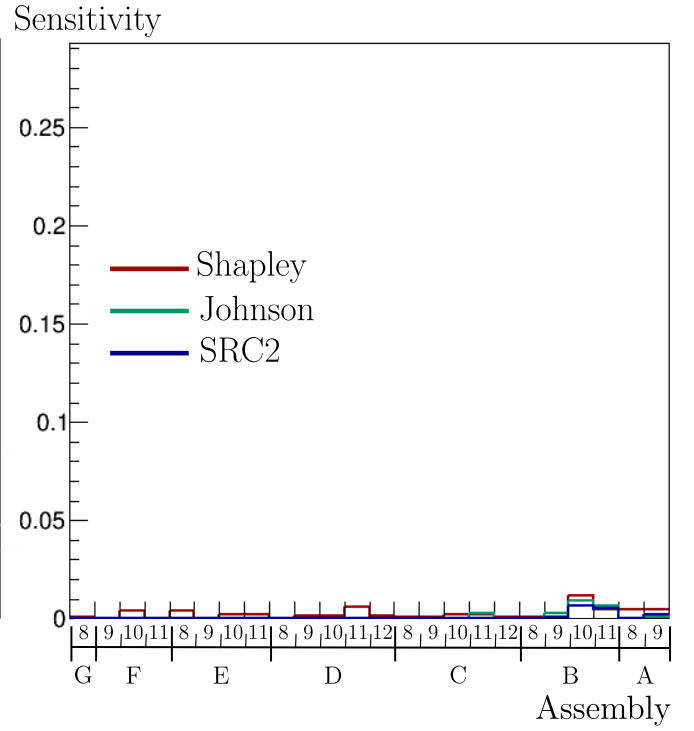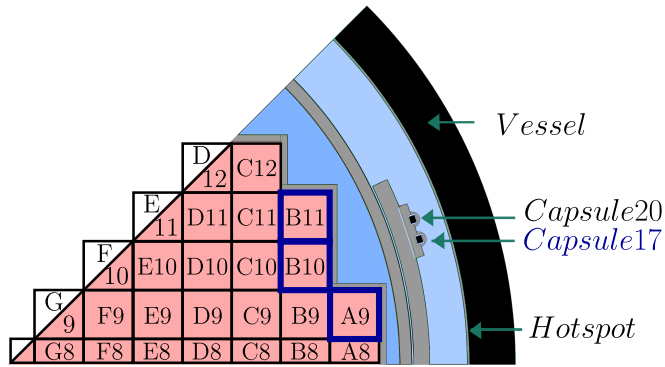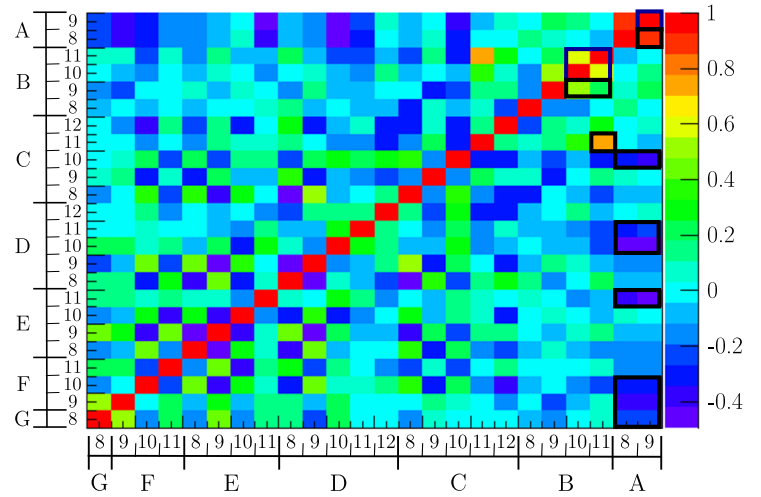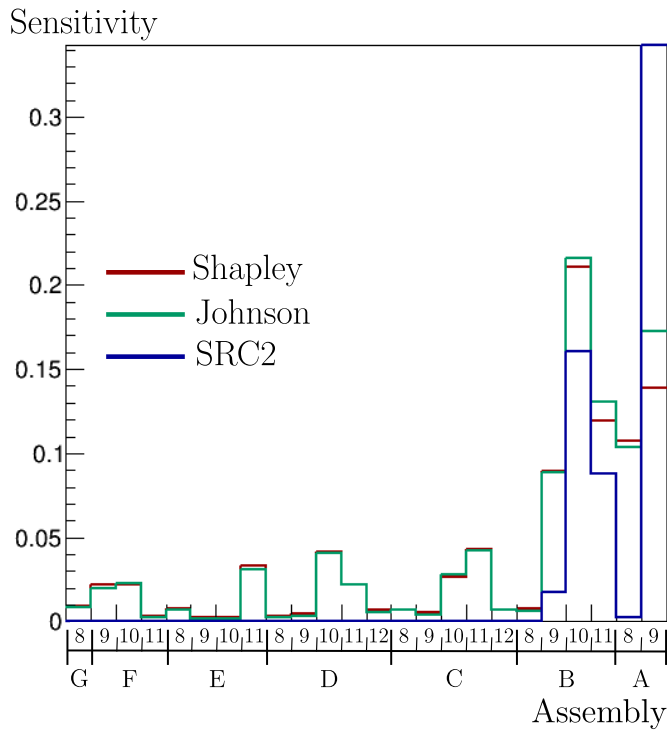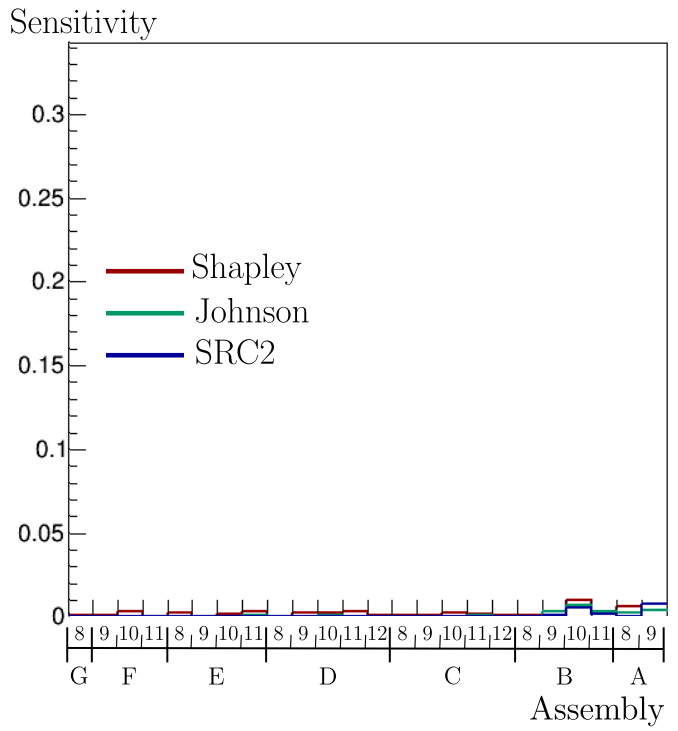Perturbed variables: the power P_{ass} released from ^{235}U and ^{239}Pu.

(a) Location of the capsule 20˚
and the assemblies.

(b) Spatial correlation data
on the assembly power.

(c) Sensitivities of ϕ_{1MeV}
as a function of the uranium released power .

(d) Sensitivities of ϕ_{1MeV}
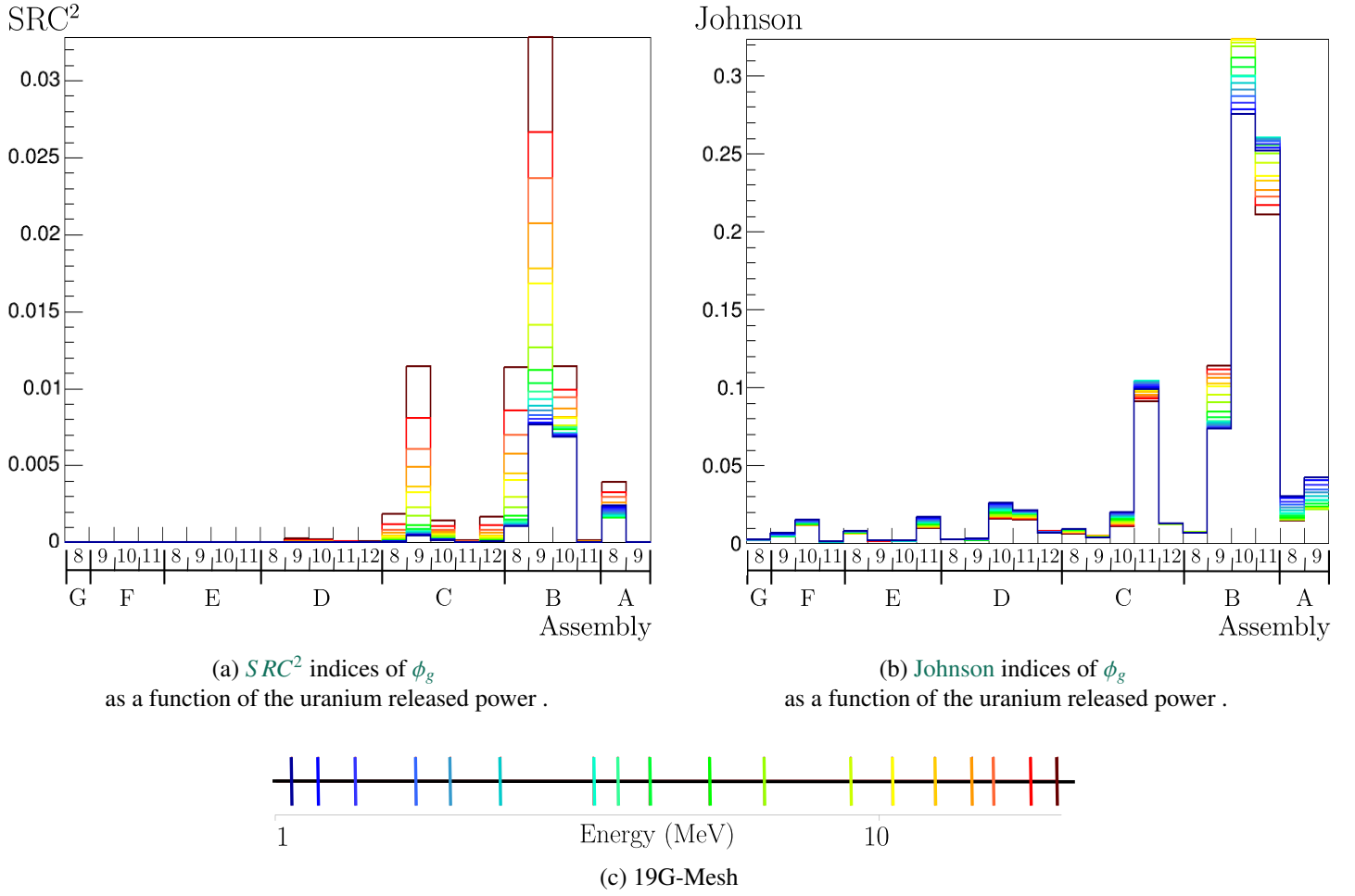as a function of the plutonium released power .

Figure V.18: **Sensitivity analysis -**
Interest output: the fast flux ϕ_{1MeV} at the capsule 20˚,
Perturbed variables: the power P_{ass} released from ^{235}U and ^{239}Pu.

119

(a) Location of the capsule 17˚
and the assemblies.

(b) Spatial correlation data
on the assembly power.

(c) Sensitivities of ϕ_{1MeV}
as a function of the uranium released power .

(d) Sensitivities of ϕ_{1MeV}
as a function of the plutonium released power .

Figure V.19: **Sensitivity analysis -**
Interest output: the fast flux ϕ_{1MeV} at the capsule 17˚,
Perturbed variables: the power P_{ass} released from ^{235}U and ^{239}Pu.

(a) SRC^2 indices of ϕ_g
as a function of the uranium released power .

(b) Johnson indices of ϕ_g
as a function of the uranium released power .

(c) 19G-Mesh

Figure V.20: **Sensitivity analysis -**
Interest output: the multigroup fast flux ϕ_g at the capsule 20°,
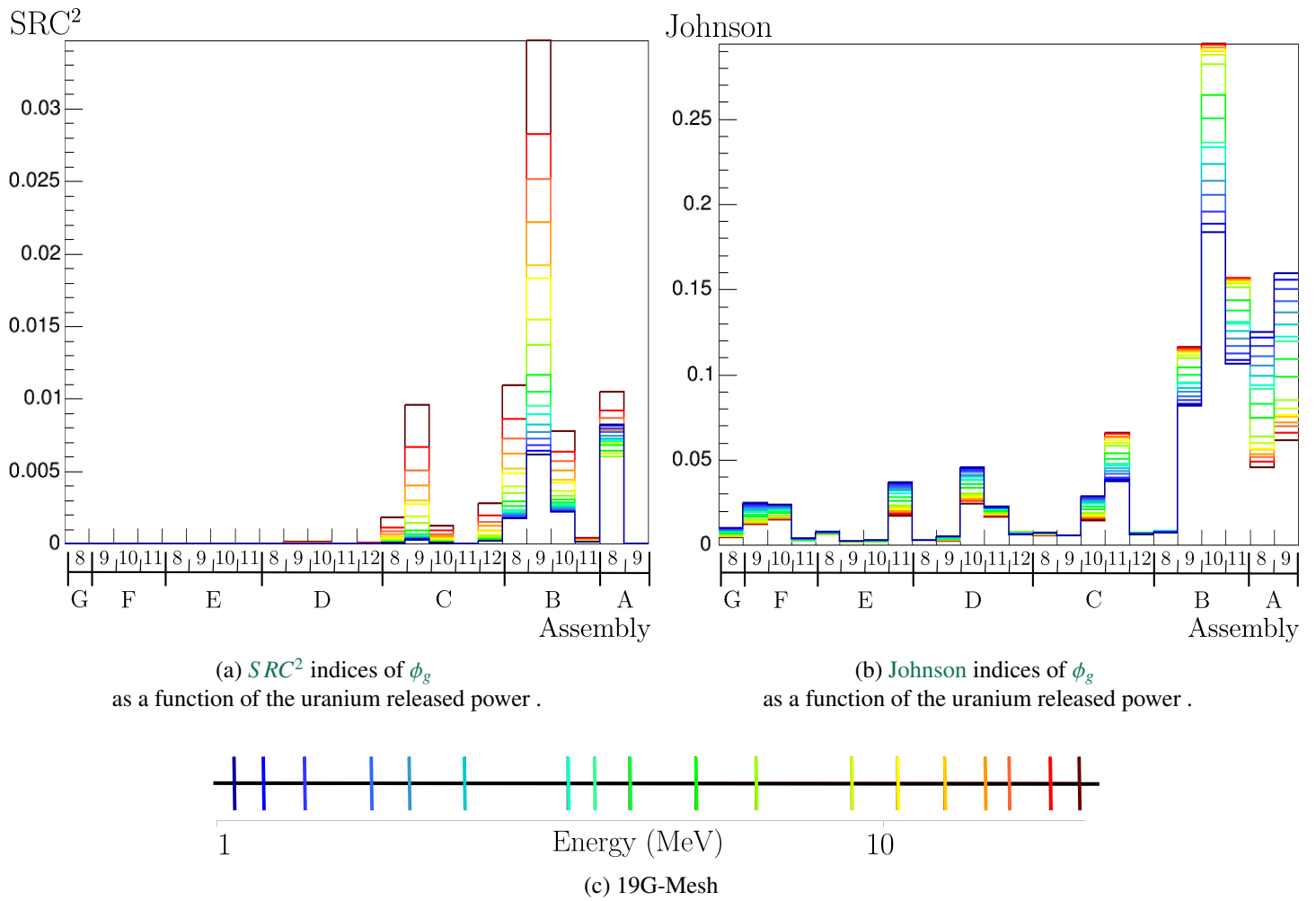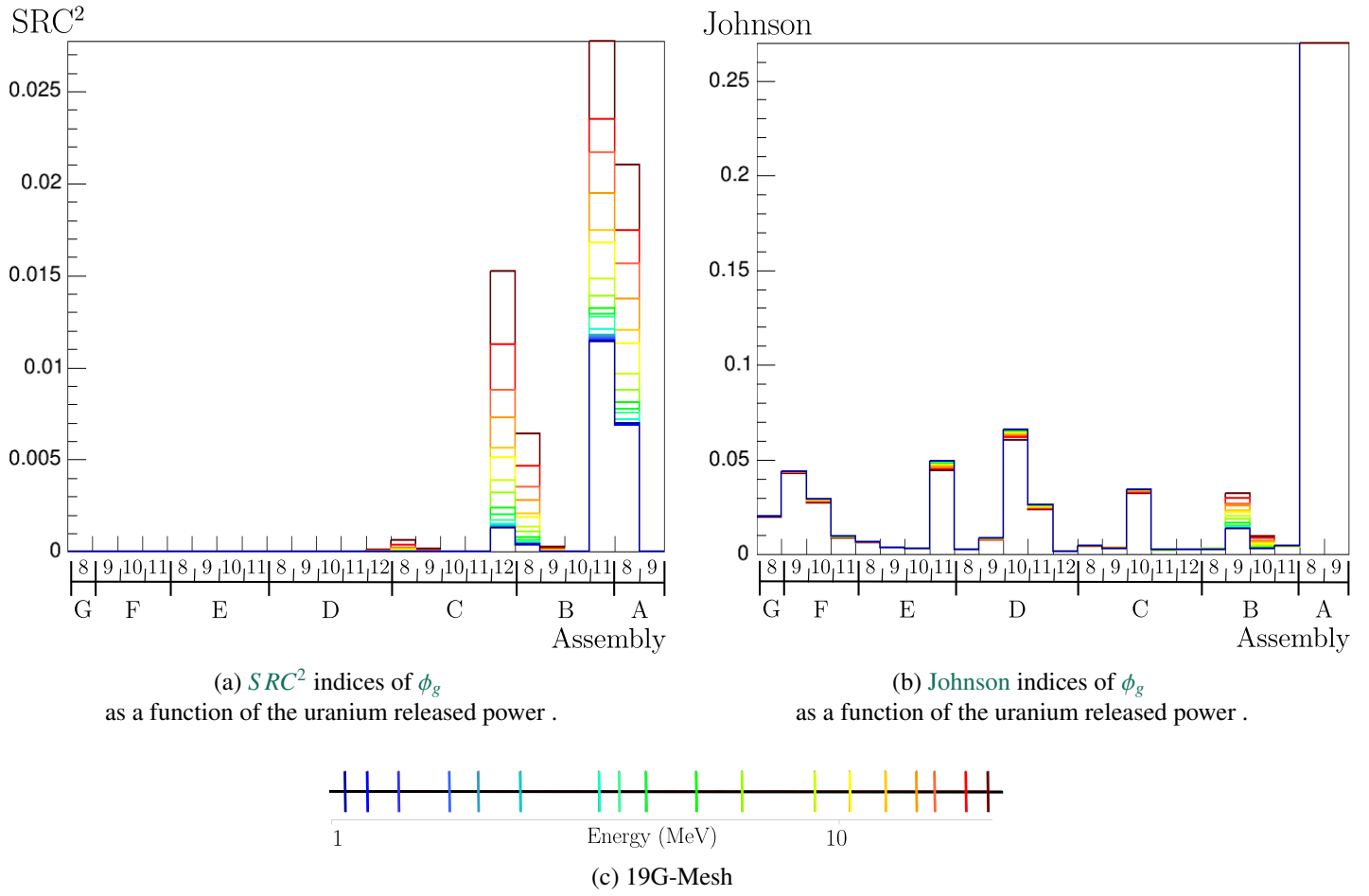Perturbed variables: the power P_{ass} released from ^{235}U and ^{239}Pu.

(a) SRC^2 indices of ϕ_g
as a function of the uranium released power .

(b) Johnson indices of ϕ_g
as a function of the uranium released power .

(c) 19G-Mesh

Figure V.21: **Sensitivity analysis -**
Interest output: the multigroup fast flux ϕ_g at the capsule 17˚,
Perturbed variables: the power P_{ass} released from ^{235}U and ^{239}Pu.

SRC²

Johnson

(a) SRC^2 indices of ϕ_g
as a function of the uranium released power .

(b) Johnson indices of ϕ_g
as a function of the uranium released power .

(c) 19G-Mesh

Figure V.22: **Sensitivity analysis -**
Interest output: the multigroup fast flux ϕ_g at the hot spot,
Perturbed variables: the power P_{ass} released from ^{235}U and ^{239}Pu.

123

3.3 Cross sections

The cross sections of various reactions and isotopes involved in the attenuation of neutrons until
the vessel has been perturbed and described in detail in Chapter IV Section 4.3 and Appendix G.
The perturbations of the 25 considered isotopes are propagated in the calculation scheme. The
aim of this section is thus to conduct a sensitivity analysis to assess the isotopes and reactions
which most contribute to the fast flux uncertainty.

The main difficulty of this step is the high number of variables (defined for various isotopes,
reactions and energies). Considering all the perturbed isotopes, there are indeed 6174 variables
(= 343 partial cross sections × 18energy groups). Since the linear regression (estimating by
Ordinary Least Square: Chapter II Section 2) requires a too big number of samples to carry out
a sensitivity analysis.

To deal with this and in order to achieve a reasonable number of perturbations, we arbitrarily consider a design of experiments with $p = 1000$ samples. An iterative strategy is then
planned to reduce the number of input parameters considered in the linear regression, without
changing the number of variables in the uncertainty propagation. Let us consider N the number
of perturbed parameters in the fast flux calculation, and n the number of parameters considered
in the sensitivity analysis. We assume at this step that we can find n parameters, the variations
of which linearly explain the variability of the fast neutron flux. In other words, it is a question
of finding n parameters such that $Var(b_{N-n})$ is negligible:

$$Var(b_{N-n}) = Var(\Phi_{1MeV-N}) - Var(\Phi_{1MeV-n}), \qquad (V.42)$$

where b_{N-n} is the bias between the calculation of the fast flux Φ_{1MeV-N} *considering the N
parameters* and the calculation of the fast flux Φ_{1MeV-n} *considering the n parameters*.

Moreover, if we assume a linear prediction model of Φ_{1MeV-n}, we can validate this strategy
by verifying that the sum $Var(b_{N-n}) + Var(\epsilon)$ is negligible:

$$Var(\Phi_{1MeV-N}) = Var(\hat{\Phi}_{1MeV-n}) + Var(b_{N-n}) + Var(\epsilon), \qquad (V.43)$$

where ϵ is defined as the error introduced by the linear estimation of Φ_{1MeV-n} (see Section
1).

To reduce the number of parameters, we first use the fact that the cross section perturbations
associated with partial reactions can be synthesized by considering the perturbations on the
redundant and total reactions. Actually, as defined in the ENDF-format (McLane, 2005), the
total cross section can be decomposed in 6 main groups of partial cross section: $\sigma_{1-TOTAL} =
\sigma_{2-ELAS} + \sigma_{4-INELAS} + \sigma_5 + \sigma_{NEXCESS} + \sigma_{18-FISSION} + \sigma_{101-DISAPP}$ where the detail is given in
Chapter IV Section 4.3.2. Those cross sections can also be combined in two common aggregate
reactions used by APOLLO3: the *scattering and absorption reactions*.

On the other hand, we assume that the isotopes, with the lowest concentrations ($\leq 1\%$) in
the materials presented in the reactor, can be negligible. This assumption is mainly supported by
the scientific literature (Kodeli, 2001; Kam et al., 1990; Haghighat et al., 1996; Remec, 1996).

Finally, the input parameters, taken into account in the following sensitivity analysis, are
thus the scattering and absorption cross sections of the 12 isotopes with the highest concentrations in the reflector and the core.

Tab. V.7 illustrates the validation of the linear prediction model of the fast neutron flux as a
function of the perturbed cross sections. The coefficients are not exactly equal to 1. This can be
explained by the fact that we do not consider in the linear regression all the input parameters.
Another explanation is that the number of perturbations is not sufficient to give more accurate
regression coefficients. This second reason will be further discussed. The coefficient remains
close to 1 and validate the use of a linear model to carry out the sensitivity analysis.

	Capsule17°	Capsule20°	Hot spot
R^2	0.988	0.989	0.942
R^2_{adj}	0.976	0.978	0.933
Q^2	0.969	0.962	0.920
Q^2_{T4}	0.956	0.950	0.901

Table V.7: Validation of the linear model of the fast neutron flux as a function of the perturbed cross sections.

	Capsule17°	Capsule20°
$\Phi_{p_1} = \Phi_{Min}$	0.89	0.37
Φ_{p_2}	0.73	0.54
Φ_{p_3}	0.82	0.25
Φ_{p_4}	0.94	0.43
Φ_{p_5}	0.91	0.45
Φ_{p_6}	0.76	0.24
$\Phi_{p_7} = \Phi_{Max}$	0.90	0.43

Table V.8: Bias (%) between the APOLLO3® and TRIPOLI4® calculations for 6 points of the global design of experiment at the capsules.

Tab. V.8 presents the bias between the APOLLO3 and TRIPOLI-4 calculations in the surveillance capsules 17 and 20. One can notice that the accuracy of the APOLLO3 calculation respect to the nominal calculation is not degraded by the cross-section perturbation.

Tab. V.9 gives the empirical standard deviation (II.24) of the fast neutron flux and the various contribution of each isotope. Since the cross sections are independent among isotopes, the contribution of each isotope are assessed as:

$$\Sigma_{y(iso)} = \sum_{i,j} \beta_i \beta_j cov(\sigma_i, \sigma_j),\tag{V.44}$$

as $\sigma_i \stackrel{\text{def}}{=} \sigma_{r_i}^{g_i}$ defines the cross section for the aggregate r_i (scattering or absorption) and for the energy group g_i of the 18G-Mesh.

It shows that the major contributors to the uncertainty are Iron, Hydrogen and Oxygen.

Fig. V.23 presents the result of the Johnson indices of the fast flux as a function of the multigroup absorption and scattering reactions for various isotopes at the hot spot. The Johnson indices of the fast flux at the capsules 17°and 20°are illustrated in Appendix E, because they give similar results to those observed for the hot spot. The scattering reactions of the isotopes ^{56}Fe, ^{16}O and ^{1}H, which are the main constituents of the various media of the reflector, have the largest contribution to the fast flux uncertainty especially in the lower energy range (around 1 to 6 MeV). This range corresponds to the energy field where the multigroup spectrum is at its highest level (see Fig. III.14). In addition, Fig. V.23 traduces the correlation among data. For the three most influential isotopes, we can observe the effects of the correlation matrix (see Chapter IV) on the Johnson Indices. In the range of 2 to 6 MeV, the ^{56}Fe scattering cross section is highly correlated (see IV.17b). The uncertainties of the scattering cross sections are mainly

due to the uncertainties of the inelastic and elastic cross sections, as shown in Fig. V.24 which presents the absolute standard deviation of the scattering partial reactions.

(%)	Capsule17°	Capsule20°	Hot spot
STD_Φ	6.59	5.98	8.29
^{56}Fe	4.27	4.27	4.09
^{1}H	4.02	3.71	5.04
^{16}O	1.70	1.54	2.20
^{238}U	0.45	0.43	0.56
^{53}Cr	0.43	0.42	0.47
^{55}Mn	0.41	0.41	0.46
^{57}Fe	0.40	0.41	0.41
^{52}Cr	0.38	0.37	0.46
^{235}U	0.36	0.36	0.41
^{60}Ni	0.30	0.29	0.32
^{10}B	0.27	0.27	0.30
^{58}Ni	0.27	0.26	0.30
Others	0.16	0.16	0.16

Table V.9: Contribution of the various isotopes and Standard deviation (STD) of the fast neutron flux.
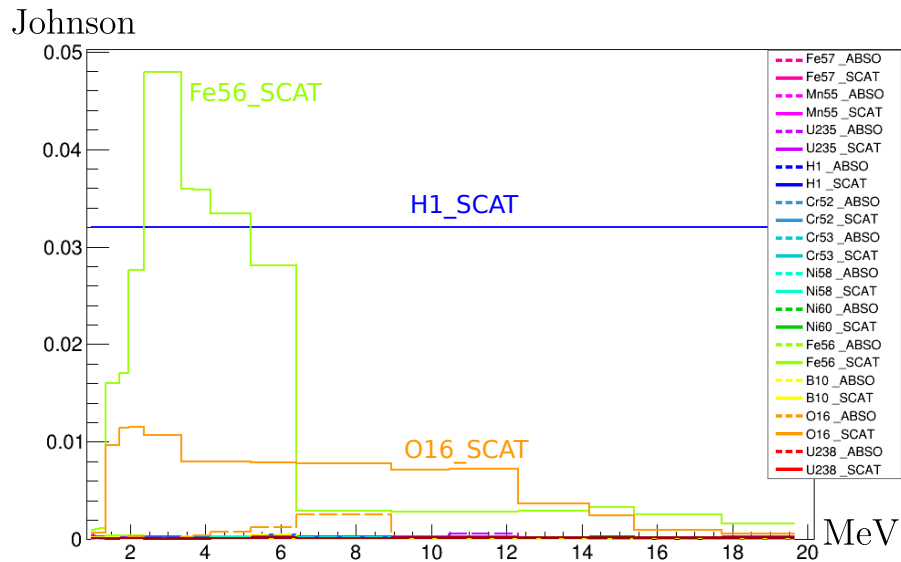
Figure V.23: Johnson Indices on the fast flux at the hot spot and associated with the multigroup scattering and absorption cross sections of various isotopes.

126
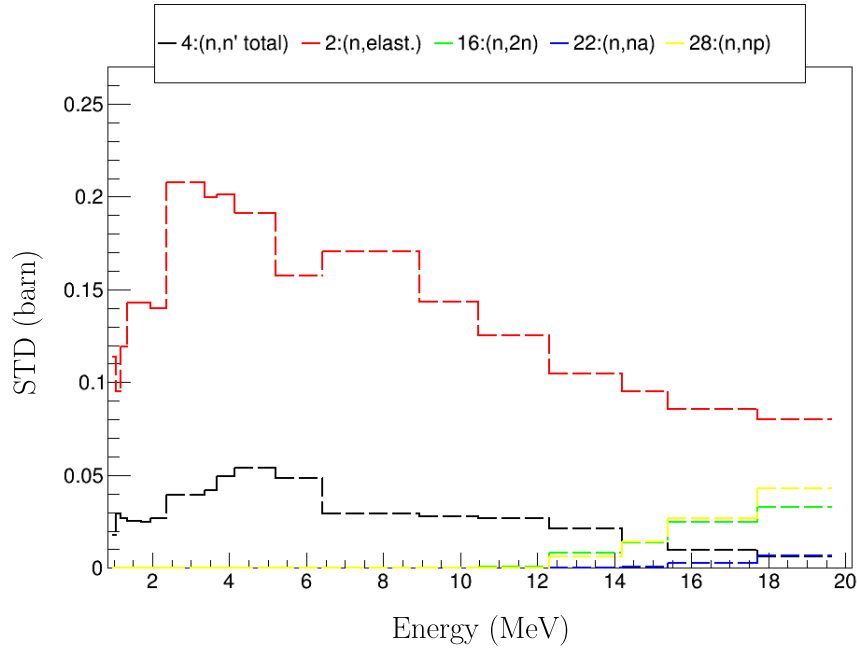
Figure V.24: Absolute Standard Deviation (STD in *barn*) of the cross sections associated with the scattering reactions of the isotope ^{56}Fe as a function of the energy groups.
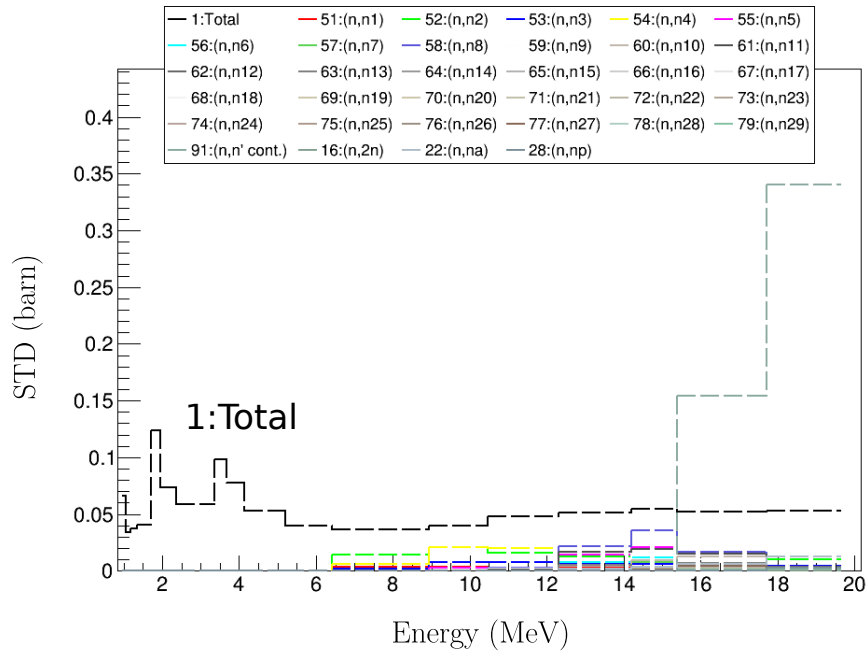
Figure V.25: Absolute Standard Deviation (STD in *barn*) of the cross sections associated with the total and scattering reactions of the isotope ^{16}O as a function of the energy.
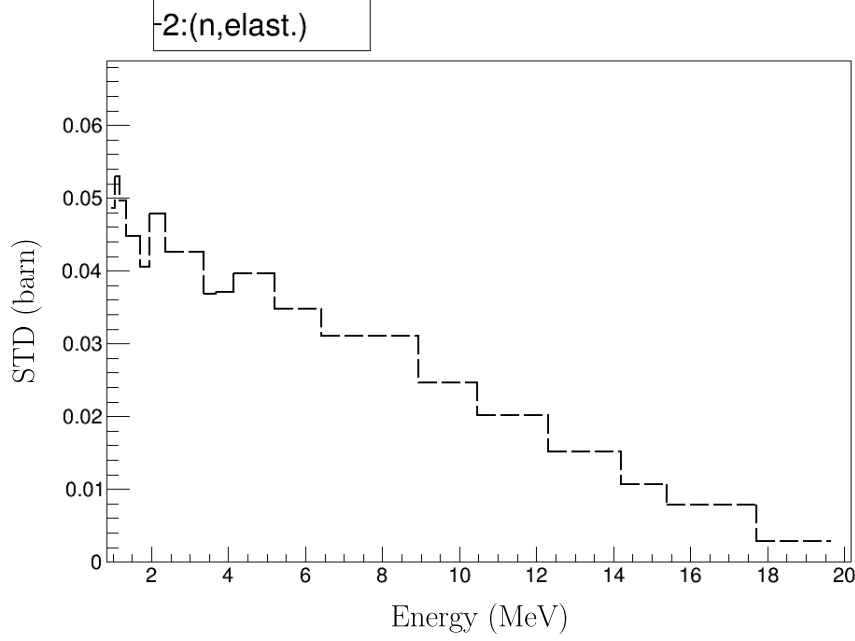
Figure V.26: Absolute Standard Deviation (STD in *barn*) of the cross sections associated with
the elastic reaction of the isotope ^{1}H as a function of the energy.

The ^{16}O scattering cross sections have a weaker influence on the fast flux uncertainty. Its
influence is more spread over the energy mesh. This is due to the shape of the correlation matrix
which contains 4 main groups (around [1-3 MeV; 3-12 MeV ; 12-16 MeV; 16-20 MeV]) where
the multigroup cross sections are highly-correlated (see IV.15b). Fig. V.25 illustrates, for ^{16}O,
the absolute standard deviation (in barns) of the various partial reactions $\sigma_p(E)$ involved in the
scattering process from the library JENDL-4.0 (2011). It also provides the absolute standard
deviation associated with the total reaction. As explained in the previous Chapter IV, to ensure
the consistency of the perturbations and consider all the provided uncertainty data, the JENDL-
4.0 evaluation suggests (with a *NC* section) to assess the perturbations of the elastic cross section
by the following rule:

$$\sigma_{MT=2}(E) = \sigma_{MT=1}(E) - \sum_p \sigma_p(E). \tag{V.45}$$

In the energy range from 1 to 6.5 MeV, the relative contributions of σ_p on the uncertainties
of $\sigma_{MT=2}$ are unknown. In that sense, the uncertainty related to the scattering reactions under
6.5 MeV results actually from the lack of knowledge on the total cross section.

In the library ENDF-B7R1 (McLane, 2005) used to define the uncertainties of the cross
sections of ^{1}H, the scattering cross sections are entirely described by the elastic cross section.
The library provides the uncertainty of the elastic cross section which comprise only one energy
group in the considered energy range of 1 to 20 MeV, as shown in Fig. IV.14b. This explains
that the Johnson indices depict a constant influence of the scattering cross sections over all the
energy mesh.

3.4 Double-differential scattering cross section

As explained in Chapter IV Section 4.4, the angular distribution can be an uncertain parameter in the definition of cross sections. The uncertainty of the angular distribution is not always provided by the nuclear evaluation files (see Appendix F). Among the most influential isotopes identified in the previous section, the ^{56}Fe is the only one whose uncertainties on the angular distribution are provided by the JEFF-3.2 file. Moreover, these uncertainties are only defined for the elastic reaction. We propose to evaluate the impact of its angular distribution uncertainty on the fast flux. This section is thus a preliminary quantitative assessment of its importance of on the fast flux. Two studies are achieved, the first only considering the uncertainty of the cross-section and the second taking into account the uncertainty of the Legendre coefficients and of the cross-section.

Table V.10 presents the results of the first and second designs of experiments, and shows that the linear regression models are sufficient to predict the perturbations of the neutron flux over 1 MeV at the surveillance capsules.

Perturbed parameters	R^2	R^2_{adj}	Q^2	$STD_{\Phi_{1MeV}}$	$STD_{Model}/STD_{\Phi_{1MeV}}$
$\sigma(E)$	0.9986	0.9985	0.9985	3.35%	0.9970%
$\sigma(E) + a_l(E)$	0.9974	0.9970	0.9958	3.41%	0.9970%

Table V.10: Linear regression model for the total flux over 1 MeV - cross-section perturbations.

The effect of *Legendre coefficient perturbation* is negligible compared to the effect of cross-section perturbation. The share of variance that can be attributed, in terms of direct influence, to the Legendre coefficient uncertainties is 3.6% compared to 96.4% for the cross-section uncertainties. In that sense, we do not account for the uncertainty of the angular dependence of the ^{56}Fe elastic cross sections in the final uncertainty quantification of the fast neutron flux.

4 Final uncertainty quantification of the fast neutron flux

In the previous sections, we have studied all the uncertainty sources of the fast neutron flux calculation. Table V.11 synthesizes the standard deviations of the fast flux resulting from all the designs of experiment, independently carried out in the last sections. It provides the quadratic sum calculated from the uncertainty of each group of variables, as:

$$QS = \sqrt{\sigma^2_{Cross-sections} + \sigma^2_{Neutron source} + \sigma^2_{Geometry-Temperature}}. \qquad (V.46)$$

	Capsule20°	Capsule17°	Hot spot	$f_{anticip-20}$	$f_{anticip-17}$
Quadratic sum	0.70	0.66	1.00	0.51	0.49
Cross-sections	0.62	0.56	0.78	0.28	0.24
Neutron source	0.31	0.31	0.42	0.24	0.18
Geometry + Temperature	0.12	0.19	0.33	0.38	0.45

Table V.11: Uncertainty quantification of the fast neutron flux and of the anticipation factors adding quadratically all the uncertainty sources described in the previous sections. Due to confidentiality, the standard deviations are normalized to the standard deviation of the fast flux received at the hot spot and obtained by quadratic sum of all the uncertainty sources: $\frac{\sigma}{QS_{Hot Spot}}$.

The last study propagates the uncertainty of all variables in order to quantify the resulting uncertainty on the fast neutron flux. Tab. V.12 provides a comparison between the quadratic

sum QS of all the uncertainty sources and the final standard deviation STD of the fast neutron flux empirically calculated from the final design of experiment.

	Capsule20°	Capsule17°	Hot spot
$\dfrac{QS}{STD}$	1.00	1.03	1.02

Table V.12: Comparison between the quadratic sum QS of all the uncertainty sources and the final standard deviation STD of the fast neutron flux.

It is important to note that the quadratic sums of the different sub-set of variables considered in the previous studies, are closer to the final uncertainty. It means that the interactions among the sub-sets are negligible and that we can consider that the fast neutron flux is linearly perturbed in the range of the accounted uncertainties. Moreover, the final uncertainty of the fast flux at the hot spot is similar to the results of (Kodeli, 2001) and is higher than the uncertainty at the capsules. As expected, the anticipation factors are less uncertain than the other parameters, and more sensible to geometrical parameters. The cross sections are the main source of uncertainty of the fast neutron flux. The final ranking of the input variables and the final uncertainties are close to the results of the (Kodeli, 2001)'s work.

Fig. V.27 presents the final distribution of the fast neutron flux. Since the output is linked linearly to the perturbations of the input parameters, the output distribution tends toward the Gaussian law.
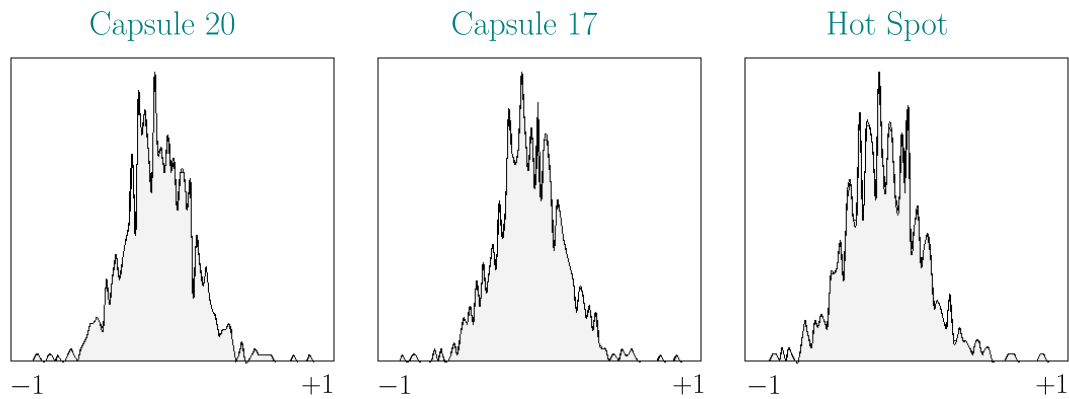
Figure V.27: The Final Standardized Distributions of the Fast Neutron Flux.

DISCUSSION

Statistic methods in the uncertainty evaluation of the fast neutron flux

The main aim of this thesis was to conduct an uncertainty assessment of the fast flux calculation for the PWR vessel. The distinctive feature of this study is the large number of uncertain variables and the presence of correlations among data which require the use of certain practices. A Total Monte Carlo approach for the uncertainty quantification of the neutron flux has been implemented for several reasons. The first is not to presuppose the linearity of interactions among data, in view of the large number of correlated input parameters. The second is to consider, during the step of uncertainty propagation, the probability distribution of the input parameters. The propagation of the latter allows to assess the probability distribution of the output variable, and thus to provide an estimation of the confidence interval of the output. In safety analysis, confidence intervals can be actually useful to quantify the level of confidence that a safety parameter lies in an interval. The last is to carry out a global sensitivity analysis based on a definition of the input uncertainties as specific and complete as possible.

On the linear modelling - This study has finally allowed to *verify that the assumption of the linearity of perturbations* was sufficient to model the perturbations of the fast neutron flux in the range of the input uncertainties. This supports the use of the methods of moments in the uncertainty quantification for the fluence calculations (see for example, the Kodeli (1993)'s work or the OECD/NEA (1997) report). One can note that the large number of input variables can make, the assessment of the regression coefficients, difficult. Indeed, as shown in Appendix C, the accuracy of the estimation of the regression coefficient is thus inversely proportional to $1/\sqrt{n}$, where n is the number of parameters to estimate. An iterative methodology has been applied in our work to get around this issue. The idea was to evaluate the regression coefficients on subsets of variables which can be treated independently of one another. This presupposes that there is no interaction among the subsets of correlated variables. In the future analysis, the linear prediction of the cross-section perturbations could be refined by using various experimental designs for the main isotopes. In reality, one has to keep in mind that in a context of Total Monte Carlo approach, the uncertainty quantification on the output model can be empirically assessed from the experimental design without regard to any output linear model. The linear prediction is only involved here for the sensitivity analysis, the purpose of which is to give information on the origin of the uncertainty of the model. In a context of uncertainty quantification, the sensitivity analysis evaluate, in fact, the impact of input uncertainties in terms of their relative contributions to uncertainty in the output. They help to prioritise efforts for uncertainty reduction, improving the quality of the data. In that sense, the objective is not to obtain a perfect linear prediction of the output but a *prediction models sufficiently accurate to give information on the uncertainty origin*.

Regarding the interpretation and the accuracy of correlation data - In addition, it is worth noting that the main limitation of this study is more based on the accuracy and the difficulty encountered to analyse the correlation data provided by the nuclear libraries. *Correlation information is in fact indispensable for a consistent perturbation of the input space*. As shown in the last chapter V of this thesis, the correlative contribution[3] can have a significant influence on the uncertainty quantification. It can therefore lead to *an underestimation of the final uncertainty of the model output*. Moreover, in a context of uncertainty reduction, it appears important to know the origin of correlations, for better dealing with the uncertainty sources. This idea is reinforced by the fact that correlations traduce the various analysis choices that were made from the mea-

---

[3]The term of *correlative contribution* is defined by Xu et al. (2008). See Chapter II

surements to the modelling process of data. A lack of knowledge on the origin of correlations make the interpretation of the sensitivity analysis difficult. For instance, it can be recalled that the *presence of zero* in correlation data does not systematically mean that there is no correlation among variables but can also mean that the *correlation is not known*. Similarly, the occurrence of correlation is *not equivalent to the existence of causality*. These two examples show us that a good understanding of the origin of correlations is necessary to fully interpret the origin of uncertainties. In the case of nuclear data, we can besides anticipate the difficulty to interpret the results of sensitivity analysis, whatever the method used, considering that there is sometimes a lack of information provided by experimentalists on the origin of potential correlations described in the international libraries. This is why, we have to be prudent in the sensitivity analysis when it comes to the interpretation of indices. Finally, without information on the origin of covariances is nearly impossible, to the first *judge of the quality of covariance data* and second *provide good interpretation of the origin of uncertainties*. In contrast, we have seen that when the interpretation of covariances is well known (see Chapter V Section 3.2.1), it is possible to track down the origin of the uncertainty and propose a way to reduce the latter. All these reasons demonstrate the need to *maintain efforts to provide accurate correlation data*.

***On the use of Shapley and Johnson indices for the sensitivity analysis* -** Recently, many authors have shown the interest of Shapley indices (Owen et al., 2017; Iooss et al., 2019) to account for the correlations among data in sensitivity analysis. The main difficulty encountered with this method is the *large number of input parameters* which can make the calculation of Shapley indices impossible. In linear case, the Shapley indices can be evaluated by an analytical formula (Broto et al., 2019) which eases the calculation of indices. This formula may be especially useful in nuclear studies for which linear formulations appear frequently in the definition of perturbation model. More generally, the linear analytical formula of the Shapley indices is part of the methods involved dealing with *multicollinearity*. The latter concept refers to the linear interaction effect of variables which are so high-correlated that the ranking of their influence on an output model becomes difficult. In other areas, as public health studies or sensory studies (Chao et al., 2008; Bi, 2012), the Shapley indices are often known as the *General Dominance Analysis* or the *LMG measures*. The main limitation of these methods is the complexity of the index calculation which is proportional to 2^n, the number of possible subsets in a set of n input parameters. For instance, in our work, the Shapley indices of 24 variables has been calculated in 8 hours. To circumvent this problem, we have mentioned two tracks. The first track is based on the Johnson indices (Johnson, 2000) which can be a good alternative to give a first physical interpretation of the sensitivity analysis. For 24 variables, the Johnson indices are calculated in few seconds for a ranking of input variables similar to the Shapley indices. The accuracy of these indices in comparison with the Shapley indices can be discussed. However, it is important to remember that in a nuclear context, the correlations among data are often not provided or not well known. To that extent, the Johnson indices appear sufficiently accurate and rapid to be used to deal with multicollinearity in nuclear studies. The second track is to detect the closest block diagonal matrix to the covariance matrix. The application of the Shapley analysis on the new matrix thanks to the Broto et al. (2019) method could allow assessing approximated sensitivity indices of our problem. As a reminder, with the analytical formula presented in (Broto et al., 2019), a reduction of one dimension divides the computing time by two. Finally, in a context of multicollinearity, Shapley and Johnson indices provide a full decomposition of the output variance, contrary to the SRC^2 indices. While SRC^2 indices give information on the *structural contribution* of inputs on the output, Shapley and Johnson inform on the origin of the uncertainty in terms of missing knowledge among the input variables. The comparison between both methods shows that a variable, which does not have direct influence, can have non-zero Shapley and Johnson indices. It is in fact important to distinguish the direct influence of a variable on an

output from its contribution in terms of uncertainty. Indeed, to correctly interpret the sensitivity analysis, it is important to remind that the correlation data traduces potentially linked among variables which can be of three natures:

- accidentally (it is normally excluded here because the correlation matrices are computed by the experimentalists from preselected variables which are potentially linked),

- physically (i.e. with a direct link of causality; it exists a physical model which links both variables),

- indirectly (it exists a hidden variable which explains the link between the known variables; This one traduce often a lack in the modelling).

The last two points translate that the *missing knowledge of an influential variable can be closely linked to the missing knowledge of another variable*. The uncertainty reduction of the model output which depends on *n* inputs are thus often limited by the *physical model* which links or not those *n* inputs. The direct importance evaluation of a variable which is measured by the SRC^2 indices remains useful to distinguish the *structural contribution* from the *correlative contribution*.

Achievements and prospects in the uncertainty evaluation of the fast neutron flux

The sensitivity analysis carried out in the thesis, allowed us to determine the most influential parameters on the fast flux uncertainty. In this section, we discuss on the assumptions made to assess the global study of the flux uncertainty and on the possible prospects of this evaluation.

About threshold energy at 1 MeV   In a context of vessel surveillance programs, it is known that the high-energy neutrons is a monitoring parameter of embrittlement. The neutron fluence over 1 MeV is defined as the standard unit of neutron exposure. The relevance of this quantity is often questioned in literature. Another embrittlement measure is the damage rate (DPA) which expresses the displacement per atom in the media (Chen, 2020). The latter takes into account the effect of all the energy spectrum on the materials. To dispose of the uncertainty on this parameter, some steps could be reconducted in this work to cover even the lowest energies. For example, the optimised number of groups in the energy mesh for the flux calculation will be greater. For a threshold fixed at 0.1 MeV, this number will be around 50 groups (as shown in Appendix A). It is due to the fact that the major structural materials, as ^{56}Fe, have more resonances below 1 MeV. Besides, the random sampling must consider the covariances in the resonance range (File 32 in ENDF format (McLane, 2005)), and the impact of self-shielding should be integrated during the generation of the perturbation factors for APOLLO3.

On the Power Map Distribution   In our work, we focussed on the propagation of the measurement uncertainties in the calculation of the fast flux. In the context of fluence studies, the final uncertainty can be underestimated if the powers defined for each assembly are not the result of measurements but come from a calculation or an adjustment between calculation and measurement. To know how to define the input uncertainty of the assembly power, it is thus essential to know which input data are used to define the core power in fluence calculations: the *calculated power*, the *measured power* and the *adjusted power*. Let us assume that the calculated power is the input of the fluence calculation. In that case, an uncertainty propagation has to be carried out to determine the correlation matrix and the uncertainty of the assembly powers, resulting from the modelling errors and the uncertainties on the input nuclear data. In the literature, several

articles have proposed to estimate the resulting uncertainty on the assembly power estimation. According to Santamarina et al. (2014) the uncertainty on the assembly power varies from 1.5% to 4% for PWR-900MWe depending on the considered covariances (COMAC, BOLNA). As mentioned by Castro González (2018), it should be noted that due to the effect of the normalisation ((Klein et al., 2012)) of the assembly power on the total core power, three regions are distinguished. The central assemblies and the peripheral assemblies have generally an upper uncertainty compared to the assemblies situated in between ((Santamarina et al., 2014; Volat et al., 2018; Perin, 2015; Castro González et al., 2016)). Those uncertainties are mainly attributed due to the uncertainty on the ^{238}U inelastic scattering cross section. On the other hand, in our work, we have neglected the impact of the uncertainty on the pin-by-pin modelling of the power. Actually, the power in the reactor is usually determined from the measurement according to an assembly-wise approximation. However, as illustrated by the spatial distribution of the adjoint flux in Chapter III Fig. III.16, the most influential emitted neutrons on the fast flux at the surveillance capsules are located at the extremity of the peripheral assemblies. This suggests that an uncertainty on the spatial source distribution in assemblies themselves can have a significant influence on the fast flux uncertainty.

On the cross sections   Even if a particular effort has been made since 2005 to improve and extend the covariance data (Salvatores et al., 2018), the covariance matrices are not all the time well known or provided by international libraries for the full nuclear data. To work around this issue, we choose to use the same list as the COMAC files for the uncertainty analysis of the fast flux. The issue is that each covariance matrix is attached to the data of its own library. In fact, covariance matrices describe the analysis choices made during the evaluation process of the associated data. They are thus evaluated in accordance with the methodology adopted to obtain the central values of their nuclear data. This is why they are attached to the data of their own library. In order to provide a critical analysis of the results obtained in this thesis for the considered uncertainties, we have thus presented in Appendix D the various standard deviations and correlations obtained from the JANIS Book (2018) Book for the main international libraries. As a reminder, in our study, the modelling of the uncertainties of the most influential isotopes ^{56}Fe, ^{1}H, and ^{16}O are respectively based on the libraries JEFF-3.3, JEFF-3.3 and JENDL-4.0. For the isotope ^{56}Fe, we have shown that the cross sections which most contribute to the fast flux uncertainty, are associated with the elastic and inelastic cross sections. One can note that the standard deviation of the inelastic cross section in the JEFF-3.3 library is, on average, lower than those of other libraries. For the elastic reaction which is the most influential cross section, the standard deviation of the JEFF-3.3 is greater than the other libraries. Taking into account that the elastic cross section is higher in the energy range $[1; 10 MeV]$, the absolute standard deviation is thus higher for the elastic cross section. In addition, the considered libraries provide different correlation matrices of both reactions, but they similarly present the anti-correlation between the inelastic and the elastic cross sections. For the isotope ^{1}H, the elastic cross section is the most influential reaction in the sensitivity analysis of this thesis. Whichever the considered library, the elastic reaction is described by high correlated cross sections for the energy over 1 MeV. It is relatively similar to the correlation matrix used in this thesis. It means that the Johnson indices could provide similar result if we use the other international libraries to model the uncertainty on the hydrogen. Lastly, for the isotope ^{16}O, we have used the JENDL-3.3 library and shown that the major contribution on the variance of the fast flux is due to the uncertainty in the total cross section. In the energy range $[1; 10 MeV]$ with the greatest influence on the fast flux, the absolute standard deviation and the associated correlation of the total cross section are on average higher for the JENDL-3.3 library. In light of these observations, we may think that the fast flux uncertainty resulting from the uncertainty quantification and propagation presented in Chapter IV, tend to be conservative in comparison with other libraries. One way

of estimating would be to generate the multigroup covariance matrices on the 19-mesh with the ERRORR module of NJOY (see Chapter IV Section 4.3.3), and use the linear regression coefficients estimated in Chapter V, to calculate an estimation of the final contribution of the 3 isotopes.

On the Angular Distribution   The cross section uncertainties are often related to the uncertainty of the energy dependence. Indeed, there is currently few information on the uncertainty of the isotope angular distributions in nuclear data library. In this work, we have proposed, for the ^{56}Fe isotope (the main isotope of the structural materials), a preliminary quantitative assessment of the importance of the elastic angular distribution on the fast flux. In Chapter V, we have shown the negligible impact of its angular distribution on the fast flux uncertainty. Even if the Legendre coefficients have no direct importance, we can note that there is currently in libraries no information on the correlation between the angular dependence and the energy dependence, while both of them depend on the same set of parameters. However, as shown by Chen (2020), for the elastic and the inelastic reaction of ^{56}Fe, for instance, the angle-integrated cross sections and low-order Legendre coefficients are highly correlated. It means that their uncertainties and their knowledge are greatly related. This work shows the interest to improve the modelling of the angular distribution uncertainties. For the continuation of our work, a new sensitivity analysis could thus be envisaged evaluating the impact of the angular distribution for other isotopes (e.g. ^{1}H, ^{16}O) and other reactions.

On a future Bayesian Inference   The uncertainty assessment carried out in this thesis notably shows that the cross-section modelling is the main source of uncertainty of the fast neutron flux. One track to be explored to reduce the impact of cross section uncertainty could be applying a Bayesian inference from FLUOLE-2 program. This experimental program recently conducted (Bourganel et al., 2018) at CEA validates the TRIPOLI-4 calculation of the fast flux in the neutron spectrum equivalent to that one present in PWR surveillance capsules and vessel.

The Bayesian-based assimilation techniques (Dos Santos, 2013) would consist in assessing the integral measurements and combining them with the output uncertainty in order to reduce the cross section uncertainties and improve the predictability of the PWR neutron scheme. This approach deserves to be investigated.

CONCLUSION

This thesis presents a new uncertainty assessment of the fast neutron flux calculation Φ_{1MeV} for the PWR vessel. It considers more recent nuclear international libraries for modelling the data and their associated covariances. Most of past studies on the uncertainty assessment of the fast flux calculation are based on the methods of moments which assume the linearity of output variation (Kodeli et al., 1996; Kam et al., 1990; Haghighat et al., 1996; Remec, 1996). This method is notably limited because it does not consider the probability distribution of uncertain parameters. In that sense, it only returns an estimate of the output statistical moments. However, in safety analysis, confidence intervals can be useful to quantify the level of confidence that a safety parameter lies in an interval. This is why, in this thesis, we carried out a Total Monte Carlo (TMC) approach (Fig. 52) to quantify the fast flux uncertainty. Considering the input uncertain parameters as random variables, it consists in propagating many perturbation samples in the calculation chain of the fast flux. The resulting output of the computer model is therefore considered as a random variable.
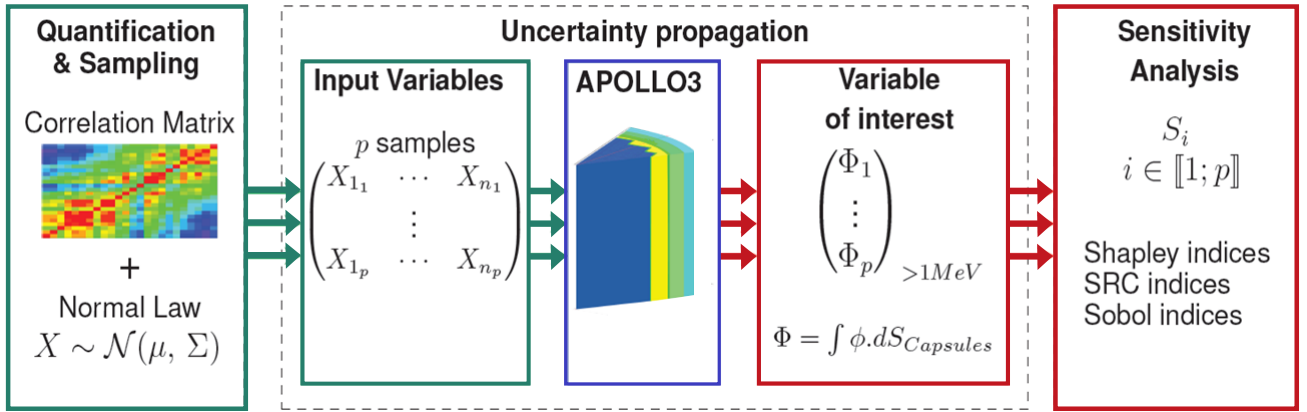
Figure V.28: Uncertainty propagation scheme by TMC approach

This approach requires a sufficient number of samples to provide a representative probability distribution of the output. The point is that in neutron transport, reference tools are usually based on stochastic codes, like TRIPOLI-4® (Brun et al., 2014) which are computationally too expensive to apply an uncertainty propagation by TMC approach. In order to reduce the fast flux calculation time, we have developed a deterministic calculation which is sufficiently rapid and accurate to be used in a TMC propagation.

The deterministic scheme is based on the 3D-SN solver MINARET of the APOLLO3® code which uses the Galerkin discontinuous finite elements approximation. We have first determined, with the AEMC tool (Mosca et al., 2011), an optimized mesh which lies on a single group between 10^{-11}MeV and 1MeV and 18 energy groups greater than 1MeV. Self-shielded and collapsed cross-section libraries were processed from a slab calculation on the optimized energy mesh.

The final flux calculation was performed on a tridimensional PWR geometry (Mosca et al., 2018) using a P3 approximation for the scattering cross sections and a S8 angular order. With this scheme the total flux over 1 MeV (Φ_{1MeV}) has been calculated in different locations of the reactor in less than 20 minutes with an error lower than 1% regarding to the TRIPOLI-4® reference. At this stage of the study, we have assumed that if the bias remained relatively constant regardless of the perturbations, the variability of the approached fast flux will be representative of the reference calculation variability.

The second step of our work was to quantify, model and propagate the input uncertainties of the deterministic flux calculation. As the past study of Kodeli (2001), we were focussed on

the sources of uncertainty which may be treated statistically, i.e. the nuclear data and the technological parameters. For each independent group of parameters, probability distributions were defined by maximum entropy principle, and the correlations, where these exist, were adapted to the deterministic calculation. To randomly sample the correlated variables, we used a Cholesky decomposition and a Maximin Latin Hypercube Sampling which ensures a good representativeness of the variation domain with a reduced number of samples.

Specifically, the *geometry parameters* and the *water temperature* were modelled by an uniform law.

By proportionality to the *power distribution* and the *fission spectra*, the neutron source were perturbed. We only considered the uncertainty on the fission spectra associated with the prompt neutrons which are more likely to cause fast fission and to leak from the core, in comparison with delayed neutrons. To randomly sample the latter, we have considered the covariances created by Berge et al. (2015) to describe the uncertainties on the Madland-Nix model, widely used in nuclear data libraries. The uncertainties on the source spatial distribution were defined from a covariance matrix representative of the spatial power measurements, and modelled by a standard deviation of 1% to 4% depending on the assembly position. The perturbations were finally carried out following an assembly-wise approximation, i.e. homogeneously in each pin of the same standard 17x17 UO_2 assembly.

To perturb the *multigroup cross sections* a calculation chain was implemented from the processing system GALILEE-1 (Coste-Delclaux et al., 2016), the NJOY code (MacFarlane, 2017) and the URANIE plateform. 343 covariance matrices (associated with the total and partial reactions of 25 isotopes) were reconstructed with the ERRORR module in coherence with the 19G-Mesh. They define the variance and the correlation of 6174 variables (343 reactions $\times$ 18 energy groups). We showed that the covariance process can produce ill-conditioned matrices which make their Cholesky decomposition impossible. To deal with this issue, we proposed an alternative method, based on the spectral decomposition, to simultaneously regularize these matrices and sample the random variables. We presented the strategy to generate consistent perturbations between the redundant and partial cross sections. The pointwise cross sections of the 25 isotopes has then been perturbed and propagated in the GROUPR procedure of NJOY. The resulting multigroup cross sections have been combined in two common aggregate reactions used by APOLLO3®: the scattering and the absorption reactions.

The uncertainty related to the energy distribution of cross sections has already been propagated by many authors, but the impact of the *angular distribution* on the fast flux were never been evaluated (Vasiliev et al., 2018). To give a first estimation of its contribution, we assessed the angular distribution uncertainty of the ^{56}Fe elastic reaction, provided by the JEFF-3.2 evaluation. The Legendre orders were then perturbed on the ENDF files directly before the NJOY multigroup processing. Finally, the resulting uncertainties were propagated in the deterministic scheme.

Lastly, we presented the results of the uncertainty propagation in the fast flux calculation and the sensitivity analysis of the relative contribution of each input on the output variance. The final uncertainty on the fast flux Φ_{1MeV} at the vessel hot spot is in accordance with the Kodeli (2001)' work.

In this context of sensitivity analysis, we showed the importance to consider the covariance matrices to propagate the input uncertainties, and analyse the contribution of each input on a physical model. We proposed a global methodology to take into account the correlation data in the context of Total Monte Carlo. To interpret the result of the sensitivity analysis, we used the Shapley Indices. Due to the time complexity of the Shapley indices, we proposed the Johnson indices, as an alternative.

Appendices

A Assessment of an optimized energy mesh over 0.1 MeV

Fig. 29 provides the result on the functional value determined by the AEMC similarly to the methods presented in Chapter 2.2 Section III, for various optimized mesh and for the flux over 0.1 MeV. It shows that the optimum number of groups in terms of accuracy seems to be between 40 and 50 groups, including one group below 0.1 MeV.
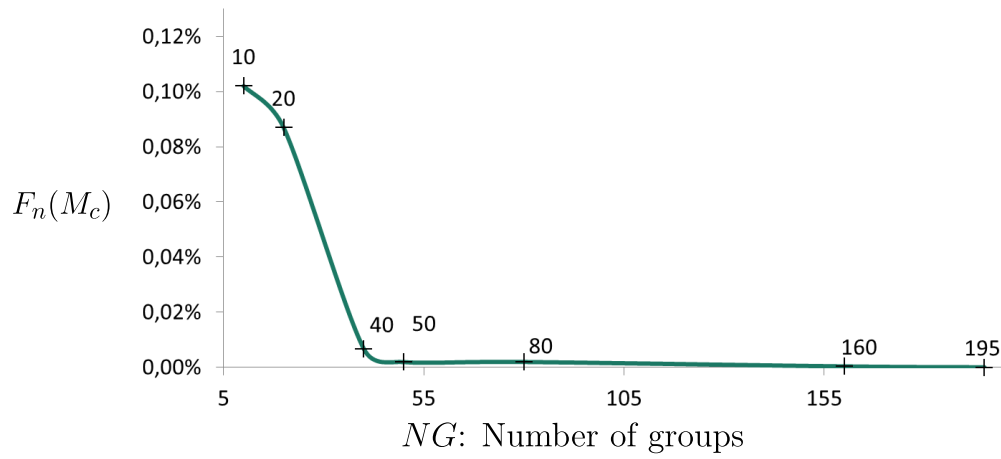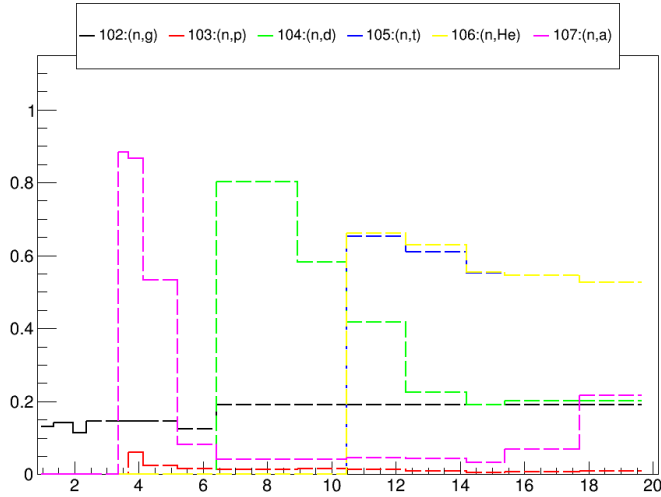
Figure 29: Functional value of the energy mesh optimization versus number of groups.

B Standard deviation of the scattering and absorption multigroup cross sections for the ^{56}Fe, ^{16}O and ^{1}H isotopes

Fig. 30, 31 and 32 present the standard deviation associated with the ^{56}Fe, ^{16}O and ^{1}H isotopes, and resulting from the process presented in Chapter IV.

(a) STD of the uncertain absorption reactions.
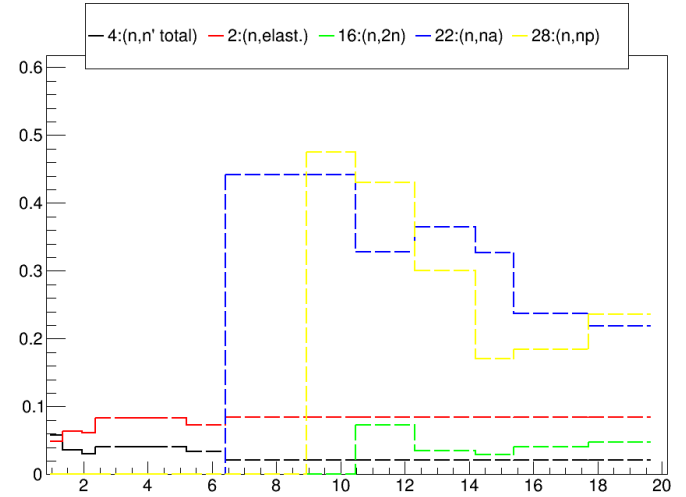
(b) STD of the uncertain scattering reactions.

Figure 30: Standard Deviation (STD in %) of the cross sections associated with the absorption and scattering reactions of the isotopes ^{56}Fe in function of the 18 energy groups of the 19G-mesh which are above 1 MeV.
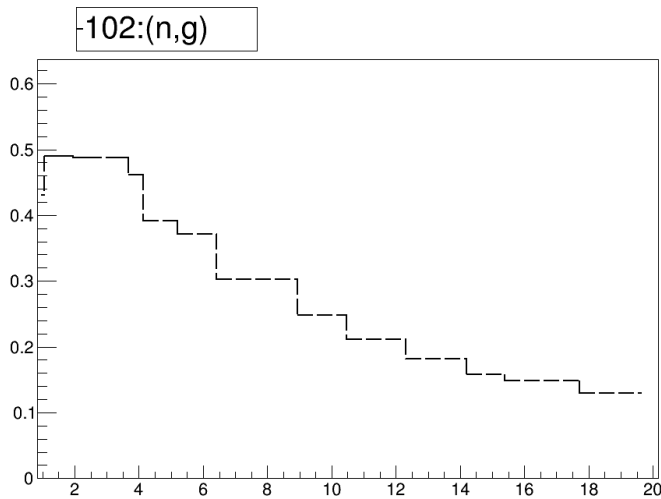
(a) STD of the uncertain absorption reactions.
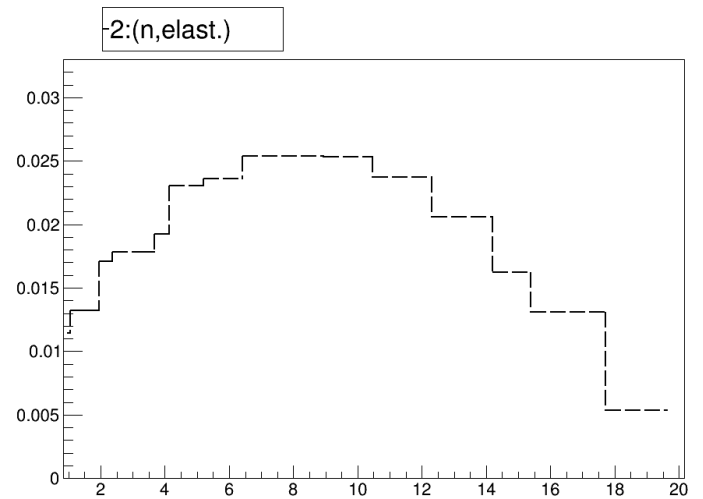
(b) STD of the uncertain scattering reactions.

Figure 31: Standard Deviation (STD in %) of the cross sections associated with the absorption and scattering reactions of the isotopes ^{1}H in function of the 18 energy groups of the 19G-mesh which are above 1 MeV.
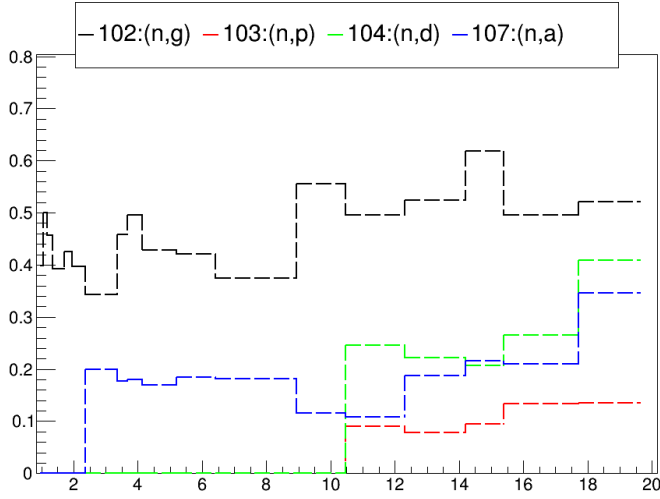
(a) STD of the uncertain absorption reactions.
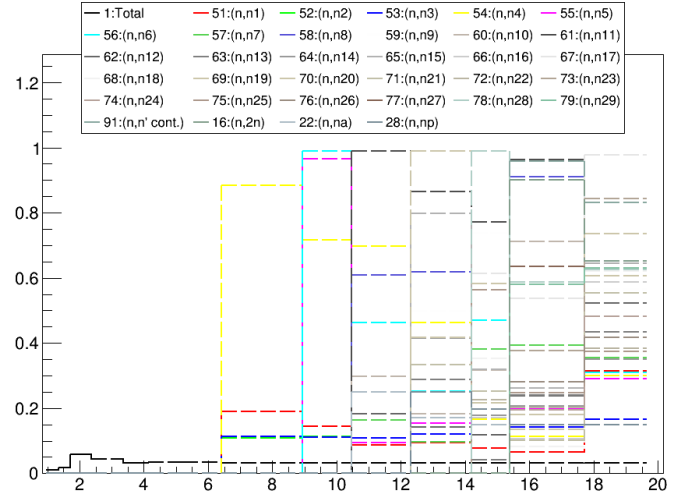
(b) STD of the uncertain scattering reactions.

Figure 32: Standard Deviation (STD in %) of the cross sections associated with the absorption and scattering reactions of the isotopes ^{16}O in function of the 18 energy groups of the 19G-mesh which are above 1 MeV.

C   Estimation of the linear model for a large number of variables

Let us reconsider the statistical design with p observations of the n input variables X and of the corresponding output response Y. The *Ordinary Least Square* method presented in Chapter II Section 2, allowed to estimate the linear regression on the output Y:

$$\mathbb{E}(Y|x_1, ..., x_n) = \beta_0 + \mathbf{x}_k\boldsymbol{\beta} \text{ and } Var(Y) = \sigma^2. \tag{47}$$

If σ^2 is known, it can be shown that:

$$\frac{\|Y - X\hat{\boldsymbol{\beta}}\|_2^2}{\sigma^2} \sim \chi_n^2, \tag{48}$$

where χ_n^2 defines the chi-square distribution and thus,

$$\mathbb{E}(\|Y - X\hat{\boldsymbol{\beta}}\|_2^2) = n\sigma^2. \tag{49}$$

When σ^2 is unknown, the variance can be estimated by:

$$\hat{\sigma}^2 = \frac{\|Y - X\hat{\boldsymbol{\beta}}\|_2^2}{p}, \tag{50}$$

And, it can be similarly shown for $p - n$ large that,

$$\mathbb{E}(\|Y - X\hat{\boldsymbol{\beta}}\|_2^2) \simeq n\hat{\sigma}^2. \tag{51}$$

The confidence domain containing the real value β is thus proportional to the number of parameters n to estimate.

D Comparison of the cross-section uncertainties for the ^{56}Fe, ^{16}O and ^{1}H isotopes and for various nuclear evaluation libraries

The inelastic and elastic cross sections of ^{56}Fe
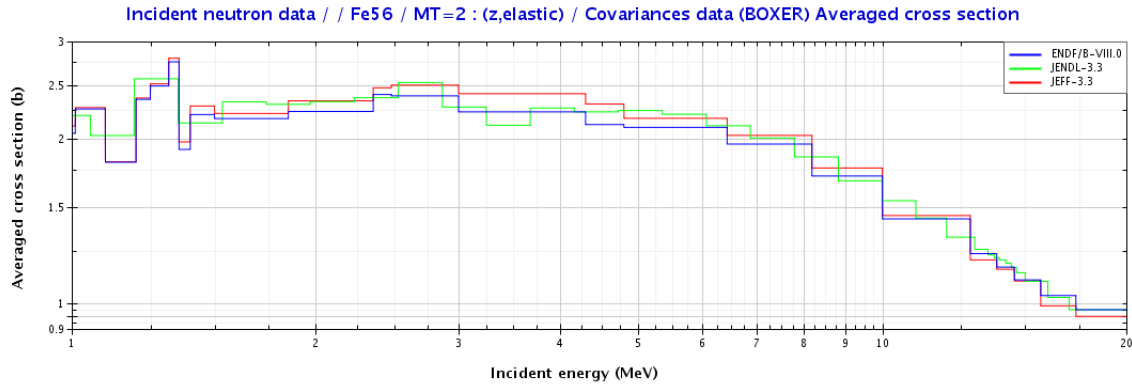
Figure 33: Multigroup cross section of the elastic cross section for the isotope ^{56}Fe
Evaluation from JANIS Books
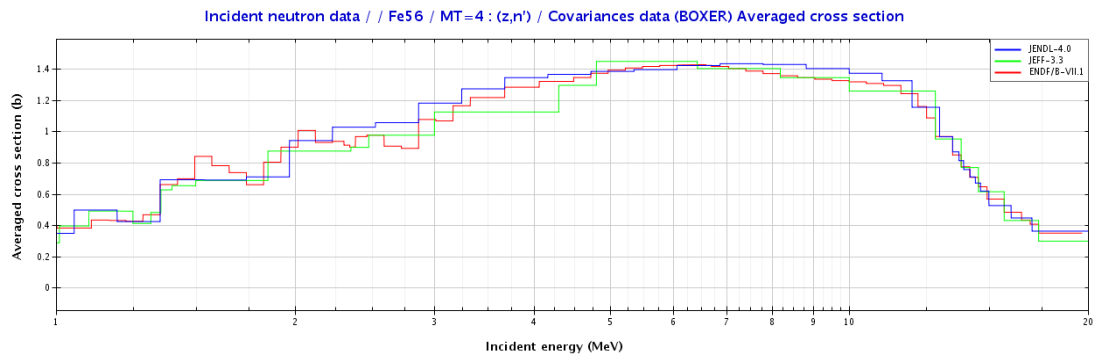
Figure 34: Multigroup cross section of the inelastic cross section for the isotope ^{56}Fe
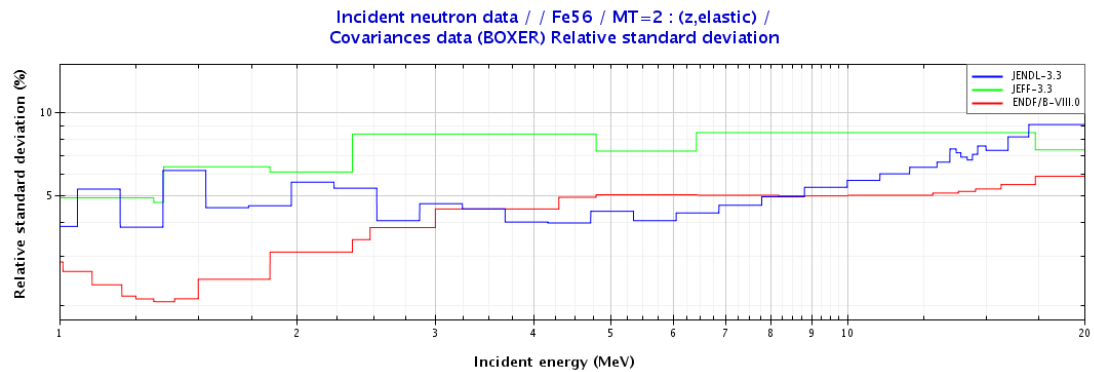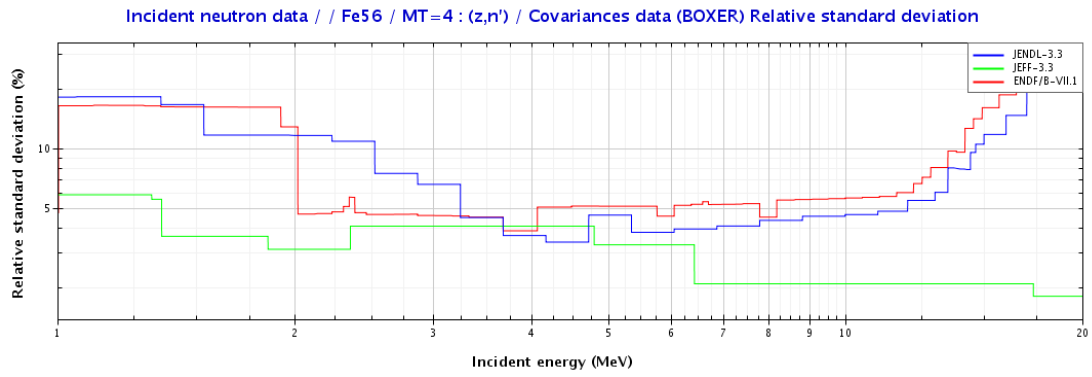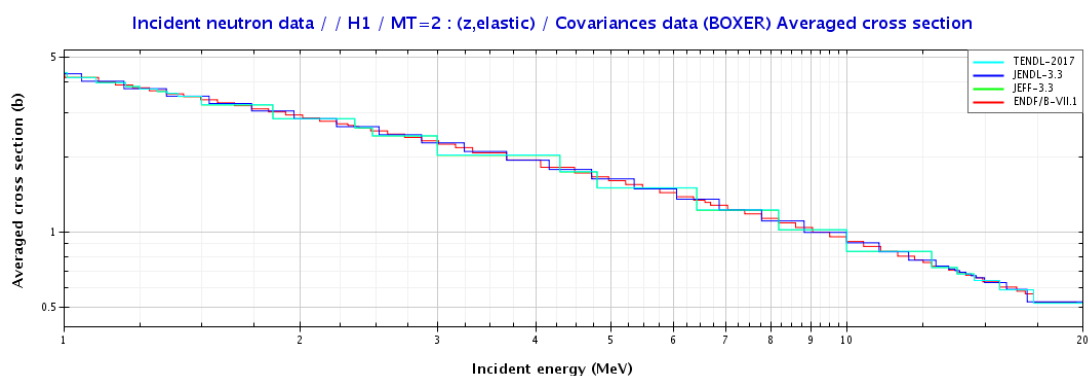Evaluation from JANIS Books

Figure 35: Relative standard deviation of the elastic cross section for the isotope ^{56}Fe
Evaluation from JANIS Books

Figure 36: Relative standard deviation of the inelastic cross section for the isotope ^{56}Fe
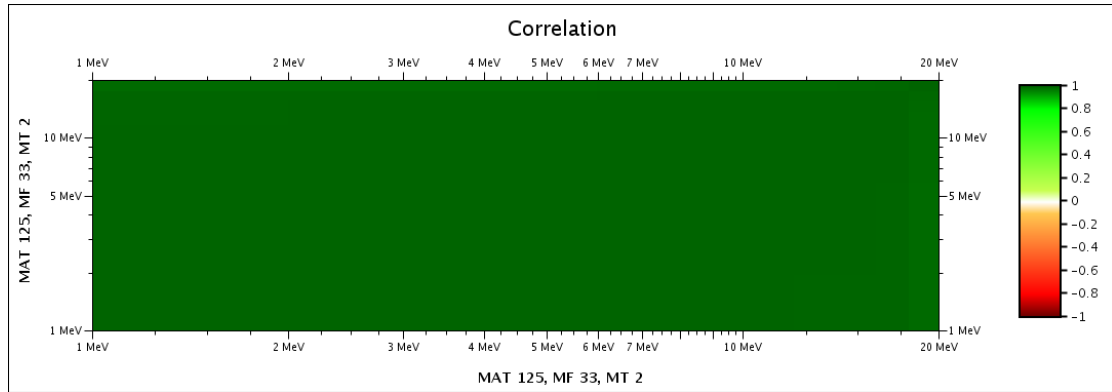Evaluation from JANIS Books
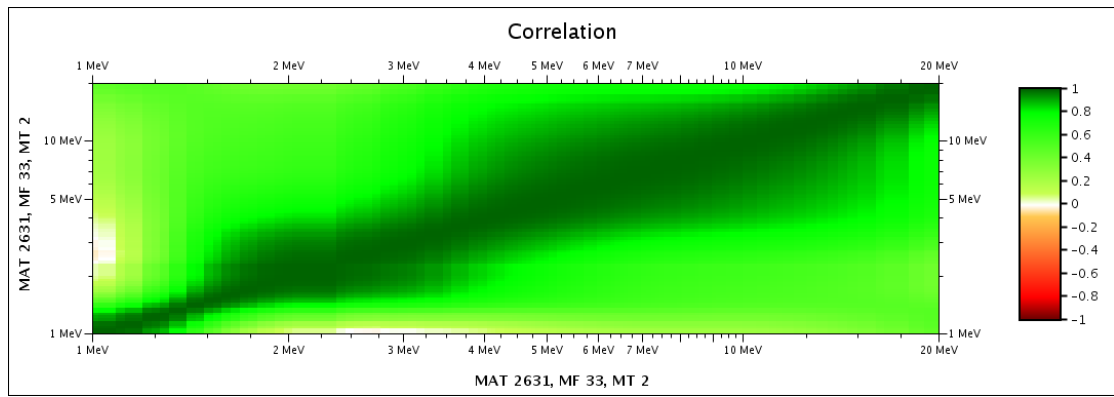
Figure 37: Correlation data of the elastic cross section for the isotope ^{56}Fe from the
ENDFB-7.0 library
Evaluation from JANIS Books
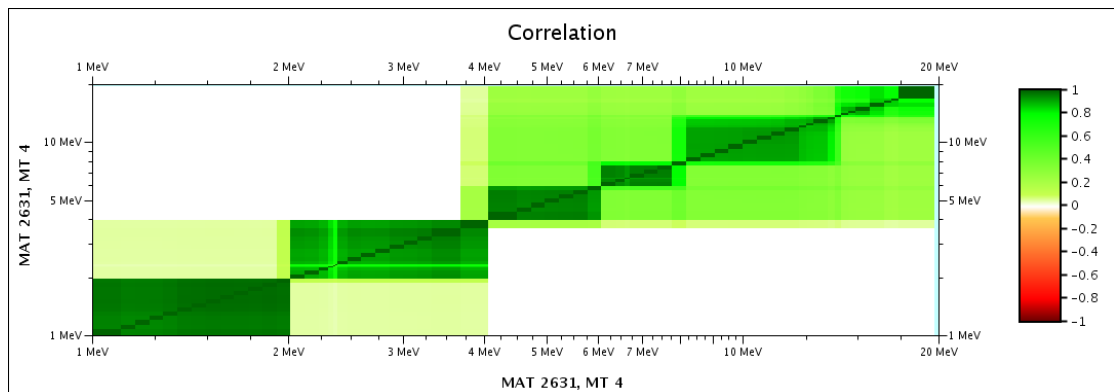
Figure 38: Correlation data of the inelastic cross section for the isotope ^{56}Fe from the
ENDFB-7.0 library
Evaluation from JANIS Books
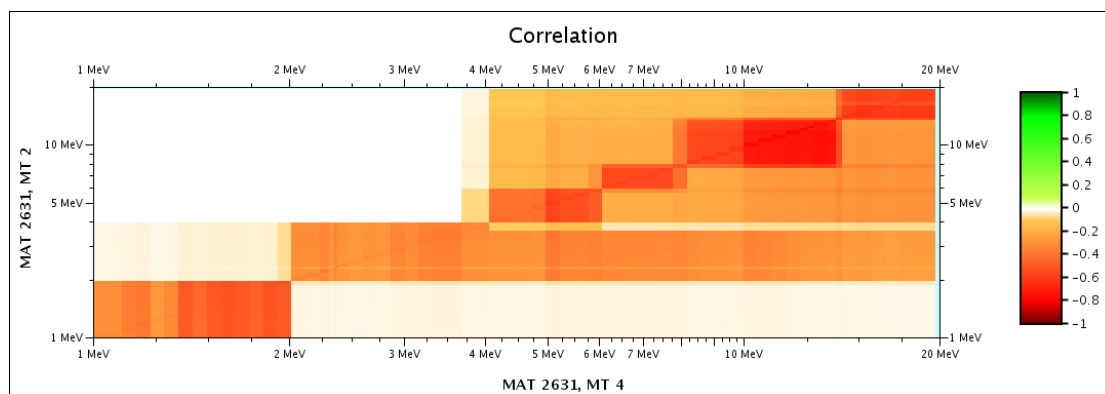
Figure 39: Correlation data between the elastic and inelastic cross sections for the isotope ^{56}Fe from the ENDFB-7.0 library
Evaluation from JANIS Books

The elastic cross section of ^{1}H

Figure 40: Multigroup cross section of the elastic cross section for the isotope ^{1}H
Evaluation from JANIS Books
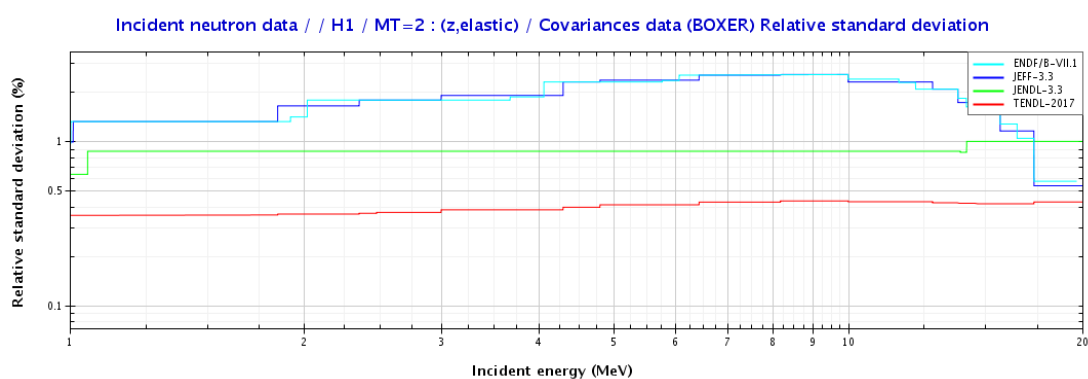
Figure 41: Relative standard deviation of the elastic cross section for the isotope ^{1}H
Evaluation from JANIS Books

Figure 42: Correlation data of the elastic cross section for the isotope ^{1}H from the ENDFB-7.0
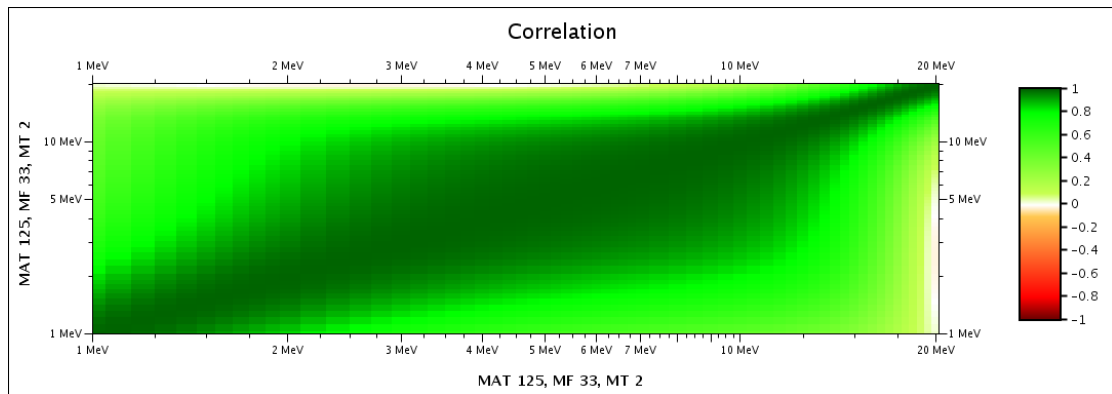library
Evaluation from JANIS Books

Figure 43: Correlation data of the elastic cross section for the isotope ^{1}H from the
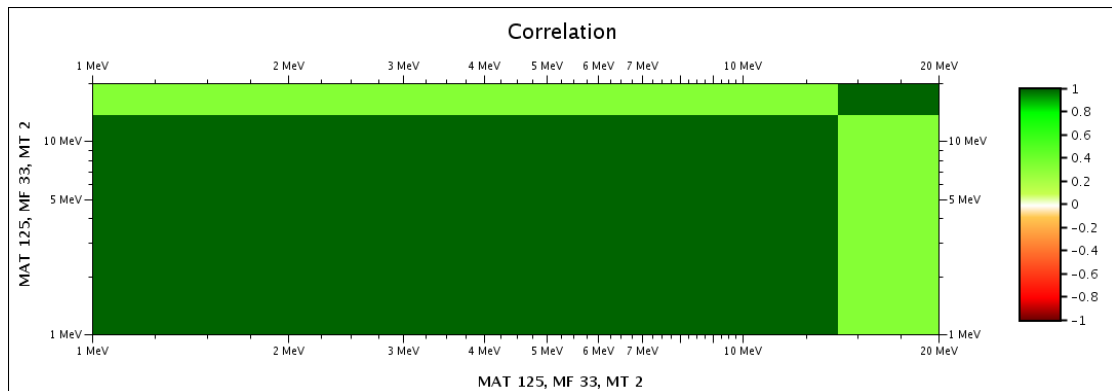TENDL-2017 library
Evaluation from JANIS Books

Figure 44: Correlation data of the elastic cross section for the isotope ^{1}H from the JENDL-3.3
library
Evaluation from JANIS Books
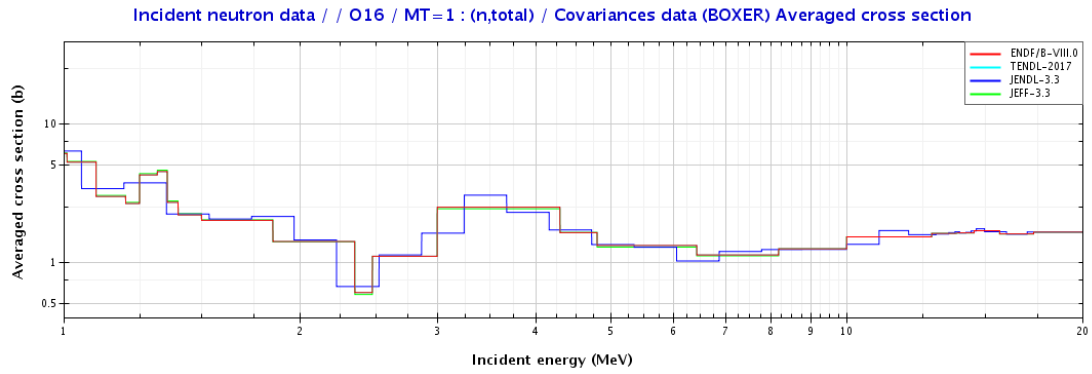
149

The total cross section of ^{16}O

Figure 45: Multigroup cross section of the total cross section for the isotope ^{16}O
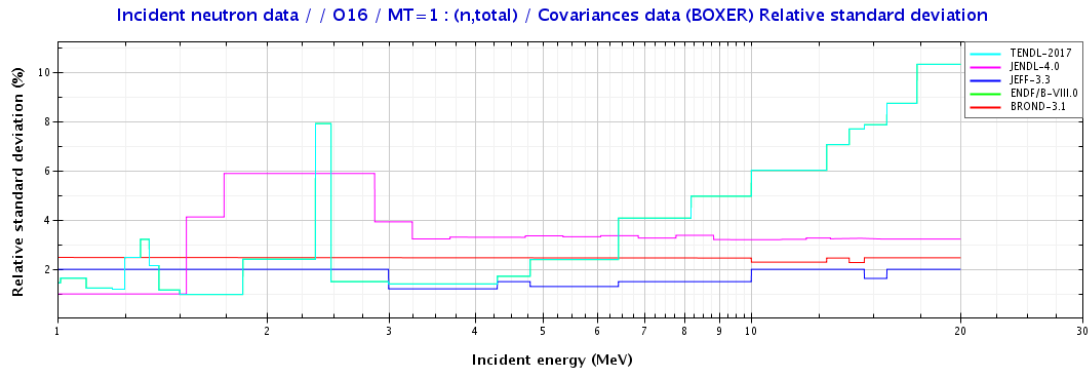Evaluation from JANIS Books

Figure 46: Relative standard deviation of the total cross section for the isotope ^{16}O
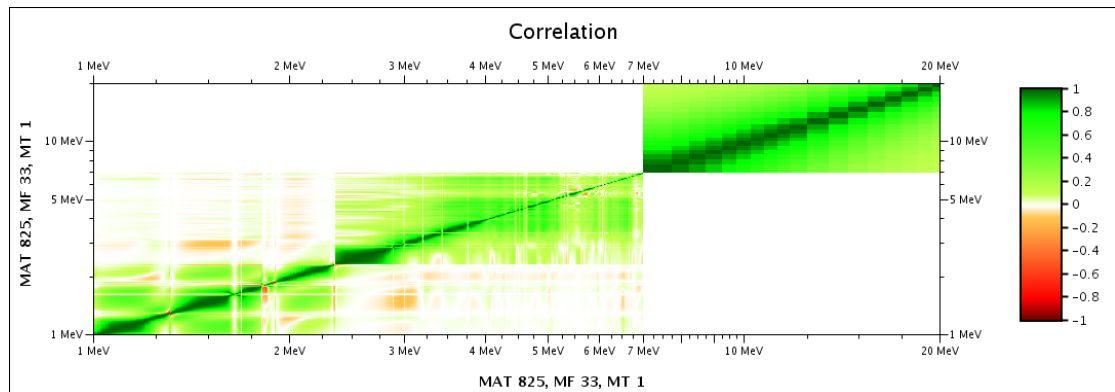Evaluation from JANIS Books

Figure 47: Correlation data of the total cross section for the isotope ^{16}O from the ENDFB-7.0
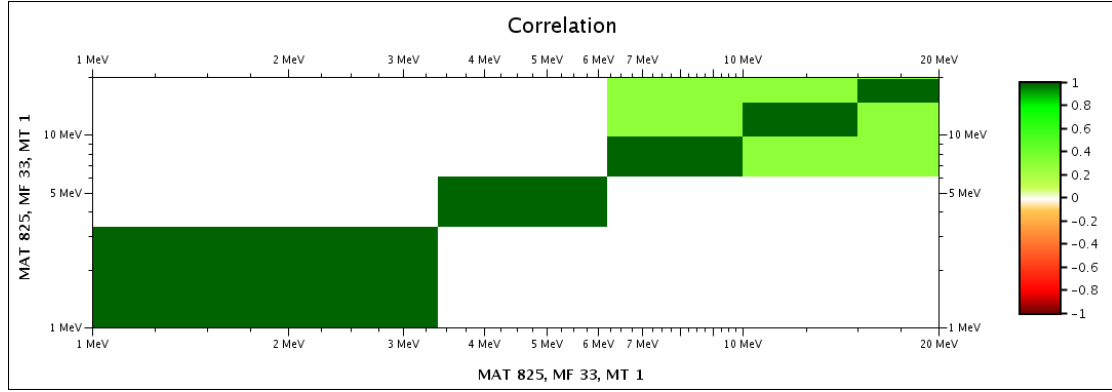library
Evaluation from JANIS Books

Figure 48: Correlation data of the total cross section for the isotope ^{16}O from the JEFF-3.3 library
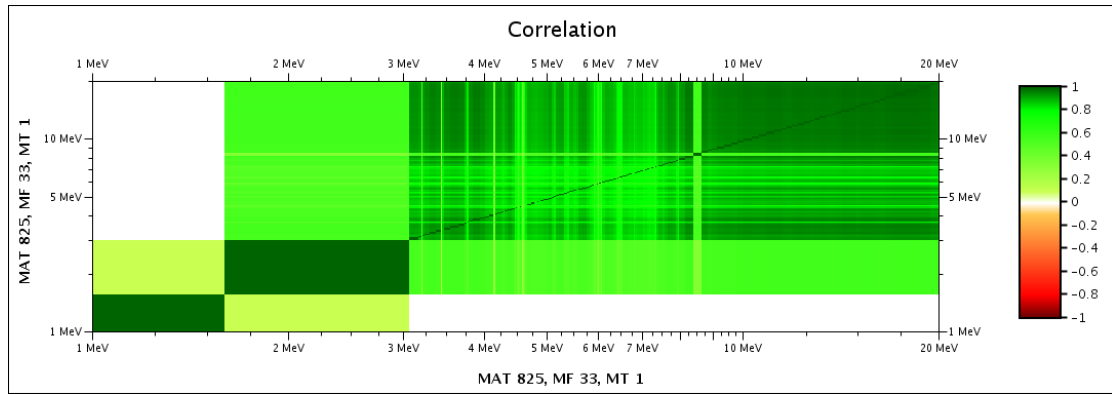Evaluation from JANIS Books

Figure 49: Correlation data of the elastic cross section for the isotope ^{16}O from the JENDL-3.3 library
Evaluation from JANIS Books

E Johnson indices of the fast flux in function of the cross sections for the absorption and scattering reactions

Johnson

Figure 50: Johnson Indices on the fast flux at the Capsule 20˚and associated with the multigroup scattering and absorption cross sections of various isotopes

Johnson

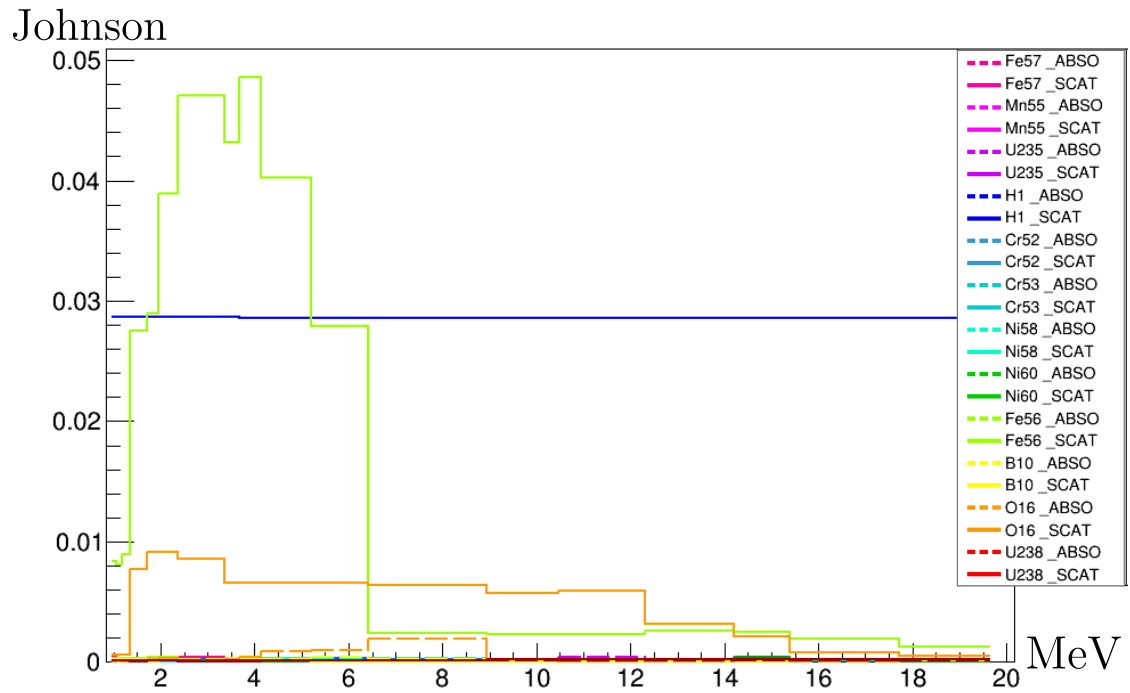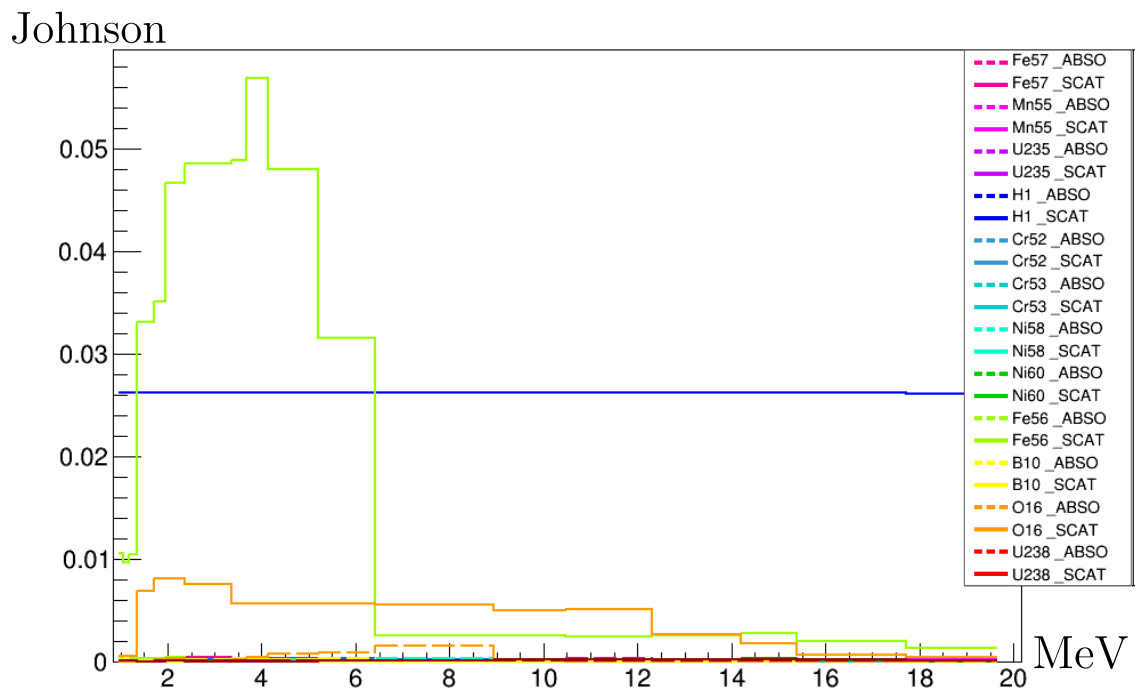Figure 51: Johnson Indices on the fast flux at the Capsule 17˚and associated with the multigroup scattering and absorption cross sections of various isotopes

F   Covariances available in the File 34 of the international libraries

Isotope	JEFF311	JEFF312	JEFF32T3	ENDFB7R1	JENDL40	TENDL12
O16					2	
U238					2	
U235					2	
He4						
Zr90			2			2
Zr91						2
Zr92			2			2
Zr94			2			2
Zr96						2
Fe56	2	2	2	2	2	2
Fe57						2
Fe58						2
Fe59						2
Cr50						2
Cr52	2	2				2
Cr53						2
Cr54						2
Ni58	2	2	2		2	2
Ni60	2	2	2		2	2
Ni61						2
Ni62						2
Ni64						2
Mn55				2 51 2 51		2
Si28						2
Si29						2
Si30						2
H1						
B10						
B11						

G Consistency rules on the cross sections

In this annexe, the strategy for all the isotopes are presented. Four sections by isotopes is potentially given:

- $NI - Type$: The first describes the covariances provided by the files considered which correspond to the NI sections of the ENDF formulation.

- $NC - Type$: The second gives the relations $\sigma_{MT}(E) = \sum_{i=1}^{NCI} C_i * \sigma_{MT_i}(E)$ among reactions, described by the NC sections of the ENDF files, and by pairs of values C_I, MT_I,

- $NCa - Type$ The third provides the missing relations to ensure the consistency of the file 3 perturbations and according to the neutron balance used by APOLLO3,

- $NCm - Type$ The fourth is given only if the ENDF file is not consistent with the neutron balance used by APOLLO3 and provides the calculation used to determine redundant reactions.

The aim is to ensure the consistency rules defined by the ENDF format:
$$\sigma_{1-TOTAL} = \sigma_{2-ELAS} + \sigma_{4-INELAS} + \sigma_5 + \sigma_{NEXCESS} + \sigma_{18-FISSION} + \sigma_{101-DISAPP}$$

$$\sigma_{4-INELAS} = \sigma_{50-91}$$
$$\sigma_{18-FISSION} = \sigma_{19} + \sigma_{21-91}$$
$$\sigma_{NEXCESS} = \sigma_{11} + \sigma_{16} + \sigma_{17} + \sigma_{22-30} + \sigma_{32-37} + \sigma_{41-42} + \sigma_{44-45}$$
$$\sigma_{101-DISAPP} = \sigma_{102-117}$$
$$\sigma_{103-z,p} = \sigma_{600-649}$$
$$\sigma_{104-z,d} = \sigma_{650-699}$$
$$\sigma_{105-z,t} = \sigma_{700-749}$$
$$\sigma_{106-z,He} = \sigma_{750-799}$$
$$\sigma_{107-z,\alpha} = \sigma_{800-849}$$
σ_5 is the sum of all reactions not given explicitly in another MT number.

^{56}Fe-JEFF32T3

MeV

	9.5e+5	2.0e+7
NI: Covariances	MT:	2; 4; 16; 22; 28; 102-107
NC: "Derived" cross sections	MT: MT_i: C_i:	1 2; 4; 16; 22; 28; 102-107 1; ...; 1
NCa: "Derived" cross sections (added to ensure consistency)	$\forall MT \in \{51\text{-}82\}$ $f_{MT} = f_{(MT_i=4)}$	

^{1}H-ENDFB7R1

MeV

9.5e+5 → 2.0e+7

NI: Covariances	MT: 2; 102
NC: "Derived" cross sections	MT: 1 MT_i: 2; 102 C_i: 1; 1

^{16}O-JENDL40

MeV

9.5e+5 → 2.0e+7

NI: Covariances	MT: 2; 16; 22; 28; 51-79; 91; 102-104; 107
NC: "Derived" cross sections	MT: 2 MT_i: 1; 16; 22; 28; 51-79; 91; 102-104; 107 C_i: 1; -1; ...; -1 - - - - - - - - - - - - MT: 4 MT_i: 51-79; 91 C_i: 1; ...; -1

^{10}B-JENDL40

MeV

9.5e+5 — 1.2e+6 — 2.0e+7

NI: Covariances	MT: 2; 102; 800; 801	MT: 1; 102; 800; 801
NC: "Derived" cross sections	MT: 1 MT_i: 2; 102; 800; 801 C_i: 1; 1; 1; 1	MT: 2 MT_i: 1; 102; 800; 801 C_i: 1; -1; -1; -1
	MT: 107 MT_i: 800; 801 C_i: 1; 1	

^{50}Cr-JEFF32T3

		MeV
9.5e+5		2.0e+7

NI: Covariances	*MT*: Correlated reactions	1; 2; 51-70; 102 {1, 2, 51, 52, 53, 54, 102}
NC: "Derived" cross sections	*MT*: *MT$_i$*: *C$_i$*:	5 1; 2; 4; 102 1; -1; ...; -1
NCa: "Derived" cross sections (added to ensure consistency)	*MT*: *MT$_i$*: *C$_i$*:	4 51-70 1; ...; 1

^{52}Cr-JEFF32T3

		MeV
9.5e+5		2.0e+7

NI: Covariances	*MT*:	1; 2; 4; 16; 22; 28; 51-70; 102-107
NC: "Derived" cross sections	*MT*: *MT$_i$*: *C$_i$*:	91 4; 51-70 1; -1; ...; -1
NCa: "Derived" cross sections (added to ensure consistency)	*MT*: *MT$_i$*: *C$_i$*:	1 2; 4; 16; 22; 28; 102-107 1; ...; 1

^{53}Cr-JEFF32T3

		MeV
9.5e+5		2.0e+7

NI: Covariances	*MT*: Correlated reactions	1; 2; 51-70; 102 {1, 2, 102}
NC: "Derived" cross sections	*MT*: *MT$_i$*: *C$_i$*:	5 1; 2; 4; 102 1; -1; ...; -1
NCa: "Derived" cross sections (added to ensure consistency)	*MT*: *MT$_i$*: *C$_i$*:	4 51-70 1; ...; 1

^{54}Cr-JEFF32T3

MeV

9.5e+5   2.0e+7

NI: Covariances	MT: Correlated reactions	1; 2; 51-70; 102 {1, 2, 51, 52, 53, 102}
NC: "Derived" cross sections	MT: MT_i: C_i:	5 1; 2; 4; 102 1; -1; ...; -1
NCa: "Derived" cross sections (added to ensure consistency)	MT: MT_i: C_i:	4 51-70 1; ...; 1

^{54}Fe-ENFB7R1

MeV

9.5e+5   1.4343e+6   2.0e+7

NI: Covariances	MT:	1; 16; 22; 28; 51-57; 91; 102-104; 107
NCm: "Derived" cross cross sections (modify to ensure consistency)	MT: 2 MT_i: 1; 16; 22; 28; 102-104; 107 C_i: 1; -1; ...; -1	MT: 2 MT_i: 1; 4; 16; 22; 28; 102-104; 107; 112 C_i: 1; -1; ...; -1 --- MT: 4 MT_i: 51-57; 91 C_i:

^{57}Fe-ENDFB7R1

MeV

9.5e+5   2.0e+7

NI: Covariances	MT:	1; 16; 22; 28; 51-55; 91; 102; 107
NC: "Derived" cross sections	MT: MT_i: C_i:	2 1; 4; 16; 22; 28; 102; 107 1; -1; ...; -1
	MT: MT_i: C_i:	4 51-55; 91 1; 1; 1

^{58}Fe-JEFF32T3

MeV

9.5e+5   2.0e+7

NI: Covariances	MT:	1; 16; 22; 51-52; 91; 102
NC: "Derived" cross sections	MT: MT_i: C_i:	2 1; 4; 16; 22; 102 1; -1; ...; -1
	MT: MT_i: C_i:	4 51-52; 91 1; 1; 1

^{55}Mn-ENDFB7R1

MeV

9.5e+5   2.0e+7

NI: Covariances	MT:	2; 16; 17; 51; 102
NC: "Derived" cross sections	MT: MT_i: C_i:	2 1; 16; 17; 51; 102 1; -1; ...; -1
	MT: MT_i: C_i:	4 51 1

^{58}Ni-JEFF32T3

MeV

9.5e+5   1.4753e+6   2.0e+7

NI: Covariances	MT:	1; 16; 22; 28; 51-53; 91; 102-107; 112
	Correlated reactions	$\{1, 16, 22, 28, 51 - 53, 91, 102 - 107, 112\}$

| NCm: "Derived" cross sections (modify to ensure consistency) | MT:
MT_i:

C_i: | 2
1; 16; 22; 28;
102-107; 112
1; -1; ...; -1 | MT:
MT_i:
C_i: | 2
1; 4; 16; 22; 28; 102-107; 112
1; -1; ...; -1 |
| | | | MT:
MT_i:
C_i: | 4
51-53; 91
1; ...; 1 |

158

^{60}Ni-JEFF32T3

MeV

9.5e+5   1.4753e+6   2.0e+7

| NI: Covariances | MT: | 1; 16; 22; 28; 51; 91; 102-107 |
| | Correlated reactions | $\{1, 16, 22, 28, 51, 91, 102 - 107\}$ |

| NCm: "Derived" cross sections (modify to ensure consistency) | MT: 2 MT_i: 1; 16; 28; 102-107 C_i: 1; -1; ...; -1 | MT: 2 MT_i: 1; 4; 16; 28; 102-107 C_i: 1; -1; ...; -1 |
| | | MT: 4 MT_i: 51; 91 C_i: 1; ...; 1 |

^{61}Ni-JEFF32T3

MeV

9.5e+5   6.8109e+6   2.0e+7

| NI: Covariances | MT: 1; 16; 28; 51-58; 91; 102; 103; 107 |

| NCm: "Derived" cross sections (modify to ensure consistency) | MT: 2 MT_i: 1; 16; 28; 102; 103; 107 C_i: 1; -1; ...; -1 | MT: 2 MT_i: 1; 4; 16; 28; 102; 103; 107 C_i: 1; -1; ...; -1 |
| | | MT: 4 MT_i: 51-58; 91 C_i: 1; ...; 1 |

^{62}Ni-JEFF32T3

MeV

9.5e+5   1.1921e+6   2.0e+7

| NI: Covariances | MT: 1; 16; 22; 28; 51-54; 91; 102-104; 107 |

| NCm: "Derived" cross sections (modify to ensure consistency) | MT: 2 MT_i: 1; 16; 22; 28; 102-104; 107 C_i: 1; -1; ...; -1 | MT: 2 MT_i: 1; 4; 16; 22; 28; 102-104; 107 C_i: 1; -1; ...; -1 |
| | | MT: 4 MT_i: 51-54; 91 C_i: 1; 1; 1; 1; 1 |

159

^{64}Ni-JEFF32T3

	9.5e+5	1.3672e+6		*MeV* 2.0e+7
NI: Covariances		*MT*: 1; 16; 28; 51; 52; 91; 102-104; 107		

NCm: "Derived" cross sections (modify to ensure consistency)	*MT*: 2 *MT$_i$*: 1; 16; 28; 51; 52 91; 102-104; 107 *C$_i$*: 1; -1; ...; -1	*MT*: 2 *MT$_i$*: 1; 4; 16; 28; 102-104; 107 *C$_i$*: 1; -1; ...; -1 *MT*: 4 *MT$_i$*: 51; 52; 91 *C$_i$*: 1; 1; 1

^{235}U-ENDFB7R1

	9.5e+5		*MeV* 2.0e+7
NI: Covariances	*MT*: Correlated reactions	1; 4; 16; 17; 18; 102 {1, 2, 18, 102}	
NCa: "Derived" cross sections (added to ensure consistency)	*MT*: *MT$_i$*: *C$_i$*:	2 1; 4; 16; 17; 18; 102 1; -1; -1; -1; -1; -1	

^{238}U-ENDFB7R1

	9.5e+5		*MeV* 2.0e+7
NI: Covariances	*MT*: Correlated reactions	1; 2; 4; 16; 18; 102 {1, 2, 4, 16, 18, 102}	
NCa: "Derived" cross sections (added to ensure consistency)	*MT*: *MT$_i$*: *C$_i$*:	1 2; 4; 16; 18; 102 1; -1; -1; -1; -1; -1	

^{90}Zr-ENDFB7R1

		MeV
	9.5e+5	2.0e+7
NI: Covariances	*MT*:	2; 4; 16; 102
NC: "Derived" cross sections	*MT*: MT_i: C_i:	1 2; 4; 16; 102 1; 1; 1; 1

^{91}Zr-ENDFB7R1

		MeV
	9.5e+5	2.0e+7
NI: Covariances	*MT*:	2; 4; 16; 102
NC: "Derived" cross sections	*MT*: MT_i: C_i:	1 2; 4; 16; 102 1; 1; 1; 1

^{92}Zr-ENDFB7R1

		MeV
	9.5e+5	2.0e+7
NI: Covariances	*MT*:	2; 4; 16; 102
NC: "Derived" cross sections	*MT*: MT_i: C_i:	1 2; 4; 16; 102 1; 1; 1; 1

^{94}Zr-ENDFB7R1

		MeV
	9.5e+5	2.0e+7
NI: Covariances	*MT*:	2; 4; 16; 102
NCa: "Derived" cross sections (added to ensure consistency)	*MT*: MT_i: C_i:	1 2; 4; 16; 102 1; 1; 1; 1

⁹⁶**Zr-ENDFB7R1**

MeV

9.5e+5   2.0e+7

NI: Covariances	MT:	2; 4; 16; 102
NC: "Derived" cross sections	MT: MT_i: C_i:	1 2; 4; 16; 102 1; 1; 1; 1

Résumé en Français

Dans les réacteurs à eau pressurisée (REP), un certain nombre de matériaux aux propriétés réflectrices permettent de réduire les fuites de neutrons produits par le cœur. Malgré la présence de ces éléments réflecteurs, certains neutrons parviennent à atteindre la cuve du réacteur. Or, une irradiation intense peut fragiliser cette dernière en altérant ses propriétés mécaniques, et ainsi limiter la durée de vie du réacteur. La cuve, qui constitue un élément irremplaçable du réacteur, est en effet la deuxième barrière de confinement des produits radioactifs. Pour s'assurer de la sûreté des réacteurs et de l'intégrité des cuves, des programmes de surveillance sont donc mis en place. Ces derniers dépendent notamment des mesures et des calculs de la fluence qui quantifie le nombre de neutrons rapides (d'énergies supérieures à 1 MeV) reçus par des capsules de surveillance pendant toute la durée de l'irradiation. La détermination de la fluence est notamment basée sur 3 données : le spectre de neutrons rapides, l'historique d'irradiation et les sections efficaces de dosimétrie. Sachant que les capsules sont placées entre le cœur et la cuve, il est ensuite possible de prédire le flux neutronique reçu par la cuve, et d'anticiper son vieillissement. La qualité de cette prédiction dépend en partie du calcul de densité neutronique. Un manque de connaissance sur ce calcul peut, en effet, obliger l'exploitant à fixer des marges de sûreté supérieures sur la durée de vie des centrales, et donc affecter les conditions de fonctionnement et le coût des installations nucléaires. C'est pourquoi il est essentiel de déterminer l'incertitude du calcul de flux à la cuve des REP.

La plupart des études passées sont basées sur une quantification de l'incertitude par la méthode des moments qui suppose une variation linéaire de la sortie du calcul. Cette hypothèse n'a jamais été vérifiée compte tenu du grand nombre de variables d'entrée et des ressources informatiques relativement limitées pour envisager l'application d'autres méthodes. Une méthode alternative est celle de l'approche Total Monte Carlo (TMC) qui consiste à considérer les paramètres d'entrées du modèle de calcul comme des variables aléatoires, et à propager les perturbations issues d'un tirage statistique dans la chaine de calcul. La sortie résultante est alors considérée elle aussi comme une variable aléatoire dont on peut estimer la distribution de probabilité. L'avantage de cette méthode est qu'elle propose une description plus précise des incertitudes du modèle, et permet de définir des quantiles et donc des intervalles de confiance qui peuvent s'avérer utiles dans le cadre d'une étude de sûreté.

C'est dans ce contexte, que cette thèse s'intègre. Elle consiste à déterminer l'incertitude du flux neutronique rapide de la cuve des REP en considérant les librairies de données nucléaires récentes et en utilisant une approche TMC pour la propagation des incertitudes d'entrées. Dans ce travail, seules les incertitudes d'entrée qui sont modélisables statistiquement, i.e. les incertitudes de modélisation ou de données nucléaires, sont considérées. La particularité de ce travail repose sur le grand nombre de paramètres d'entrées corrélés. En effet, dans les applications de neutroniques, les données d'entrées tendent à être corrélées du fait de la succession de modèles physiques utilisés pour reconstruire les données d'intérêt à partir de la mesure de quantités observables. La prise en compte de ces données de corrélations et la grande dimension de l'espace des paramètres d'entrées nécessitent ainsi la mise en place de méthodologies adaptées qui seront décrites dans cette thèse.

La thèse se divise en deux parties. La première partie constituait de deux chapitres fournit un état de l'art des méthodes et de la théorie nécessaires pour réaliser une analyse d'incertitude de calcul neutronique. Le premier chapitre (Chapitre 1) décrit le principe d'interactions et de transport des neutrons, ainsi que les méthodes de résolution de l'équation du transport utilisées dans ce travail. Une section de ce chapitre est également dédiée aux évaluations des données nucléaires et à l'origine de leurs incertitudes. Le deuxième chapitre (Chapitre 2) se concentre sur les méthodologies de quantification d'incertitude et de sensibilités.

La deuxième partie présente les méthodes et les résultats de la thèse, en trois chapitres. Ces derniers décrivent les différentes étapes de l'approche TMC adoptée: la spécification du calcul de flux neutronique (Chapitre 3), la modélisation, le tirage et la propagation des incertitudes

(Chapitre 4), et l'analyse de sensibilité des paramètres d'entrée (Chapitre 5).
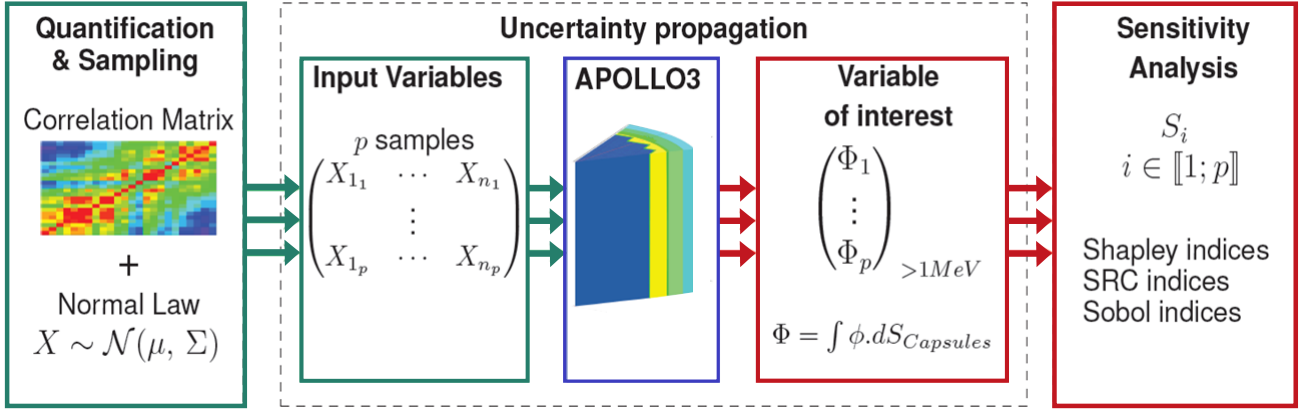

Figure 52: Uncertainty propagation scheme by TMC approach

Le Chapitre 3 décrit le calcul mis en place dans la thèse pour déterminer le flux de neutrons d'énergie supérieur à 1 MeV reçu par la cuve. En France, les calculs de référence de fluence sont généralement basés sur l'utilisation de codes stochastiques de transport neutronique (par exemple TRIPOLI-4). Le problème est que les calculs de quantification d'incertitude par approche TMC, nécessitent un grand nombre d'itérations de calcul pour une estimation correcte de l'incertitude de sortie. Les calculs stochastiques sont donc trop coûteux pour être envisagés dans ce travail. Par comparaison, les calculs déterministes sont plus rapides, et permettent de déterminer le flux dans n'importe quelle partie du réacteur et dans différents groupes énergétiques en un seul calcul. L'objectif de ce chapitre est donc de définir un schéma de calcul déterministe suffisamment rapide pour une approche TMC, et relativement précis vis-à-vis du calcul stochastique de référence. Ce calcul a été réalisé en deux étapes. Une bibliothèque multiparamétrée de sections efficaces auto-protégées a d'abord été générée simultanément par : une homogénéisation spatiale sur une traverse 1D représentative des matériaux du cœur à la cuve, et une condensation énergétique sur un maillage optimisé à 19 groupes (dont 18 au-dessus de 1 MeV) par l'optimisateur AEMC.

Le calcul final du flux est ensuite réalisé par le solveur SN MINARET sur une configuration 3D de REP, et avec une approximation P3 pour les sections efficaces de scattering, et un ordre angulaire S8. Ce schéma nous permet de calculer en moins de 20 min, le flux reçu par l'ensemble du réacteur et avec une précision à 1% vis-à-vis du calcul de référence TRIPOLI-4. À ce stade de l'étude, nous supposons que le biais entre ces deux calculs restera relativement constant vis-à-vis des perturbations introduites dans l'approche TMC, et donc que la variabilité du flux de sortie du calcul déterministe sera représentative de celle du calcul de référence.

Le Chapitre 4 introduit ensuite la méthodologie adoptée pour la modélisation, la quantification, le tirage aléatoire et la propagation des incertitudes des paramètres d'entrée. En particulier, les méthodes utilisées pour assurer la consistance des données sont présentées. Les distributions de probabilité sont définies par principe de maximum entropie, et les corrélations, quand elles existent, sont adaptées au calcul déterministe. La décomposition Cholesky permet de générer des perturbations en cohérence avec les corrélations en se ramenant à un problème de paramètres indépendants. Ces derniers sont par ailleurs tirés via un MaxiMin Latin Hypercube Sampling qui assure une bonne représentativité du domaine de variation pour un nombre réduit d'échantillons.

Due aux grands nombres de paramètres d'entrée, une stratégie itérative est employée pour la propagation des incertitudes. 5 plans d'expériences sont générés indépendamment en considérant le jeu de variables suivantes : les paramètres technologiques (distribution de puissance,

tolérance de fabrication, température de l'eau dans le circuit primaire, impuretés), le spectre de fission, la distribution spatiale de la puissance, les sections efficaces et la distribution angulaire des sections efficaces. Ces 5 plans d'expériences vont permettre de déterminer les variables qui contribuent le plus à l'incertitude sur le flux rapide. Un plan d'expérience final sera utilisé pour propager les incertitudes de l'ensemble des variables résultantes dans la chaine de calcul.

La source neutronique est en particulier perturbée par proportionnalité avec la distribution de puissance et le spectre de fission des neutrons prompts. Les incertitudes de la distribution spatiale de puissance sont définies à partir de corrélations représentatives des mesures de puissance, et un écart-type allant de 1 à 4% selon la position de l'assemblage. Les facteurs de perturbations résultant du tirage statistique sont ensuite propagés moyennant chaque assemblage. Par ailleurs, les covariances utilisées pour la modélisation des incertitudes du spectre de fission sont issues du travail de Berge, L. et basées sur le modèle de Madland-Nix communément utilisé par les bibliothèques de données nucléaires.

Pour perturber les sections efficaces multigroupes, une chaine de calcul est implémentée en couplant le système de traitement GALILEE-1, le code NJOY et la plateforme URANIE. Au total, 343 matrices de covariances (associées aux réactions totales et partielles de 25 isotopes et de 18 énergies groupes) sont reconstruites notamment grâce au module ERRORR d'NJOY et en cohérence avec le maillage énergétique à 19 groupes du calcul de flux, précédemment optimisé. Néanmoins, certaines de ces matrices ressortent mal conditionnées du processus ER-RORR, rendant impossible le tirage statistique par décomposition Cholesky des variables associées. Pour contourner ce problème, une méthode alternative basée sur la décomposition en valeurs singulières est proposée, pour simultanément régulariser ces matrices et tirer aléatoirement les variables aléatoires. De plus, la stratégie employée pour générer des perturbations consistantes entre les réactions partielles et les réactions redondantes est présentée dans ce même chapitre. Les perturbations sont ensuite appliquées sur les sections ponctuelles de 25 isotopes et propagées dans le module de mise en groupe GROUPR d'NJOY. Les perturbations sur les agrégats de réactions utilisées par APOLLO3 sont enfin déterminées.

De nombreux auteurs ont ainsi déterminé les effets des incertitudes liés à la distribution énergétique des sections efficaces. Cependant, l'impact de leur distribution angulaire sur le calcul de flux rapide n'a jamais été évalué. Pour donner une première estimation de sa contribution, nous avons donc considéré la réaction élastique du $Fe56$ qui constitue le principal composant de l'acier des matériaux du réflecteur. La bibliothèque JEFF-3.2 fournit en effet l'information permettant de perturber les ordres de Legendre utilisés pour le calcul de la section de scattering de la réaction élastique du $Fe56$. Les ordres de Legendre sont ainsi perturbés dans notre travail directement dans les fichiers ENDF qui constituent les entrées du traitement de mise en groupe d'NJOY.

Le Chapitre 5 expose pour finir les résultats de la propagation des incertitudes précédemment modélisées. La stratégie itérative, précédemment évoquée, permet de définir 6 analyses de sensibilités associées aux 6 plans d'expériences décrits dans le précédent chapitre. L'objectif de chaque analyse est de déterminer parmi les sous-groupes de variables, les contributions de chaque entrée sur la variance du flux. Les premières sections du chapitre 5 présentent les méthodologies adoptées pour conduire les analyses de sensibilités. L'incertitude finale et la distribution des perturbations du calcul de flux rapide permettent de déterminer un intervalle de confiance autour de la valeur nominale du flux, et de montrer que le flux évolue linéairement en fonction des perturbations des paramètres d'entrée. L'existence d'un modèle de description linéaire des interactions permet de simplifier les méthodes d'analyse de sensibilité. Elle valide, par ailleurs, l'hypothèse de linéarité qui a largement été prise dans les études passées sur le calcul d'incertitude du flux rapide.

Ce résultat nous permet d'introduire le concept de multicolinéarité. Dans un contexte

d'analyse de sensibilité d'un modèle linéaire, ce concept traduit la difficulté à discriminer le pouvoir explicatif de variables corrélées. Les indices SRC², utilisés dans le cadre de variables indépendantes, sont, en effet, mis en défaut en présence de corrélations entre les paramètres d'entrée. Pour prendre en compte l'effet des corrélations dans les analyses de sensibilité, Owen et Iooss ont récemment montré l'intérêt des indices de Shapley, classiquement utilisés en théorie des jeux. Dans le cas linéaire, les indices de Shapley peuvent être déterminés analytiquement. Ils peuvent être calculés à partir des coefficients multiples de déterminations multiples, eux-mêmes liés aux coefficients multiples de corrélations semi-partielles. L'objet des premières sections est ainsi d'illustrer la stratégie adoptée et de présenter ces notions utilisées pour la première fois dans une étude de neutronique. Ce travail montre, par ailleurs, la difficulté d'application des indices de Shapley pour un grand nombre de paramètres d'entrée. Le temps de calcul étant proportionnelle à 2 puissances n paramètres, il devient rapidement impossible de calculer les indices de Shapley. Deux alternatives sont donc envisagées. La première alternative revient à trouver la matrice par bloc la plus proche de la matrice de covariances des paramètres, afin de traiter de manière indépendante chaque sous-bloc de variables corrélées. La deuxième alternative consiste à calculer les indices de Johnson qui ramènent le problème initial à un problème orthogonal. Les résultats de la thèse montrent que les indices de Johnson sont suffisants pour apporter une indication sur les contributions des variables vis-à-vis de la variance de la variable d'intérêt. Quelle que soit la méthode utilisée, on montre dans ce travail, l'intérêt de considérer les données de corrélation. Il s'agit de préserver la consistance des données perturbées, et d'interpréter leurs influences en termes d'incertitude sur la variable de sortie étudiée.

Dans les dernières sections du Chapitre 5, les 5 analyses de sensibilités sont finalement conduites pour les 5 sous-groupes de paramètres indépendants. Ceci fournit un premier jeu de variables influentes, et un dernier plan d'expériences est considéré pour propager une analyse globale, compte tenu de l'ensemble des paramètres. Les sections efficaces sont les principales sources d'incertitudes. La distribution angulaire de la section efficace élastique du Fe56, et les impuretés dans l'acier ont une influence négligeable sur la variance du flux rapide. L'incertitude de flux rapide est finalement donnée par quantification de l'écart-type sur les perturbations du flux.

Bibliography

Allen, D. M. (1974). The relationship between variable selection and data agumentation and a method for prediction. *Technometrics*, 16(1):125–127.

Archier, P. et al. (2014). CONRAD evaluation code: Development status and perspectives. *Nuclear Data Sheets*, 118:488–490.

Bedford, T. (1998). Sensitivity indices for (tree)-dependant variables. In *Proceedings of the Second International Symposium on Sensitivity Analysis of Model Output (SAMO98)*, pages 17–20.

Bell, G. I. and Glasstone S. (1970). *Nuclear Reactor Theory*. Van Nostrand Reinhold Company, Krieger Pub Co.

Berge, L. (2015). *Contribution à la modélisation des spectres de neutrons prompts de fission - Propagation d'incertitudes sur un calul de fluence cuve*. PhD thesis, Université Grenoble Alpes.

Berge, L. et al. (2015). Study on prompt fission neutron spectra and associated covariances for 235U(nth,f) and 239Pu(nth,f). *Physics Procedia*, 64:55–61.

Bi, J. (2012). A review od statistical methods for determination of relative importance of correlated predictors and identification of drivers of consumer liking. *Journal of Sensory Studies*, 27(2):87–101.

Blanchard, J., Damblin, G., Martinez, J., and G., A. (2019). The Uranie platform : an open source software for optimisation, meta-modelling and uncertainty analysis. *EPJ Nuclear Sciences Technology*, 5(4).

Bourganel, S. et al. (2018). Analysis of the FLUOLE-2 program: UOX/MOX core loading configurations. In *Reactor Dosimetry: 16th International Symposium*. ASTM International.

Bouriquet, B. (2015). Nuclear core activity reconstruction using heterogeneous instruments with data assimilation. *EPJ Nuclear Sciences & Technologies*, 1:18.

Bouriquet, B. et al. (2015). Nuclear core activity reconstruction using heterogeneous instruments with data assimilation. *EPJ Nuclear Sciences & Technologies*, 1:18.

Broto, B., Bachoc, F., Depecker, M., and Martinez, J. (2019). Sensitivity indices for independent groups of variables. *Mathematics and Computers in Simulation*, 163:19–31.

Broto, B. et al. (2018). Sensitivity indices for independent groups of variables. *MascotNum Annual Conference*.

Brun, E. et al. (2014). TRIPOLI-4®, CEA, EDF and areva reference monte carlo code. In *SNA+ MC 2013-Joint International Conference on Supercomputing in Nuclear Applications+ Monte Carlo*, page 06023. EDP Sciences.

Brun, R. and Rademakers, F. (1997). ROOT - an object oriented data analysis framework. *Nuclear Instruments and Methods in Physics Research Section A: Accelerators, Spectrometers, Detectors and Associated Equipment*, 389(1-2):81–86.

Budescu, D. V. and Azen, R. (2003). The dominance analysis approach for comparing predictors in multiple regression. *Psychological methods*, 8(2):129.

Cabellos, O. et al. (2014). Propagation of nuclear data uncertainties for PWR core analysis. *Nuclear Engineering and Technology*, 46(3):299–312.

Castro González, E. (2018). *Methodologies for sensitivity/uncertainty analysis using reactor core simulators with application to pressurized water reactors*. PhD thesis, Universidad Politécnica de Madrid,Industriales.

Castro González, E. et al. (2016). Improving PWR core simulations by monte carlo uncertainty analysis and bayesian inference. *Annals of Nuclear Energy*, 95:148–156.

Chao, Y.-C. et al. (2008). Quantifying the relative importance of predictors in multiple linear regression analyses for public health studies. *Journal of occupational and environmental hygiene*, 5(8):519–529.

Chen, S. (2020). *Maitrise des biais et incertitudes des sections efficaces et de la modélisation de la cinématique associées aux réactions nucléaires conduisant aux dommages dans les matériaux sous irradiation*. PhD thesis, Université Grenoble Alpes.

Cohen, J. and Cohen, P. (2014). *Applied Multiple Regression/Correlation Analysis for the Behavioral Sciences*. Psychology Press.

Coste-Delcaux, M. (1996). Implementation of a sub-group method for self-shielding calculations in APOLLO2 code. *International Conference on the Physics of Reactors, PHYSOR*, 1(3):323–331.

Coste-Delcaux, M. (2006). *Modélisation du phénomène d'autoprotection dans le code de transport multigroupe APOLLO2*. PhD thesis, Conservatoire National des Arts et Métiers.

Coste-Delclaux, M. et al. (2016). GALILEE-1: a validation and processing system for ENDF-6 and GND evaluations. In *EPJ Web of Conferences*, volume 111, page 06005. EDP Sciences.

Courant, R. and Hilbert D. (2008). *Methods of Mathematical Pyhsics, Partial Differential Equations*. John Wiley & Sons.

Cukier, R. I. et al. (1973). Study of the sensitivity of coupled reaction systems to uncertainties in rate coefficients. *The Journal of chemical physics*, 59(8):3873–3878.

Devijver, E. and Galopin, M. (2018). Block-diagonal covariance selection for high-diemnsional gaussian graphical models. *Journal of the American Statistical Association*, 113(521):306–314.

Dos Santos, N. (2013). *Optimisation de l'approche de représentativité et de transposition pour la conception neutronique de programmes expérimentaux dans les maquettes critiques*. PhD thesis, Université Grenoble Alpes.

Dupré, A. et al. (2015). Towards modelling and validation enhancements of the psi mcnpx fast neutron fluence computational scheme based on recent PWR experimental data. *Annals of Nuclear Energy*, 85:820–829.

Ezure, H. (1988). Estimation of most probable power distribution in bwrs by least squares method using in-core measurements. *Journal of Nuclear Science and Technology*, 25(9):731–740.

Habert, B. et al. (2010). Retroactive generation of covariance matrix of nuclear model parameters using marginalization techniques. *Nuclear Science and Engineering*, 166(3):276–287.

Haghighat, A. et al. (1996). Uncertainties in transport theory pressure vessel neutron fluence calculations. *Transactions of the American Nuclear Society*, 74:140–142.

Hassler, L. A. et al. (1985). Babcock & wilcox reactor vessel surveillance service activities. pages 61–67.

Hoeffding, W. (1992). A class of statistics with asymptotically normal distributions. In *Breakthroughs in Statistics*, pages 308–334. Springer.

Iooss, B. et al. (2019). Shapley effects for sensitivity analysis with correlated inputs: comparisons with sobol' indices, numerical estimation and applications. *IMT - Institut de Mathematiques de Toulouse, EDF R& D, submitted to Elsevier*.

JANIS Book (2018). The data bank. http://www.oecd-nea.org/janisweb/book/neutrons/.

Jaynes, E. T. (1957). Information theory and statistical mechanics i. *Physical review*, 106(4):620.

JEFF-3.1 (2013). Validation of the jeff-3.1 nuclear data library: Jeff report 23.

JENDL-4.0 (2011). Jendl-4.0: A new library for nuclear science and engineering. *Journal of Nuclear Science and Technology*, 48(1):1–30.

Johnson, J. (2000). A heuristic method for estimating the relative weight of predictor variables in multiple regression. *Multivariate behavioral research*, 35(1):1–19.

Johnson, R. (1966). The minimal transformation to orthonormality. *Psychometrika*, 31(1):61–66.

Kam, F. et al. (1990). Neutron fluence calculations and uncertainty analysis. In *Proceedings*, page 179.

Kessedjian, G. (2015). *Des données nucléaires expérimentales à l'évaluation : contribution à l'analyse statistique dans la réduction des données et les tests d'hypothèses – application à la fission*. Habilitation a Diriger les Recherches (HDR), Laboratoire de Physique Subatomique et de Cosmologie, École Doctorale de physique de Grenoble, France.

King, G. B. et al. (2019). Direct comparison between bayesian and frequentist uncertainty quantification for nuclear reactions. *Physical Review Letters*, 122(23):232502.

Klein, M. et al. (2012). Interaction of loading pattern and nuclear data uncertainties in reactor core calculations. *PHYSOR2012, Knoxville*, pages 96–161.

Kodeli, I. (1993). *Etudes des incertitudes sur la fluence dans les cuves des REP. Ajustement des donnees de base*. PhD thesis, Université Paris 11.

Kodeli, I. (2001). Multidimensional deterministic nuclear data sensitivty and uncertainty code system: Method and application. *Nuclear Science and Engineering*, 138(1):45–66.

Kodeli, I. et al. (1996). Assessment of uncertainties for PWR pressure vessel surveillance – french experience. *Transactions of the American Nuclear Society*, 74:142–144.

Kucherenko, S. et al. (2012). Estimation of global sensitivity indices for models with dependent variables. *Computer Physics Communications*, 183(4):937–946.

Lahaye, S. (2018). Choice of positive distribution law for nuclear data. *EPJ Nuclear Sciences & Technologies*, 4:38.

Lee, C. E. (1961). *Mechanical quadrature and transport equations*, volume 2573. Los Alamos Scientific Laboratory of the University of California.

Lipovetsky, S. and Conklin, M. (2001). Analysis of regression in game theory approach. *Applied Stochastic Models in Business and Industry*, 17(4):319–330.

Livolant, M. and Jeanpierre, F. (1974). *Autoprotection dans les réacteurs nucléaires*. Rapport CEA - R-4533.

MacFarlane, R. E. (2017). The njoy nuclear data processing system, version 2012. Technical report, Los Alamos National Lab.(LANL), Los Alamos, NM (United States).

Margolin, B. Z. et al. (2005). Prediction of temperature dependence of fracture toughness as a function of neutron fluence for pressure-vessel steels by using the unified curve method. *Strength of materials*, 37(3):243–253.

Marguet, S. (2011). *The Physics of Nuclear Reactors*. Springer.

Martinez, J. (2018). *Analyse de sensibilité de variables dépendantes par les indices de Shapley*.

McLane, V. (2005). ENDF-6 data formats and procedures for the evaluated nuclear data file ENDF-VII.

Mosca, P. et al. (2011). An adaptative energy mesh constructor for multigroup library generation for transport codes. *Nuclear Science and Engineering*, 167(1):40–60.

Mosca, P. et al. (2013). MINARET, improvements in transport calculations by the energy-dependent fission spectra and subgroup method for mutual self-shielding. *Nuclear Science and Engineering*, 175(3):266–282.

Mosca, P. et al. (2018). MINARET, deterministic model of PWR fast fluence for uncertainty propagations with the code APOLLO3®. In *Reactor Dosimetry: 16th International Symposium*. ASTM International.

Mounier, C. (2011). Manuel d'utilisation de GALILEE v0.3.0. Technical Report SERMA/LLPR/RT/11-52149/A, CEA.

Nowak, M. (2018). *Accelerating Monte Carlo particle transport with adaptively generated importance maps*. PhD thesis, Université Paris-Saclay, PHENIICS.

OECD/NEA (1997). Computing radiation dose to reactor pressure vessel and internals. Technical report, NEA/NSC/DOC (96) 5, 1997, OECD-NEA.

Owen, A. B. et al. (2017). On shapley value for measuring importance of dependent inputs. *SIAM/ASA Journal on Uncertainty Quantification*, 5(1):986–1002.

Perin, Y. (2015). Challenge of PWR new core design simulation: A focus on uncertainties due to nuclear data and reflector modelling. *Progress in Nuclear Energy*, 84:89–96.

Privas, E. (2015). *Contribution à l'évaluation des incertitudes sur les sections efficaces neutroniques, pour les réacteurs à neutrons rapides*. PhD thesis, Laboratoire d'Étude Physique, CEA, I-MEP2.

Rakotomalala, R. (2017). French course on the correlation analysis. *Université Lumière Lyon 2, France*.

Remec, I. (1996). On the uncertainty of neutron transport calculations for reactor pressure vessel surveillance. *Transactions of the American Nuclear Society*, 74:144–145.

Reuss, P. (2012). *Neutron Physics*. EDP sciences.

Riley, J. D. (1955). Solving systems of linear equations with a positive definite, symmetric, but possibly ill-conditioned matrix. *Mathematical tables and other aids to computation*, pages 96–101.

Saltelli, A. et al. (2008). *Global sensitivity analysis: the primer*. John Wiley and sons.

Salvatores, M. et al. (2018). Production and use of nuclear parameter covariance data: an overview of challenging cross cutting scientific issues. *EPJ Nuclear Sciences & Technologies*, 4:20.

Sanchez, R. et al. (2010). APOLLO2 years 2010. *Nuclear engineering and technology*, 42(5):474–499.

Santamarina, A. et al. (2014). Nuclear data uncertainty propagation on power maps in large LWR cores. In *JAEA-Conf–2014-003*.

Schneider, D. et al. (2016). APOLLO3®: CEA/DEN deterministic multi-purpose code for reactor physics analysis. In *Proc. Int. Conf. Physics of Reactors (PHYSOR2016)*.

Shannon, C. E. (1948). A mathematical theory of communication. *Bell system technical journal*, 27(3):379–423.

Smith, C. L. (1994). Uncertainty propagation using taylor series expansion and a spreadsheet. *Journal of the Idaho Academy of Science*, 30(2):93–105.

Smith, R. C. (2014). *Uncertainty Quantification: Theory, Implementation, and Applications*, volume 12. Society for Industrial and Applied Mathematics.

Sobol, I. M. (1993). Sensitivity estimates for nonlinear mathematical models. *Mathematical modelling and computational experiments*, 1(4):407–414.

Steele, L. E. (1983). *Status of USA nuclear reactor pressure vessel surveillance for radiation effects*, volume 784. ASTM International.

Vasiliev, A. et al. (2018). On the importance of the neutron scattering angular distribution for the LWR fast neutron dosimetry. *PHYSOR*, 50.

Vassiliev, O. N. (2017). *Monte Carlo Methods for Radiation Transport: Fundamentals and Advanced Topics*. Springer.

Venn, J. (1880). On the diagrammatic and mechanical representation of propositions and reasonings. *The London, Edinburgh, and Dublin philosophical magazine and journal of science*, 10(59):1–18.

Volat, L. et al. (2018). A stochastic method to propagate uncertainties along large cores deterministic calculations. *EPJ Nuclear Sci. Technol.*, 4(12).

Xu, C. et al. (2008). Uncertainty and sensitivity analysis for models with correlated parameters. *Reliability Engineering & System Safety*, 93(10):1563–1573.

Zeng, B. et al. (2017). Geometric views of partial correlation coefficient in regression analysis. *International Journal of Statistics and Probability*, 6(3).

Titre : Quantification de l'incertitude du flux neutronique rapide reçu par la cuve d'un réacteur à eau pressurisée

Mots clés : Incertitudes, flux neutronique, Johnson, Sensibilité, Shapley, Multicolinéarité

Résumé : Pour s'assurer de la sûreté des réacteurs et de l'intégrité de leurs cuves, des programmes de surveillance sont mis en place. Ces derniers dépendent notamment du calcul de densité neutronique qui quantifie le nombre de neutrons rapides (susceptibles de modifier les propriétés mécaniques de la cuve) reçus par les capsules de surveillance. Or, un manque de connaissances sur ce calcul peut obliger l'exploitant à fixer des marges de sûreté supérieures sur la durée de vie des centrales, et donc affecter les conditions de fonctionnement et le coût des installations nucléaires. C'est pourquoi il est essentiel de déterminer l'incertitude du calcul de flux à la cuve des REP.

La plupart des études passées sont basées sur une quantification de l'incertitude par la méthode des moments qui suppose une variation linéaire de la sortie du calcul. Cette hypothèse n'a jamais été vérifiée compte tenu du grand nombre de variables d'entrée et des ressources informatiques relativement limitées pour envisager l'application d'autres méthodes. Une méthode alternative est celle de l'approche Total Monte Carlo (TMC) qui consiste à considérer les paramètres d'entrée du modèle de calcul comme des variables aléatoires, et à propager les perturbations issues d'un tirage statistique dans la chaîne de calcul. L'avantage de cette méthode est qu'elle propose une description plus précise des incertitudes du modèle, et permet de définir des quantiles et donc des intervalles de confiance qui peuvent s'avérer utiles dans le cadre d'une étude de sûreté. C'est dans ce contexte, que cette thèse s'intègre. Elle consiste à déterminer l'incertitude du flux neutronique rapide de la cuve des REP en considérant les librairies de données nucléaires récentes et en utilisant une approche TMC pour la propagation des incertitudes d'entrée. La particularité de ce travail repose sur le grand nombre de paramètres d'entrées corrélés qui nécessite la mise en place de méthodologies adaptées.

En particulier, les indices de Shapley et de Johnson qui sont peu connus dans le domaine du nucléaire, sont proposés dans cette thèse dans le cadre de l'analyse globale de sensibilité d'un problème multicolinéaire.

Title : Uncertainty quantification of the fast flux calculation for a PWR vessel

Keywords : Neutron flux, Uncertainty, Sensitivity Analysis, Multicolinearity, Shapley, Johnson

Abstract : The vessel neutron irradiation, which cannot be replaced, is one of the limiting factors for pressurized water reactor (PWR) lifetime. Surveillance programmes are therefore necessary for safety assessment and for verifying the vessel structural integrity. The quality of radiation damage prediction depends in part on the calculation of the fast neutron flux. In that sense, a lack of knowledge on the fast neutron flux will require larger safety margins on the plant lifetime affecting operating conditions and the cost of nuclear installations. To make correct decisions when designing the plant lifetime and on safety margins for PWR reactors, it is therefore essential to assess the uncertainty in vessel flux calculations.

Most of the past studies on the flux uncertainty quantification are based on the methods of moments which assumes a linear output variation. This method was most commonly used because the calculation capabilities of computers prevented from conducting more accurate methods. In a non-linear case, the first order hypothesis appears insufficient for an accurate prediction of the output variance. An alternative method is the Total Monte Carlo approach (TMC) which consists in randomly sampling the input data and propagating the perturbations on the calculation chain. The advantage of this method is that it does not make any assumptions on the linear interactions or small input changes among data. It considers the probability distributions of input parameters and thus provides a more precise description of input uncertainties.

It is within this context that this thesis was conducted. It consists in performing a new uncertainty assessment of the fast flux calculation for the PWR vessel considering the data of recent international nuclear libraries.

The special feature of this thesis lies in the large number of uncertain parameters which are closely correlated with each other. The uncertainty on the fast flux, considering all the uncertain parameters, is finally estimated for the vessel hot spot. More generally, in this context of sensitivity analysis, we show the importance to consider the covariance matrices to propagate the input uncertainties, and to analyze the contribution of each input on a physical model. The Shapley and Johnson indices are especially used in a multicolinearity context between the inputs and the output.